ISSN 1854-6250

APEM
journal

Advances in Production Engineering & Management

Volume 21 | Number 1 | March 2026

University of Maribor
Published by CPE
apem-journal.org

Advances in Production Engineering & Management

Identification Statement

ISSN 1854-6250 | Abbreviated key title: **Adv produc engineer manag** | Start year: 2006
ISSN 1855-6531 (on-line)

Published quarterly by **Chair of Production Engineering (CPE)**, **University of Maribor**
Smetanova ulica 17, SI – 2000 Maribor, Slovenia, European Union (EU)

Phone: 00386 2 2207522, Fax: 00386 2 2207990
Language of text: English

APEM homepage: apem-journal.org
University homepage: www.um.si

APEM Editorial

Editor-in-Chief

Miran Brezocnik
apem@apem-journal.org
University of Maribor, Faculty of Mechanical Engineering
Smetanova ulica 17, SI – 2000 Maribor, Slovenia, EU

Desk Editor

Martina Meh
desk1@apem-journal.org
Janez Gotlih
desk2@apem-journal.org

Website Technical Editor

Lucija Brezocnik
desk3@apem-journal.org

Editorial Board Members

Eberhard Abele, Technical University of Darmstadt, Germany
Bojan Acko, University of Maribor, Slovenia
Joze Balic, University of Maribor, Slovenia
Agostino Bruzzone, University of Genoa, Italy
Borut Buchmeister, University of Maribor, Slovenia
Ludwig Cardon, Ghent University, Belgium
Nirupam Chakraborti, Indian Institute of Technology, Kharagpur, India
Edward Chlebus, Wroclaw University of Technology, Poland
Igor Drstvensek, University of Maribor, Slovenia
Illes Dudas, University of Miskolc, Hungary
Mirko Ficko, University of Maribor, Slovenia
Vlatka Hlupic, University of Westminster, UK
David Hui, University of New Orleans, USA
Pramod K. Jain, Indian Institute of Technology Roorkee, India
Isak Karabegović, University of Bihać, Bosnia and Herzegovina
Janez Kopac, University of Ljubljana, Slovenia
Changsong Ma, Geely University of China, China
Qingliang Meng, Jiangsu University of Science and Technology, China
Lanndon A. Ocampo, Cebu Technological University, Philippines
Iztok Palcic, University of Maribor, Slovenia
Krsto Pandza, University of Leeds, UK
Andrej Polajnar, University of Maribor, Slovenia
Antonio Pouzada, University of Minho, Portugal
R. Venkata Rao, Sardar Vallabhbhai National Inst. of Technology, India
Rajiv Kumar Sharma, National Institute of Technology, India
Katica Simunovic, J. J. Strossmayer University of Osijek, Croatia
Daizhong Su, Nottingham Trent University, UK
Soemon Takakuwa, Nagoya University, Japan
Nikos Tsourveloudis, Technical University of Crete, Greece
Tomo Udiljak, University of Zagreb, Croatia
Ivica Veza, University of Split, Croatia

OPEN ACCESS

Subsidizer: The journal is subsidized by Slovenian Research and Innovation Agency

Creative Commons Licence (CC): Content from published paper in the APEM journal may be used under the terms of the Creative Commons Attribution 4.0 International Licence (CC BY 4.0). Any further distribution of this work must maintain attribution to the author(s) and the title of the work, journal citation and DOI.

Statements and opinions expressed in the articles and communications are those of the individual contributors and not necessarily those of the editors or the publisher. No responsibility is accepted for the accuracy of information contained in the text, illustrations or advertisements. Chair of Production Engineering assumes no responsibility or liability for any damage or injury to persons or property arising from the use of any materials, instructions, methods or ideas contained herein.

Published by CPE, University of Maribor.

Advances in Production Engineering & Management is indexed and abstracted in the **WEB OF SCIENCE** (maintained by **Clarivate**): **Science Citation Index Expanded**, **Journal Citation Reports** – Science Edition, **Current Contents** – Engineering, Computing and Technology • **Scopus** (maintained by **Elsevier**) • **EBSCO**: Academic Search Alumni Edition, Academic Search Complete, Academic Search Elite, Academic Search Premier, Engineering Source, Sales & Marketing Source, TOC Premier • **ProQuest**: CSA Engineering Research Database – Cambridge Scientific Abstracts, Materials Business File, Materials Research Database, Mechanical & Transportation Engineering Abstracts, ProQuest SciTech Collection • **TEMA** (**DOMA**) • The journal is listed in **Ulrich's** Periodicals Directory and **Cabell's** Directory

University of Maribor
Chair of Production Engineering (CPE)

Advances in Production Engineering & Management

Volume 21 | Number 1 | March 2026 | pp 1–158

Contents

Journal homepage: apem-journal.org

ISSN 1854-6250 (print)
ISSN 1855-6531 (on-line)

Published by CPE, University of Maribor.

Scope and topics

Advances in Production Engineering & Management (*APEM journal*) is an interdisciplinary refereed international academic journal published quarterly by the *Chair of Production Engineering* at the *University of Maribor*. The main goal of the *APEM journal* is to present original, high quality, theoretical and application-oriented research developments in all areas of production engineering and production management to a broad audience of academics and practitioners. In order to bridge the gap between theory and practice, applications based on advanced theory and case studies are particularly welcome. For theoretical papers, their originality and research contributions are the main factors in the evaluation process. General approaches, formalisms, algorithms or techniques should be illustrated with significant applications that demonstrate their applicability to real-world problems. Although the *APEM journal* main goal is to publish original research papers, review articles and professional papers are occasionally published.

Fields of interest include, but are not limited to:

Additive Manufacturing Processes
Advanced Production Technologies
Artificial Intelligence in Production
Assembly Systems
Automation
Big Data in Production
Block Chain in Manufacturing
Computer-Integrated Manufacturing
Cutting and Forming Processes
Decision Support Systems
Deep Learning in Manufacturing
Discrete Systems and Methodology
e-Manufacturing
Evolutionary Computation in Production
Fuzzy Systems
Human Factor Engineering, Ergonomics
Industrial Engineering
Industrial Processes
Industrial Robotics
Intelligent Manufacturing Systems
Joining Processes
Knowledge Management
Logistics in Production
Machine Learning in Production
Machine-to-Machine Economy
Machine Tools
Machining Systems
Manufacturing Systems
Materials Science, Multidisciplinary
Mechanical Engineering
Mechatronics
Metrology in Production
Modelling and Simulation
Numerical Techniques
Operations Research
Operations Planning, Scheduling and Control
Optimisation Techniques
Project Management
Quality Management
Risk and Uncertainty
Self-Organizing Systems
Smart Manufacturing
Statistical Methods
Supply Chain Management
Virtual Reality in Production

APEM journal
Advances in Production Engineering & Management
Volume 21 | Number 1 | March 2026 | 5–15
https://doi.org/10.14743/apem2026.1.557
ISSN 1854-6250
Journal home: apem-journal.org
Original scientific paper

Coordination of material supply chains under multidimensional stochastic risks

Yang, C.[a], **Jian, M.**[a,*], **Fang, X.**[b]

[a]School of Transportation and Logistics, Southwest Jiaotong University, Chengdu, P.R. China
[b]International College, Krirk University, Bangkok, Thailand

ABSTRACT

This paper investigates optimal decision-making and coordination in a material supply chain under multidimensional stochastic risks, including uncertain demand, yield, and processing activities. By analyzing a system consisting of a manufacturer and a supplier, we derive the unique optimal purchasing and stocking decisions that maximize the expected profit of the integrated supply chain. A wholesale price contract is proposed to coordinate decentralized participants, incorporating risk allocation through a linear combination of production cost risk and sales profit risk. The key findings indicate that elevated risk dimensions lead to an increase in optimal order and inventory quantities. However, they also result in a reduction in system profit and a narrowing of the coordination price range. Numerical analyses demonstrate that, when faced with heightened multidimensional risks, enterprises should increase safety stocks and ordering levels to maintain supply stability. At the same time, supply chain members should negotiate wholesale prices within a more restricted interval to achieve effective coordination. Contract flexibility and risk sharing become more significant in maintaining efficiency under high-uncertainty conditions. Sensitivity analysis demonstrates the robustness of the proposed mechanism, emphasizing its flexibility in profit sharing under stochastic conditions. This study contributes to supply chain risk management by providing a generalized contract framework that aligns decentralized decisions with centralized optimization, thereby ensuring stability and efficiency in high-risk industrial environments.

ARTICLE INFO

Keywords:
Material supply chain;
Coordination contract;
Wholesale price;
Demand uncertainty;
Yield uncertainty;
Processing uncertainty;
Supply chain risk

**Corresponding author:*
jianming@swjtu.edu.cn
(Jian, M.)

Article history:
Received 8 May 2025
Revised 15 April 2026
Accepted 17 April 2026

1. Introduction

This paper investigates the design of a generalized coordination mechanism for coordinating material supply chains across diverse uncertainty dimensions. These uncertainty dimensions arise from demand, yield, and processing activities [1]. Multiple uncertain risks affect the availability of materials during their transit from suppliers to construction projects. These risks can lead to performance degradation, cost escalation, scheduling delays, and ultimately, project failures [2, 3]. Consequently, inadequate supply chain management (SCM) can be regarded as a potential contributor to cost overruns and delays in the construction industry. Although the concept of supply chain management has its roots in the manufacturing industry, enterprises in the materials industry can also reap benefits from implementing such best-practice approaches in certain processes [4]. Nevertheless, SCM remains underdeveloped in the construction industry [5]. Furthermore, despite its significant potential, the application of supply chain risk management in the materials industry has yet to be investigated.

In the past few decades, both practitioners and scholars have emphasized that the complexity of engineering and construction exposes it to more significant risks than other industries. These risks can lead to reduced performance, increased costs, schedule delays, and ultimately, project failure [1]. There have been numerous natural and man-made disasters (e.g., earthquakes, economic crises, wars, terrorist attacks, and sanctions) that disrupt the operations of the material supply chain. Coleman [6] found extensive evidence showing that the frequency of disruptions caused by man-made disasters has increased exponentially since the 20th century. These disruptions have been observed to be increasing in both the probability of occurrence and their magnitude [7]. Supply chain disruptions are inevitable, making all supply chains risky [8]. Therefore, the effective management of risks in materials supply chains is of crucial importance for the successful delivery of projects.

More precisely, compared with other industries, large-scale engineering projects have faced a substantial number of risks due to the strategic characteristics of materials, the complexity of construction techniques, the dynamic construction environment, the participation of diverse stakeholders, and the lengthy construction cycle [9]. Ineffective supply chain management can be considered a potential cause of some of the cost overruns and delays in the engineering industry. Consequently, risk management is increasingly regarded in the engineering project management literature as a means to increase the probability of success of complex engineering projects [10]. Effective risk management systems aimed at preventing project performance deterioration, time delays, and unnecessary costs have prompted scholars to propose various risk management approaches [11]. Taroun conducted a review of 50 years of risk modeling and assessment in construction projects and argued that there is a disparity between practice and theory, that managers mainly rely on their experience, and that the application of the analytical tools proposed in the literature is highly limited.

In the face of uncertain risks across different dimensions, a fundamental issue that needs to be resolved is how the manufacturer (or supplier) formulates optimal purchasing (or stocking) decisions and how to mitigate these risks. To the best of our knowledge, no existing literature has explored the problem of optimal decision-making for materials with uncertainties in project demand, yield, and processing operations. Moreover, even fewer scholars have analyzed the coordinated contract design based on risk allocation among firms within the framework of a material integration system. The traditional "manufacturer + suppliers" model has the drawbacks of unstable transactions and contracts. In contrast, the manufacturer ⁻ supplier model based on the material integration system can ensure a stable contractual relationship, effectively reduce transaction costs, and contribute to the healthy and sustainable development of industrialization [12].

Therefore, based on the paradigm assumption that stochastic distributions describe multidimensional uncertain risks, this paper investigates the optimal procurement and inventory decisions of the manufacturer and the supplier, and proposes a coordinated contract encompassing multidimensional stochastic risks. The primary contribution of this article lies, on one hand, in extending the research on material operations optimization to scenarios where demand, yield, and processing activities are all stochastic, and conducting a distinctive analysis of the optimal decisions of the manufacturer and the supplier under multidimensional stochastic risks. Additionally, the sensitivity of the optimal decision to risk variations is explored. On the other hand, a coordinated wholesale-price contract covering risks is proposed, enabling the manufacturer and the supplier to flexibly share the optimal profit of the channel. Moreover, this contract can also coordinate the material supply chain with stochastic yield and demand or only stochastic demand, which is why it is defined as a generalized coordinated contract.

The subsequent sections review the relevant literature. Section 3 defines the modeling assumptions and notational implications. Section 4 analyzes optimal decisions and simulations. The final section presents the conclusions.

2. Literature review

The optimal procurement decision of the firm under uncertainty can be traced back to the groundbreaking research of Arrow *et al.* [13]. They initially derived an optimal inventory model where the future demand flow is a random variable with a known probability distribution. To address the fundamental issue of how random yields impact the production or ordering decision in a periodic review system, Wang and Gerchak examined a periodic review production system characterized by random yield and demand uncertainty [14]. Numerous scholars have extended the research on firms' procurement or production under supply and demand stochasticity from multiple perspectives [15, 16]. Particularly, in the literature on project management, risk management is increasingly regarded as a means to enhance the probability of success in complex engineering projects [10]. Nevertheless, studies indicate that project managers inadequately utilize risk management practices [17]. More precisely, compared with other industries, the construction industry has been confronted with numerous risks owing to factors such as the strategic nature of its products, the complexities of construction techniques, the changing building environment, the involvement of diverse stakeholders, and long production cycles [11]. Therefore, the necessity of establishing an effective risk management system to prevent project performance degradation, time delays, and undesired costs has compelled project management scholars to propose a variety of risk management approaches.

The allocation of uncertain risks during the sales period poses a substantial impediment to inter-firm cooperation [18]. To mitigate these risks, Pasternack initially investigated a supply-chain coordination contract, namely the buyback contract, from the perspective of quantity buyback. That is, in the face of demand uncertainty, upstream firms commit to repurchasing the remaining inventory of downstream firms at the end of the sales period [19]. Over the subsequent three decades, scholars have formulated contracts to coordinate decentralized supply chains under stochastic demand from multiple viewpoints, such as revenue-sharing contracts, quantity flexibility contracts, and sales rebate contracts [20]. As an expansion of the uncertainty risk dimension, He and Zhang proposed several risk-sharing contracts that distribute the random yield risk among the involved parties [21]. Güler and Bilgiç proposed two contracts for coordinating the supply chain under forced compliance, where both customer demand and supplier yield are random [22]. Hu *et al.* examined a flexible purchasing policy considering random yield and demand uncertainty and proposed a revenue-sharing policy with an order penalty and rebate contract to fully coordinate the supply chain [23]. Güler and Keskin found that the randomness in yield does not alter the coordination capacity of the contracts but influences the values of the contract parameters [24]. Cai *et al.* introduced an option contract to enhance the performance of the inventory supply chain under yield uncertainty and stochastic demand [25]. Sonntag and Kiesmüller considered a single-stage production system with a favorable production time and random yield [26]. Stojic *et al.* presented the proposed model for monitoring and managing business risks in industrial systems [27].

Game theory and evolutionary game models have emerged as important tools for research on supply chain coordination and risk-sharing. Wang *et al.* [28] established a game-theory framework to optimize the cooperation and profit-sharing mechanisms between manufacturers and suppliers, offering a valuable reference for vertical cooperation and benefit distribution within supply chains. Zhao *et al.* [29] proposed an ANP–Hopfield neural network approach for supply chain stress testing, thereby enriching the quantitative methods for risk assessment and resilience verification under high degrees of uncertainty. Xi *et al.* [30] analyzed the influence of retailer fairness concerns on freshness-keeping efforts and pricing strategies in fresh agricultural product supply chains and explored effective coordination mechanisms, providing insights for contract design under behavioral factors. Xu *et al.* [31] employed evolutionary game models to conduct a comparative analysis of the impact of fairness concerns on resource-sharing decisions in manufacturing enterprises, uncovering the decision-making logic of cooperative behavior under risk asymmetry. Ji *et al.* [32] investigated the influence of government guidance on the production mode selection of automobile enterprises based on an evolutionary game, expanding the application scenarios of game theory in supply chain decisions with external policy interventions.

Regarding risk allocation contracts, He and Zhang proposed several risk-sharing contracts that allocate random yield risk among parties and evaluate supply chain performance [21]. They considered three scenarios in which the retailer shares random yield risk with the supplier. Zhou *et al.* constructed a model in which the retailer formulates a risk-sharing contract for the manufacturer under conditions of random yield and private productivity information to analyze the interaction between risk-sharing and asymmetric information [33]. Behzadi *et al.* comprehensively reviewed the relatively scarce literature on quantitative risk management models for agricultural supply chains [34]. Besik *et al.* developed an integrated multi-tiered competitive agricultural supply chain network model in which farming and processing firms engage in competition to sell their differentiated products [35]. Our model takes into account multidimensional stochastic risks in the coordination contract parameters. In this model, multidimensional stochastic risks are incorporated into the coordination contract parameters, and the designed contract can be implemented as the cooperative system provides a stable environment.

3. The model

This paper considers a material integration system comprising a manufacturer (M) and a supplier (S), in which the manufacturer organizes the supplier to supply materials to fulfill the project needs. Fig. 1 shows a schematic of this collaboration system. In a desirable situation, the manufacturer can schedule the supplier to supply q units of material with a random project need X. However, the supplier may need to stock Q units due to various risks (e.g., uncontrollable processing failures, poor humidity management, etc.). Hence, we are interested in how to determine the optimal q and Q under a combination of uncertainties and how the manufacturer and the supplier can design the cooperative contract to achieve the optimal profit. The following generalized assumptions are introduced to address these questions.

Project material demand, material stock, and processing activities are assumed to be random. In practical applications, decision-makers often use probability distributions to characterize the uncertainties they face, as demonstrated in the classic newsvendor problem[16]. This approach is well established in the literature [1, 16, 20]. The assumptions are as follows.

1. Let X be a random project material needs variable on a closed interval $[\underline{X}, \overline{X}]$, $\underline{X}, \overline{X} \in \mathcal{R}^{+}$. The probability density function (p.d.f.) and cumulative distribution function (c.d.f.) of variable X are $f(x)$ and $F(x)$, respectively. $F(x)$ has monotonically increasing, second-order continuous differentiable, and reversible properties. Define $\overline{F}(x) = 1 - F(x)$, and the mean of demand is μ_x.
2. The actual materials yield is UQ units, where U is a random variable on the closed interval $[\underline{U}, \overline{U}]$, $0 \leq \underline{U} < \overline{U} \leq 1$. The p.d.f and c.d.f of U are $g(u)$ and $G(U)$, respectively. $G(U)$has monotonically increasing, second-order continuous differentiable, and reversible properties.
3. Materials need to go through a series of processing activities before being applied to the project, such as stocking, picking, packing, transportation, etc. It is assumed that the processes are random and that the final quantity on the project is $Omin(UQ, q)$, where variable O is random on a closed interval $[\underline{O}, \overline{O}]$, $0 \leq \underline{O} < \overline{O} \leq 1$. The p.d.f. and c.d.f. of O are $m(o)$ and $M(o)$, respectively. $M(o)$ has monotonically increasing, second-order continuous differentiable, and reversible properties. The mean of variable O is μ_O.

   Although there are multiple uncertain risks in the material supply chain, for the sake of computational simplicity, this study posits that decision-makers, namely manufacturers and suppliers, are risk neutral and engage in collaboration through wholesale contracts. Risk neutrality is widely utilized in supply chain coordination literature to ensure analytical tractability when focusing on contract design and risk allocation [13, 20, 21]. In practical situations, construction material supply chains involve long-term integrated systems, where firms diversify risks at the corporate level, leading to approximately risk-neutral operational decisions at the project level [5, 15]. Since this paper emphasizes coordination and risk allocation through wholesale price contracts, risk neutrality helps to clarify the mechanism without introducing unnecessary complexity. Therefore,
4. The manufacturer purchases q units of materials for w per unit, where q is the decision variable, and w is the contract parameter.
5. The supplier plans to stock Q units of materials for the cost c_S per unit, in which Q is the decision variable.
6. The manufacturer receives $min(UQ, q)$ units of materials and has $Omin(UQ, q)$ units applied to the project at unit price p after a series of processing activities with cost c_M per unit, where we assume p is an exogenous variable. Such an assumption is reasonable when a

particular supplier and manufacturer cannot influence the global market.

In summary, given the wholesale contract, the manufacturer purchases q units, and the supplier stocks Q units. However, the former receives $min(UQ,q)$ units, and the final quantity of materials available for application is $O\ min(UQ,q)$ due to uncertainties. Furthermore, the salvage value and stock-out penalty for the materials are assumed to be zero.

Assuming a zero salvage value and a zero stock-out penalty represents a standard simplification within supply chain coordination and newsvendor-based models. This simplification is employed to ensure analytical tractability without sacrificing generality [16, 19, 20]. This assumption facilitates the isolation of the impacts of multidimensional risks (including demand, yield, and processing uncertainty) and the coordination mechanism. It is extensively adopted in research concentrating on contract design and risk allocation [21, 24]. Extensions incorporating positive salvage or stock-out costs would merely adjust the optimal thresholds without altering the core coordination structure of the proposed wholesale price contract.

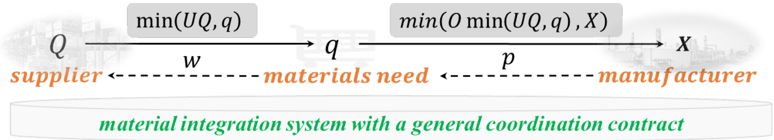

Fig. 1 Schematic diagram of the material integration system under uncertainties

4. Model analysis

The model analysis is conducted in two parts. Initially, the optimal decision, which serves as a benchmark for the material integration system, is determined. Subsequently, the wholesale price incorporating risk factors is formulated to encourage the decisions of the manufacturer and the supplier to align with the benchmark.

4.1 Optimal decisions

The expected profit function of the material integration system is shown as Eq. 1,

$$\Pi = pE[min(Omin(UQ,q),X)] - c_M E[min(UQ,q)] - c_S Q \tag{1}$$

The first item in Eq. 1 represents the expected revenue from the project, and the last two represent the cost of the manufacturer's processing activities and the supplier's stock, respectively. Let $L(Q,q)$ and $S(Q,q)$ be the manufacturer's expected purchasing and expected sales quantity, respectively. Then we can calculate the optimal decisions of the system shown in proposition 1.

$$L(Q,q) = E[min(UQ,q)] = Q\left[\int_{\underline{U}}^{q/Q} \overline{G}(u)du + \underline{U}\right],$$

$$S(Q,q) = E[min(Omin(UQ,q),X)] = \begin{Bmatrix} \underline{X} + Q\int_{\underline{U}}^{q/Q}\int_{\underline{O}}^{\overline{O}} ug(u)\overline{M}(o)\overline{F}(ouQ)dodu + \\ \int_{\underline{U}}^{q/Q}\int_{\underline{X}}^{uOQ} g(u)\overline{F}(x)dxdu + \overline{G}(q/Q)\left[q\int_{\underline{O}}^{\overline{O}}\overline{M}(o)\overline{F}(oq)do + \int_{\underline{X}}^{Oq}\overline{F}(x)dx\right] \end{Bmatrix}.$$

Proposition 1. There is a unique set of optimal values (Q^*,q^*) that maximizes function Π and satisfies Eq. 2,

$$\begin{cases} \int_{\underline{O}}^{\overline{O}}\{\overline{M}(o)\overline{F}(oq^*)[1-r(oq^*)]\}do + \underline{O}\overline{F}(\underline{O}q^*) = \frac{c_M}{p} \\ \int_{\underline{U}}^{q^*/Q^*}\int_{\underline{O}}^{\overline{O}}\{ug(u)\overline{M}(o)\overline{F}(ouQ^*)[1-r(ouQ^*)]\}dodu + \int_{\underline{U}}^{q^*/Q^*}\{ug(u)\underline{O}\overline{F}(u\underline{O}Q^*)\}du = \frac{c_M\int_{\underline{U}}^{q^*/Q^*}ug(u)du + c_S}{p} \end{cases} \tag{2}$$

where, $r(x) = xf(x)/\overline{F}(x)$.

Let Π^* be the optimal value of the material integration system, which can be calculated by taking (Q^*,q^*) into Eq. 1.

We can see from Eq. 2 that the manufacturer's optimal purchasing does not include the randomness of material yield. The risk of both processing and demand affect the manufacturer's optimal purchasing. However, the risk of yield, processing, and material demand affects the supplier's optimal stock quantity.

To illustrate the practical implications of the model, an empirical case analysis is carried out using a large-scale transportation infrastructure project in western China. This project involves the procurement of core construction materials, including high-strength steel bars, ready-mixed concrete, and asphalt mixtures. All these materials are subject to significant multidimensional stochastic risks, which are presented as follows. (1) Demand uncertainty: The actual consumption of materials fluctuates due to the dynamic nature of construction progress, adjustments in geological conditions, and design modifications. Based on the project's historical consumption data, it conforms to a normal distribution $X \sim N(60{,}10^2)$ (unit: tons/period). (2) Supply/yield uncertainty: The production yield of steel bars and concrete is affected by the quality of raw materials and the stability of the production line, with a random yield rate $U \sim N(0.8{,}0.1^2)$. (3) Processing/transportation uncertainty: Random losses occur during the transportation and on-site processing of materials as a result of road conditions, loading/unloading operations, and mixing errors. The processing efficiency is characterized by a normal distribution $O \sim N(0.8{,}0.2^2)$. These parameters are fully consistent with the project's actual operational data, providing real-world industrial validation for the proposed model.

Scenario I in Table 1 presents the optimal purchasing (77.60) and optimal stock (88.00) decisions under the given parameter assignment and the optimal profit (20.53) of the system under these optimal decisions.

Table 1 Optimal values for given parameter assignments

Scenarios	q^*	Q^*	θ	Θ	w_L/p	w_U/p	Π^*/p
I	77.60	88.00	1.27	0.72	0.13	0.42	20.53
II	65.24	80.00	1.15	0.81	0.12	0.51	27.37
III	62.53	62.53	1.00	0.91	0.10	0.61	32.14

Note: $X{\sim}N(60{,}10^2), U{\sim}N(0.8{,}0.1^2), O{\sim}N(0.8{,}0.2^2), [\underline{U}, \overline{U}] = [\underline{O}, \overline{O}] = [0.2{,}1.0], \left(\frac{c_M}{p}, \frac{c_S}{p}\right) = (0.30{,}0.10)$

Corollary 1 is an extension of the firm's optimal decision. More specifically, if $S(Q,q)$ is modified as $\int_{\underline{X}}^{q} \overline{F}(x)dx + \underline{X} - Q \int_{\underline{U}}^{q/Q} \overline{F}(uQ)G(u)du$, then proposition 1 reduces to an optimization decision solution when the yield and demand of materials are random. If $L(Q,q)$ is modified to be q, and $S(Q,q)$ is corrected to be $\int_{\underline{X}}^{q} \overline{F}(x)dx + \underline{X}$, Eq. 2 reduces to an optimization decision problem that only assumes random demand.

Corollary 1. (1) When the randomness of the processing activity is not considered, the optimal values that maximize (q^*, Q^*) the system's profit can be calculated as Eq. 3,

$$\begin{cases} p\overline{F}(q^*) - c_M = 0 \\ p\left[\frac{q^*}{Q^*}\overline{F}(q^*)G(q^*/Q^*) - \int_{\underline{U}}^{q^*/Q^*} G(u)\overline{F}(uQ^*)[1 - r(uQ^*)]du\right] - c_M \int_{\underline{U}}^{q^*/Q^*} ug(u)du - c_S = 0 \end{cases}. \tag{3}$$

and (2) when only market demand is considered as a random variable, the optimal decision is shown as Eq. 4,

$$q^* = Q^* = \overline{F}^{-1}\left(\frac{c_M + c_S}{p}\right). \tag{4}$$

In Model I, the yield, processing operations, and demand are assumed to be stochastic. In Model II, there is no risk associated with processing operations, and in Model III, only the demand is stochastic. As can be observed from Table 1, with the expansion of risk, the manufacturer's procurement volume (q^*) increases, which further necessitates the supplier to hold a larger inventory of materials (Q^*). Fig. 2 depicts the trend of the manufacturer's procurement quantity in relation to its cost structure. From this, it can be seen that as the manufacturer's cost gradually rises, their procurement quantity tends to decline. Simultaneously, Fig. 2 also indicates that the magnitude of the decrease in the manufacturer's procurement volume increases as the type of risk intensifies.

Likewise, Fig. 3 depicts the supplier's production quantity decision. It is evident that the supplier's optimal production quantity declines as both its own cost structure and that of the manufacturer increase. Additionally, Fig. 3 shows that for any given party's cost structure, the supplier's optimal production quantity decreases in relation to the given cost structure. Moreover, by comparing the three scenarios in Fig. 3, it is shown that the supplier's optimal production rises as the type of risk escalates.

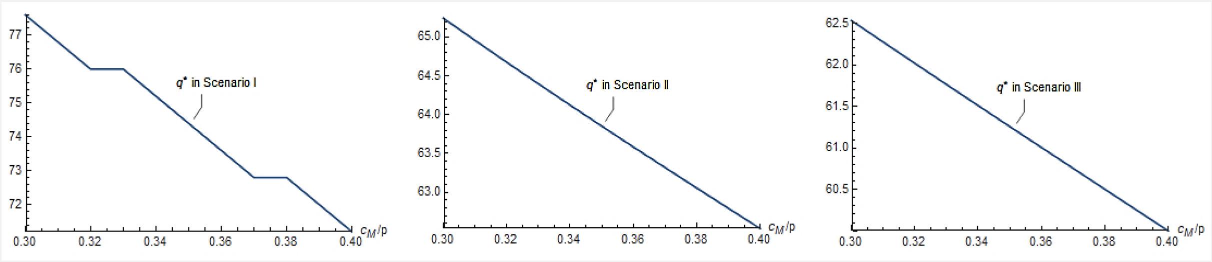

Fig. 2 The changes of q^* with the cost structure in different scenarios

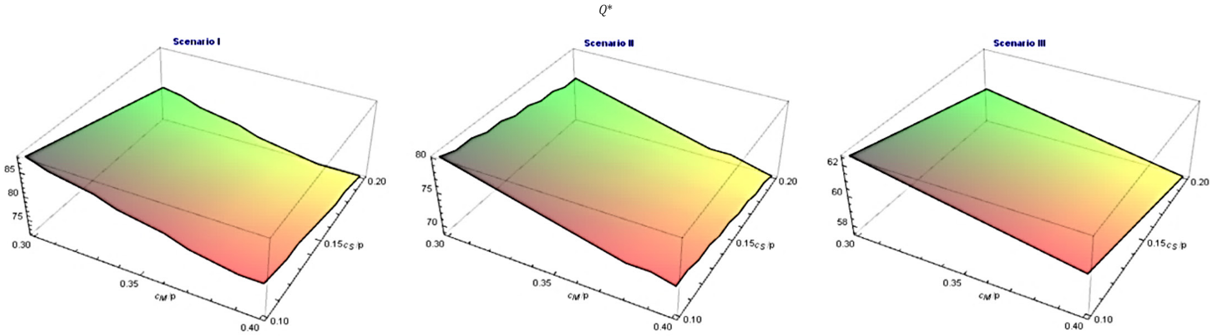

Fig. 3 Changes in Q^* with parties' cost structures under different scenarios

4.2 Contract design

The question is how these rational entities can distribute this optimal "resource" in the context of multiple stochastic risks. In order to achieve this, not only do the manufacturer and the supplier jointly share various stochastic risks, but their optimal decisions also align with those of the material integration system.

Given the wholesale contract, the expected profit functions of the manufacturer (π_M) and the supplier (π_S) are shown in Eq. 5,

$$\begin{cases} \pi_M = pE[min(Omin(UQ,q),X)] - (w + c_M)E[min(UQ,q)] \\ \pi_S = wE[min(UQ,q)] - c_S Q \end{cases} \tag{5}$$

In Eq. 5, the wholesale price serves as the sole link facilitating the profit transfer between the manufacturer and the supplier. Proposition 2 demonstrates the existence of an acceptable wholesale price, enabling both the manufacturer and the supplier to attain Pareto optimality.

Proposition 2. Consider the parameter w shown in Eq. 6,

$$w = \delta c_S \theta + (1 - \delta)(p\Theta - c_M), \tag{6}$$

and $\delta \in (0,1), \theta = Q/L\,, \Theta = S/L$. Under the wholesale price contract with the parameter w, the manufacturer's and the supplier's profit functions are shown in Eq. 7,

$$\begin{cases} \pi_M(Q,q) = \delta\Pi(Q,q) \\ \pi_S(Q,q) = (1 - \delta)\Pi(Q,q) \end{cases} \tag{7}$$

Moreover, the set (q^*, Q^*) represents the manufacturer's optimal procurement and the supplier's optimal inventory. The wholesale contract coordinates the material integration system.

The proposition suggests that δ represents the manufacturer's share of the profit within the material integration system. Consequently, a wholesale price contract with parameter w can coordinate the system and allocate profit arbitrarily. The specific profit split selected likely hinges on the firm's relative bargaining power. As the manufacturer's bargaining position is enhanced, an increase in δ is anticipated.

Parameters θ and Θ describe different random risks in the material integration system. $\theta, \in [1, \infty)$ is a ratio of the supplier's optimal stock quantities to the manufacturer's expected purchasing and reflects the random yield risk of materials. The larger the value of θ is, the lower the expected purchasing will be, which means that the random yield risk of the materials is more significant. Conversely, the manufacturer's expected purchasing quantity tends towards the supplier's optimal stock when $\theta \to 1$, which means there is almost no random yield risk. $\Theta, \in (0,1]$

represents the ratio of the manufacturer’s expected sales quantity to its expected purchasing. The value of Θ reflects the combined risk of the random yield, processing activities, and demand. The larger the value of Θ is, the closer the project sales are to the manufacturer’s expected purchasing; by contrast, the expected sales quantity is close to zero when $\Theta \to 0$. In the case of the given risk, Table 1 mentioned above shows the values of θ and Θ of the three models.

Notably, w serves as the link between the manufacturer and the supplier and is used to achieve the purpose of profit sharing and risk allocation. On the one hand, it is a linear combination of $c_S\theta$ and $(p\Theta - c_M)$, representing the stock cost risk and sales-profit risk. It can be calculated that $w_L = c_S\theta$ when $\delta \to 1$, which indicates that the value per unit purchased from the supplier is meager. At this time, the manufacturer’s purchasing cost is low and captures the entire optimal profit of the material integration system. Conversely, we have $w_U = (p\Theta - c_M)$ when $\delta \to 0$, the supplier obtains the highest selling price, and the manufacturer must pay a higher marginal purchasing cost. Parameter w is also a function of both parameters θ and Θ. These two parameters characterize the risks derived from the material integration system's random yield, processing activities, and demand. Hence, risk allocation is achieved between the manufacturer and the supplier based on the coordinated wholesale price contract.

The proposed wholesale price contract can be systematically implemented in practical material supply chains through a standardized operational approach. First, channel members calibrate stochastic parameters such as demand, yield, and processing efficiency based on historical industrial data. Second, the system-optimal procurement quantity (q^*) and stocking quantity (Q^*) are jointly calculated to align individual decisions with the integrated optimum. Third, the feasible coordination wholesale price range ($[w_L, w_U]$) is determined to ensure acceptable profits for both parties. Fourth, the profit-sharing coefficient (δ) is negotiated according to relative bargaining power and risk-bearing capacity. Finally, the contract can be applied within the long-term material integration system to achieve sustained risk sharing and efficient operation. This implementation path ensures the operability, transparency, and stability of the coordination mechanism in real industrial scenarios.

As can be observed from Table 1, the coordination thresholds for wholesale prices vary across the three models. Fig. 4 depicts the variability of the coordinated wholesale price in relation to the firms' cost structure under the three scenarios. A comparison of the three models indicates that as the dimension of risks gradually expands, the range of coordination prices progressively contracts. In other words, as the level of risk increases, the range of wholesale prices available for negotiation between manufacturers and suppliers diminishes.

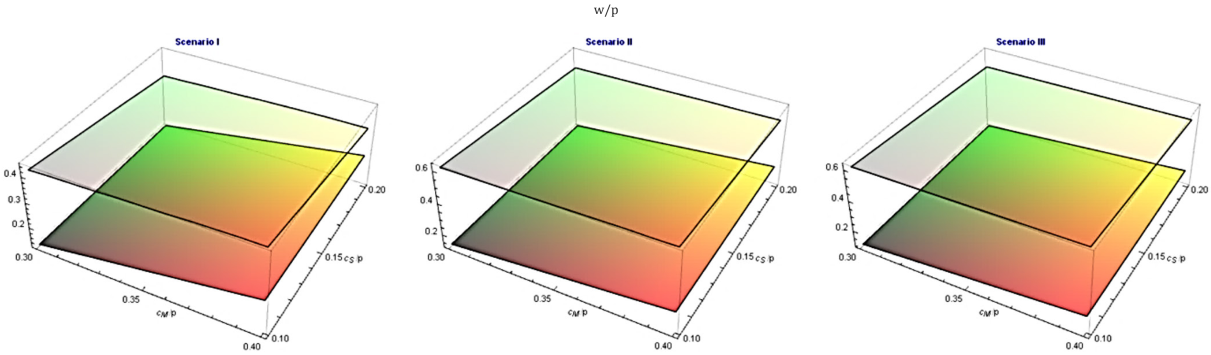

Fig. 4 Changing rules of coordinated wholesale prices with firms' cost structures

Proposition 2 demonstrates that a wholesale-price contract incorporating risk factors can achieve coordination between the manufacturer and the supplier within the material integration system. In this case, their decisions align with the system's optimal decisions. Consequently, when the wholesale-price contract is configured according to Eq. 6, the manufacturer's optimal purchase quantity q^* and the supplier's optimal stock Q^* can be derived from Proposition 1. Subsequently, the material integration system's optimal profit Π^* can be computed in accordance with Eq. 1. Table 1 documents q^*, Q^*, and Π^* for three models under the assumption that the stochastic risk is $X \sim N\ (60,10^2), U \sim N\ (0.8,0.1^2)$, and $O \sim N\ (0.8,0.2^2)$, respectively. Fig. 5 depicts the influence of fluctuations (i.e., variance changes) in each risk on the optimal profitability of an integrated supply chain. One key finding is that as the dimension of risk (or the variance of risk) increases, the optimal profit declines.

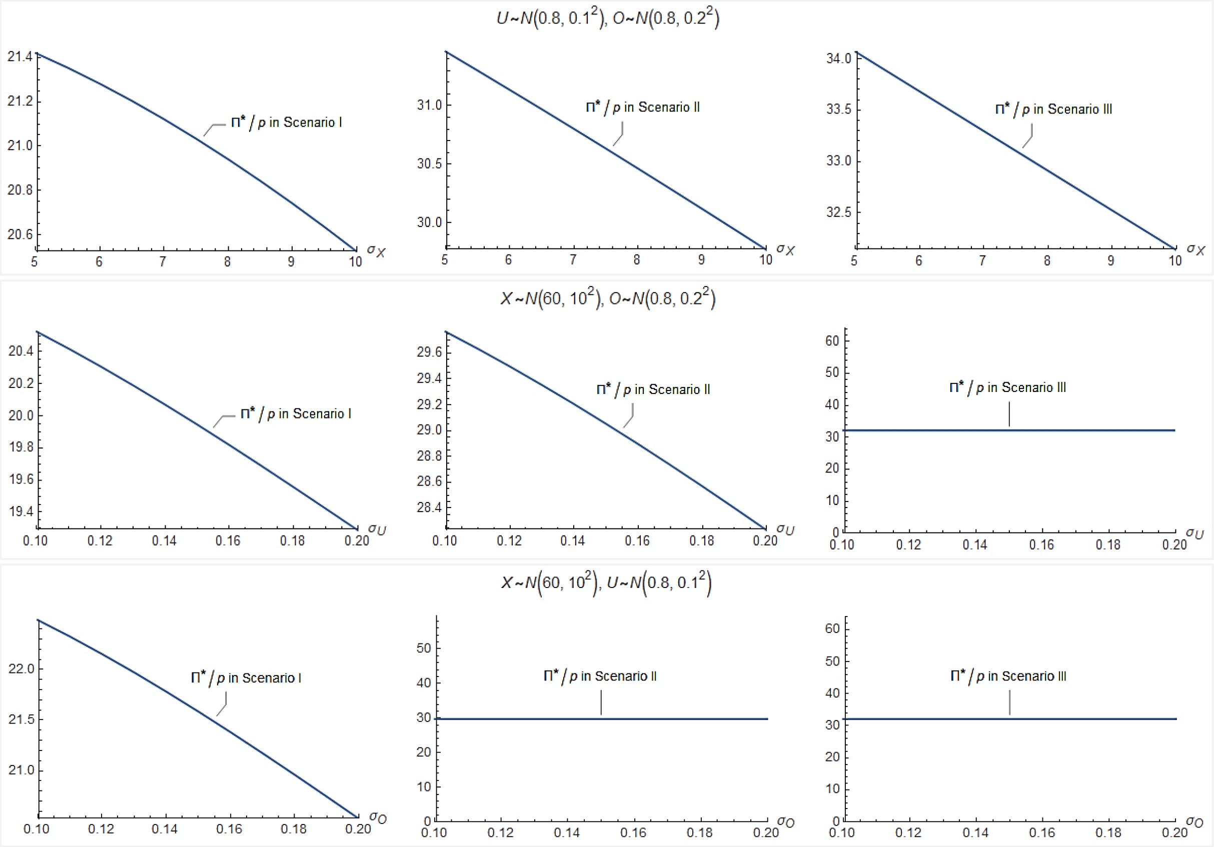

Fig. 5 Variation in the integrated supply chain's optimal profit with risk fluctuations

5. Conclusion

This paper investigates the optimal decision-making and risk allocation mechanism for the manufacturer and the supplier within the framework of the material integration system under conditions of random materials demand, yield, and processing activities. The main conclusions are as follows.

First, there is a set of optimal decision-making strategies that maximize the expected profit of the material integration system. Specifically, when faced with stochastic risks of various dimensions within the material integration system, the manufacturer's optimal procurement quantity and the supplier's optimal inventory level are unique. These can be calculated according to Proposition 1 and Corollary 1. The numerical and sensitivity analysis indicates that as the risk dimension increases, the optimal decisions of both the manufacturer and the supplier gradually increase, whereas the optimal expected profit gradually declines. Meanwhile, it is found that the manufacturer's optimal procurement quantity rises with the increase in risk (i.e., variance). Additionally, as the risk increases, the supplier's optimal inventory level ascends, while the optimal profit of the integrated system declines.

Second, the designed wholesale-price contract incorporating multidimensional random risks can coordinate the actions of the participants. Both the manufacturer and the supplier can flexibly allocate the optimal expected profit of the material integration system. In this simple wholesale-price contract, the negotiated transaction price is a linear combination of the inventory-cost risk and sales-profit risk. This implies that the coordinated wholesale price will be determined when the material supply chain is risk-free. However, as the risk dimension broadens, the lower bound of the coordinated trading price gradually increases due to the increase in θ. Meanwhile, its upper bound gradually decreases due to the decrease in Θ. Consequently, the price range for coordinating the material supply chain narrows as the risk dimension increases. The sensitivity analysis validates this conclusion, as depicted in Fig. 4. The contract with multidimensional risk factors can be executed once the firms participate in the material integration system.

In summary, the major contribution of this paper lies in its analysis of an operations research model to address the optimal decision-making problem for the manufacturer and the supplier under the conditions of random demand, yield, and processing operations. A comprehensively coordinated wholesale price contract integrating multidimensional risks is formulated to flexibly allocate the optimal profit of the integrated system. The imbalance between supply and demand influences the price fluctuations of materials. Hence, it would be more practical to consider optimal decision-making and coordination contracts with endogenous price variables.

Moreover, this paper assumes that the costs of the manufacturer and the supplier are common knowledge. However, under multiple uncertainties, validating these costs presents challenges, which directly influence the determination of wholesale-price parameters. Additionally, it is assumed that the salvage value and stock-out costs of the materials are zero. Nevertheless, these assumptions significantly impact the structure of the decision-making problem. Based on this paper, these aspects shape the directions for future research.

Acknowledgments

This work was carried out with the financial support of the Youth Program of Chongqing Social Science Planning (No. 2024NDQN043), the Program of Chongqing Municipality Natural Science Foundation (2023NSCQ-MSX3688); the Western Project of National Social Science Foundation (No. 23XGL037); the CSC (grant number 201908505102).

References

[1] Xing, G.M., Zhong, Y.G., Zhou, Y.-W., Cao, B. (2025). Distributionally robust production and pricing for risk-averse contract-farming supply chains with uncertain demand and yield, *Transportation Research Part E: Logistics and Transportation Review*, Vol. 198, Article No. 104074, doi: 10.1016/j.tre.2025.104074.

[2] Zou, Y., Kiviniemi, A., Jones, S.W. (2017). Retrieving similar cases for construction project risk management using Natural Language Processing techniques, *Automation in Construction*, Vol. 80, 66-76, doi: 10.1016/j.autcon.2017.04.003.

[3] Wiśniewski, T. (2025). Using large language models (LLMs) to support simulation-based optimization in supply chain management, *Advances in Production Engineering & Management*, Vol. 20, No. 4, 491-506, doi: 10.14743/apem2025.4.554.

[4] Ellram, L.M., Tate, W.L., Billington, C. (2004). Understanding and managing the services supply chain, *Journal of Supply Chain Management*, Vol. 40, No. 3, 17-32, doi: 10.1111/j.1745-493X.2004.tb00176.x.

[5] Liao, L.H., Yang, C., Quan, L.R. (2023). Construction supply chain management: A systematic literature review and future development, *Journal of Cleaner Production*, Vol. 382, Article No. 135230, doi: 10.1016/j.jclepro.2022.135230.

[6] Coleman, L. (2006). Frequency of man-made disasters in the 20th century, *Journal of Contingencies and Crisis Management*, Vol. 14, No. 1, 3-11, doi: 10.1111/j.1468-5973.2006.00476.x.

[7] Blackhurst, J., Craighead, C.W., Elkins, D., Handfield, R.B. (2005). An empirically derived agenda of critical research issues for managing supply-chain disruptions, *International Journal of Production Research*, Vol. 43, No. 19, 4067-4081, doi: 10.1080/00207540500151549.

[8] Craighead, C.W., Blackhurst, J., Rungtusanatham, M.J., Handfield, R.B. (2007). The severity of supply chain disruptions: Design characteristics and mitigation capabilities, *Decision Sciences*, Vol. 38, No. 1, 131-156, doi: 10.1111/j.1540-5915.2007.00151.x.

[9] Zeng, J., An, M., Smith, N.J. (2007). Application of a fuzzy based decision making methodology to construction project risk assessment, *International Journal of Project Management*, Vol. 25, No. 6, 589-600, doi: 10.1016/j.ijproman.2007.02.006.

[10] Olechowski, A., Oehmen, J., Seering, W., Ben-Daya, M. (2016). The professionalization of risk management: What role can the ISO 31000 risk management principles play?, *International Journal of Project Management*, Vol. 34, No. 8, 1568-1578, doi: 10.1016/j.ijproman.2016.08.002.

[11] Taroun, A. (2014). Towards a better modelling and assessment of construction risk: Insights from a literature review, *International Journal of Project Management*, Vol. 32, No. 1, 101-115, doi: 10.1016/j.ijproman.2013.03.004.

[12] Xia, N., Zou, P.X.W., Griffin, M.A., Wang, X., Zhong, R. (2018). Towards integrating construction risk management and stakeholder management: A systematic literature review and future research agendas, *International Journal of Project Management*, Vol. 36, No. 5, 701-715, doi: 10.1016/j.ijproman.2018.03.006.

[13] Arrow, K.J., Harris, T., Marschak, J. (1951). Optimal inventory policy, *Econometrica*, Vol. 19, No. 3, 250-272, doi: 10.2307/1906813.

[14] Wang, Y., Gerchak, Y. (1996). Periodic review production models with variable capacity, random yield, and uncertain demand, *Management Science*, Vol. 42, No. 1, 130-137, doi: 10.1287/mnsc.42.1.130.

[15] Shishehgarkhaneh, M.B., Moehler, R.C., Fang, Y.H., Aboutorab, H., Hijazi, A.A. (2024). Construction supply chain risk management, *Automation in Construction*, Vol. 162, Article No. 105396, doi: 10.1016/j.autcon.2024.105396.

[16] Fang, X., Wang, R., Yuan, F.J., Gong, Y., Cai, J.R., Wang, Y.L. (2020). Modelling and simulation of fresh-product supply chain considering random circulation losses, *International Journal of Simulation Modelling*, Vol. 19, No. 1, 169-177, doi: 10.2507/IJSIMM19-1-CO5.

[17] Papke-Shields, K.E., Beise, C., Quan, J. (2010). Do project managers practice what they preach, and does it matter to project success?, *International Journal of Project Management*, Vol. 28, No. 7, 650-662, doi: 10.1016/j.ijproman.2009.11.002.

[18] Fang, X., Huang, Y., He, J., Lai, Y., Chen, S., Liang, G. (2024). An operations optimisation model for fresh food produce supply chain considering time-varying freshness and consumer utility, *Economic Computation and Economic Cybernetics Studies and Research*, Vol. 58, No. 3, 38-52, doi: 10.24818/18423264/58.3.24.03.

[19] Pasternack, B.A. (1985). Optimal pricing and return policies for perishable commodities, *Marketing Science*, Vol. 4, No. 2, 166-176, doi: 10.1287/mksc.4.2.166.

[20] Cachon, G.P., Lariviere, M.A. (2005). Supply chain coordination with revenue-sharing contracts: Strengths and limitations, *Management Science*, Vol. 51, 30-44, doi: 10.1287/mnsc.1040.0215.

[21] He, Y., Zhang, J. (2008). Random yield risk sharing in a two-level supply chain, *International Journal of Production Economics*, Vol. 112, No. 2, 769-781, doi: 10.1016/j.ijpe.2007.06.003.

[22] Güler, M.G., Bilgiç, T. (2009). On coordinating an assembly system under random yield and random demand, *European Journal of Operational Research*, Vol. 196, No. 1, 342-350, doi: 10.1016/j.ejor.2008.03.002.

[23] Hu, F., Lim, C.-C., Lu, Z. (2013). Coordination of supply chains with a flexible purchasing policy under yield and demand uncertainty, *International Journal of Production Economics*, Vol. 146, No. 2, 686-693, doi: 10.1016/j.ijpe.2013.08.024.

[24] Güler, M.G., Keskin, M.E. (2013). On coordination under random yield and random demand, *Expert Systems with Applications*, Vol. 40, No. 9, 3688-3695, doi: 10.1016/j.eswa.2012.12.073.

[25] Cai, J., Zhong, M., Shang, J., Huang, W. (2017). Coordinating VMI supply chain under yield uncertainty: Option contract, subsidy contract, and replenishment tactic, *International Journal of Production Economics*, Vol. 185, 196-210, doi: 10.1016/j.ijpe.2016.12.032.

[26] Sonntag, D., Kiesmüller, G.P. (2018). Disposal versus rework – Inventory control in a production system with random yield, *European Journal of Operational Research*, Vol. 267, No. 1, 138-149, doi: 10.1016/j.ejor.2017.11.019.

[27] Stojic, N., Delic, M., Bojanic, T., Jokanovic, B., Tasic, N. (2024). Integrated model of risk management in business processes in industrial systems, *International Journal of Simulation Modelling*, Vol. 23, No. 3, 412-423, doi: 10.2507/IJSIMM23-3-689.

[28] Wang, Y.L., Chen, J.H., Song, M.L., Tang, F. (2025). Optimizing cooperation strategies for new energy vehicle manufacturers and technology suppliers: A game theory approach, *Advances in Production Engineering & Management*, Vol. 20, No. 3, 340-350, doi: 10.14743/apem2025.3.544.

[29] Zhao, Y., Rao, H., Pei, J., Su, X. (2025). An ANP-hopfield neural network based approach for supply chain stress testing, *Tehnički Vjesnik – Technical Gazette*, Vol. 32, No. 2, 415-424, doi: 10.17559/TV-20240501001513.

[30] Xi, J., Lai, L., Li, Y., Yang, D. (2025). The coordination mechanism of fresh agricultural products supply chain: A game-theoretic approach considering retailer's fairness concern and price competition, *Economic Computation and Economic Cybernetics Studies and Research*, Vol. 59, No. 1, 120-137, doi: 10.24818/18423264/59.1.25.08.

[31] Xu, W., Xu, S., Liu, D.Y., Awaga, A.L., Rabia, A.C., Zhang, Y.Y. (2024). Impact of fairness concerns on resource-sharing decisions: A comparative analysis using evolutionary game models in manufacturing enterprises, *Advances in Production Engineering & Management*, Vol. 19, No. 2, 223-238, doi: 10.14743/apem2024.2.503.

[32] Ji, X., Xu, W., Aslam, R., Yin, Y. (2024). The influence of government on automobile enterprise's production methods: An evolutionary game based study, *Economic Computation and Economic Cybernetics Studies and Research*, Vol. 58, No. 4, 223-240, doi: 10.24818/18423264/58.4.24.14.

[33] Zhou, C., Tang, W., Lan, Y. (2018). Supply chain contract design of procurement and risk-sharing under random yield and asymmetric productivity information, *Computers & Industrial Engineering*, Vol. 126, 691-704, doi: 10.1016/j.cie.2018.10.022.

[34] Behzadi, G., O'Sullivan, M.J., Olsen, T.L., Zhang, A. (2018). Agribusiness supply chain risk management: A review of quantitative decision models, *Omega*, Vol. 79, 21-42, doi: 10.1016/j.omega.2017.07.005.

[35] Besik, B., Nagurney, A., Dutta, P. (2023). An integrated multi-tiered supply chain network model of competing agricultural firms and processing firms: The case of fresh produce and quality, *European Journal of Operational Research*, Vol. 307, No. 1, 364-381, doi: 10.1016/j.ejor.2022.07.053.

APEM journal
Advances in Production Engineering & Management
Volume 21 | Number 1 | March 2026 | pp 16–24
https://doi.org/10.14743/apem2026.1.558
ISSN 1854-6250
Journal home: apem-journal.org
Original scientific paper

A calibrated ensemble framework for multi-class defect evaluation in ceramic sanitaryware manufacturing

Ozcetin, E.[a,*], **Simsek, S.**[a]

[a]Department of Industrial Engineering, Faculty of Engineering and Natural Sciences, Hitit University, Corum, Turkiye

ABSTRACT

Reliable defect evaluation is essential in ceramic sanitaryware manufacturing, where inspection outcomes directly influence rework decisions, process control, and delivery performance. In practice, defect assessment is often affected by operational variability, class imbalance, and human-dependent inspection procedures, which limit the repeatability and consistency of quality control decisions. This study formulates multi-class defect classification as a practical quality control problem and investigates the robustness of production-data-based decision-support in an industrial environment. The analysis is based on a real-world dataset comprising 11,071 production records collected under routine operating conditions. Defect labels were assigned through a two-stage quality control procedure involving trained inspectors and supervisory verification. Multinomial logistic regression, support vector machines with radial basis function kernels, and CatBoost were evaluated as base classifiers. A probability-based voting ensemble was developed to integrate the complementary decision structures, and posterior probabilities were calibrated using Platt scaling prior to aggregation to improve decision consistency. Experimental results show that the proposed calibrated ensemble improves Macro-F1 from 0.7126 (logistic regression) to 0.7211 and enhances minority-class recall, leading to more balanced performance under severe class imbalance. The findings indicate that probability calibration and ensemble integration contribute to improved stability and interpretability of defect evaluation. Overall, the proposed framework provides a practically deployable decision-support layer that supports more consistent rework decisions and more reliable quality control in industrial production settings.

ARTICLE INFO

Keywords:
Ceramic sanitaryware;
Defect classification;
Production data;
Class imbalance;
Ensemble learning;
Probability calibration;
Industrial quality control

**Corresponding author:*
erdenerozcetin@hitit.edu.tr
(Ozcetin, E.)

Article history:
Received 18 March 2026
Revised 6 April 2026
Accepted 13 April 2026

1. Introduction

Ceramic sanitaryware products such as washbasins, toilets, and bidets are required to meet high standards in terms of aesthetics, hygiene, and mechanical durability [1]. Accordingly, quality control plays a critical role in ceramic sanitaryware manufacturing, where production defects such as cracks, retouch-related imperfections, and shape irregularities directly translate into reprocessing costs, increased scrap rates, and delivery risks. In today's highly competitive market and large-scale production environments, accurate and consistent defect evaluation is therefore essential not only as a manufacturing activity, but also as a quality control task in which the defect state of each product is inferred from multiple sources of evidence.

In practice, inspection in ceramic sanitaryware production is still predominantly performed through manual visual assessment by experienced operators. This corresponds to a human-centered inspection procedure whose output is affected by operator-dependent variability, fatigue, and attention, as well as by changing observation conditions. Moreover, the high throughput of modern production lines limits the feasibility of fully manual inspection. These limitations motivate automated inspection frameworks that can be regarded as industrial inspection systems, where the measurand is the defect-related condition of the product surface and geometry, and the overall inspection outcome depends on the inspection context (illumination, surface texture, product positioning, and data acquisition settings) and subsequent data processing.

Early studies on ceramic defect detection primarily focused on image processing and morphological analysis techniques [2-4]. While these approaches demonstrated that several surface defects can be detected algorithmically, their robustness under real production conditions has often remained limited. In industrial production settings, defect assessment is highly influenced by operational variability, including changes in process conditions, heterogeneous manufacturing environments, and differing reporting practices. Unless evaluation procedures are deliberately designed to account for such factors, the repeatability of inspection decisions may be compromised. In line with this perspective, Karimi and Asemani [5] noted that no single inspection technique is capable of capturing the full range of ceramic defect mechanisms. In other words, these findings suggest that improving inspection practice requires not only the development of advanced recognition algorithms, but also a clearer definition of the industrial context and a systematic evaluation of system reliability under variable operating conditions.

In addition to traditional image-based inspection, researchers have increasingly turned to data-driven methods to analyze defect formation by incorporating production and process variables. Dengiz *et al.* [6] showed that data mining techniques can be used to relate defect characteristics to specific manufacturing practices, whereas Kesharaju and Nagarajah [7] reported that integrating optimization strategies with learning-based models leads to improved classification performance. From a production-oriented perspective, such approaches can be interpreted as data processing and estimation mechanisms that integrate heterogeneous operational information with inspection outcomes to support decision-making. However, to be informative in practical industrial settings, these studies should go beyond accuracy reporting and explicitly address the industrial context, evaluation procedures, and robustness of results under realistic sources of operational variability and class imbalance.

Despite these advances, a persistent challenge in ceramic sanitaryware defect classification is the imbalanced and partially overlapping structure of defect categories. Certain defects, such as cracks, are relatively frequent and comparatively separable. On the other hand, others, including retouch-related defects, are rarer and share characteristics with multiple fault mechanisms. This imbalance makes model training more challenging and can lead to biased performance if the evaluation procedure is not designed to reflect operational priorities. In practical terms, the goal is not only to improve predictive performance but also to obtain reliable and stable decision outcomes across defect types, minimizing systematic misclassification of minority yet operationally important categories.

Motivated by these considerations, this study investigates multi-class defect evaluation in ceramic sanitaryware manufacturing using a real-world industrial dataset comprising 11,071 production observations. The dataset is derived directly from operational records and is analyzed with minimal intervention to preserve authentic production characteristics. Owing to sparsity in several defect categories, the task is formulated using three industrially relevant classes: Crack, Retouch, and Other. The proposed analysis is positioned as a production-data-based quality-control and decision-support layer that operates on routinely collected production information, aiming to enhance the consistency and practical usability of inspection outcomes. Unlike prior ceramic defect studies that mainly report accuracy, this study emphasizes decision reliability by integrating probability calibration with ensemble-based evaluation under severe class imbalance using real-world production data.

We comparatively evaluate multinomial logistic regression, support vector machines with a radial basis function kernel, and CatBoost. In addition, we propose a probability-based voting ensemble that integrates the complementary strengths of individual classifiers. Particular attention is given to categorical feature handling, probability calibration, and systematic hyperparameter optimization to support a more disciplined performance evaluation under class imbalance. In detail, the experimental design emphasizes metrics that better reflect operational reliability under imbalance (e.g., class-sensitive performance measures), and reports results in a way that facilitates replication in similar industrial quality control settings.

This study makes three main contributions. First, it provides a comprehensive empirical analysis of defect evaluation based on large-scale, real production data, with an explicit focus on industrial quality control and inspection reliability in ceramic sanitaryware manufacturing. Second, it demonstrates that a carefully designed probability-based ensemble can yield more balanced and reliable performance under severe class imbalance, supporting robust decision-making at high throughput. Third, by incorporating process-related variables and relatively interpretable modeling components, the proposed framework offers a practical decision-support tool that can be integrated into existing quality control workflows in ceramic sanitaryware manufacturing.

2. Background

Automated defect detection and classification in ceramic manufacturing have received increasing attention due to the limitations of manual inspection and the increasing complexity of production processes. Early studies mostly focused on image processing and morphological analysis to identify surface defects on ceramic products. Forest [2] demonstrated that relatively simple image-based techniques could be used to identify visible surface irregularities, thereby providing an early foundation for automated inspection systems. Elbehiery *et al.* [3] subsequently introduced a low-cost and portable solution for detecting common defects, including cracks and pinholes, through morphological processing. In a similar vein, Hocenski *et al.* [4] employed image analysis methods to recognize edge defects, scratches, glazing faults, and texture anomalies, illustrating that several inspection activities could be partially automated.

Despite these developments, later studies pointed out that purely image-based inspection methods often lack robustness under real production conditions [8]. Rahaman and Hossain [9] observed that performance obtained in controlled environments tends to decline when faced with low contrast, surface noise, and fluctuating illumination. Karimi and Asemani [5] also noted that no single image processing technique can adequately represent the wide range of ceramic defect types, thereby underscoring the need for complementary approaches. In sum, these results suggest that inspection performance is strongly affected by operational variability, which in turn limits reliability and transferability across different manufacturing settings.

Parallel to classical vision-based inspection, data-driven approaches using production and process variables have been explored to support defect evaluation [6]. In a related direction, Kumru [10] proposed a fuzzy logic-based evaluation framework for sanitaryware quality assessment to reduce subjectivity and improve decision consistency. These lines of work motivate defect evaluation strategies that leverage routinely collected manufacturing data rather than relying solely on surface appearance.

More recently, the literature has increasingly shifted toward deep learning-based defect detection [11]. Recent studies report strong performance improvements through architectural optimization and lightweight backbones [12, 13]. For example, Wan *et al.* [14], Carvalho *et al.* [15], and Lu *et al.* [16] optimized YOLOv5 models and reported good performances. In addition, Chen *et al.* [17] proposed a multi-scale defect detection model for 3D-printed ceramic components. A recent contribution by Diao *et al.* [18] introduced a GhostNet-based lightweight YOLOv10s variant.

Across both machine learning and deep learning studies, class imbalance and partial overlap among defect categories are repeatedly identified as major obstacles in multi-class settings. Dominant classes (e.g., crack-related defects) tend to be easier to separate, whereas rarer or process-dependent defects are harder to distinguish. This makes class-sensitive evaluation essential, since aggregate accuracy alone can mask systematic errors on minority but operationally important defect categories. In this context, evaluation protocols that combine class-wise performance reporting with transparent decision rules become particularly important for industrial adoption.

Overall, the literature indicates that ceramic defect analysis has progressed from classical image processing to modern deep learning detectors and production-data–driven decision support. Nevertheless, challenges related to operational variability, class imbalance, and deployability remain. Building on these insights, the present study focuses on defect evaluation using a large-scale, real production dataset under industrial class imbalance.

3. Materials and methods

In this study, automated defect classification is treated as an evaluation process rather than a purely predictive task. Accordingly, the methodological design is guided by principles of measurement reliability, uncertainty management, and output stability.

In ceramic sanitaryware manufacturing, uncertainty arises from subjective visual judgments, overlapping defect mechanisms, and variability in production processes. These factors influence both the consistency of reference labels and the reliability of model predictions. To limit their effects, probabilistic calibration and ensemble aggregation are applied to stabilize output distributions and improve repeatability under different operating conditions. Within this context, classification confidence is viewed as a quantitative indicator of measurement reliability, which allows decision thresholds to be adjusted in line with operational risk considerations.

3.1 Data source

This study is based on real operational production data collected from a ceramic sanitaryware manufacturing company operating in Türkiye. The dataset comprises 11,071 production records obtained under routine industrial conditions and reflects authentic process variability. Each record corresponds to a single product unit and includes numerical and categorical variables that describe material properties, process parameters, and production conditions.

From a quality control standpoint, each product's defect condition is treated as the target quantity, whereas production and process variables provide indirect evidence for its assessment. Data were collected through routine monitoring practices, without artificial modification, resampling, or synthetic augmentation. This strategy helps maintain the authenticity of the production setting and supports the practical relevance of the analysis.

Defect labels were first assigned during routine quality control activities by experienced inspectors. When uncertainties arose, the samples were re-examined by a senior supervisor, and the final decision was reached through mutual agreement. This two-step annotation procedure enhances the consistency of the reference labels used for model training and testing. To further reinforce the reliability of the labeling process, a randomly selected subset of records was additionally reviewed by an independent domain expert in order to check for potential inconsistencies and borderline cases.

Although formal inter-annotator agreement metrics were not recorded, the two-stage inspection procedure, consensus-based validation of uncertain cases, and additional independent review of a subset of samples were designed to enhance label consistency under real production conditions. This approach reflects common industrial quality-control practice, where operational feasibility often limits the use of formal annotation protocols.

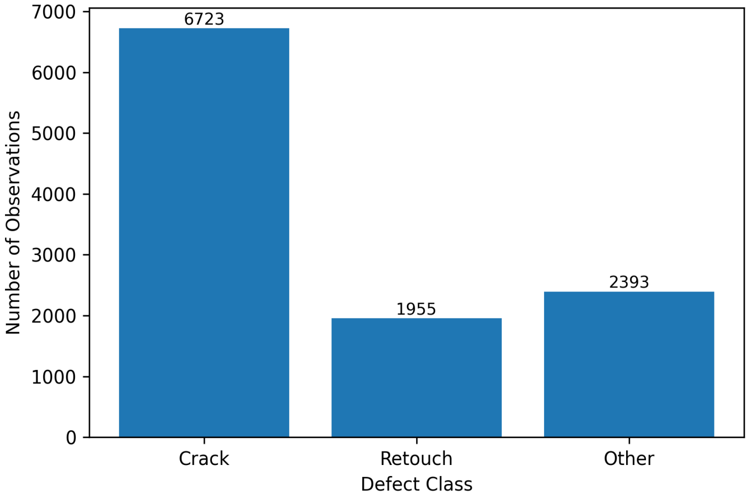

Fig. 1 Distribution of defect classes in the production dataset

Because several defect categories were represented by relatively few observations, the original labels were consolidated into three operationally meaningful classes: Crack, Retouch, and Other. The Other category includes air bubbles, pinholes, deformation defects, and assembly-related imperfections. Although these defect types differ in their physical characteristics, they were combined due to their comparable implications for downstream quality control, particularly with respect to rework and rejection decisions. In practice, these defects are mainly identified through the same visual inspection routines and production monitoring mechanisms, which further supports their joint treatment within a unified class structure. In addition, the dataset displays a pronounced class imbalance. As shown in Fig. 1, Crack defects form the majority class with 6,723 instances, while Retouch and Other are represented by 1,955 and 2,393 samples, respectively. This uneven distribution reflects realistic production conditions but poses considerable challenges for model training and performance assessment. Accordingly, class-aware evaluation metrics and probability calibration are emphasized throughout the analysis.

3.2 Feature preparation and candidate models

The dataset includes seven process- and material-related input variables representing indirect measurement channels of defect formation: five categorical variables (product category, kiln type, clay type, casting area, and drying chamber) and two continuous variables (thixotropy and mold age). Product category denotes the five main sanitaryware groups produced on the line (washbasin, toilet, bidet, urinal, and shower tray). Kiln type reflects four firing configurations used in production. Clay type distinguishes two material formulations with different raw-material composition and firing behavior (a fine-grained, high-density formulation for high-temperature firing and smooth-surface products, and a coarser, lower-density formulation typically used for thicker-walled products). The casting area refers to the specific location where casting and shaping are performed, covering eight distinct areas within the production line. The drying chamber denotes the controlled pre-firing drying environment, consisting of seven chambers, whose temperature and humidity conditions are known to affect crack formation and deformation. Furthermore, thixotropy is a rheological property that describes material flow behavior under mechanical stress. It is commonly expected to influence surface-related defects through its effects on application and adhesion. Mold age indicates the number of casting cycles a mold has completed and is linked to wear-related changes that may impact geometric stability and surface quality.

During data preprocessing, numerical features were standardized to have zero mean and unit variance in order to improve numerical stability and maintain comparability across learning algorithms. Categorical variables were encoded using one-hot representations for multinomial logistic regression and support vector machines, whereas CatBoost relied on its built-in permutation-based encoding scheme to process categorical information efficiently.

Three supervised learning models reflecting complementary modeling strategies were examined: multinomial logistic regression, support vector machines with a radial basis function kernel, and CatBoost. Logistic regression was adopted as a linear probabilistic baseline and trained with class-weighted loss and L2 regularization. Support vector machines employed a soft-margin formulation to capture nonlinear decision boundaries, with kernel and penalty parameters tuned via cross-validation. CatBoost was used to model complex nonlinear interactions among process variables, incorporating early stopping and regularization mechanisms to limit model complexity.

To exploit the complementary strengths of individual classifiers, a probability-based voting ensemble was constructed (see Fig. 2). Let $p_m^{(k)}$ denote the posterior probability assigned to class k by model m. The ensemble prediction is obtained as

$$\hat{y} = \arg\max_{k\in\kappa} \sum_{m=1}^{M} w_m p_m^{(k)}, \tag{1}$$

where w_m represents the weight associated with model m, and M denotes the number of base classifiers. Both equal-weight and performance-informed weighting strategies were examined. In the performance-informed scheme, weights were proportional to validation Macro-F1 scores and normalized to sum to unity.

To improve the reliability of posterior probability estimates, post-hoc probability calibration was applied using Platt scaling (sigmoid method) implemented via the CalibratedClassifierCV framework on validation data prior to ensemble aggregation. This calibration step ensures that probabilistic outputs are comparable across models and supports transparent and stable decision-making.

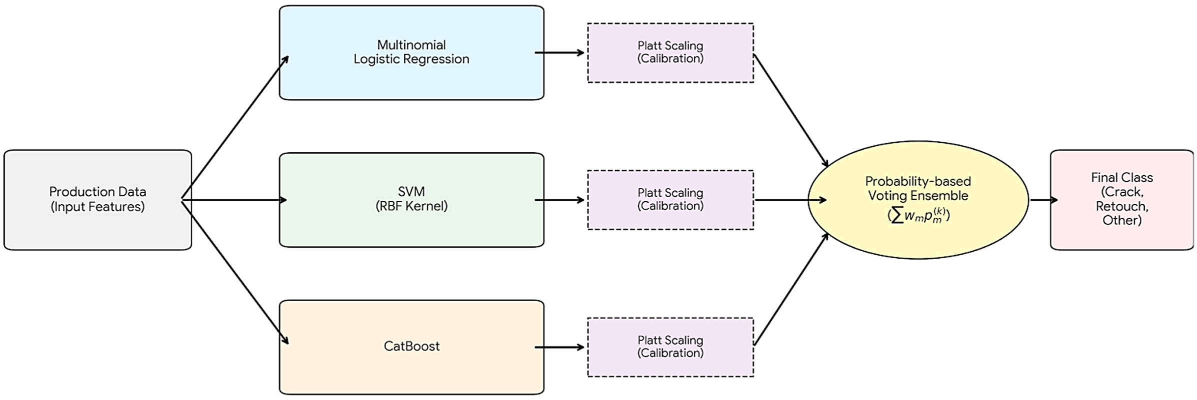

Fig. 2 Architecture of the proposed probability-based voting ensemble model

3.3 Experimental design and performance evaluation

The dataset was split into training and test sets using stratified sampling to preserve class proportions; 25 % of the observations were reserved as an external test set. No data from the test set was used during feature engineering, probability calibration, or hyperparameter tuning. Within the training set, hyperparameter optimization was performed using Optuna with 100 trials under a 5-fold cross-validation scheme. All experiments were conducted using a fixed random seed to ensure reproducibility. Macro-F1 was selected as the primary optimization objective to reflect balanced performance across imbalanced classes.

To support a more production-oriented interpretation of model outputs, probability-based decision behavior was examined through calibrated probability outputs and class-wise performance reporting. All preprocessing and modeling steps were implemented within a unified computational pipeline; stochastic components were controlled via fixed random seeds, and the complete experimental configuration was documented to support reproducibility. Calibration quality was evaluated on validation data to ensure that probabilistic outputs used in ensemble aggregation are comparable and decision-relevant.

4. Results and discussion

This section presents and discusses the empirical findings obtained from the comparative evaluation of individual classifiers and the proposed probability-based ensemble using real production data. The primary objective is to assess classification performance under industrial class imbalance and to examine the reliability of model outputs from a production-oriented perspective.

Table 1 reports the overall predictive performance of multinomial logistic regression, support vector machines, CatBoost, and the proposed ensemble on the external test set. As shown in Table 1, logistic regression and support vector machines achieve competitive Macro-F1 scores, while CatBoost exhibits slightly lower generalization performance in the present production-data context. The ensemble outperforms individual models in terms of balanced performance, indicating that probabilistic aggregation contributes to improved robustness under heterogeneous operating conditions. The proposed ensemble not only improves Macro-F1 performance but also reduces inter-fold performance variance and enhances probability calibration, leading to more stable and reliable decision support in production settings.

Table 1 Overall classification performance of individual models and the proposed ensemble

Model	Accuracy	Macro precision	Macro recall	Macro F1
Logistic regression	0.7695	0.7376	0.6946	0.7126
SVM (RBF)	0.7673	**0.7445**	0.6797	0.7047
CatBoost	0.7565	0.7260	0.6602	0.6838
Voting ensemble	**0.7731**	0.7345	**0.7099**	**0.7211**

Table 2 Class-wise precision, recall, and F1-score for each classifier on the test dataset

Class	Model	Precision	Recall	F1-Score
Crack	Logistic Regression	0.8011	0.8721	0.8351
	SVM (RBF)	0.7869	**0.8876**	0.8342
	CatBoost	0.7839	0.8870	0.8323
	Voting Ensemble	**0.8158**	0.8614	**0.8380**
Retouch	Logistic Regression	0.6939	0.5562	0.6175
	SVM (RBF)	**0.7155**	0.5194	0.6019
	CatBoost	0.7003	0.4683	0.5613
	Voting Ensemble	0.6608	**0.6094**	**0.6340**
Other	Logistic Regression	0.7179	0.6555	0.6853
	SVM (RBF)	**0.7311**	0.6321	0.6780
	CatBoost	0.6939	0.6254	0.6579
	Voting Ensemble	0.7249	**0.6589**	**0.6912**

Table 3 Confusion matrix of the proposed ensemble classifier on the test dataset

True / Predicted	Crack	Retouch	Other
Crack	1448	115	118
Retouch	161	298	30
Other	116	38	394

Detailed class-wise precision, recall, and F1-scores are summarized in Table 2. The results indicate that Crack defects are consistently detected with high accuracy across all models, reflecting their distinctive process-related signatures and higher frequency in the dataset. In contrast, Retouch defects exhibit substantially lower recall values and higher misclassification rates, primarily due to their partial overlap with both Crack and Other categories. This behavior highlights the intrinsic difficulty of reliably distinguishing retouch-related imperfections based solely on routinely collected production variables.

The confusion matrix corresponding to the ensemble classifier is presented in Table 3. Systematic confusion between the Retouch and Other classes is clearly observed. This pattern confirms that these categories share overlapping operational characteristics. From a quality-system perspective, such misclassification patterns represent a critical source of uncertainty, as they may lead to unstable rework decisions and inconsistent quality assessments in high-throughput production environments.

To support meaningful probability-based aggregation, posterior class probabilities were calibrated using Platt scaling prior to ensemble integration. The improved consistency of probabilistic outputs contributes to more stable decision behavior, reinforcing the interpretation of model predictions as measurement-informed indicators rather than purely statistical classifications. Moreover, after calibration, the Brier score decreased from 0.244 to 0.197, and the expected calibration error was reduced from 0.098 to 0.049.

Overall, the results demonstrate that defect evaluation based on routinely collected production data can be formulated as a reliable quality control support process when appropriate preprocessing, probability calibration, and ensemble integration are employed. Rather than maximizing aggregate accuracy alone, the proposed evaluation strategy emphasizes balanced performance, decision stability, and operational interpretability. These characteristics are essential for deploying machine learning-assisted inspection systems in industrial quality control, where consistent and transparent measurement outcomes are required for effective process control and continuous improvement.

In addition, the relevance of individual features was further examined using permutation-based importance analysis to assess their contribution to decision reliability. Since the proposed ensemble integrates posterior probabilities from multiple classifiers, direct attribution of decision behavior to individual input variables is not straightforward. Therefore, a model-agnostic permutation approach was adopted to quantify the marginal contribution of each feature to classification performance in terms of changes in Macro-F1 score.

The analysis indicates that thixotropy represents the most influential process variable, as its random perturbation resulted in the largest performance degradation. This finding highlights the critical role of material flowability and shaping behavior in defect formation, which is consistent with established ceramic manufacturing knowledge. Clay type and drying chamber variables likewise showed high importance scores. This indicates that defect occurrence is closely associated with material properties and environmental process conditions throughout production.

Mold age and product category exhibited moderate importance, indicating that these variables may influence defect formation indirectly through their effects on process stability and geometric properties. By contrast, casting location showed limited individual impact, and kiln-related variables displayed negligible importance, pointing to relatively uniform firing conditions within the examined production system. Namely, these results suggest that the proposed production-oriented framework not only enhances classification reliability but also yields practical insights into the key process pathways associated with defect generation.

Beyond overall performance, the results highlight that defect evaluation based on routinely collected production variables is inherently constrained by operational variability and partially unobserved factors. In particular, systematic confusion between Retouch and Other suggests that the available process descriptors may not fully capture the latent mechanisms driving subtle surface-related imperfections. This limitation is consistent with the measurement interpretation of the problem, where repeatability and decision reliability depend not only on the learning algorithm but also on the representativeness of observation channels and the stability of the operating context. The proposed calibration-aware ensemble reduces bias toward dominant classes and provides more stable probability-based decisions; however, residual errors indicate that additional contextual variables (e.g., operator-, shift-, and maintenance-related metadata) may be required to further improve reliability in high-throughput settings. The stability of feature rankings was further verified across cross-validation folds, indicating that the identified key process variables consistently contribute to classification reliability.

From an operational perspective, the observed improvement in class-balanced performance and minority-class recall contributes to more consistent rework decisions, reduces the risk of systematic misclassification, and supports more stable quality control processes in high-throughput production environments.

Furthermore, it should be noted that the dataset used in this study originates from a single production facility. While this limits the direct generalizability of model-specific results, the proposed framework is designed as a transferable decision-support approach. In different industrial settings, the same methodology can be applied by re-calibrating model parameters and adapting feature representations to local production conditions. In addition, the aggregation of multiple defect types into the Other category, while necessary to ensure statistical robustness, may lead to a loss of defect-specific information. However, this grouping reflects practical industrial decision-making, where defects with similar operational consequences are often treated collectively. Future work will focus on more fine-grained defect categorization as larger and more balanced datasets become available.

Lastly, the temporal stability of the model across different production periods, work shifts, and potential process drift could not be directly assessed within the scope of the current dataset. This aspect is critical for long-term deployment of data-driven quality control systems and will be addressed in future studies through time-aware validation and continuous monitoring approaches.

5. Conclusion

This study investigated production-data-based multi-class defect evaluation in ceramic sanitaryware manufacturing from a practical industrial quality control perspective. Using 11,071 real-world industrial observations and a two-stage quality-control labeling procedure, multinomial logistic regression, SVM (RBF), CatBoost, and a calibrated probability-based voting ensemble were evaluated under severe class imbalance. The results show that probability calibration and ensemble aggregation improve balanced performance and decision consistency, supporting the use of routinely collected process data as an indirect data-driven input for defect assessment.

Model-agnostic permutation analysis further indicates that defect behavior is primarily driven by material and process-condition variables, with thixotropy, clay type, and drying environment emerging as key contributors to classification reliability. At the same time, remaining misclassifications—especially between structurally similar defect categories—suggest that part of the decision uncertainty arises from latent and context-dependent factors that are not explicitly represented in the current dataset. Future work will focus on integrating operator-, shift-, and maintenance-related metadata to explicitly model contextual uncertainty and enhance decision consistency and reliability in high-throughput environments.

Acknowledgement

The authors would like to thank the industrial partner for providing access to real production data and supporting the development of this study. The authors also acknowledge the valuable insights obtained from practical manufacturing experience during the design of the experimental framework.

References

[1] Ozcetin, E., Ozturk, G., Ozturk, Z.K., Kasimbeyli, R., Kasimbeyli, N. (2023). A decision support system for consolidated distribution of a ceramic sanitary ware company, *Expert Systems with Applications*, Vol. 213, Part A, Article No. 118785, doi: 10.1016/j.eswa.2022.118785.

[2] Forrest, A.K. (2003). Surface defect detection on ceramics, In: Graves, M., Batchelor, B. (eds.), *Machine vision for the inspection of natural products*, Springer, London, United Kingdom, 191-213, doi: 10.1007/1-85233-853-9_6.

[3] Elbehiery, H., Hefnawy, A., Elewa, M. (2005). Surface defects detection for ceramic tiles using image processing and morphological techniques, In: *Proceedings of the Third World Enformatika Conference,* Istanbul, Turkey, 158-162.

[4] Hocenski, Z., Keser, T., Baumgartner, A. (2007). A simple and efficient method for ceramic tile surface defects detection, In: *Proceedings of 2007 IEEE International Symposium on Industrial Electronics*, Vigo, Spain, 1606-1611, doi: 10.1109/ISIE.2007.4374844.

[5] Karimi, M.H., Asemani, D. (2014). Surface defect detection in tiling industries using digital image processing methods: Analysis and evaluation, *ISA Transactions*, Vol. 53, No. 3, 834-844, doi: 10.1016/j.isatra.2013.11.015.

[6] Dengiz, O., Smith, A.E., Nettleship, I. (2006). Two-stage data mining for flaw identification in ceramics manufacture, *International Journal of Production Research*, Vol. 44, No. 14, 2839-2851, doi: 10.1080/00207540500534454.

[7] Kesharaju, M., Nagarajah, R. (2017). Particle swarm optimization approach to defect detection in armour ceramics, *Ultrasonics*, Vol. 75, 124-131, doi: 10.1016/j.ultras.2016.07.008.

[8] Hanzaei, S.H., Afshar, A., Barazandeh, F. (2017). Automatic detection and classification of the ceramic tiles' surface defects, *Pattern Recognition*, Vol. 66, 174-189, doi: 10.1016/j.patcog.2016.11.021.

[9] Rahaman, G.M.A., Hossain, M.M. (2009). Automatic defect detection and classification technique from image: A special case using ceramic tiles, *arXiv,* doi: 10.48550/arXiv.0906.3770.

[10] Kumru, M. (2013). Assessing the visual quality of sanitary ware by fuzzy logic, *Applied Soft Computing*, Vol. 13, No. 8, 3646-3656, doi: 10.1016/j.asoc.2013.03.012.

[11] Zhou, M., Wu, T., Xia, Z., He, B., Kong, L.B., Su, H. (2025). Research progress in deep learning for ceramics surface defect detection, *Measurement*, Vol. 242, Part B, Article No. 115956, doi: 10.1016/j.measurement.2024.115956.

[12] Abbas, S., Moumen, H., Abbas, F. (2023). Efficient method using attention based convolutional neural networks for ceramic tiles defect classification, *Revue d'Intelligence Artificielle*, Vol. 37, No. 1, 53-62, doi: 10.18280/ria.370108.

[13] Fei, Z., Zhao, R., Xin, K., Chen, G., Xiang, X. (2026). Defect detection of ceramic substrates based on improved YOLOv9 algorithm, *International Journal of Machine Learning and Cybernetics*, Vol. 17, No. 1, Article No. 29, doi: 10.1007/s13042-025-02835-2.

[14] Wan, G., Fang, H., Wang, D., Yan, J., Xie, B. (2022). Ceramic tile surface defect detection based on deep learning, *Ceramics International*, Vol. 48, No. 8, 11085-11093, doi: 10.1016/j.ceramint.2021.12.328.

[15] Carvalho, R., Morgado, A.C., Gonçalves, J., Kumar, A., Rolo, A.G.E.S., Carreira, R., Soares, F. (2023). Computer-aided visual inspection of glass-coated tableware ceramics for multi-class defect detection, *Applied Sciences*, Vol. 13, No. 21, Article No. 11708, doi: 10.3390/app132111708.

[16] Lu, Q., Lin, J., Luo, L., Zhang, Y., Zhu, W. (2022). A supervised approach for automated surface defect detection in ceramic tile quality control, *Advanced Engineering Informatics*, Vol. 53, Article No. 101692, doi: 10.1016/j.aei.2022.101692.

[17] Chen, W., Zou, B., Yang, G., Zheng, Q., Lei, T., Huang, C., Liu, J., Li, L. (2024). A real-time detection system for multiscale surface defects of 3D printed ceramic parts based on deep learning, *Ceramics International*, Vol. 50, No. 8, 13101-13112, doi: 10.1016/j.ceramint.2024.01.220.

[18] Diao, J., Wei, H., Zhou, Y., Diao, Z. (2025). A deep learning-based algorithm for ceramic product defect detection, *Applied Sciences*, Vol. 15, No. 12, Article No. 6641, doi: 10.3390/app15126641.

APEM journal
Advances in Production Engineering & Management
Volume 21 | Number 1 | March 2026 | pp 25–39
https://doi.org/10.14743/apem2026.1.559
ISSN 1854-6250
Journal home: apem-journal.org
Original scientific paper

Emergency production dispatching under sudden disruptions: A tripartite evolutionary game approach

Cheng, R.[a], **Zhao, Z.B.**[a,*], **Liu, J.D.**[a], **Sheng, S.Y.**[a]

[a]School of Management, Harbin Institute of Technology, Harbin, P.R. China

ABSTRACT

Sudden disruptions, including equipment failures, supply interruptions, and extreme events, can quickly make shop-floor schedules infeasible. Yet emergency production dispatching is often treated as a stand-alone rescheduling problem that overlooks coordination and enforcement. This study frames disruption response in industrial parks as a coupled production-control and governance problem and develops a tripartite evolutionary game model involving a local coordination authority, manufacturing firms, and an upper-level government. The model examines how proactive dispatching, cooperative rescheduling, and supervision co-evolve under bounded rationality. Using replicator dynamics, Jacobian stability analysis, and numerical simulations, we identify the conditions under which cooperative emergency dispatching becomes stable. The findings are based on a simulation-based evolutionary game model rather than on calibrated industrial case data. Results show that resource support, cooperation gains, and credible penalties promote proactive dispatching, whereas high adjustment costs weaken firms' willingness to cooperate. Rising monitoring costs reduce the attractiveness of strict supervision, while effective horizontal cooperation partly substitutes for vertical enforcement. From a practical perspective, emergency dispatching is more effective when firms' adjustment burdens are reduced, repeated cooperation is rewarded, passive behavior is credibly disciplined, and supervision remains effective but sustainable.

ARTICLE INFO

Keywords:
Emergency production dispatching;
Industrial park coordination;
Manufacturing disruption;
Evolutionary game;
Bounded rationality;
Sensitivity analysis

**Corresponding author:*
zhaozebin@hit.edu.cn
(Zhao, Z.B.)

Article history:
Received 6 April 2026
Revised 25 April 2026
Accepted 27 April 2026

1. Introduction

In recent years, manufacturing systems have been increasingly exposed to sudden disruptions such as natural hazards, major accidents, pandemics, cyber incidents, and critical utility outages [1]. These shocks can trigger abrupt capacity loss, material shortages, and cascading schedule infeasibility across workshops, plants, and industrial parks [2]. In shop-floor execution, delayed dispatching and rescheduling may amplify work-in-process accumulation, delivery failures, and ripple effects along supply networks [3]. Consequently, emergency production dispatching, such as rapid rescheduling and real-time production control after a disruption, has become a central issue in production planning, scheduling, and control under risk and uncertainty.

However, emergency dispatching in real manufacturing settings is rarely a purely technical optimization problem. Particularly in manufacturing clusters and industrial parks, it is a multi-actor coordination process. A local coordination authority must activate emergency plans and mobilize shared resources; manufacturing firms must decide whether to cooperate with rescheduling measures such as capacity sharing and overtime; and upper-level government agencies often intervene through supervision and resource support. Because these actors face different costs, constraints, and accountability pressures, technically feasible dispatching policies may fail to materialize when incentives are misaligned.

To address this challenge, this study frames disruption response as a coupled production-control and governance problem. We develop a tripartite evolutionary game model involving a local coordination authority, manufacturing firms, and an upper-level government. The study examines how proactive dispatching, cooperative rescheduling, and supervision co-evolve under bounded rationality. The contributions are threefold. First, the study reframes emergency production dispatching as a coupled governance and scheduling implementation problem rather than a purely technical optimization task. Second, it provides a tractable tripartite evolutionary mechanism to explain when cooperative dispatching becomes evolutionarily stable. Third, it offers policy and managerial insights on how to design incentive-compatible emergency dispatching schemes that converge reliably under bounded rationality.

The remainder of this paper is organized as follows. Section 2 reviews the relevant literature. Section 3 presents the problem description and the tripartite evolutionary game model. Section 4 analyzes the stability of equilibrium points. Section 5 reports numerical simulations and sensitivity analyses. The final section summarizes conclusions and implications.

2. Literature review

A substantial literature has examined manufacturing disruption management through operations research and industrial engineering approaches, including predictive–reactive rescheduling, dynamic scheduling, robust and stochastic formulations, dispatching and repair heuristics, and simulation-based optimization [4-6]. Meanwhile, Industry 4.0 and smart manufacturing infrastructures have advanced data-driven decision support for real-time monitoring and schedule adaptation, with recent reviews highlighting digitally enabled smart manufacturing scheduling [7]. However, much of this scheduling-centric research evaluates performance conditional on implementable schedules, often treating stakeholder compliance, information sharing, and cross-organizational coordination as exogenous or costless. This assumption is restrictive when emergency dispatching depends on multi-actor joint action under accountability and incentive conflicts.

Existing studies have increasingly viewed disruption response as shaped by behavioral, organizational, and governance factors. Research on environmental emergencies highlights the role of rescuers' emotions and occupational safety [8], while other studies examine incentives, safety compliance, and public-private collaboration in disruption contexts [9, 10]. Game-theoretic models have been used to explain how subsidies, penalties, and contract terms affect stakeholder participation in emergency collaboration, post-disruption recovery, and resource sharing [11, 12]. Related studies further show that financial constraints, capacity limits, and procurement decisions jointly influence disaster and emergency response effectiveness [13]. However, many existing models remain dyadic, such as supplier–manufacturer interactions, and often rely on full-rationality, static, or leader–follower assumptions. These settings limit their ability to capture boundedly rational adaptation and enforcement dynamics in time-pressured emergencies. Although tripartite evolutionary games have been applied in some emergency management contexts, their use in emergency production dispatching and industrial-park rescheduling remains limited, particularly for explaining the co-evolution of vertical supervision and horizontal capacity reallocation.

Studies on industrial and social accident decision-making have shown that negative emotions, decision concerns, task modes, and risk preferences affect decision time, confidence, and behavioral choices [14, 15]. Evolutionary game theory offers a natural analytical lens for this problem because emergency response strategies are shaped by bounded rationality, learning, and repeated interactions across drills and real incidents. Rather than assuming perfect rationality, evolutionary games describe how strategy shares evolve based on relative payoffs and how a system may converge to an evolutionary stable strategy under specific incentive and cost structures [16]. Recent studies have applied tripartite evolutionary game frameworks to technology adoption and multi-stakeholder coordination in production and logistics [17, 18]. Recent studies have further used this approach to examine manufacturing capacity sharing and AI delivery technology adoption, showing its applicability to multi-stakeholder strategy evolution in production and logistics systems [19, 20]. These studies typically combine equilibrium stability analysis with numerical simulation to identify the parameters that drive convergence to desirable states. Nonetheless, the application of such frameworks to emergency production dispatching, especially under vertical administrative governance, remains underdeveloped.

3. Evolutionary game theory model

3.1 Basic assumptions and game description

To study implementable emergency production dispatching, we consider a tripartite evolutionary interaction within an industrial park or manufacturing cluster. In this setting, disruptions may render pre-planned schedules infeasible and require rapid rescheduling and capacity reallocation. The three stakeholders are a local coordination authority, manufacturing firms, and an upper-level government. In this study, emergency production dispatching is interpreted as the implementation process that makes disrupted production plans executable, rather than as a substitute for a shop-floor scheduling or rescheduling algorithm. Operationally, it may involve order resequencing, machine reassignment, changeover acceleration, overtime arrangement, expedited procurement, temporary outsourcing, cross-firm capacity sharing, and delivery-priority adjustment. A scheduling model may generate candidate rescheduling plans and indicators such as recovery time, tardiness reduction, throughput loss, capacity utilization, and adjustment cost, while the governance layer developed here explains whether these plans can be implemented through proactive coordination, firm cooperation, and appropriate supervision. The local coordination authority represents the industrial-park operator or regional manufacturing coordination office responsible for activating emergency production plans, integrating information, and organizing cross-firm dispatching. Manufacturing firms execute shop-floor actions such as sequence changes, changeovers, overtime, expedited procurement, and temporary capacity sharing. The upper-level government acts as a supervisory and support body that enforces compliance and allocates emergency resources when needed. The model focuses on how vertical supervision and horizontal capacity reallocation jointly shape the evolution of implementable dispatching.

Hypothesis 1 (Bounded rationality and evolutionary adaptation). The local coordination authority, manufacturing firms, and the upper-level government are denoted as Player 1, Player 2, and Player 3. Decision-makers operate under bounded rationality and cannot fully anticipate others' actions in time-pressured disruption response. Strategy adjustments follow payoff-driven learning, imitation, or reinforcement based on observed performance in drills and real incidents. As disruption experiences accumulate, the proportions of agents adopting alternative strategies evolve over time and may converge to an evolutionarily stable state.

Hypothesis 2 (Strategic choice and probability). Each player has two alternative strategies. The local coordination authority chooses proactive dispatching or passive response. Let the probability of proactive dispatching be x $\in [0,1]$, and passive response be $1 - x$. Manufacturing firms choose active cooperation or non-cooperation in emergency rescheduling and capacity reallocation. Let the probability of active cooperation be $y \in [0,1]$, and non-cooperation be $1 - y$. The upper-level government chooses between strict supervision and loose supervision. Let the probability of strict supervision be z $\in [0,1]$ and that of loose supervision be $1 - z$.

Hypothesis 3 (Payoffs of the local coordination authority). If the local coordination authority adopts proactive dispatching, it incurs a coordination cost D reflecting plan activation, cross-firm dispatching, information integration, and resource mobilization, and obtains an operational continuity benefit B, representing improved delivery reliability and reduced disruption losses at the system level. Under strict supervision, it can receive resource support A, such as emergency funding, logistics capacity, or prioritized utilities. When firms actively cooperate, the authority gains an additional effectiveness benefit C, reflecting higher implementability of rescheduling, faster recovery of throughput, and reduced spillovers enabled by capacity pooling. If the authority adopts a passive response, it suffers a delay-related loss E, may be penalized by the upper-level government F, and experiences a credibility loss G that weakens its future coordination capability.

Hypothesis 4 (Payoffs of the manufacturing firms). If a manufacturing firm chooses active cooperation, it gains a reputation benefit and may receive a local incentive H, but bears adjustment costs J, including overtime, setup and changeover, sequence deviations, expedited procurement, and additional coordination effort. Non-cooperation avoids part of J in the short run but results in a reputation loss K and a penalty L associated with noncompliance in emergency production arrangements. When proactive dispatching and cooperation occur jointly, manufacturing firms obtain a long-term collaboration payoff X, capturing persistent advantages such as preferential access to shared resources, repeated coordination efficiency, and improved recovery performance in subsequent disruptions.

Hypothesis 5 (Payoffs of the upper-level government). Strict supervision yields a system stability benefit M and a regulatory performance payoff P, reflecting reduced regional production interruptions and improved resilience of manufacturing supply capacity, but incurs supervision and coordination costs Q. When the local coordination authority is proactive, an additional resilience gain O is realized through reduced cascading risks and faster restoration of production and logistics functions. Loose supervision leads to a credibility loss R and an escalation risk cost S, as local inaction or firm noncompliance can amplify disruption impacts and require higher-cost interventions later.

3.2 Evolutionary game model design

Following the established hypotheses above, the strategic interaction is encapsulated within a mixed-strategy game framework, which is detailed in Table 1.

Table 1 Tripartite payoff matrix

Manufacturing firms			Upper-level government	
			Strict supervision (z)	Loose supervision $(1-z)$
Local coordination authority	Proactive dispatching (x)	Active cooperation (y)	$A+B+C-D-I$ $H+I-J-N+X$ $M+O+P-Q-A$	$A+B+C-D-I$ $H+I-J+X$ $-R-S$
		Non-cooperation $(1-y)$	$A+B-D+L$ $-K-L-N$ $M+O+P-Q-A$	$A+B-D+L$ $-K-L$ $-R-S$
	Passive dispatching $(1-x)$	Active cooperation (y)	$-D-E-F-G-I$ $H+I-J-N$ $M+P-Q$	$-D-E-F-G-I$ $H+I-J$ $-R-S$
		Non-cooperation $(1-y)$	$-D-E-F-G+L$ $-K-L-N$ $M+P-Q$	$-D-E-F-G+L$ $-K-L$ $-R-S$

4. Model analysis

4.1 Evolution and stable strategy of local coordination authority

Upon examining Table 1, it is evident that the anticipated payoff E_{11} of the local coordination authority when adopting proactive dispatching is given by Eq. 1.

$$\begin{gathered} E_{11} = yz(A+B+C-D-I) + y(1-z)(A+B+C-D-I) \\ +(1-y)z(A+B-D+L) + (1-y)(1-z)(A+B-D+L) \end{gathered} \tag{1}$$

The expected return E_{12} for the local coordination authority when adopting a passive response is calculated as shown in Eq. 2.

$$\begin{gathered} E_{12} = yz(-D-E-F-G-I) + y(1-z)(-D-E-F-G-I) \\ +(1-y)z(-D-E-F-G+L) + (1-y)(1-z)(-D-E-F-G+L) \end{gathered} \tag{2}$$

The overall payoff E_1 for the local coordination authority is given by Eq. 3.

$$E_1 = xE_{11} + (1-x)E_{12} \tag{3}$$

Therefore, the replicator dynamic equation describing the evolution of the local coordination authority's strategy can be expressed by Eq. 4.

$$\begin{aligned} F(x) = \frac{\mathrm{d}x}{\mathrm{d}t} &= x(E_{11} - E_1) = x(1-x)(E_{11} - E_{12}) \\ &= -x(x-1)(A + B + E + F + G + Cy) \end{aligned} \tag{4}$$

The derivative of $F(x)$ with respect to x can be obtained in Eqs. 5 and 6.

$$\frac{\mathrm{d}\big(F(x)\big)}{\mathrm{d}x} = (1-2x)(A + B + E + F + G + Cy) \tag{5}$$

$$G(y, z) = A + B + E + F + G + Cy \tag{6}$$

When $y = \frac{A+B+E+F+G}{-C}$, $\frac{\mathrm{d}(F(x))}{\mathrm{d}x} \equiv 0$; when $y \neq \frac{A+B+E+F+G}{-C}$, $F(x) = 0$, then $x = 0$ and $x = 1$ are two equilibrium points and need to be classified and discussed.

Proposition 1. If the probability y of manufacturing firms choosing active cooperation is higher than$\frac{\mathrm{A+B+E+F+G}}{\mathrm{-C}}$, x will be stable at 1. Conversely, if y is lower than $\frac{\mathrm{A+B+E+F+G}}{\mathrm{-C}}$, the probability x will be stable at 0 as presented in Eq. 7.

$$x = \begin{cases} 0 & y < \dfrac{A + B + E + F + G}{-C} \\ [0,1] & y = \dfrac{A + B + E + F + G}{-C} \\ 1 & y > \dfrac{A + B + E + F + G}{-C} \end{cases} \tag{7}$$

The replication dynamics and the evolutionary stable strategies associated with the local coordination authority's preference for proactive measures are illustrated in Fig. 1. Here, V_{12}represents the probability x that the local coordination authority adopts proactive dispatching, whereas V_{11}denotes the probability $1 - x$ that it adopts passive dispatching. Proposition 1 indicates that when manufacturing firms exhibit a higher tendency y to actively cooperate in emergency rescheduling and resource reallocation, the local coordination authority is more likely to converge to proactive dispatching. Conversely, if firms tend to withhold cooperation and free-ride on others' adjustment efforts, the local coordination authority's incentives to mobilize resources and coordinate emergency dispatching weaken, and the evolutionary dynamics drive it toward a passive response. As a result, the evolutionary process ultimately leads the local coordination authority to favor proactive emergency dispatching as the stable strategy in manufacturing disruption recovery.

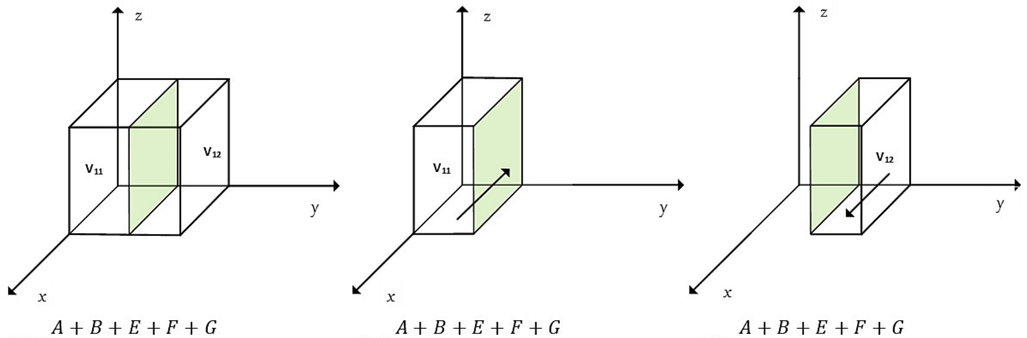

$y = \frac{A + B + E + F + G}{-C}$ $y < \frac{A + B + E + F + G}{-C}$ $y > \frac{A + B + E + F + G}{-C}$

Fig. 1 Strategic evolution landscape of local coordination authority

4.2 Evolution and stable strategy of manufacturing firms

The expected return E_{21} of the manufacturing firms choosing active cooperation is shown in Eq. 8.

$$\begin{aligned} E_{21} &= xz(H + I - J - N + X) + x(1-z)(H + I - J + X) \\ &+ (1-x)z(H + I - J - N) + (1-x)(1-z)(H + I - J) \end{aligned} \tag{8}$$

The expected return E_{22} of the manufacturing firms choosing non-cooperation is obtained according to Eq. 9.

$$\begin{gathered}E_{22} = xz(-K - L - N) + x(1 - z)(-K - L) \\ +(1 - x)z(-K - L - N) + (1 - x)(1 - z)(-K - L)\end{gathered} \tag{9}$$

The average return E_2 of the manufacturing firms choosing the mixed strategy is derived as presented in Eq. 10.

$$E_2 = yE_{21} + (1 - y)E_{22} \tag{10}$$

The replication dynamic equation for the active cooperation strategy is given by Eq. 11, and the derivative of $F(y)$ with respect to y can be obtained in Eq. 12.

$$F(y) = \frac{\mathrm{d}y}{\mathrm{d}t} = y(E_{21} - E_2) = -y(y - 1)(H + I - J + K + L + X * x) \tag{11}$$

$$\frac{d\big(F(y)\big)}{dy} = (1 - 2y)(H + I - J + K + L + Xx) \tag{12}$$

When $x = \frac{H+I-J+K+L}{-X}$, $\frac{\mathrm{d}(F(y))}{\mathrm{d}y} \equiv 0$; when $x \neq \frac{H+I-J+K+L}{-X}$, $F(y) = 0$, then $y = 0$ and $y = 1$ are two equilibrium points and need to be classified and discussed.

Proposition 2. If the likelihood x that the local coordination authority adopts proactive emergency production dispatching is higher than $\frac{H+I-J+K+L}{-X}$, the proportion of manufacturing firms choosing active cooperation in emergency rescheduling will converge to 1. Conversely, if the probability x is lower than $\frac{H+I-J+K+L}{-X}$, the proportion of firms choosing active cooperation will converge to 0. To sum up, the probability y of manufacturing firms choosing active cooperation is shown in Eq. 13.

$$y = \begin{cases} 0 & if \quad x < \dfrac{H + I - J + K + L}{-X} \\ [0{,}1] & if \quad x = \dfrac{H + I - J + K + L}{-X} \\ 1 & if \quad x > \dfrac{H + I - J + K + L}{-X} \end{cases} \tag{13}$$

The replication dynamics and the evolutionary stable strategies associated with manufacturing firms' preference for active cooperation are illustrated in Fig. 2. Here, V_{21} represents the probability that manufacturing firms adopt active cooperation, whereas V_{22} denotes the probability of non-cooperation. Proposition 2 implies that when the local coordination authority actively initiates emergency dispatching, firms are more likely to participate in implementable rescheduling actions, thereby converging to active cooperation. In contrast, when the local coordination authority remains passive and provides limited coordination, firms face weaker incentives and fewer long-term benefits from participating, and the evolutionary dynamics drive them toward non-cooperation.

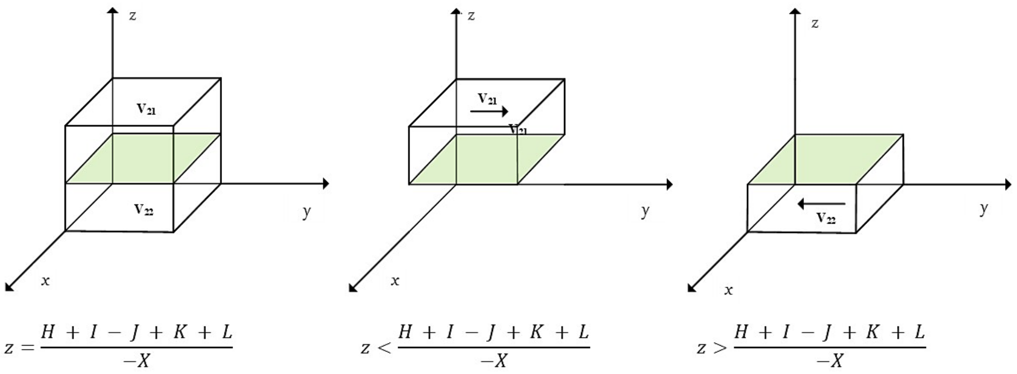

$z = \frac{H + I - J + K + L}{-X}$ $z < \frac{H + I - J + K + L}{-X}$ $z > \frac{H + I - J + K + L}{-X}$

Fig. 2 Strategic evolution landscape of manufacturing firms

4.3 Evolution and stable strategy of upper-level government

The expected return E_{31} of the upper-level government choosing strict supervision is listed in Eq. 14.

$$\begin{aligned} E_{31} &= xy(M+O+P-Q-A)+x(1-y)(M+O+P-Q-A) \\ &+(1-x)y(M+P-Q)+(1-x)(1-y)(M+P-Q) \end{aligned} \tag{14}$$

The expected return E_{32} for the upper-level government opting for loose supervision is calculated in Eq. 15.

$$\begin{aligned} E_{32} &= xy(-R-S)+x(1-y)(-R-S) \\ &+(1-x)y(-R-S)+(1-x)(1-y)(-R-S) \end{aligned} \tag{15}$$

The average expected income E_3 of the upper-level government follows directly from Eq. 16.

$$E_3 = zE_{31}+(1-z)E_{32} \tag{16}$$

Therefore, the upper-level government replication dynamic equation can be expressed by Eq. 17, and the derivative of $F(z)$ with respect to z can be obtained in Eq. 18.

$$F(z)=\frac{dz}{dt}=z(E_{31}-E_3)=-z(z-1)(M+P-Q+R+S-Ax+Ox) \tag{17}$$

$$\frac{d\big(F(z)\big)}{dz}=(1-2z)(M+P-Q+R+S-Ax+Ox) \tag{18}$$

When $x=\frac{M+P-Q+R+S}{A-O}$, $\frac{\mathrm{d}(F(z))}{\mathrm{d}z}\equiv 0$; when $x\neq\frac{M+P-Q+R+S}{A-O}$, $F(z)=0$ then $z=0$ and $z=1$ are two equilibrium points and need to be classified and discussed.

Proposition 3. If the value of x falls below $\frac{M+P-Q+R+S}{A-O}$, the likelihood of the upper-level government enforcing stringent oversight remains consistently at its maximum; if the probability x is higher than $\frac{M+P-Q+R+S}{A-O}$, the chance of the upper-level government opting for stringent supervision will consistently be at its minimum. The probability z of the superior government choosing strict supervision is shown in Eq. 19.

$$z=\begin{cases} 1 & x<\dfrac{M+P-Q+R+S}{A-O} \\ [0,1] & x=\dfrac{M+P-Q+R+S}{A-O} \\ 0 & x>\dfrac{M+P-Q+R+S}{A-O} \end{cases} \tag{19}$$

Fig. 3 illustrates the dynamics of replication and the evolutionary stable strategies pertaining to the upper-level government's selection of strict supervision measures.

V_{31} signifies the likelihood of the upper-level government opting for strict supervision, whereas V_{32} denotes the chance of selecting a loose supervision approach. Proposition 3 delineates that in the scenario where the local coordination authority is inclined towards passive dispatching, the upper-level government will be more likely to implement strict regulatory strategies. On the other hand, if the local coordination authority demonstrates proactive dispatching, the higher authority will be inclined to adopt a more relaxed regulatory approach.

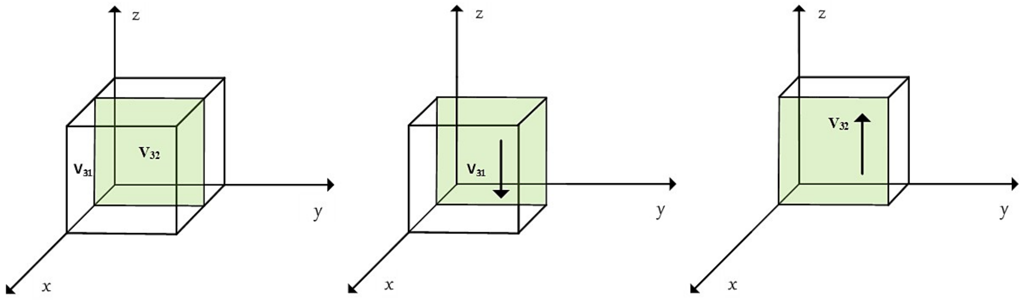

$x=\frac{M+P-Q+R+S}{A-O}$ $\quad x>\frac{M+P-Q+R+S}{A-O}$ $\quad x<\frac{M+P-Q+R+S}{A-O}$

Fig. 3 Strategic evolution landscape of upper-level government

4.4 System evolution stability analysis

By solving the system of equations where $F(x) = 0$, $F(y) = 0$, and $F(z) = 0$ simultaneously, we obtain eight candidate equilibrium points corresponding to the pure-strategy combinations of the three players, namely $E_1(0,0,0)$, $E_2(0,1,0)$, $E_3(0,0,1)$, $E_4(0,1,1)$, $E_5(1,0,0)$, $E_6(1,1,0)$, $E_7(1,0,1)$ and $E_8(1,1,1)$. These equilibria represent the corner solutions of the state space, where each strategy share takes a boundary value of 0 or 1 and the population adopts a single strategy with certainty. We then evaluate local stability at each equilibrium by substituting these points into the Jacobian matrix and examining the signs of the associated eigenvalues. This study focuses on pure-strategy boundary equilibria because they correspond to institutionally interpretable long-run regimes in emergency production dispatching, such as proactive dispatching versus passive response, active cooperation versus non-cooperation, and strict supervision versus loose supervision. Interior mixed equilibria may exist when payoff differences are exactly balanced, but in this application they are better understood as threshold or indifference states rather than robust governance regimes. Therefore, the subsequent stability analysis concentrates on pure-strategy equilibria, while mixed equilibria are acknowledged as a possible direction for future extensions.

According to Lyapunov stability theory, local stability in a replicator dynamic system can be assessed by examining the eigenvalues of the Jacobian matrix of the system at an equilibrium point [21]. The Jacobian is obtained by taking the first-order partial derivatives of the replicator dynamic equations with respect to the state variables, and it therefore summarizes how small perturbations in strategy proportions propagate through the evolutionary process. An equilibrium is asymptotically stable if the real parts of all eigenvalues are strictly negative, implying that any small deviation from the equilibrium decays over time and the trajectories converge back to that point. By contrast, if at least one eigenvalue has a non-negative real part, the equilibrium is locally unstable, because perturbations will not be damped and may instead grow or drive the system toward alternative equilibria. In this study, the derivative matrix, denoted here as J, is defined in the subsequent manner in Eq. 20.

$$J = \begin{bmatrix} \frac{\partial F(x)}{\partial x} & \frac{\partial F(x)}{\partial y} & \frac{\partial F(x)}{\partial z} \\ \frac{\partial F(y)}{\partial x} & \frac{\partial F(y)}{\partial y} & \frac{\partial F(y)}{\partial z} \\ \frac{\partial F(z)}{\partial x} & \frac{\partial F(z)}{\partial y} & \frac{\partial F(z)}{\partial z} \end{bmatrix} \tag{20}$$

$$= \begin{bmatrix} (1-2x)(A+B+E+F+G+C*y) & -x(x-1)C & 0 \\ -y(y-1)X & (1-2y)(H+I-J+K+L+Xx) & 0 \\ -z(z-1)(O-A) & 0 & (1-2z)(M+P-Q+R+S-Ax+Ox) \end{bmatrix}$$

By substituting E_1 through E_8 into the Jacobian matrix, the eigenvalues of the equilibrium points in Table 2 can be obtained. As shown in Table 2, the equilibrium points E_1 at the origin, E_2, E_3 and E_4 each have positive eigenvalues. Consequently, points E_1 through E_4 do not represent evolutionarily stable strategies (ESS).

Table 2 Eigenvalue analysis of the Jacobian matrix at equilibrium points

Equilibrium point	λ_1	λ_2	λ_3	Stability conclusion	Condition
$E_1(0,0,0)$	$A+B+E+F+G$	$H+I+K+L-J$	$M+P+R+S-Q$	Unstable point	
$E_2(0,1,0)$	$A+B+C+E+F+G$	$J-I-H-K-L$	$M+P+R+S-Q$	Unstable point	
$E_3(0,0,1)$	$A+B+E+F+G$	$H+I+K+L-J$	$Q-P-M-R-S$	Unstable point	
$E_4(0,1,1)$	$A+B+C+E+F+G$	$J-I-H-K-L$	$Q-P-M-R-S$	Unstable point	
$E_5(1,0,0)$	$-A-B-E-F-G$	$H+I-J+K+L+X$	$M+O+P-Q+R+S-A$	ESS	Eigenvalues are all less than 0
$E_6(1,1,0)$	$-A-B-C-E-F-G$	$J-I-H-K-L-X$	$M+O+P-Q+R+S-A$	ESS	Eigenvalues are all less than 0
$E_7(1,0,1)$	$-A-B-E-F-G$	$H+I-J+K+L+X$	$A+Q-M-O-P-R-S$	ESS	Eigenvalues are all less than 0
$E_8(1,1,1)$	$-A-B-C-E-F-G$	$J-I-H-K-L-X$	$A+Q-M-O-P-R-S$	ESS	Eigenvalues are all less than 0

The system shows four stable states under certain conditions. Notably, the equilibrium state $E_8(1,1,1)$ is particularly noteworthy as it represents an ideal balance. In this state, the local coordination authority initiates proactive dispatching, and manufacturing firms engage in active cooperation, all under the strict supervision of higher-level governments. This equilibrium symbolizes the effective collaboration among various entities. However, it is important to note that this stable state does not represent the Pareto optimal state of the system. The Pareto optimal state is identified as $E_6(1,1,0)$, characterized by more relaxed supervision from higher-level governments. Concurrently, local coordination authority and manufacturing firms demonstrate enhanced cooperative behaviors, leading to the minimal total system cost. Nevertheless, achieving this equilibrium typically necessitates substantial autonomy on the part of both local coordination authority and manufacturing firms. The stability conditions of equilibrium point $E_8(1,1,1)$ are listed in Eqs. 21 and 22.

$$J - I - H - K - L - X < 0 \tag{21}$$

$$A - M - O - P + Q - R - S < 0 \tag{22}$$

The following section of this research employs numerical simulations to visualize the interactions among the three emergency entities at the equilibrium state $E_8(1,1,1)$.

5. Numerical simulation analysis

In the initial stages of the numerical simulations conducted in Python, assigning values to parameters that influence the system is crucial. The literature primarily presents two methods for parameter assignment. One is based on theoretical stability analysis, and the other is based on empirical data from real cases [22]. Due to the scarcity of real-life data, this study opts for a parameter assignment method grounded in the results of stability analysis.

The parameters are normalized payoff values for simulation-based mechanism analysis rather than direct monetary estimates from a specific industrial park. Nevertheless, they have observable industrial counterparts. Coordination costs, firm adjustment costs, and supervision costs can be linked to labor hours, communication costs, overtime, changeover, setup, expedited procurement, outsourcing, inspection frequency, and monitoring expenditure, while operational benefits can be proxied by reductions in recovery time, order tardiness, work-in-process accumulation, and throughput loss. Thus, the numerical setting is used as a theoretically consistent baseline scenario, and future studies may calibrate the parameters using scheduling logs, MES/ERP records, disruption reports, and cost accounting data.

Therefore, the managerial implications derived from the simulations should be understood as mechanism-oriented implications based on comparative parameter changes, rather than as precise predictions for a particular industrial park. The sensitivity analysis is used to test how changes in key payoff components affect evolutionary trajectories under the same baseline structure.

Specifically, this study assigns values to the parameters of the tripartite evolutionary game system. These assignments are designed to ensure that the parameters comply with the stability determination theorem for the equilibrium point $E_8(1,1,1)$ in the system. The details of the parameter assignments are as follows.

$$\begin{array}{llllll} A = 4 & B = 2 & C = 1.5 & E = 2.2 & F = 2.5 & G = 3 \\ H = 1.8 & I = 0.9 & J = 6 & K = 3.5 & L = 1.3 & M = 2.6 \\ O = 1 & P = 1.7 & Q = 5 & R = 5 & S = 1.9 & X = 0.8 \end{array}$$

5.1 Initial evolution path analysis

Using the parameter values specified above, numerical experiments were conducted, and the initial evolutionary trajectory of the system is shown in Fig. 4. The numerical simulation results are consistent with the theoretical analysis. Specifically, the stability of the equilibrium point $E_8(1,1,1)$ dictated the parameter assignments, and the simulation results evolved toward this state, thereby validating the accuracy of the theoretical predictions. Furthermore, it is observed that the convergence state of the system remains consistent across different initial conditions. This indicates that while the initial values influence the rate of system evolution, they do not affect the system's eventual stable state. The stability of the system remains intact regardless of variations in initial conditions, as these do not alter the fundamental stability judgment criteria.

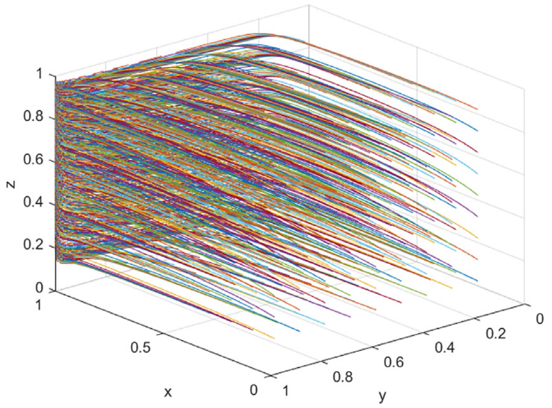

Fig. 4 Initial trajectory of the system's equilibrium at the point (1,1,1)

5.2 Sensitivity analysis

The initial evolutionary path indicates that the system's stable state depends on the characteristic values of each equilibrium point. To reduce the influence of initial-value fluctuations in the sensitivity analysis, the initial strategy probabilities of all three game players are uniformly set to 0.5.

Local coordination authority's proactive dispatching and resource support from the upper-level government

In the simulations, upper-level government resource support was set to $A = 4, 8$, and 16, with the evolutionary trajectories shown in Fig. 5. The results indicate that higher support accelerates the local coordination authority's convergence toward proactive dispatching by reducing the coordination burden of rescheduling, information integration, and cross-plant capacity pooling. Meanwhile, increased support makes the upper-level government more inclined toward looser supervision, reflecting the budgetary and administrative burden of combining strict oversight with substantial support. By contrast, support has limited direct impact on manufacturing firms' strategies, since it mainly operates through the vertical government-to-authority channel. Unless converted into firm-level compensation for changeover, overtime, or expedited procurement costs, firms do not treat it as an immediate payoff improvement.

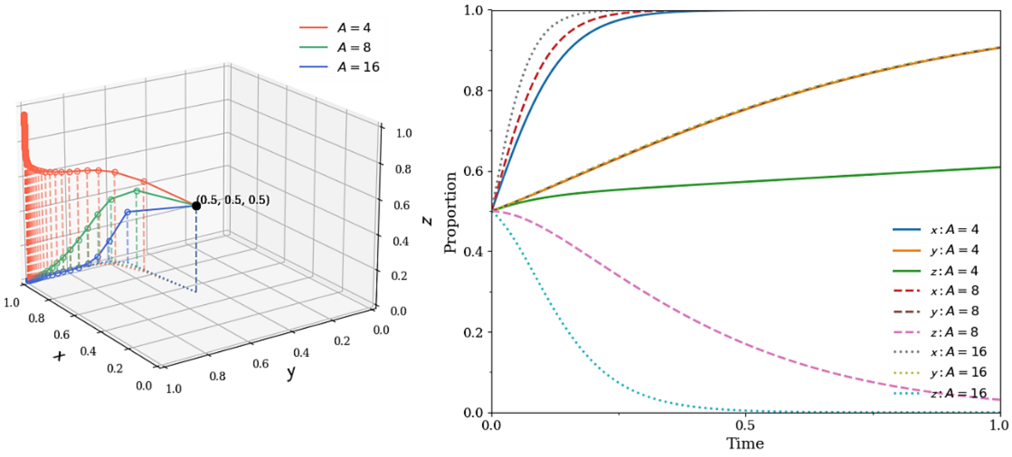

Fig. 5 The impact of changes in upper-level resource support

Dispatching effectiveness gains generated by manufacturing firms' active cooperation

To assess cooperation-driven effectiveness gains, we set the additional gain from firms' active cooperation to $C = 1, 15$, and 45, with evolutionary trajectories shown in Fig. 6. The results indicate that higher C accelerates the local coordination authority's convergence toward proactive emergency dispatching by improving schedule feasibility, shortening recovery time, and reducing shop-floor congestion such as work-in-process accumulation and cross-plant spillovers. Meanwhile, as C increases, the upper-level government becomes less inclined to maintain strict supervision, suggesting that stronger horizontal coordination reduces the marginal returns of costly vertical enforcement. Overall, cooperation-induced effectiveness gains mainly affect the authority's dispatching stance and secondarily influence supervisory intensity.

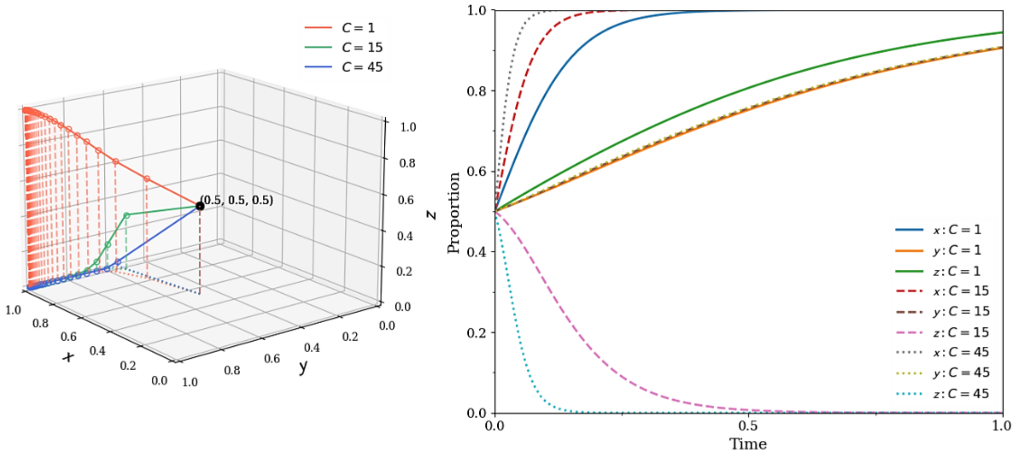

Fig. 6 The impact of changes in cooperation gains from firms' active collaboration

Passive dispatching by the local coordination authority and penalties imposed by the upper-level government

In the simulations, the penalty intensity imposed by the upper-level government on the local coordination authority's passive dispatching was set to $F = 2, 5$, and 10, and the corresponding evolutionary trajectories are presented in Fig. 7. The results show that stronger penalties reduce the local coordination authority's tendency to remain passive and accelerate its shift toward proactive emergency dispatching. Meanwhile, the upper-level government's propensity to maintain strict supervision declines as F increases, suggesting an adaptive response under bounded rationality. Once deterrence effectively disciplines passive behavior, the marginal return to sustained high-intensity supervision diminishes relative to its costs. The role of penalties is therefore analogous to that of cooperation-induced effectiveness gains (parameter C) in promoting proactive dispatching, implying that an implementable emergency dispatching scheme should combine credible sanctions with mechanisms that enhance the operational benefits of cooperation.

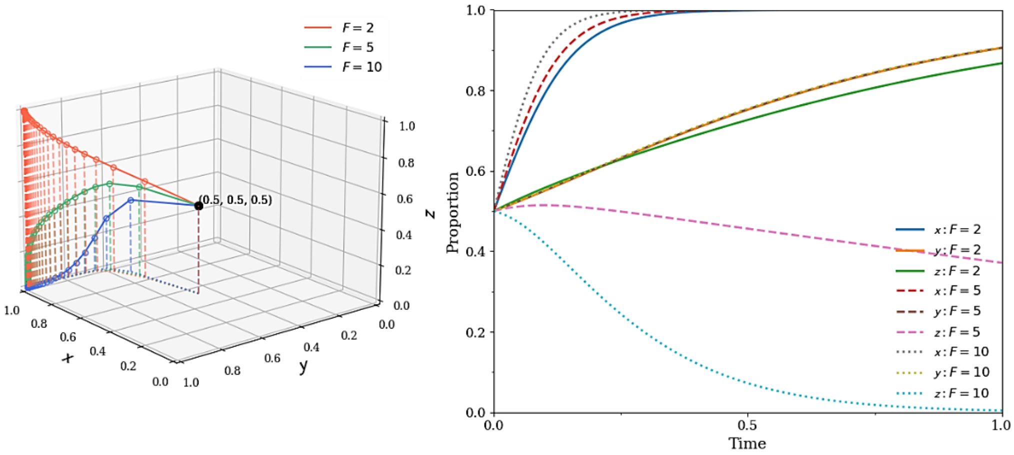

Fig. 7 The impact of changes in penalty F imposed by the upper-level government

Manufacturing firms' dispatching adjustment costs

The adjustment costs borne by manufacturing firms when engaging in cooperative emergency rescheduling and capacity reallocation were set to $J = 6$, 12, and 24, with the simulation results reported in Fig. 8. Higher adjustment costs slow convergence toward active cooperation. When J increases from 6 to 12, non-cooperation becomes more attractive. The impact is concentrated on firms' own strategy dynamics, while the local coordination authority and the upper-level government are only weakly affected, indicating that dispatching adjustment costs mainly operate through firms' private cost–benefit calculus. From a policy and mechanism design perspective, lowering the effective adjustment costs through targeted compensation, expedited procurement support, or temporary capacity subsidies can increase firms' willingness to cooperate and improve the implementability and stability of emergency dispatching at the industrial-park level.

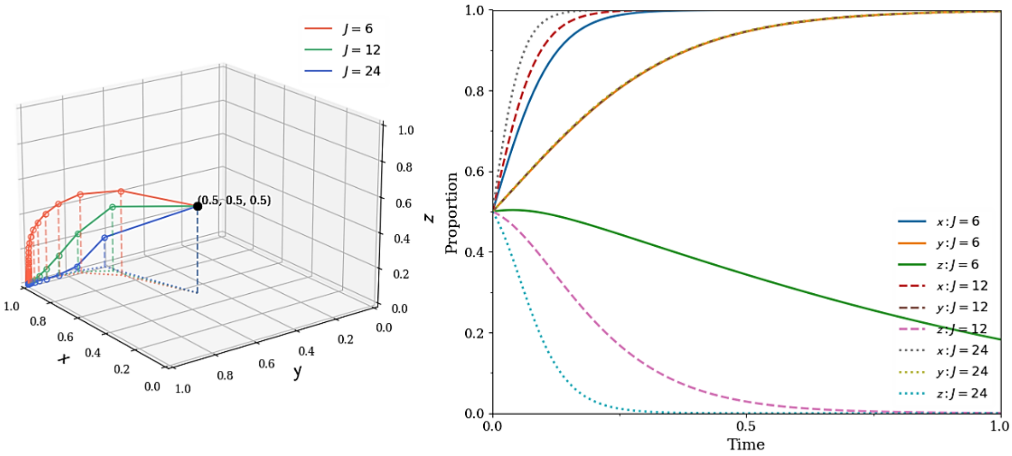

Fig. 8 The impact of firms' resource adjustment costs

Supervision costs of the upper-level government

In the simulations, the supervision cost borne by the upper-level government under strict supervision was set to $Q = 5, 10$, and 20, and the corresponding evolutionary trajectories are presented in Fig. 9. The results show that higher supervision costs reduce the attractiveness of strict supervision and shift the upper-level government toward looser supervision, with a noticeable change as Q increases from 10 to 20. This pattern is consistent with boundedly rational adjustment. As enforcement becomes more expensive, its net payoff declines relative to a low-intensity supervisory stance. The direct impact of supervision cost on the local coordination authority and manufacturing firms is limited, implying that supervision cost mainly operates through the upper-level government's own cost–benefit calculus. Therefore, effective oversight design should prioritize cost-efficient enforcement and monitoring arrangements so that supervisory intensity remains sustainable without undermining the overall stability of emergency dispatching.

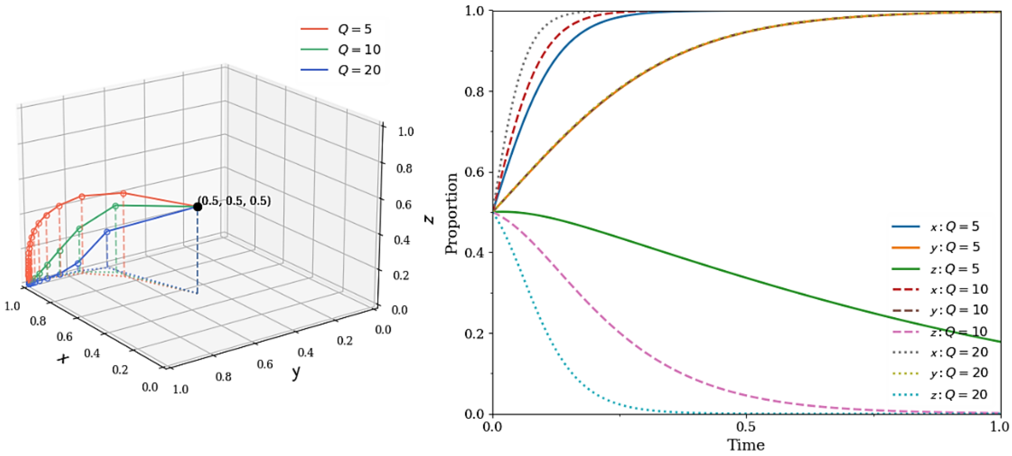

Fig. 9 The impact of changes in the supervision cost

Long-term collaboration payoffs for manufacturing firms

The long-term collaboration payoff for manufacturing firms was set to $X = 0.8$, 28, and 56, with results shown in Fig. 10. Larger X accelerates firms' convergence toward active cooperation, especially in the early evolutionary stage, while its marginal effect weakens as the system stabilizes. This suggests that long-term benefits, such as preferential access to shared capacity, priority support in future disruptions, and relational gains from coordination, can motivate cooperation but show diminishing returns. X has limited direct influence on the local coordination authority and upper-level government, indicating that public actors' strategies depend on broader cost–benefit considerations. Therefore, policy design should strengthen credible long-term cooperation rewards while coordinating them with enforcement and support instruments.

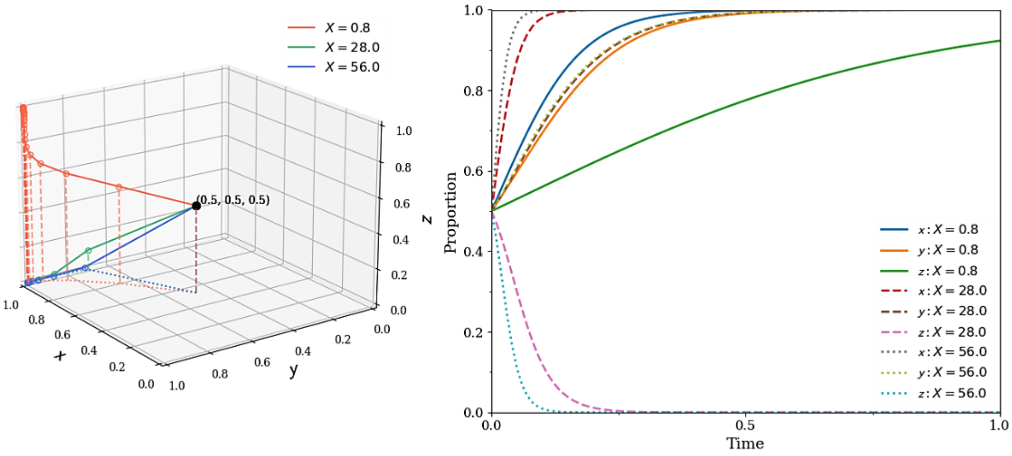

Fig. 10 The impact of changes in the long-term collaboration payoff X

5.3 Comparison of simulation analysis results

Local coordination authority

Across the sensitivity experiments, the local coordination authority's shift toward proactive dispatching is mainly shaped by resource support (A), cooperation-induced effectiveness gains (C), and penalties for passive response (F). Greater upper-level resource support accelerates proactive dispatching by easing implementation constraints in emergency plan activation, schedule revision, information integration, and cross-plant capacity pooling. Higher cooperation-induced effectiveness gains further reinforce this shift by improving schedule feasibility, reducing shop-floor congestion, and supporting throughput recovery. Stronger penalties for passive dispatching also discourage delayed coordination by increasing the expected cost of inaction. Overall, proactive dispatching becomes evolutionarily stable when the authority has sufficient enabling capacity (A), can convert cooperation into execution gains (C), and faces credible discipline (F) against passivity.

Manufacturing firms

Manufacturing firms' strategy dynamics are mainly driven by adjustment costs (J) and long-term collaboration payoffs (X), reflecting a private implementation calculus distinct from public actors. Higher adjustment costs slow the shift toward active cooperation and may push firms toward non-cooperation once costs become moderate, suggesting that the key bottleneck is often shop-floor feasibility rather than willingness. These costs include overtime, changeovers, sequence deviations, expedited procurement, temporary capacity rental, and coordination effort. In contrast, larger long-term collaboration payoffs promote early cooperation, although their marginal effect weakens as the system stabilizes. Overall, firms cooperate when short-run execution costs (J) are manageable and participation offers credible future advantages (X), such as priority access to shared capacity and stable cross-firm routines.

Upper-level government

The upper-level government's supervisory strategy is mainly driven by strict supervision cost (Q), which includes monitoring, inspection, and coordination expenses during disruptions. As Q increases, the system shifts toward looser supervision, reflecting boundedly rational adjustment to the declining net returns of costly oversight. Higher resource support (A) also weakens strict supervision by increasing fiscal and administrative burdens. Moreover, stronger cooperation-induced effectiveness gains (C) and penalties on passive dispatching (F) reduce the need for continuous high-intensity enforcement. This indicates a substitution mechanism: when horizontal cooperation improves rescheduling implementability or deterrence disciplines passivity, strict supervision yields smaller marginal benefits. Therefore, sustainable oversight should rely on cost-efficient monitoring, selective enforcement, and dynamic adjustment according to rescheduling implementability and firm-level cooperation effectiveness.

In this study, emergency production dispatching is interpreted as the implementation process that makes disrupted production plans executable, rather than as a substitute for a shop-floor scheduling or rescheduling algorithm. Operationally, it may involve order resequencing, machine reassignment, changeover acceleration, overtime arrangement, expedited procurement, temporary outsourcing, cross-firm capacity sharing, and delivery-priority adjustment. A scheduling model may generate candidate rescheduling plans and indicators such as recovery time, tardiness reduction, throughput loss, capacity utilization, and adjustment cost, while the governance layer developed here explains whether these plans can be implemented through proactive coordination, firm cooperation, and appropriate supervision.

6. Conclusion

This study develops a tripartite evolutionary game model to explain how emergency production dispatching becomes implementable when disruptions invalidate shop-floor schedules and require rapid rescheduling. The findings show that emergency dispatching is not only a technical rescheduling problem, but also a governance implementation problem shaped by coordination, firm cooperation, and supervision.

The main implication is that robust disruption response requires a balanced mechanism that reduces firms' adjustment burdens, strengthens repeated cooperation benefits, maintains credible discipline, and calibrates supervision intensity to actual rescheduling implementability. The model is most applicable to settings with a similar coordination-cooperation-supervision structure, such as manufacturing clusters, shared-capacity platforms, multi-plant production networks, and regional emergency supply coordination systems. Future research can calibrate the payoff parameters with industrial data and connect the governance layer to optimization-based rescheduling models.

Acknowledgement

This paper is based on a research project supported by the National Natural Science Foundation of China (No. 72174044) (No. 72504070).

References

[1] Liu, H., Han, Y., Zhu, A. (2022). Modeling supply chain viability and adaptation against underload cascading failure during the COVID-19 pandemic, *Nonlinear Dynamics*, Vol. 110, No. 3, 2931-2947, doi: 10.1007/s11071-022-07741-8.

[2] Khalili-Damghani, K., Tavana, M., Ghasemi, P. (2022). A stochastic bi-objective simulation-optimization model for cascade disaster location-allocation-distribution problems, *Annals of Operations Research*, Vol. 309, No. 1, 103-141, doi: 10.1007/s10479-021-04191-0.

[3] Singh, R.K., Modgil, S., Acharya, P. (2019). Assessment of supply chain flexibility using system dynamics modeling, *Global Journal of Flexible Systems Management*, Vol. 20, Suppl. 1, 39-63, doi: 10.1007/s40171-019-00224-7.

[4] Duenas, A., Petrovic, D. (2008). An approach to predictive-reactive scheduling of parallel machines subject to disruptions, *Annals of Operations Research*, Vol. 159, 65-82, doi: 10.1007/s10479-007-0280-3.

[5] Sawik, T. (2014). On the robust decision-making in a supply chain under disruption risks, *International Journal of Production Research*, Vol. 52, No. 22, 6760-6781, doi: 10.1080/00207543.2014.916829.

[6] Leung, C.S.K., Lau, H.Y.K. (2020). Simulation-based optimization for material handling systems in manufacturing and distribution industries, *Wireless Networks*, Vol. 26, No. 7, 4839-4860, doi: 10.1007/s11276-018-1894-x.

[7] Rossit, D.A., Tohmé, F., Frutos, M. (2019). A data-driven scheduling approach to smart manufacturing, *Journal of Industrial Information Integration*, Vol. 15, 69-79, doi: 10.1016/j.jii.2019.04.003.

[8] Lu, J.T., Yang, N.D., Ye, J.F., Wu, H. (2014). The influence paths of emotion on the occupational safety of rescuers involved in environmental emergencies: Systematic review article, *Iranian Journal of Public Health*, Vol. 43, No. 11, 1478-1485.

[9] Gabler, C.B., Richey Jr, R.G., Stewart, G.T. (2017). Disaster resilience through public-private short-term collaboration, *Journal of Business Logistics*, Vol. 38, No. 2, 130-144, https://doi.org/10.1111/jbl.12152.

[10] Kovács, G., Falagara Sigala, I. (2021). Lessons learned from humanitarian logistics to manage supply chain disruptions, *Journal of Supply Chain Management*, Vol. 57, No. 1, 41-49, doi: 10.1111/jscm.12253.

[11] Diehlmann, F., Lüttenberg, M., Verdonck, L., Wiens, M., Zienau, A., Schultmann, F. (2021). Public-private collaborations in emergency logistics: A framework based on logistical and game-theoretical concepts, *Safety Science*, Vol. 141, Article No. 105301, doi: 10.1016/j.ssci.2021.105301.

[12] Zhang, M., Kong, Z. (2022). A tripartite evolutionary game model of emergency supplies joint reserve among the government, enterprise and society, *Computers & Industrial Engineering*, Vol. 169, Article No. 108132, doi: 10.1016/j.cie.2022.108132.

[13] Ye, Y., Jiao, W., Yan, H. (2020). Managing relief inventories responding to natural disasters: Gaps between practice and literature, *Production and Operations Management*, Vol. 29, No. 4, 807-832 doi: 10.1111/poms.13136.

[14] Lu, J.T., Yang, N.D., Ye, J.F., Liu, X.G., Mahmood, N. (2015). Connectionism strategy for industrial accident-oriented emergency decision-making: A simulation study based on PCS model, *International Journal of Simulation Modelling*, Vol. 14, No. 4, 633-646, doi: 10.2507/IJSIMM14(4)6.315.

[15] Lu, J., Yang, N., Ye, J., Lei, T., Mahmood, N. (2015). Differential effects of specific negative emotions on individual risk preference behaviors under social accidents: An analysis from the perspective of affective computing theory, *Revista de Cercetare si Interventie Sociala*, Vol. 50, 172-192.

[16] Friedman, D. (1991). Evolutionary games in economics, *Econometrica*, Vol. 59, No. 3, 637-666, doi: 10.2307/2938222.

[17] Zhang, J., Li, L. (2022). Intelligent construction technology adoption driving strategy in China: A tripartite evolutionary game analysis, *Journal of Environmental and Public Health*, Vol. 2022, Article No. 9372443, doi: 10.1155/2022/9372443.

[18] Wang, G., Hu, X., Wang, T., Liu, J., Feng, S., Wang, C. (2024). Tripartite evolutionary game analysis of a logistics service supply chain cooperation mechanism for network freight platforms, *International Journal of Intelligent Systems*, Vol. 2024, No. 1, Article No. 4820877, doi: 10.1155/2024/4820877.

[19] Wang, T.Y., Zhang, H. (2023). Blockchain-based tripartite evolutionary game study of manufacturing capacity sharing, *Advances in Production Engineering & Management*, Vol. 18, No. 2, 225-236, doi: 10.14743/apem2023.2.469.

[20] Lin, S.Y., Zheng, M.Y., Chen, J.L. (2025). Tripartite evolutionary game analysis of the adoption of AI delivery technology, *Advances in Production Engineering & Management*, Vol. 20, No. 4, 475-490, doi: 10.14743/apem2025.4.553.

[21] Sastry, S. (1999). Lyapunov stability theory, In: *Nonlinear systems: analysis, stability, and control*, Springer, New York, USA, 182-234, doi: 10.1007/978-1-4757-3108-8_5.

[22] Stuart, A.M., Humphries, A.R. (1994). Model problems in numerical stability theory for initial value problems, *SIAM Review*, Vol. 36, No. 2, 226-257, doi: 10.1137/1036054.

APEM journal
Advances in Production Engineering & Management
Volume 21 | Number 1 | March 2026 | pp 40–56
https://doi.org/10.14743/apem2026.1.560
ISSN 1854-6250
Journal home: apem-journal.org
Oroginal scientific paper

Optimization of a truck-autonomous unmanned vehicle distribution network with mobile charging and PV-storage integration

Liu, Y.H.[a,*], **Shi, X.L.**[a]

[a]School of Economics and Management, Beijing Jiaotong University, Beijing, P.R. China

ABSTRACT

This study investigates the collaborative optimization of routing and charging in a distribution network comprising electric trucks (ETs) and autonomous unmanned vehicles (AUVs), supported by mobile photovoltaic (PV) storage charging. A comprehensive optimization model is developed to minimize the total daily operating cost of the logistics enterprise, encompassing vehicle acquisition, staffing, energy consumption, charging, and penalties. The model simultaneously determines coordinated ET-AUV delivery routes, mobile charging schedules, and parking node locations. The PV-storage system is incorporated as a green power-supply constraint, directly influencing charging costs. To address the model's complexity, an enhanced hybrid frog-leaping algorithm is proposed. This algorithm incorporates an initial solution construction method to improve population quality, an advanced local deep search to increase search efficiency, and diversity control strategies with clone selection programs to maintain population diversity. The effectiveness of the developed algorithm is validated through multiple case studies with varying customer sizes. Computational experiments on instances with up to 60 customers indicate that, compared with the ET-only mode, the proposed ET-AUV collaborative mode reduces total daily operating costs by 18.61 %, decreases staffing costs by 62.5 %, and lowers penalty costs by 23.21 %, thereby enhancing customer satisfaction and operational resilience. Sensitivity analysis shows that system efficiency depends on several operational parameters. Increases in ET payload and range are the main drivers of cost reduction. Additionally, the average speeds of both vehicle types have a critical U-shaped effect on total costs.

ARTICLE INFO

Keywords:
Unmanned delivery;
Truck-autonomous unmanned vehicle routing optimization;
Mobile charging;
Photovoltaic storage charging;
Hybrid frog leaping algorithm;
Electric vehicle routing;
Energy-constrained routing

**Corresponding author:*
13811117792@126.com
(Liu, Y.H.)

Article history:
Received 12 December 2025
Revised 10 March 2026
Accepted 15 March 2026

1. Introduction

The rapid development of the Internet has accelerated the growth of online retail and e-commerce, creating substantial opportunities and demands for the logistics industry. However, these advancements have also introduced significant challenges, particularly regarding urban last-mile delivery. Increasing labour costs and restrictions on courier working hours impede logistics companies from providing efficient, stable, and nearly continuous distribution services, which places considerable pressure on fulfilment rates and cost management. Traditional delivery methods also increase physical contact between couriers and recipients, raising safety concerns, especially during public health emergencies. In densely populated areas such as campuses and residential complexes, truck access is frequently restricted. Moreover, as an energy-intensive sector, the logistics industry contributes significantly to greenhouse gas emissions. Population growth and urbanization have further intensified issues in urban distribution, including high energy consumption, extended delivery times, and increased carbon emissions. In response to increasing distribution demand, rising customer expectations, worsening environmental pollution, growing urban traffic pressure, and other issues, innovative, high-quality, and automated distribution methods have become central to the competitiveness of the logistics industry during transformation and upgrading.

Within the evolution of intelligent logistics, unmanned delivery robots are emerging as a significant alternative to traditional delivery methods and are establishing a new business model in the modern logistics sector. In contrast to drones, autonomous unmanned vehicles (AUVs), although slower, are not constrained by low-altitude airspace regulations in urban areas, demonstrate greater adaptability to diverse weather conditions, and feature multiple compartments for distributing goods to various customers in a single trip. Furthermore, they generate substantially lower noise levels, making them more suitable for routine urban distributions [1]. Srinivas *et al.* [2] recently reviewed the literature on AUV routing and classified existing research into two categories: distribution modes relying solely on AUVs and those assisted by trucks, based on problem characteristics and application domains. Research on the former remains limited, primarily due to the inherent limitations of AUVs, such as reduced speed, limited range, and restricted payload [3]. Conversely, truck-assisted distribution modes present more advantages.

The truck-autonomous unmanned vehicle routing problem (TAUVRP) has become a significant focus of recent research. Based on system characteristics, TAUVRP is typically classified into two categories: the two-tier concept and the mothership concept [4]. In the two-tier concept, trucks operate at the first tier, transporting parcels from the warehouse to an AUV warehouse, which then delivers parcels to final customers at the second tier [5-7]. In the mothership concept, trucks are modified into mothership systems equipped with AUVs, traveling to various neighbourhoods and deploying AUVs to deliver parcels to nearby customers. Jennings and Figliozzi [8] and Simoni *et al.* [9] examine the mothership concept, focusing on scenarios where trucks do not wait at the same parking node for AUVs to return; however, neither study considers time window constraints. In contrast, Chen *et al.* [10] and Chen *et al.* [11] investigate a TAUVRP that incorporates time windows, requiring trucks to remain at the parking node until all dispatched AUVs have returned. Yu *et al.* [4] further categorize TAUVRPs based on whether trucks serve customers directly. In one type, trucks function as both mobile platforms for dispatching and collecting AUVs and as service providers to customers. In the other type, trucks serve solely as mobile platforms for dispatching and collecting AUVs. Building on this classification, Yu *et al.* [12] propose a TAUVRP that addresses simultaneous pickup and delivery. More recently, Mokhtari-Moghadam *et al.* [13] investigate the integrated optimization problem of AUV-drone collaborative distribution. In some cases, customer delivery demands may exceed the payload capacity of AUVs. If these demands are indivisible, serving such customers becomes infeasible. Therefore, incorporating multiple split deliveries by AUVs is essential for effectively addressing TAUVRP in urban environments.

Battery capacity limitations require AUVs to undergo multiple recharges during delivery trips, particularly when operating in truck-assisted modes. Most existing research on TAUVRP focuses on diesel trucks, with limited attention given to the use of electric trucks (ETs) and the charging of AUVs during transportation. Yu *et al.* [14] are among the few to address the optimization of ET-assisted distribution routes, utilizing ETs to provide on-board wireless charging for AUVs to improve delivery efficiency. To resolve ET charging challenges, various technologies such as fixed and mobile charging are employed to enhance convenience. Although fixed charging is the most prevalent, truck drivers may need to take detours to access charging stations, resulting in unnecessary power consumption. Additionally, long charging times can lead to queuing at stations, thereby reducing delivery efficiency [15]. To mitigate these issues, mobile charging vehicles (MCVs) can be deployed at strategic locations along ET routes, offering greater charging flexibility [16]. Integrated scheduling of ETs and MCVs is therefore essential for optimizing logistics and delivery systems. The decarbonisation of freight transportation through MCVs is also influenced by indirect carbon emissions associated with charging. If electricity is generated from thermal power, the widespread adoption of electric vehicles may undermine carbon reduction efforts. Consequently, research increasingly focuses on renewable energy charging facilities. Solar photovoltaic (PV) systems have been identified as a promising solution for enhancing the environmental benefits of logistics electrification [17]. Integrating PV systems, energy storage systems (ESS), and charging piles effectively addresses the mismatch between PV generation and charging demand [18].

In summary, this study introduces MCVs, PV storage charging stations, and a multiple split distribution model to construct, for the first time, a truck-autonomous unmanned vehicle distribution network considering mobile photovoltaic storage charging (TAUVDN-MPSC). The contribution is threefold. First, for the TAUVDN-MPSC, a comprehensive optimization model is developed to simultaneously optimize ET-AUV distribution routes, mobile charging schedules, and parking-node locations while accounting for environmental, operational, and customer-service considerations. The objective is to minimize the sum of vehicle purchase cost, staffing cost, energy consumption cost, charging cost, and penalty cost. Secondly, given the complexity of the established model, an improved hybrid frog leaping algorithm (IHFLA) is proposed. This involves introducing an initial solution construction algorithm to enhance the quality of the population, developing an improved local deep search to improve local search efficiency, and incorporating diversity control strategies and clonal selection procedures to ensure population diversity. Finally, the performance of the IHFLA is validated using specially designed test cases of different scales. Sensitivity analysis is also applied to explore the impact of vehicle load and endurance mileage on the total operating cost. This is intended to provide key theoretical support and practical guidance for achieving a green, intelligent, and integrated urban logistics and distribution system.

2. Mathematical model

2.1 Problem statement

The TAUVDN-MPSC can be described as follows. Based on the actual urban distribution scenario, each ET carries AUVs and goods from the distribution centre and returns to the distribution centre after completing a daily distribution service, as shown in Fig. 1. ETs are not allowed to directly deliver goods to customers and must wait at the parking nodes to collect all AUVs they have dispatched before visiting the next parking node or returning to the distribution centre. Each parking node is visited by at most one ET. AUVs depart from the parking nodes to perform customer distribution services. Each customer has a soft time window $[e_i, l_i]$ and can only be visited by one AUV. Considering vehicle load constraints, this study assumes three AUV distribution modes: (1) single distribution, where the AUV completes a distribution service and returns to the parking node, then travels to the next location with the ET; (2) split distribution, where the same AUV makes multiple round trips to the parking node to provide distribution services to the same customer; (3) multiple distributions, where the same AUV makes multiple round trips to the same parking node to provide distribution services to different customers.

During the distribution operation, when the battery of an ET runs low, the distribution centre will arrange an MCV to charge it at the selected mobile charging node. After completing the charging, the MCV will proceed to the next mobile charging node or return to the distribution centre. The mobile charging node is selected from the unvisited parking nodes. It is assumed that the MCV arrives at the mobile charging node no later than the arrival time of the ET. ETs also serve as a mobile charging platform. When the AUV is mounted on the ET and travels to the next node, the AUV utilizes the time it spends on the ET to obtain electricity from the ET through wireless charging technology. In this way, energy flows from MCV to ET and then to AUVs, forming a complete chain supply. One MCV can charge multiple ETs, while each ET is only served by one MCV. The MCV carries a large battery and does not require recharging during service. A PV storage charging station is built at the distribution centre, where only PV output is generated on the generation side, providing charging for the MCVs, ETs, and AUVs parked at the distribution centre.

To standardize the description of mathematical models, a directed graph $G = (V, A)$ is given. The node set V includes a distribution centre V_0, a customer set V_c, a mobile charging node set V_{mc}, and a parking node set V_r. The arc set A includes an ET arc set A_1, an AUV arc set A_2, and an MCV arc set A_3. The ET set and the MCV set are denoted by K and M, respectively.

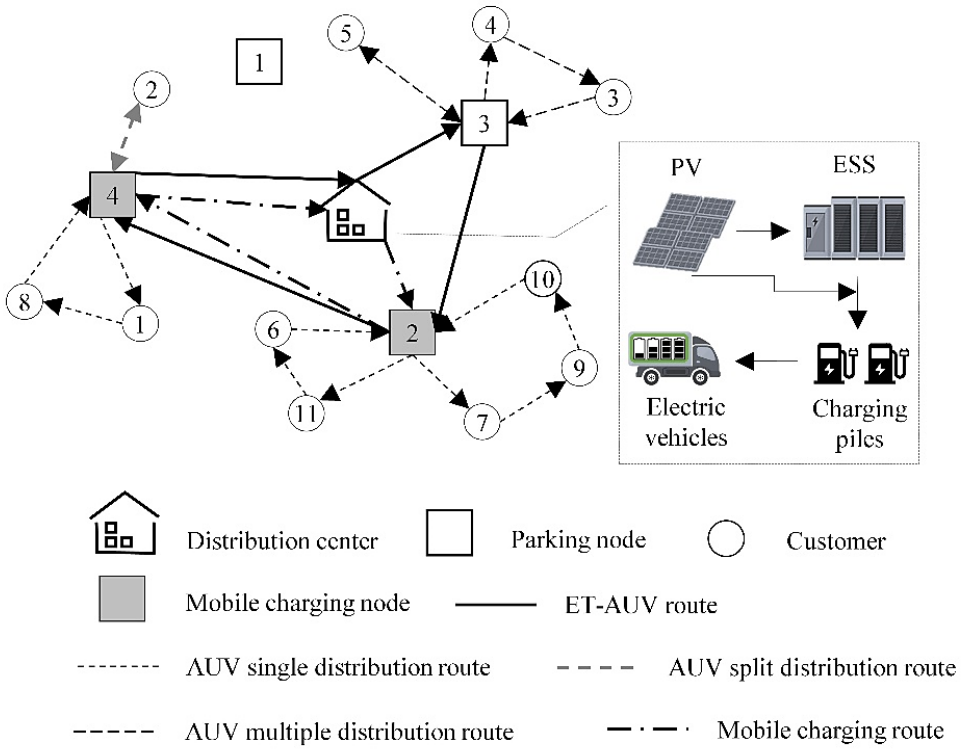

Fig. 1 Truck-unmanned vehicle distribution network

2.2 Symbol description

The settings and specific meanings of model decision variables and parameters are shown in Tables 1 and 2, respectively.

Table 1 Decision variables

Variables	Description
$x_{ij}^{AUV_k}$	1 indicates the AUV belonging to ET k passes arc (i,j), otherwise 0
y_j	1 means parking node j is selected, otherwise 0
z_j	1 indicates parking node j is selected as the mobile charging node, otherwise 0
$x_{ij}^{ET_k}$	1 indicates ET k passes arc (i,j), otherwise 0
$x_{ij}^{MCV_m}$	1 indicates MCV m passes arc (i,j), otherwise 0
$y_{j,mk}$	1 indicates MCV m at mobile charging node j provides charging services for ET k, otherwise 0

Table 2 Model parameters

Parameters	Description	Parameters	Description
pc_{AUV}	Cost of an AUV converted into one day	M_{MCV}	Unloaded mass of MCVs
sub_{AUV}	Cost of government subsidies equivalent to one day for AUVs	v_{ET}	Average running speed of ETs
pc_{ET_k}	The purchase price of an ET converted into one day	v_{MCV}	Average driving speed of MCVs
pc_{MCV_m}	One day purchase price of an MCV	v_{AUV}	Average driving speed of AUVs
c_{salary}	Average salary of a staff member	c_{mc}	Mobile charging price
c_w^{AUV}	Waiting time cost of AUVs	c_{PV}	PV charging price
c_d^{AUV}	Penalty time cost of AUVs	sub_{pv}	PV charging subsidy
$wt_i^{AUV_k}$	Early arrival time of AUVs	$pt_i^{AUV_k}$	Delay time of AUVs
$E_{d,j}^{ET_k}$	Battery power when ET leaves node j	C_{ET}	Maximum payload of ETs
c_w^{MCV}	Waiting time cost of MCVs	$at_i^{ET_k}$	Arrival time of ET

Table 2 (Continuation)

Parameters	Description	Parameters	Description
t_{ij}	Travel time along the arc (i,j)	st_i	Customer service time
$E_{a,j}^{ET_k}$	Battery power when ET arrives at node j	d_i	Customer demand
$E_{d,V_0}^{MCV_m}$	Battery power when MCV leaves V_0	C_{AUV}	Maximum payload of AUVs
$P_{ij}^{EV_k}$	Power demand of ETs passing through $(i,j) \in A_1$	Ψ	A large positive number
$P_{ij}^{AUV_k}$	Power demand of AUVs passing through $(i,j) \in A_2$	$at_j^{MCV_m}$	Arrival time of MCVs
P_{ij}^{MCV}	Power demand of MCVs passing through $(i,j) \in A_3$	E_{cap}^{AUV}	Battery capacity of AUVs
N_{AUV}^{max}	Maximum number of AUVs that can be carried by an ET	E_{cap}^{ET}	Battery capacity of ETs
$E_{d,j}^{AUV_k}$	Battery power when AUV leaves node i	E_{cap}^{MCV}	Battery capacity of MCVs
$E_{a,j}^{AUV_k}$	Battery power when AUV arrives at node i	λ	Regression coefficient
t_{full}^{ET}	Full charging time for ETs	ϕ	Battery efficiency
t_{full}^{MCV}	Full charging time for MCVs	g	Universal gravitation
e_{min}^{MCV}	Minimum remaining battery capacity of MCV	c_r	Rolling friction coefficient
e_{min}^{ET}	Minimum remaining battery capacity of ETs	c_d	Air drag coefficient
M_{ET}	Unloaded mass of ETs	ρ	Air density
$u_j^{ET_k}$	Load weight when ET arrives at j	f_s	Frontage
M_{AUV}	Unloaded mass of AUVs	α_{ij}	Slope
$N_{AUV}^{ET_k}$	Number of AUVs carried by an ET k	r_c	Charging efficiency
$u_j^{AUV_k}$	Load weight when AUV arrives at j	r_u	Utilization efficiency

2.3 Model formulation

The total operating cost of the logistics enterprise per day includes the vehicle purchase cost $C_{purchase}$, staffing cost C_{salary}, charging cost $C_{charging}$, energy consumption cost C_{cons}, and penalty cost $C_{penalty}$, as shown in Eq. 1. The vehicle purchase cost includes the purchase cost of pure electric trucks, driverless vehicles, and mobile charging vehicles, as shown in Eq. 2. Considering the government's subsidy and incentive policies for driverless vehicles, the purchase cost of driverless vehicles equals the procurement cost of driverless vehicles minus the government subsidies. The personnel cost is determined by the average salary of one logistics personnel and the required number of vehicles, as shown in Eq. 3. The calculation of charging cost is shown in Eq. 4, where the third term considers the waiting cost of mobile charging vehicles arriving at the mobile charging node ahead of schedule. In addition, the first term of Eq. 4 comprehensively considers the energy consumption of ET driving and the power consumption of ET for wireless charging of AUVs when calculating the total charging power provided by MCV, ensuring the balance and logical closure of the energy flow. Therefore, this mechanism is consistent with the mobile energy replenishment concept of MCV, but extends the charging level to end unmanned devices. Eq. 5 gives the energy consumption cost, where the energy consumption of pure electric trucks, driverless vehicles, and mobile charging vehicles during operation is shown in Eqs. 6 to 8, respectively. The penalty cost refers to the cost incurred when the driverless vehicle fails to meet the customer's time window during delivery, as shown in Eq. 9. For customers who require split delivery, the time window constraint is evaluated based on the start time of the first service for the customer.

$$min\, Z = min\left(C_{purchase} + C_{salary} + C_{charging} + C_{cons} + C_{penalty}\right) \tag{1}$$

$$\begin{aligned} C_{purchase} = & \sum_{k \in K} \sum_{j \in V_c} \left(pc_{ET_k} \times x_{V_0 j}^{ET_k} + (pc_{AUV} - sub_{AUV}) N_{AUV}^{ET_k} \right) \\ & + \sum_{m \in M} \sum_{j \in V_{mc}} \left(pc_{MCV_m} \times x_{V_0 j}^{MCV_m} \right) \end{aligned} \tag{2}$$

$$C_{salary} = c_{salary} \left(\sum_{k \in K} \sum_{j \in V_c} x_{V_0 j}^{ET_k} + \sum_{m \in M} \sum_{j \in V_{mc}} x_{V_0 j}^{MCV_m} \right) \tag{3}$$

$$\begin{aligned} C_{charging} = &\sum_{j\in V_{mc}}\sum_{m\in M}\sum_{k\in K} z_j y_{j,mk} c_{mc}\left(E_{d,j}^{ET_k} - E_{a,j}^{ET_k}\right) \\ &+ \sum_{m\in M}\left(c_{pv} - sub_{pv}\right)\left(E_{d,V_0}^{MCV_m} - E_{a,V_0}^{MCV_m}\right) \\ &+ \sum_{m\in M}\sum_{j\in V_{mc}} z_j\left(c_w^{MCV} \times wt_j^{MCV_m}\right) \end{aligned} \tag{4}$$

$$\begin{aligned} C_{cons} = c_{cons}\lambda\phi\Bigg(&\sum_{k\in K}\left(\sum_{(i,j)\in A_1} t_{ij}x_{ij}^{ET_k}P_{ij}^{ET_k} + \sum_{(i,j)\in A_2} t_{ij}x_{ij}^{AUV_k}P_{ij}^{AUV_k}\right) \\ &+ \sum_{m\in M}\sum_{(i,j)\in A_3} t_{ij}x_{ij}^{MCV_m}P_{ij}^{MCV}\Bigg) \end{aligned} \tag{5}$$

$$P_{ij}^{ET_k} = v_{ET}\left(g\left(\sin(\alpha_{ij}) + c_r\cos(\alpha_{ij})\right)\left(M_{ET} + u_j^{ET_k} + N_{ADV}^{ET_k}M_{ADV}\right) + \frac{c_d\rho f_s {v_{ET}}^2}{2}\right) \tag{6}$$

$$P_{ij}^{AUV_k} = v_{AUV}\left(g\left(\sin(\alpha_{ij}) + c_r\cos(\alpha_{ij})\right)\left(M_{AUV} + u_j^{ADV_k}\right) + \frac{c_d\rho f_s {v_{AUV}}^2}{2}\right) \tag{7}$$

$$P_{ij}^{MCV} = v_{MCV}\left(gM_{MCV}\left(\sin(\alpha_{ij}) + c_r\cos(\alpha_{ij})\right) + \frac{c_d\rho f_s {v_{MCV}}^2}{2}\right) \tag{8}$$

$$C_{penalty} = \sum_{k\in K}\sum_{i\in V_c}\left(c_w^{AUV} \times wt_i^{AUV_k} + c_d^{AUV} \times pt_i^{AUV_k}\right) \tag{9}$$

s.t.

$$\sum_{(i,j)\in A_1} x_{ij}^{ET_k} = \sum_{(i,j)\in A_1} x_{ji}^{ET_k} \qquad \forall j \in V_c, k \in K \tag{10}$$

$$\sum_{(i,j)\in A_3} x_{ij}^{MCV_m} = \sum_{(i,j)\in A_3} x_{ji}^{MCV_m} \qquad \forall j \in V_{mc}, m \in M \tag{11}$$

$$\sum_{(i,j)\in A_2} x_{ij}^{AUV_k} = \sum_{(i,j)\in A_2} x_{ji}^{AUV_k} \qquad \forall j \in V_c, k \in K \tag{12}$$

$$x_{V_0 j}^{ET_k} = x_{iV_0^{'}}^{ET_k} \le 1 \qquad \forall i,j \in V_c, k \in K \tag{13}$$

$$x_{ji}^{AUV_k} = x_{oj}^{AUV_k} \qquad \forall i,o \in V_c, j \in V_r, k \in K \tag{14}$$

$$\sum_{i\in V_c} x_{ji}^{AUV_k} \ge 1 \qquad \forall j \in V_r, k \in K \tag{15}$$

$$\sum_{k\in K}\sum_{j\in V_r} x_{ji}^{AUV_k} \ge 1 \qquad \forall i \in V_c \tag{16}$$

$$N_{ADV}^{ET_k} + u_j^{ET_k} < C_{ET} \qquad \forall j \in V_r, k \in K \tag{17}$$

$$u_j^{AUV_k} < C_{AUV} \qquad \forall j \in V_c, k \in K \tag{18}$$

$$N_{AUV}^{ET_k} \le N_{AUV}^{max} \qquad {\scriptstyle \forall k\in K} \tag{19}$$

$$N_{AUV}^{ET_k} \le \max_{V_r} \left\{ \sum_{j \in V_c} x_{V_r j}^{AUV_k} \right\} \qquad \forall k \in K \tag{20}$$

$$at_i^{ET_k} + \max \left\{ st_i, \frac{z_i \left(E_{d,i}^{ET_k} - E_{a,i}^{ET_k} \right)}{r_c} \right\} + t_{ij} - at_j^{ET_k} \le \Psi \left(1 - x_{ij}^{ET_k} \right) \qquad \forall (i,j) \in A_1, i \in V_c, k \in K \tag{21}$$

$$at_i^{AUV_k} + wt_i^{AUV_k} + st_i + t_{ij} - pt_i^{AUV_k} - at_j^{AUV_k} \le \Psi \left(1 - x_{ij}^{AUV_k} \right) \qquad \forall (i,j) \in A_2, i \in V_c, k \in K \tag{22}$$

$$wt_i^{AUV_k} = \max \left\{ 0, e_i - at_i^{AUV_k} \right\} \qquad \forall i \in V_c, k \in K \tag{23}$$

$$pt_i^{AUV_k} = \max \left\{ 0, at_i^{AUV_k} - l_i \right\} \qquad \forall i \in V_c, k \in K \tag{24}$$

$$at_i^{MCV_m} \le at_i^{ET_k} + \Psi \left(1 - y_{i,mk} \right) \qquad \forall i \in V_{mc}, k \in K, m \in M \tag{25}$$

$$wt_j^{MCV_m} = \max \left\{ 0, at_j^{ET_k} - at_j^{MCV_m} \right\} \qquad \forall j \in V_{mc}, k \in K, m \in M \tag{26}$$

$$at_i^{ET_k} + r_c \left(E_{d,i}^{ET_k} - E_{a,i}^{ET_k} \right) + t_{ij} \le at_j^{MCV_m} + \Psi \left(1 - x_{ij}^{MCV_m} \right) \qquad \forall (i,j) \in A_3, i \in V_{cm}, k \in K, m \in M \tag{27}$$

$$E_{cap}^{ET} = r_u \times t_{full}^{ET} \times r_c + e_{min}^{ET} \tag{28}$$

$$E_{cap}^{MCV} = r_u \times t_{full}^{MCV} \times r_c + e_{min}^{MCV} \tag{29}$$

$$0 < E_{a,j}^{AUV_k} \le E_{d,i}^{AUV_k} - P_{ij}^{AUV_k} t_{ij} x_{ij}^{AUV_k} + E_{cap}^{AUV} \left(1 - x_{ij}^{AUV_k} \right) \qquad \forall (i,j) \in A_2, k \in K \tag{30}$$

$$0 < E_{a,j}^{ET_k} \le E_{d,i}^{ET_k} - P_{ij}^{ET_k} t_{ij} x_{ij}^{ET_k} + E_{cap}^{ET} \left(1 - x_{ij}^{ET_k} \right) \qquad \forall (i,j) \in A_1, k \in K \tag{31}$$

$$0 < E_{a,j}^{MCV_m} \le E_{d,i}^{MCV_m} - P_{ij}^{MCV} t_{ij} x_{ij}^{MCV_m} + E_{cap}^{MCV} \left(1 - x_{ij}^{MCV_m} \right) \qquad \forall (i,j) \in A_3, m \in M \tag{32}$$

$$E_{d,j}^{AUV_k} \le E_{cap}^{AUV} \qquad \forall j \in V_r, k \in K \tag{33}$$

$$y_j \ge x_{ji}^{ET_k} \qquad \forall i \in V_r, k \in K \tag{34}$$

$$y_j = \sum_{(i,j) \in A_1} x_{ji}^{ET_k} \qquad \forall j \in V_r, k \in K \tag{35}$$

$$x_{ji}^{AUV_k} \le y_j \qquad \forall i \in V_c, k \in K \tag{36}$$

$$\sum_{i \in V_c} x_{ji}^{AUV_k} \ge y_j \qquad \forall j \in V_r, k \in K \tag{37}$$

$$z_j \le y_j \qquad \forall j \in V_r \tag{38}$$

$$y_{j,mk} \le z_j \qquad \forall j \in V_{mc}, m \in M, k \in K \tag{39}$$

$$z_j = \sum_{(i,j) \in A_3} x_{ij}^{MCV_m} \qquad \forall j \in V_{mc}, m \in M \tag{40}$$

Eqs. 10 to 12 represent flow balance constraints. Eq. 13 ensures that each ET is dispatched only once and returns to the distribution centre after completing its delivery task. Eq. 14 indicates that the AUV departs from the parking node and returns to the same node after completing its delivery. In addition, for a given AUV and parking node, when there is no split distribution or multiple distribution mode, Eq. 15 takes the value of 1; otherwise, Eq. 15 takes a value greater than 1. Eq. 16 indicates that each customer needs to be visited by an AUV and can be visited once or multiple times, meaning that when there is a split distribution mode, customers will be served by AUVs multiple times. Eq. 17 limits the number of AUVs and goods carried by an ET to its payload. Eq. 18 limits the goods an AUV carries to its payload. Eqs. 19 and 20 state that the number of AUVs carried by an ET must not exceed either the maximum number of AUV journeys dispatched at all parking nodes or the specified maximum number of vehicles. Eqs. 21 and 22 represent time flow constraints for ETs and AUVs. Eqs. 23 and 24 are customer time window constraints. Eq. 25 ensures the MCV arrives at the mobile charging node no later than the ET. Eq. 26 gives the waiting time for the MCV. Eq. 27 provides a time flow constraint for the MCV. Eqs. 28 and 29 specify that all ETs and MCVs are fully charged when departing the distribution centre. Eq. 30 limits the travel distance of AUV and ensures its battery remains within capacity. According to Eq. 31, the energy of an ET arriving at node j cannot exceed its level when departing node i minus the consumption on arc $(i,j) \in A_1$. According to Eq. 32, the power level of an MCV when it reaches node j is not higher than the power level when it leaves node i minus the consumption through arc $(i,j) \in A_3$. The battery capacity will not exceed its limit at any time. If node i is the selected mobile charging node, subtract the electricity the MCV provides to the ET from the amount it has when leaving node i. Constraint 33 ensures that the battery state of the AUV is fully charged when it is first dispatched from its ET. In split distribution or multiple distribution modes, AUVs return to the ET and may depart again before being recharged, resulting in departures with less than maximum battery capacity. Eqs. 34 and 35 state that selecting a parking node requires ET visitation. Eqs. 36 and 37 are spatial coordination constraints for ETs and AUVs; that is, if parking node j is selected, it will serve at least one AUV dispatch activity. Eq. 38 limits charging node selection to chosen parking nodes. Eqs. 39 to 40 require that if an ET charges at a mobile charging node j, there must be a visiting MCV.

3. Solution approach

This study proposes IHFLA to address the TAUVDN-MPSC. The designed algorithm primarily consists of four stages: initial population construction, memeplex division, local deep search, and population shuffling, as illustrated in Fig. 2.

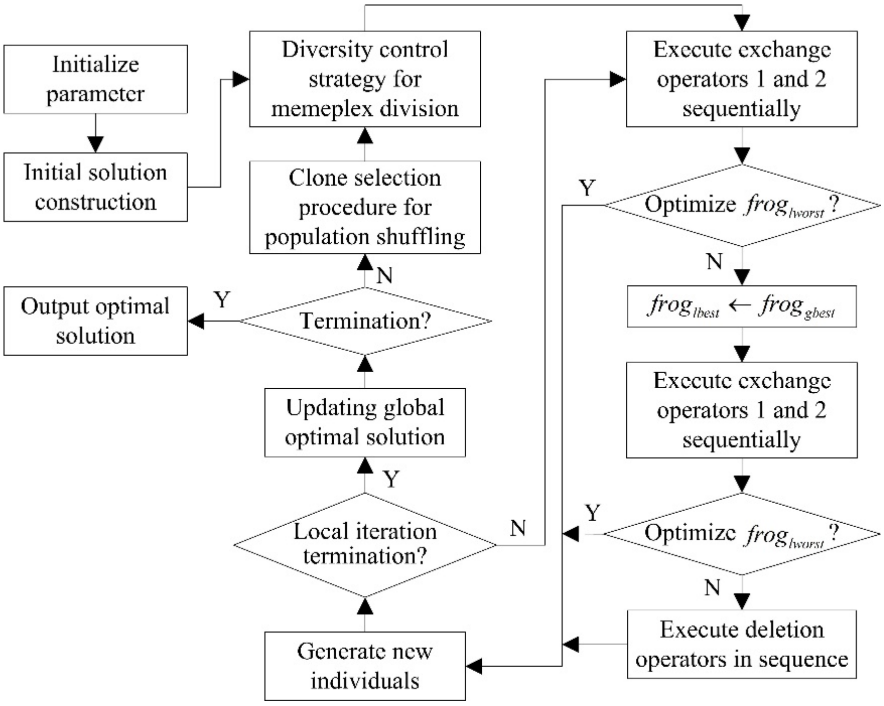

Fig. 2 Algorithm framework

The specific steps are as follows:

Step 1: Initial solution construction

Each individual represents a solution, encoded in three distinct parts (see Fig. 3). The first part specifies the routes of ETs. For example, ET 1 departs from distribution centre 0, visits parking nodes 3, 2, and 4 sequentially, then returns to 0. The second part details the routes of AUVs. For instance, AUV 1 initiates its route from parking node 3, returns to this node after serving customer 5, and subsequently serves customers 4 and 3 after reloading goods, before returning again to parking node 3. The third part outlines the routes of MCVs. For example, MCV 1 departs from distribution centre 0, charges the ET at parking nodes 2 and 4 in sequence, and finally returns to 0. Based on this encoding structure, the initial solution construction method is defined in steps 1-1 to 1-3, after which the generated initial solution is copied to N_{Pop}. Give $n_{Gen} = 1$.

Step 1-1: Initialize set $S_{AUV}^{dp} = \emptyset$, $V_r^{'} \leftarrow V_r$.

Step 1-1-1: Randomly select a customer as initial customer $c_{start} \in V_c$ and delete it.

Step 1-1-2: Randomly select $r_{dp} \in V_r^{'}$.

Step 1-1-3: If $d_{start} > C_{AUV}$, the AUV will go to and from the parking node $\left\lceil \frac{d_{start}}{C_{AUV}} \right\rceil$ times, and put the corresponding split distribution route $l_{AUV,s}^{new}$ in S_{AUV}^{dp}, return to step 1-1-1; If $d_{start} \leq C_{AUV}$, perform steps 1-1-4.

Step 1-1-4: If $V_c \neq \emptyset$, perform step 1-1-5; Otherwise, output S_{AUV}^{dp}.

Step 1-1-5: Select $c_{in} \in V_c$ to insert into the route of c_{start}. The best feasible insertion position is determined by Eq. 41.

If the range of AUV is violated after inserting c_{in}, it will not be inserted, and the current AUV route l_{AUV}^{cur} will be placed into S_{AUV}^{dp}. If $\left|S_{AUV}^{dp}\right| \geq N_{AUV}^{max}$, delete $r_{dp} \in V_r^{'}$ and return to step 1-1-1, otherwise directly return to step 1-1-1.

If the range of AUV is met after inserting c_{in}, but $d_{dp}^{now} \geq C_{ET}$ ($d_{dp}^{now}$is the sum of all customer demands connecting r_{dp}), it will not be inserted, and put l_{AUV}^{cur} into S_{AUV}^{dp}. If $\left|S_{AUV}^{dp}\right| \geq N_{AUV}^{max}$, delete $r_{dp} \in V_r^{'}$ and return to step 1-1-1, otherwise directly return to step 1-1-1.

If the range of AUV is met and $d_{dp}^{now} < C_{ET}$ after inserting c_{in}, but $d_{AUV}^{now} \geq C_{AUV}$ (d_{AUV}^{now} is the distribution demand of AUV after inserting c_{in}), insert r_{dp} before c_{in}, and check whether the range of AUV is met. If violated, c_{in} will not be inserted and put l_{AUV}^{cur} into S_{AUV}^{dp}. If $\left|S_{AUV}^{dp}\right| \geq N_{AUV}^{max}$, delete $r_{dp} \in V_r^{'}$and return to step 1-1-1, otherwise directly return to step 1-1-1. Otherwise, insert r_{dp} and c_{in} in turn, and delete $c_{in} \in V_c$, then put multiple delivery route $l_{AUV,m}^{new}$ in S_{AUV}^{dp}. If $\left|S_{AUV}^{dp}\right| \geq N_{AUV}^{max}$, delete $r_{dp} \in V_r^{'}$ and return to step 1-1-1, otherwise directly return to step 1-1-1. If $d_{AUV}^{now} < C_{AUV}$, insert c_{in}, delete $c_{in} \in V_c$, and return to step 1-1-4.

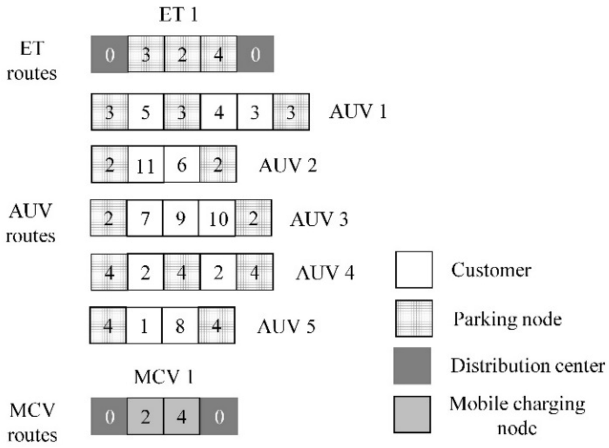

Fig. 3 Solution code representation

$$IC(i, c_{in}, j) = \beta_1\left(t_{ic_{in}} + t_{c_{in}j} - \gamma t_{ij}\right) + \beta_2\left(at_{j,new}^{AUV_k} - at_j^{AUV_k}\right) + \beta_3\left(l_{c_{in}} - at_{c_{in}}^{AUV_k}\right) \tag{41}$$

where β_1, β_2 and β_3 are non-negative weight values and, $at_{j,new}^{AUV_k}$ is the new arrival time.

Step 1-2: Initialize set $S_{r,k} = \emptyset$, $V_{mc} = \emptyset$, and $T_{tw} = \emptyset$.
Step 1-2-1: Random select a parking node as the start parking node $r_{start} \in V_r$ and delete it.
Step 1-2-2: Initialize set $IV_r = \emptyset$. Store the remaining nodes of V_r into IV_r from small to large according to the distance to r_{start}.
Step 1-2-3: Traverse IV_r. If there is no parking node that meets the capacity limit of ETs after inserting, put the current ET route l_k^{cur} in $S_{r,k}$ and return to step 1-2-1. Otherwise, the selected parking node r_{dp} will be inserted between r_{start} and V_0, and delete it from V_r. Then, obtain a new ET route l_k^{new}.
Step 1-2-4: If the range of ET is violated, put r_{dp} into V_{mc}, and calculate the time of arrival and departure node r_{dp} as the time window, and put into T_{tw}
Step 1-2-5: If $V_r \neq \emptyset$, $r_{start} \leftarrow r_{dp}$, return to step 1-2-2; Otherwise, put l_k^{new}into $S_{r,k}$, and output, $S_{r,k}$, T_{tw} and V_{mc}.
Step 1-3: Initialize set $S_{mc} = \emptyset$.
Step 1-3-1: Randomly select a charging node as the starting charging point $s_{start} \in V_{mc}$ and delete it.
Step 1-3-2: Initialize set $IS_{mc} = \emptyset$. Store the remaining nodes of V_{mc} into IS_{mc} from small to large according to the distance to r_{start}.
Step 1-3-3: Traverse IS_{mc}. If there is no charging node that meets the available battery capacity of MCV after inserting, put the current MCV route l_k^{cur} into S_{mc}, and return to step 1-3-1;
Step 1-3-4: If it exist but does not meet Eq. 25, put l_k^{cur} into S_{mc} and return to step 1-3-1; Otherwise, insert the selected charging node s_{select} between s_{start} and V_0 to obtain a new MCV route l_k^{new}.
Step 1-3-5: If $V_{mc} \neq \emptyset$, return to step 1-3-2; Otherwise, put l_k^{new} into S_{mc}, and output S_{mc}.

Step 2: Memeplex division

The diversity control strategy [19] is used to divide the population N_{Pop} into N_M groups with the same size. First, the individuals are sorted according to the target value from small to large and stored in S_{Pop}. Then, the first N_M individuals in each group are taken as the first individual and deleted from S_{Pop}. After that, calculate the diversity values between the newly assigned individuals and the non-assigned individuals in S_{Pop}, and select the individuals with large diversity values to insert into the corresponding population. On this basis, memeplex groups are divided.

Step 3: Local deep search

Step 3-1: Determine global optimal individual $frog_{gbest}$ of the current population, and let $n_M = 1$
Step 3-2: Select a memeplex M_j.
Step 3-3: Let $l = 1$.
Step 3-4: Determine local optimal individual$frog_{lbest}$ and local worst individual$frog_{lworst}$ in M_j. Execute the exchange operators 1 and 2 in turn.

Exchange operator 1: Randomly select ET routes (l_k^{lbest} and l_k^{lworst}) from $frog_{lbest}$ and $frog_{lworst}$, respectively, and exchange them. Delete the duplicate customers in current $frog_{lworst}$, merge the distribution routes of the same parking node r_{same}, and judge whether the payload of ET is met. If not, delete the customers of r_{same} in the original $frog_{lworst}$ until the payload is met. Identify the unserved customers in $frog_{lworst}$ and insert back based on Eq. 41. If no feasible insertion location is found, a new distribution route is created and assigned to the nearest feasible parking node. Update the route number to generate a new individual $frog_{new}$.

Exchange operator 2: Randomly select parking nodes (r^{lbest} and r^{lworst}) from $frog_{lbest}$ and $frog_{lworst}$, respectively, and exchange them. Delete the duplicate customers in current $frog_{lworst}$, and check whether the payload of ET is met. If not, delete the customers served by other parking nodes until the payload is met. After that, the operation is the same as that in exchange operator 1.

Step 3-5: If $frog_{new}$ is not better than $frog_{lworst}$, $frog_{lbest} \leftarrow frog_{gbest}$, execute the exchange operators 1 and 2 in turn.

Step 3-6: If $frog_{new}$ is still not better than $frog_{lworst}$, execute the deletion operators for $frog_{lworst}$ in turn to generate $frog_{new}$.

Parking node deletion operator: Select the parking node with the least number of service customers and close it. Insert the deleted customer back based on Eq. 41. If no feasible insertion location is found, a new AUV route will be created and assigned to the nearest parking node.

Customer node deletion operator: Randomly select a customer and delete it. Insert this customer into other AUV routes based on Eq. 41. After that, the operation is the same as that in parking node deletion operator.

Step 3-7: Record $E_{a,r_{dp}}^{ET_k}$ and $E_{d,r_{dp}}^{ET_k}$ of ETs at each r_{dp}. If $E_{a,r_{dp}}^{ET_k} \leq 0$, the previous parking node of r_{dp} is selected as the mobile charging node, and then execute step 1-3 to optimize the MCV routes.

Step 3-8: If $l = L$, go to step 3-9. Otherwise let $l = l + 1$, return to step 3-4.

Step 3-9: If $n_M = N_M$, go to step 4. Otherwise let $n_M = n_M + 1$, return to step 3-2.

Step 4: Termination

If $n_{Gen} = n_{Gen}^{max}$, output the optimal solution. If $n_{Gen} < n_{Gen}^{max}$, go to step 5.

Step 5: Population shuffling

The clone selection procedure is used for population shuffling. First, the number of each cloned individual is calculated to generate a cloned population. Next, for each selected individual, first execute the parking node deletion operator, followed by the customer node deletion operator, based on the mutation probability. This sequence creates a new solution. Finally, use the roulette mechanism to select N_{Pop} individuals from the cloned population to form a new population, then return to step 2.

4. Results and discussion

4.1 Parameter condition setting

This study simulates a square urban area of $[0,30]^2$ km and divides it from inside to outside into Region 1 (city centre), Region 2 (surrounding area), Region 3 (suburban area), and Region 4 (external area). It is assumed that distribution centres are randomly distributed in Region 4, customers are evenly distributed in Regions 1, 2, and 3, and delivery points are evenly distributed in Region 2. Candidate delivery points are set as 1/5 of the number of customers. The number of customers is set to $|V_C| = \{20,30,40,50,60\}$, thus constructing 5 cases, namely Case 20-4, Case 30-6, Case 40-8, Case 50-10, and Case 60-12.

Due to the consideration of split distribution, 20 % of customer demands are evenly distributed within [5,30] kg, while the remaining customer demands are evenly distributed within [5,20] kg. The soft time window of customers is generated based on Solomon [20]. According to the average salary of on-duty employees in Beijing, the average salary of a logistics worker is 345 Yuan RMB/person·day. The range of the ET is set to 220 km, the battery capacity is 43 kWh, the driving speed is 40 km/h, and the self-weight is 1900 kg. The effective load is set to half of its payload, which is 600 kg. Its service life is assumed to be 10 years, so the purchase cost equivalent to one day is 35.56 Yuan RMB/vehicle·day. The minimum remaining battery capacity is equal to 20 % of the battery capacity. Taking Starship as an example, an ET can carry up to 6 AUVs. The maximum range of each AUV is 20 km, the driving speed is 10 km/h, the payload is 20 kg, the self-weight is 80 kg, and the charging rate is 5 kW. Its service life is assumed to be 5 years, so the purchase cost and subsidy converted into one day are 21.92 Yuan RMB/vehicle·day and 6.58 Yuan RMB/vehicle·day, respectively. The average service duration of ETs at parking nodes is set to 10 minutes. Additionally, the MCV is equipped with a battery capacity of 200 kWh, weighing 4500 kg and capable of a driving speed of 40 km/h. Its service life is assumed to be 10 years, so the purchase cost equivalent to one day is 164.38 Yuan RMB/vehicle·day. Currently, the cost of directly using PV generation to charge in China ranges from 0.40 to 0.70 Yuan RMB/kWh, while a subsidy of 0.03 to

0.05 Yuan RMB/kWh is provided. This study uses the median value, where the PV charging price is 0.55 Yuan RMB/kWh and the PV charging subsidy is 0.04 Yuan RMB/kWh. The mobile charging price is 0.77 Yuan RMB/kWh. For parameters related to energy consumption, refer to Demir *et al.* [21] and Goeke and Schneider [22]. For parameters related to algorithms, refer to Song *et al.* [23]. All experimental procedures are executed using MATLAB R2021a encoding.

4.2 Algorithm performance analysis

To evaluate the performance of IHFLA, this study compares IHFLA with the Genetic Algorithm (GA). In GA, individual selection is based on roulette wheel selection; crossover operation involves exchanging all AUV routes served by the same ET, and mutation operation targets individual customers for mutation. For each test case, both algorithms are run 10 times, and the optimal objective value Z_{best}^{IHFLA} (Z_{best}^{GA}), average objective value $\bar{Z}^{IHFLA}$ ($\bar{Z}^{GA}$), and average running time $\bar{t}^{IHFLA}$ ($\bar{t}^{GA}$) are recorded. Indicators Gap_1, Gap_2, and Gap_3 represent the differences in optimal objective value, average objective value, and average running time between the two algorithms, as shown in formulas (42) to (44). As shown in Table 3, the optimal objective values obtained by IHFLA in the five test cases are all lower than those obtained by GA, with an average of -5.60 % across all cases. In terms of average objective value, the average across all cases is -9.80 %, indicating that IHFLA significantly outperforms GA. The average running time of IHFLA is lower than that of GA in three cases; while in the remaining two cases, the value is below 5.00 %. However, the average across all cases is -5.87 %. Therefore, in most cases, the running speed of IHFLA is comparable to or even superior to that of GA. Overall, IHFLA exhibits better stability than GA.

$$Gap_1 = \frac{\left(Z_{best}^{IHFLA} - Z_{best}^{GA}\right)}{Z_{best}^{GA}} \times 100\ \% \tag{42}$$

$$Gap_2 = \frac{\left(\bar{Z}^{IHFLA} - \bar{Z}^{GA}\right)}{\bar{Z}^{GA}} \times 100\ \% \tag{43}$$

$$Gap_3 = \frac{\left(\bar{t}^{IHFLA} - \bar{t}^{GA}\right)}{\bar{t}^{GA}} \times 100\ \% \tag{44}$$

Table 3 Indicator analysis

Cases	Gap_1 (%)	Gap_2 (%)	Gap_3 (%)
Case 20-4	-0.85	-2.51	-16.71
Case 30-6	-7.67	-13.10	-12.42
Case 40-8	-8.77	-14.17	-9.10
Case 50-10	-4.96	-9.26	4.59
Case 60-12	-5.76	-9.97	4.31
Average	-5.60	-9.80	-5.87

Large-scale instances with 60 client nodes more accurately reflect real-world scenarios, as the solution space expands exponentially and leads to more frequent and complex constraint conflicts. This study examines the search behaviour and performance of the IHFLA in addressing such large-scale instances. Fig. 4 presents the total operating cost of the logistics enterprise per day as a function of the number of iterations. The horizontal axis represents the number of iterations, while the vertical axis indicates the total operating cost of the logistics enterprise per day. The convergence curve for IHFLA demonstrates a rapid reduction in the initial objective function value, with most optimization completed within approximately 150 iterations. Subsequently, the algorithm enters a fine search phase and stabilizes near the optimal value after about 200 iterations, resulting in a smooth curve and the lowest convergence platform. These results indicate that IHFLA achieves high-quality solutions with fewer iterations, effectively balancing exploration and exploitation in large-scale, complex optimization, thereby improving both search efficiency and solution quality.

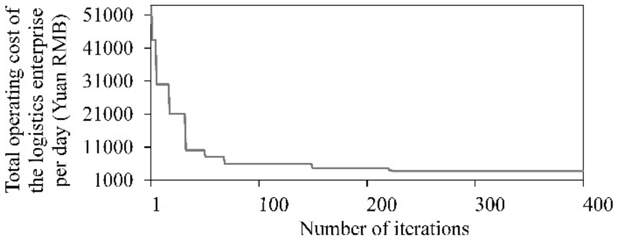

Fig. 4 Algorithm iteration convergence curve

4.3 Comparison of different distribution methods

This study presents a large-scale case involving 60 customers, comparing the traditional distribution method using only ETs with a transformed approach that incorporates both ETs and AUVs, as shown in Table 4. The ET-AUV distribution method reduces total operating costs by 18.61 % and lowers penalty costs by 23.21 %, indicating improved customer satisfaction and the ability to handle more complex distribution tasks. This innovation has led to changes in both fixed and variable costs. The traditional method requires six ETs, while the ET-AUV distribution method uses only two ETs, and AUVs do not require drivers, resulting in a 62.50 % reduction in staffing costs. In the traditional approach, ETs must visit all customers sequentially. In contrast, the ET-AUV distribution method allows multiple AUVs to be deployed from a parking node to serve nearby customers simultaneously, significantly reducing total distribution time. AUVs can use sidewalks or designated routes, are less affected by traffic congestion, and better meet customer time windows.

The number of ETs has been reduced from six to two. Despite this, the acquisition cost of six new AUVs is higher than the cost savings from reducing four ETs. This one-time investment is offset by significant savings in staffing and penalty costs during daily operations. The number of MCVs has been reduced from two to one. However, service targets have changed from six ETs to two ETs and six AUVs. This change increases total charging volume and charging costs. The distribution routes are longer, leading to increased total energy consumption. This results in a slight increase in energy consumption costs. Although vehicle purchase and charging costs rise with the ET-AUV distribution method, it still offers lower total operating costs, better human resource efficiency, and greater operational resilience than using only ETs.

Table 4 Comparison of optimization results under different distribution methods

Indicators	Only ET distribution method	ET-AUV distribution method
Total operating cost of the logistics enterprise per day (Yuan RMB)	4709.13	3832.58
Length of distribution routes (km)	127.60	137.67
Number of ETs (Vehicles)	6	2
Number of AUVs (Vehicles)	0	6
Number of MCVs (Vehicles)	2	1
Vehicle purchase cost (Yuan RMB)	542.12	1094.50
Staffing cost (Yuan RMB)	2760.00	1035.00
Charging cost (Yuan RMB)	355.46	639.99
Energy consumption cost (Yuan RMB)	787.02	859.96
Penalty cost (Yuan RMB)	264.52	203.13

4.4 Sensitivity analysis

This study is based on a large-scale calculation example involving 60 customers. It conducts sensitivity analysis of the payload and range, and runs IHFLA 10 times, recording the optimal solution. The results can provide appropriate operational decision-making references for practical operations.

Sensitivity analysis of payloads for ETs and AUVs

With other parameters remaining unchanged, this study analyses the impact of different payloads for ETs and AUVs on the total operating costs of the logistics enterprise per day. Sensitivity analysis is conducted by increasing or decreasing the baseline by 25 % each time, as shown in Fig. 5.

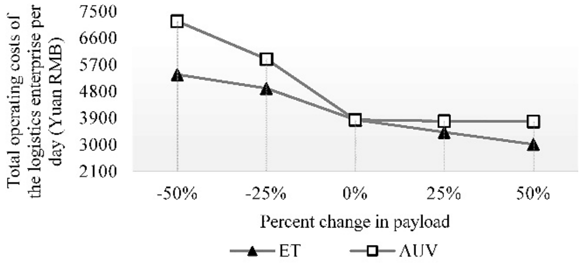

Fig. 5 Sensitivity analysis of payloads for ETs and AUVs

As the payload of ETs increases, the total operating costs show a downward trend. When the payload is too small (-50 %), the transport capacity of ETs is severely insufficient, requiring the deployment of more ETs to complete the same tasks, leading to increased staffing, energy consumption, charging, and vehicle purchase costs. When the payload increases by 25 % or more, the amount of cargo transported per trip increases, reducing the number of ETs required and spreading staffing and vehicle purchase costs. As the payload of AUV increases, the total operating costs show a trend of significant decrease followed by a slight increase. When the load is too small (-50 %), AUVs cannot effectively perform delivery tasks. It is necessary to deploy a large number of AUVs or make multiple round trips, leading to extremely complex scheduling, a surge in charging demand, and a large number of violations of time windows, ultimately resulting in a more than doubling of the total operating costs. When the payload increases by 25 % or more, the total operating costs remain almost unchanged, indicating that additional payload is redundant in most scenarios. In summary, as the most effective lever for reducing the total operating costs, ETs with greater payload should be preferred or deployed, subject to regulatory and road conditions. In contrast, when configuring the payload of AUVs, decision-makers should analyse the weight distribution of daily delivery orders and select a payload value that can cover the vast majority of order scenarios.

Sensitivity analysis of ranges for ETs and AUVs

Fig. 6 shows the impact of ETs and AUVs on the total operating costs of the logistics enterprise per day under different ranges. Similarly, sensitivity analysis is performed by increasing or decreasing the reference value by 25 % each time.

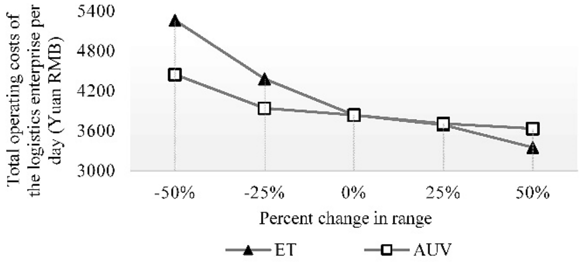

Fig. 6 Sensitivity analysis of ranges for ETs and AUVs

With the increase in the range of ETs, the total operating costs show a downward trend, and the penalty for the reduced range is far greater than the revenue from the increased range. When the range is too small (-50 %), ETs need to frequently and urgently call MCVs to charge in order to ensure daily distribution and operation, resulting in increased charging costs and charging waiting time. At the same time, due to the disruption of the distribution rhythm, the penalty cost for violating the time window surged. When the range increases slightly (+25 %), the endurance redundancy allows more flexible route planning, reduces the number of charges in the middle of a trip, and the total operating cost decreases slightly. With the further increase of the range of ETs, economies of scale have emerged, that is, a sufficient range may enable some vehicles to realize one-day charging, significantly reducing the dependence on mobile charging, and the costs of charging, vehicle purchase, staffing, and penalty have decreased significantly. With the increase in the range of AUVs, the change in the total operating cost presents an L-shaped curve. That is, when the range increases by 25 % or more, the utility of additional range decreases, because a single delivery usually does not require such a long mileage, and the cost savings are minimal. However, when the range is significantly reduced (-50 %), the AUVs cannot effectively cover the customers around the parking node, and more AUVs need to be configured to meet the distribution demand, which greatly increases the charging time and scheduling complexity, resulting in an increase in energy consumption, charging, vehicle purchase, and penalty costs. To sum up, the range of ETs is the cornerstone to ensure the stability of the system. The cost savings from investing in a longer ET range are significant. The key to the range design of the AUV is to match the business scenario, which only needs to cover the distribution distance of most customers and leave a certain safety margin. Therefore, in the case of limited resources, priority should be given to ensuring the range of ETs.

Sensitivity analysis of average speed for ETs and AUVs

Holding all other parameter settings constant, this study examined the effects of varying average speeds of ETs and AUVs on the total operating costs of the logistics enterprise per day. Sensitivity analysis is performed by adjusting the benchmark speed by increments of 25 % above and below the baseline, as illustrated in Fig. 7.

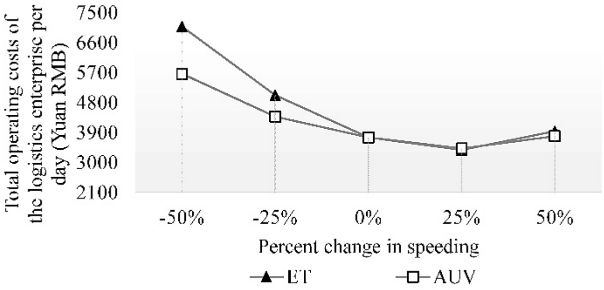

Fig. 7 Sensitivity analysis of average speed for ETs and AUVs

With the increase in the average speed of ETs, the total operating costs of the logistics enterprise per day show a U-shaped trend: it first decreases, then increases. When the speed is reduced by 50 %, the driving time doubles. This leads to two serious consequences. First, ETs arrive late at delivery nodes, causing batch delays in all AUV delivery tasks and sharply increasing time penalty costs. Second, prolonged driving time raises energy consumption per kilometre because of low motor efficiency, nearly doubling daily operating costs for logistics companies. When the average speed increases by 25 %, it approaches the economic speed. At this point, unit energy consumption drops to the optimal level, and punctuality is greatly improved. The penalty costs decrease significantly, making the total operating costs of the logistics enterprise per day reach their lowest point. If the average speed increases by 50 %, air resistance grows with the square of speed, causing a sharp rise in energy consumption costs. The potential to further reduce time penalty costs becomes very limited, leading to a rebound in total operating costs of the logistics enterprise per day. These patterns show that ETs have an optimal economic speed range. Decision-makers should keep the speed near this range to balance energy efficiency and punctuality. However, actual urban traffic conditions make truck speeds a random variable controlled by the environment, not something companies can fully manage. When traffic impacts are considered, the effect of speed changes on costs is even more pronounced.

With the rise in average speed of AUVs, the total operating costs of the logistics enterprise per day show a U-shaped trend. Costs first decrease, then increase, but the amount of fluctuation stays relatively small. When the average speed drops by 50 %, the delivery time becomes too long. This delay causes many customer services to fall outside the time window, sharply raising late penalty costs. Although energy use per mile is low at slower speeds, longer driving times increase auxiliary system energy consumption. This boosts charging costs and leads to a significant overall increase in total operating costs compared to the baseline. At 25 % higher average speed, vehicles match customer time window requirements better, minimizing penalty costs. Although unit energy use rises, total operating costs decrease, reaching their best level. If speed increases by 50 %, air resistance sharply raises per-mile energy use. Early arrivals then cause new penalties, increasing total operating costs. This shows that the average speed needs flexible adjustment based on customer time window requirements. If the time window is loose, speed can drop to save energy consumption. If it is strict, speed should be moderately raised to ensure service. However, avoid excessive speed, which causes a rebound in energy use.

5. Conclusion

This study develops a comprehensive optimization model for an unmanned distribution system using ETs, AUVs, and MCVs to minimize the total operating costs of the logistics enterprise per day. The IHFLA algorithm developed to solve this model demonstrates significant advantages in both computational time and cost performance. Compared to the ET-only distribution, the ET-AUV distribution method offers lower total operating costs, improved human resource efficiency, and greater operational resilience. Sensitivity analysis indicates that the efficiency of the ET-AUV system depends largely on the core performance parameters. To reduce total operating costs, it is most effective to prioritize ETs with larger payloads, within the limits of laws, regulations, and road conditions. When resources are limited, enhancing the range of ETs should be the main focus. For AUVs, decision-makers should select payload and range values that meet most application needs, rather than maximizing these parameters unnecessarily. The average speeds of both ETs and AUVs have a U-shaped effect on total cost; therefore, ET speed should be kept within an economic range to balance energy consumption and punctuality, while AUV speed should be adjusted flexibly according to customer time windows to avoid higher costs caused by excessively low or high speeds.

In future research, we will consider soft time windows and resource-sharing mechanisms, allowing a parking node to be shared by multiple ETs over time or enabling multi-vehicle coordination through dynamic scheduling mechanisms, so that the model more closely reflects the complexity and variability of real-world distribution environments. The PV energy storage modelling will be expanded into a time-varying energy management system, considering factors such as sunshine intensity, energy storage status, and dynamic electricity prices, to achieve collaborative optimization of energy flow and logistics, making the model more closely aligned with actual operating scenarios. Moreover, future research will incorporate time-varying traffic and random fluctuations to simulate travel time uncertainty, as well as dynamic customer order arrivals and cancellations to create a dynamic demand scenario. Additionally, we will utilize Monte Carlo simulations and similar methods to evaluate the performance of the proposed model in stochastic environments, quantifying cost fluctuations and service failure rates under various disturbances. Further work will also explore dynamic rescheduling strategies and backup resource configurations, such as reserve AUVs, to strengthen the resilience of the system.

References

[1] Ghiani, G., Guerriero, E., Manni, E., Pareo, D. (2025). Combining autonomous delivery robots and traditional vehicles with public transportation infrastructure in last-mile distribution, *Computers & Industrial Engineering*, Vol. 203, Article No. 111001, doi: 10.1016/j.cie.2025.111001.

[2] Srinivas, S., Ramachandiran, S., Rajendran, S. (2022). Autonomous robot-driven deliveries: A review of recent developments and future directions, *Transportation Research Part E: Logistics and Transportation Review*, Vol. 165, Article No. 102834, doi: 10.1016/j.tre.2022.102834.

[3] Ulmer, M.W., Streng, S. (2019). Same-day delivery with pickup stations and autonomous vehicles, *Computers & Operations Research*, Vol. 108, 1-19, doi: 10.1016/j.cor.2019.03.017.

[4] Yu, S., Puchinger, J., Sun, S. (2020). Two-echelon urban deliveries using autonomous vehicles, *Transportation Research Part E: Logistics and Transportation Review*, Vol. 141, Article No. 102018, doi: 10.1016/j.tre.2020.102018.

[5] Campuzano, G., Lalla-Ruiz, E., Mes, M. (2025). The two-tier multi-depot vehicle routing problem with robot stations and time windows, *Engineering Applications of Artificial Intelligence*, Vol. 147, Article No. 110258, doi: 10.1016/j.engappai.2025.110258.

[6] Jin, Z., Lu, M., Li, X., Zhang, S., Hsu, S.C. (2025). Multi-objective optimization of two-echelon delivery with autonomous delivery vehicles and electric two-wheelers, *Computers & Industrial Engineering*, Vol. 203, Article No. 110999, doi: 10.1016/j.cie.2025.110999.

[7] Wei, Y., Wang, Y., Hu, X. (2025). The two-echelon truck-unmanned ground vehicle routing problem with time-dependent travel times, *Transportation Research Part E: Logistics and Transportation Review*, Vol. 194, Article No. 103954, doi: 10.1016/j.tre.2024.103954.

[8] Jennings, D., Figliozzi, M. (2019). Study of sidewalk autonomous delivery robots and their potential impacts on freight efficiency and travel, *Transportation Research Record: Journal of the Transportation Research Board,* Vol. 2673, No. 6, 317-326, doi: 10.1177/0361198119849398.

[9] Simoni, M.D., Kutanoglu, E., Claudel, C.G. (2020). Optimization and analysis of a robot-assisted last mile delivery system, *Transportation Research Part E: Logistics and Transportation Review*, Vol. 142, Article No. 102049, doi: 10.1016/j.tre.2020.102049.

[10] Chen, C., Demir, E., Huang, Y. (2021). An adaptive large neighborhood search heuristic for the vehicle routing problem with time windows and delivery robots, *European Journal of Operational Research*, Vol. 294, No. 3, 1164-1180, doi: 10.1016/j.ejor.2021.02.027.

[11] Chen, C., Demir, E., Huang, Y., Qiu, R. (2021). The adoption of self-driving delivery robots in last mile logistics, *Transportation Research Part E: Logistics and Transportation Review*, Vol. 146, Article No. 102214, doi: 10.1016/j.tre.2020.102214.

[12] Yu, S., Puchinger, J., Sun, S. (2022). Van-based robot hybrid pickup and delivery routing problem, *European Journal of Operational Research*, Vol. 298, No. 3, 894-914, doi: 10.1016/j.ejor.2021.06.009.

[13] Mokhtari-Moghadam, A., Salhi, A., Yang, X., Nguyen, T.T., Pourhejazy, P. (2025). A multi-objective approach for the integrated planning of drone and robot assisted truck operations in last-mile delivery, *Expert Systems with Applications*, Vol. 269, Article No. 126434, doi: 10.1016/j.eswa.2025.126434.

[14] Yu, S., Puchinger, J., Sun, S. (2024). Electric van-based robot deliveries with en-route charging, *European Journal of Operational Research*, Vol. 317, No. 3, 806-826, doi: 10.1016/j.ejor.2022.06.056.

[15] Yang, S., Zhang, R., Ma, Y., Zuo, X. (2025). Adaptive large neighborhood search incorporating mixed-integer linear programming for electric vehicle routing problem with mobile charging and nonlinear battery degradation, *Applied Soft Computing*, Vol. 175, Article No. 112988, doi: 10.1016/j.asoc.2025.112988.

[16] Çatay, B., Sadati, I. (2023). An improved matheuristic for solving the electric vehicle routing problem with time windows and synchronized mobile charging/battery swapping, *Computers & Operations Research*, Vol. 159, Article No. 106310, doi: 10.1016/j.cor.2023.106310.

[17] Calise, F., Fabozzi, S., Vanoli, L., Vicidomini, M. (2021). A sustainable mobility strategy based on electric vehicles and photovoltaic panels for shopping centers, *Sustainable Cities and Society*, Vol. 70, Article No. 102891, doi: 10.1016/j.scs.2021.102891.

[18] Wang, Y., Liu, X.Z. (2022). Day-ahead and intra-day two-stage optimal control of photovoltaic-energy storage charging station based on GRU-MPC, *Electric Power Automation Equipment*, Vol. 42, No. 10, 177-183, (in Chinese).

[19] Luo, J., Li, X., Chen, M.-R., Liu, H. (2015). A novel hybrid shuffled frog leaping algorithm for vehicle routing problem with time windows, *Information Sciences*, Vol. 316, 266-292, doi: 10.1016/j.ins.2015.04.001.

[20] Solomon, M.M. (1987). Algorithms for the vehicle routing and scheduling problems with time window constraints, *Operations Research*, Vol. 35, No. 2, 254-265, doi: 10.1287/opre.35.2.254.

[21] Demir, E., Bektaş, T., Laporte, G. (2011). A comparative analysis of several vehicle emission models for road freight transportation, *Transportation Research Part D: Transport and Environment*, Vol. 16, No. 5, 347-357, doi: 10.1016/j.trd.2011.01.011.

[22] Goeke, D., Schneider, M. (2015). Routing a mixed fleet of electric and conventional vehicles, *European Journal of Operational Research*, Vol. 245, No. 1, 81-99, doi: 10.1016/j.ejor.2015.01.049.

[23] Song, M.-X., Li, J.-Q., Han, Y.-Q., Han, Y.-Y., Liu, L.-L., Sun, Q. (2020). Metaheuristics for solving the vehicle routing problem with the time windows and energy consumption in cold chain logistics, *Applied Soft Computing*, Vol. 95, Article No. 106561, doi: 10.1016/j.asoc.2020.106561.

APEM journal
Advances in Production Engineering & Management
Volume 21 | Number 1 | March 2026 | pp 57–74
https://doi.org/10.14743/apem2026.1.561
ISSN 1854-6250
Journal home: apem-journal.org
Original scientific paper

A data-to-decision framework for selecting turning conditions of C3604 brass

Le, V.-P.[a], **Nguyen, V.-H.**[a,*]

[a]Faculty of Mechanical Engineering and Mechatronics, Phenikaa University, Hanoi, Vietnam

ABSTRACT

This study presents a data-to-decision workflow that combines surrogate modeling, multi-objective optimization, and decision-making in a single procedure. Four surrogate models, including Kolmogorov–Arnold Networks (KAN), CatBoost (CAT), Gradient Boosting Regressor (GBR), and LightGBM (LGB), were trained under a unified preprocessing and Bayesian tuning scheme and evaluated on held-out data. The retained models were then embedded in NSGA-III to generate the Pareto front for the trade-off between surface roughness (*Ra*) and material removal rate (*MRR*). To move from the Pareto set to a single operating condition, the candidate solutions were further assessed using multiple MCDA methods under different objective weighting schemes, and the resulting rankings were combined through rank aggregation (Borda, Copeland, Kemeny–Young, Robust Rank Aggregation). A turning case study on C3604 free-cutting brass, using cutting speed, feed, depth of cut, nose radius, and coolant condition as inputs, showed that the final recommendation remained stable across different weighting and ranking settings. Experimental verification at selected Pareto points agreed well with the predicted values, with relative errors of about 5 % for both *Ra* and *MRR*. The results show that the proposed workflow provides a practical and consistent route from limited machining data to a final operating decision.

ARTICLE INFO

Keywords:
C3604 brass;
Data-to-decision;
Surrogate modeling;
Kolmogorov–Arnold network (KAN);
NSGA-III;
MCDA;
Machining optimization;
Multi-objective optimization

**Corresponding author:*
hai.nguyenvan1@phenikaa-uni.edu.vn
(Nguyen, V.-H.)

Article history:
Received 5 April 2026
Revised 16 April 2026
Accepted 19 April 2026

1. Introduction

Optimizing machining parameters remains a core need in modern manufacturing because practitioners must simultaneously satisfy diverse performance targets—surface integrity, tool consumption, throughput, mechanical loads (forces and power), and increasingly energy-related indicators—under real shop-floor constraints involving machine capability, tool geometry, coolant strategy, and safety. The problem is inherently multi-objective and constraint-laden, so it benefits from decision processes that make trade-offs explicit and reproducible, rather than relying on ad hoc tuning. Recent studies in the field underscore both the energy and efficiency imperative and the practicality of multi-objective modeling and optimization in machining applications, reinforcing the need for auditable, data-driven parameter selection [1-3].

Machining datasets are often small, heterogeneous, and strongly affected by setup-dependent variation, which makes reliable parameter selection difficult even before the optimization stage is considered. In machining experiments, continuous cutting variables such as cutting speed, feed, and depth of cut are commonly mixed with categorical factors such as coolant mode, insert geometry, and tool condition, while the measured outputs may also contain interaction effects, process noise, and metrology scatter [4]. Under these conditions, a single-stage analysis is usually not sufficient. A practically useful framework should first establish predictive surrogates that can generalize beyond the limited experimental runs, because overfitted models provide little value for downstream optimization or engineering decision-making [5].

Recent machining studies increasingly move toward an integrated route in which validated surrogate models are used to approximate process responses, evolutionary search is then employed to construct the trade-off surface among conflicting objectives, and a decision layer is finally introduced to identify an implementable operating point from the Pareto set [2, 6]. This shift is important because direct trial-and-error selection is inefficient in multi-factor machining problems, whereas optimization-only studies often stop at reporting Pareto fronts without resolving the final engineering choice in a transparent way [7].

When only a limited number of experiments are available, the predictive stage becomes one of the most critical parts of the workflow. Machining data often combine nonlinear process behavior with a mixture of continuous and categorical inputs, so different surrogate models may respond quite differently to the same dataset. In this setting, tree-based ensembles can be effective for structured tabular data, whereas neural or spline-based models may better capture smoother but coupled response patterns. Even so, no model should be assumed to be the best in advance for every machining response, and model selection needs to be based on actual predictive performance rather than preference or convention [8, 9]. This issue becomes even more important in multi-objective optimization, because the Pareto front is only as reliable as the surrogates used to construct it. If the retained models are unstable or locally biased, the optimization stage may still produce solutions that appear attractive numerically but are less trustworthy from a physical or machining perspective [10]. The same caution applies to the final decision stage. Obtaining a well-spread Pareto set does not automatically resolve which setting should be implemented, since the preferred solution may still change with the weighting scheme and ranking rule adopted. For that reason, transparent multi-criteria procedures and objective weighting methods are needed not only to compare alternatives, but also to make the final recommendation more stable and technically defensible [11, 12].

Recent studies have also demonstrated the practical value of combining modelling, optimization, and confirmation experiments in turning applications. For instance, recent work on dry turning of Inconel 625 [13] and Inconel 825 [14] reported effective optimization of quality-related and productivity-related responses under experimentally validated conditions. However, the transition from the optimized solution set to a final and methodologically robust engineering recommendation is still less explicitly addressed in many such studies.

Most machining studies do not carry the whole process through from prediction to optimization and then to final decision-making. Many papers stop after reporting model accuracy, while others present a Pareto front but leave the final choice to a single ranking method or a fixed set of weights. In such cases, it is difficult to know whether the recommended setting is genuinely robust or simply favored by one particular decision rule [2, 5]. This issue is more critical when the dataset is small, because any instability in the predictive model can carry over into the optimization stage and finally affect the selected solution. Another limitation is that convergence of the optimization algorithm and experimental confirmation of the chosen setting are not always reported together. Without both, the final recommendation may appear reasonable in computation, yet remain insufficiently supported from a machining point of view [15]. For this reason, a more complete data-to-decision workflow is still needed, one that links surrogate modeling, Pareto search, and the final selection step in a transparent and technically traceable way.

This study aims to establish a practical data-to-decision workflow for machining applications with limited experimental data. Rather than focusing on a single modeling or optimization technique, the work integrates surrogate modeling, multi-objective optimization, and MCDA into a consistent and traceable procedure. The objective is to ensure that the final recommended setting is not only accurate in prediction, but also stable under different decision assumptions.

The proposed framework is then examined through a turning case study on C3604 free-cutting brass, where *Ra* and *MRR* are considered as the primary objectives. This combination allows the study to evaluate both the predictive capability of the models and the robustness of the final decision in a realistic machining context.

This study develops an integrated data-to-decision workflow for machining parameter selection under limited data conditions. The proposed approach links surrogate modeling, multi-objective optimization, and multi-criteria decision-making within a single procedure, with particular attention to how the final solution is affected by model behavior and decision assumptions. Instead of relying on one surrogate model or a fixed ranking rule, the framework emphasizes consistency across the predictive, optimization, and selection stages, so that the recommended setting remains stable when different weighting or ranking strategies are considered. The workflow is then examined through a turning case study on C3604 brass, where the trade-off between *Ra* and *MRR* is used to evaluate both predictive performance and decision robustness.

2. Data to decision framework

The proposed framework provides a structured route for converting machining data into an implementable parameter recommendation. As illustrated in Fig. 1, the workflow consists of six linked stages, from data preparation to experimental confirmation of the selected solution. The purpose is not only to obtain accurate predictions, but also to ensure that the final operating point remains technically reasonable and robust at the decision stage.

2.1 Stage 1: Data acquisition and preprocessing

The first stage establishes the dataset used for model development. In machining applications, the data typically include controllable cutting parameters and measured performance responses, with both numerical and categorical variables appearing in the same dataset [1, 14]. In the present study, the dataset is formed from the designed turning experiments, using cutting speed, feed, depth of cut, nose radius, and coolant condition as inputs, and surface roughness and material removal rate as the main outputs. Before modeling, categorical variables are encoded, continuous variables are checked for consistency, and the data are split into training and test subsets. For the productivity response, *MRR* is calculated from turning kinematics, while Ra is obtained from post-process measurement [2].

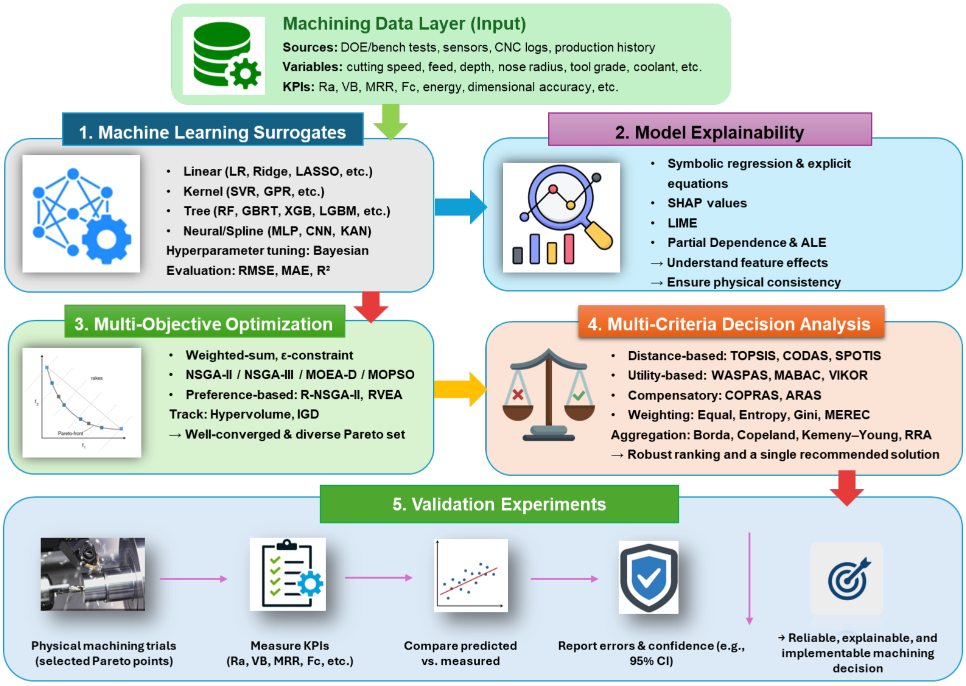

Fig 1 Generalized data-to-decision workflow for machining optimization

2.2 Stage 2: Machine-learning surrogate modeling

The second stage uses surrogate models to describe the relationship between machining inputs and outputs. This step is particularly important when the available dataset is limited, because the optimization stage requires fast and repeatable evaluation over the feasible design space [17]. Different model families may behave differently on the same machining dataset, especially when nonlinear effects and mixed input types are present [18]. Therefore, several candidate models are compared under the same preprocessing and tuning procedure, and their performance is evaluated using RMSE, MAE, and R^2. The best-performing surrogates are then retained for downstream optimization.

2.3 Stage 3: Model explainability

The third stage examines whether the retained models behave in a physically meaningful way. Explainability tools are used to identify the dominant input variables and to clarify how they influence the predicted responses [19]. For interpretable model forms such as KAN, the learned relationships can also be examined in a more explicit form [20]. This stage helps connect predictive performance with machining knowledge and reduces the risk of relying on numerically accurate but physically doubtful trends.

2.4 Stage 4: Multi-objective optimization

Once the surrogate models have been retained, they are used in a multi-objective optimization step to generate non-dominated machining conditions. In this study, the optimization seeks a balance between surface quality and productivity, represented by Ra and MRR. NSGA-III is employed to approximate the Pareto front, while convergence and spread are checked before the candidate solutions are passed to the decision stage [21].

2.5 Stage 5: Multi-criteria decision analysis

Because the Pareto front usually contains several feasible alternatives, a separate decision stage is needed to identify a single implementable setting. MCDA methods are therefore used to rank the Pareto candidates under defined weighting schemes [20-21]. Since the final ranking may vary with the weighting and scoring method, objective weighting and rank aggregation are included to reduce dependence on a single method and improve the robustness of the final recommendation [5].

2.6 Stage 6: Experimental validation

The final stage verifies the selected solutions experimentally. Representative Pareto points are retested under the same machining conditions, and the measured responses are compared with the predicted values using absolute and relative error [24]. This step is necessary to confirm that the selected operating point is not only favorable in computation, but also reliable in actual machining practice.

Overall, the framework links data preparation, surrogate modeling, explainability, optimization, decision analysis, and experimental confirmation in a single workflow. In this way, limited experimental data can be translated into a final machining recommendation that is both technically interpretable and practically verifiable.

3. A turning case study

To verify the practical applicability of the proposed data-to-decision framework, a turning case study was conducted on C3604 free-cutting brass. The study considers the main controllable parameters, including V_c, f, a_p, R_E, and CL, with the aim of balancing Ra and MRR. The following subsections describe the experimental setup and the implementation of the proposed workflow.

3.1 Experimental setup

Turning experiments were performed on a UGINT L2100 CNC lathe (11 kW spindle, automatic feed control). The work material was C3604 free-cutting brass, supplied as round bars of uniform hardness and diameter; cylindrical blanks (30 mm diameter, 100 mm length) were prepared. A

DCGT11304/08 AK carbide insert for non-ferrous alloys was mounted on a standard toolholder with controlled overhang and alignment.

A D-optimal (coordinate-exchange) design targeting a two-factor-interaction (2FI) model was generated with 40 randomized runs and no blocks. Five factors were studied, including V_c, f, a_p, and two categorical R_E and CL conditions. The discrete levels actually tested are listed in Table 1. Randomization was used to minimize temporal drift and nuisance effects.

Cutting parameters followed a designed matrix of V_c, f, a_p, R_E, and CL. Ra was measured after each run using a portable stylus profilometer (0.8 mm cutoff, 5 mm sampling length); the mean of three traces was recorded.

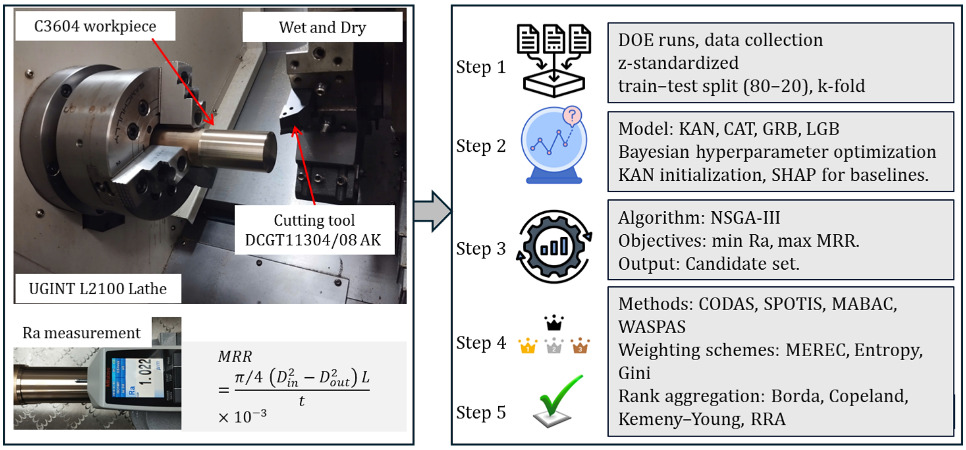

Fig 2 Integrated experimental setup and data-to-decision workflow for turning of C3604 brass

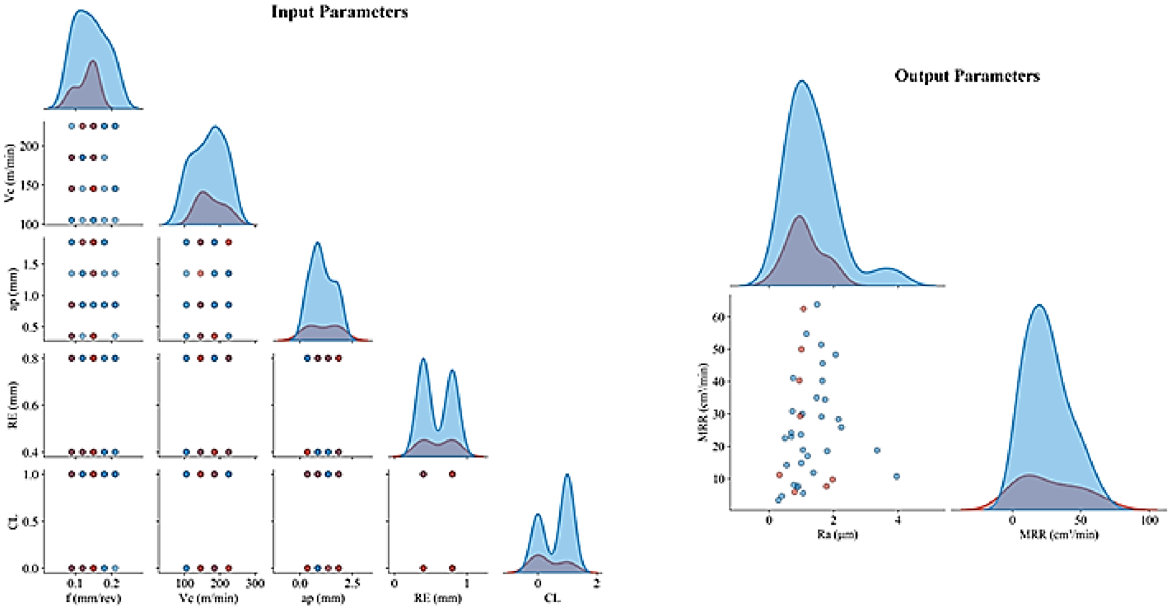

Fig. 3 Pairplot illustrating the distribution and overlap of train and test datasets for both input and output parameters in the C3604 turning experiment

Table 1 Experimental turning conditions

Parameter	Unit	Levels
Cutting speed (V_c)	m/min	105, 145, 185, 225
Feed (f)	mm/rev	0.09, 0.12, 0.15, 0.18, 0.21
Depth of cut (a_p)	mm	0.35, 0.85, 1.35, 1.85
Tool grade	–	Korloy DCGT11304/08
Coolant (CL)	–	"0" = Dry, "1" = Flood (emulsion 6-8 %),
Tool nose radius (R_E)	mm	"0" = 0.4 mm, "1" = 0.8 mm
Machine tool	–	UGINT L2100 CNC lathe

The material removal rate was computed from turning kinematics:

$$MRR = \frac{\pi/4\left(D_{in}^{2} - D_{out}^{2}\right)L}{t} \times 10^{-3} \tag{1}$$

where D_{in} and D_{out} are the initial and final diameters (mm), L is the machined length (mm), and t is the machining time (min). Fig. 2 illustrates the overall setup, showing the brass workpiece, cutting tool configuration, and surface-roughness measurement arrangement. Meanwhile, Fig. 3 summarizes the input factors and output responses considered in the turning process.

3.2 Implementation of the data-to-decision workflow

Surrogate modeling

To model the mapping from machining inputs to performance responses, four surrogate models were considered, including KAN, CAT, GBR, and LGB.

KAN is based on the Kolmogorov–Arnold representation theorem, which states that a multivariate function can be represented as a superposition of univariate functions. Accordingly, a target function $f(x_1, \dots, x_n)$ can be expressed as:

$$f(x_1, \dots, x_n) = \sum_{q=1}^{2n+1} \Phi_q \left(\sum_{p=1}^{n} \phi_{q,p}\,(x_p) \right) \tag{2}$$

where $\phi_{q,p}(\cdot)$ and $\Phi_q(\cdot)$ are univariate functions.

In KAN, these functions are implemented as learnable spline-based mappings, replacing fixed activation functions used in conventional neural networks. This formulation allows the model to approximate complex nonlinear relationships while retaining a degree of interpretability, as the contribution of each input variable can be examined through the learned univariate functions.

In contrast, CAT, GBR, and LGB belong to the family of tree-based ensemble models, which are widely used for tabular datasets. These methods approximate the target function by combining multiple regression trees:

$$\hat{y}(x) = \sum_{k=1}^{K} f_k\,(x), f_k \in \mathcal{T} \tag{3}$$

where each f_k represents a decision tree. In boosting-based methods such as GBR and LGB, trees are added sequentially to minimize a loss function:

$$\hat{y}^{(t)}(x) = \hat{y}^{(t-1)}(x) + \eta f_t(x)$$

where η is the learning rate. LGB improves computational efficiency through histogram-based splitting, while CAT enhances performance on categorical variables using ordered boosting and encoding strategies.

Given the machining dataset

$$\mathcal{D} = \{(x_i, y_i)\}_{i=1}^{N} \tag{4}$$

with $x_i = \left[V_c, f, a_p, R_E, CL\right]$ and y_i represents the response *Ra* or *MRR*, the surrogate model approximates:

$$\hat{y} = \mathcal{F}(x;\theta) + \varepsilon \tag{5}$$

where $\mathcal{F}(x;\theta)$ is the regression model KAN, CAT, GBR, and LGB, θ are learnable parameters, and ε denotes model residuals.

Model parameters are estimated by minimizing the mean-squared error:

$$\min_{\theta} \mathcal{L}(\theta) = \frac{1}{N}\sum_{i=1}^{N}\left(y_i - \mathcal{F}(x_i;\theta)\right)^2 \tag{6}$$

For model development, the dataset was split into training and test subsets (80/20). A 5-fold cross-validation procedure was applied only within the training set for hyperparameter tuning, while the held-out test set was used for final model evaluation.

Hyperparameter optimization was performed using Bayesian optimization with a Gaussian Process surrogate $g(\lambda)$ to minimize the validation loss [25]:

$$\lambda^* = arg\min_{\lambda \in \Lambda} E[\mathcal{L}_{val}(\lambda)] \tag{7}$$

where λ denotes the hyperparameter vector. The next query point is selected by maximizing the Expected Improvement (EI), defined as follows [26]:

$$\mathrm{EI}(\lambda) = \left(\mu_{min} - \mu(\lambda)\right)\Phi(Z) + \sigma(\lambda)\phi(Z), \quad Z = \frac{\mu_{min} - \mu(\lambda)}{\sigma(\lambda)} \tag{8}$$

The model with the lowest cross-validated RMSE and the highest R^2 is retained for multi-objective optimization.

Bi-objective optimization

After the surrogate models for *Ra* and *MRR* were established, they were used in the optimization stage to search for machining conditions that balance surface quality and productivity. In this study, the problem involves two conflicting objectives:

$$\min_x f_1(x) = Ra(x), \qquad \max_x f_2(x) = MRR(x) \tag{9}$$

subject to operational bounds:

$$V_c \in \left(V_c^{min}, V_c^{max}\right), f \in \left(f^{min}, f^{max}\right) a_p \in \left(a_p^{min}, a_p^{max}\right), R_E \in (0,\ 1), CL \in (0,1).$$

A solution x is considered Pareto-optimal if there is no other feasible solution x' that gives a lower *Ra* and a higher *MRR* at the same time, with at least one of the two being strictly better. Accordingly, the Pareto-optimal set is defined as

$$P^* = \{x \in \Omega | \nexists x' \in \Omega : Ra(x') \leq Ra(x), \forall j,\ MRR(x') \leq MRR(x)\} \tag{10}$$

To obtain this set, NSGA-III was employed as the search algorithm. In the present study, NSGA-III works directly with the retained surrogate models instead of repeated physical trials, which makes it possible to examine a large number of candidate settings within the allowable parameter ranges. The resulting Pareto front represents the trade-off between finish and productivity, and its convergence behavior was monitored using hypervolume and IGD [21].

MCDA-based ranking

The Pareto solutions obtained from NSGA-III represent different trade-offs between *Ra* and *MRR*. Since only one operating condition is required in practice, these solutions were further ranked using MCDA.

Each Pareto solution was treated as an alternative, with *Ra* and *MRR* as the decision criteria. Because lower *Ra* is preferred while higher *MRR* is desirable, they were treated as cost-type and benefit-type criteria, respectively. The criteria were normalized to [0, 1] using for benefit-type:

$$f'_{\mathrm{ij}} = \frac{f_{\mathrm{ij}} - f_j^{\mathrm{min}}}{f_j^{\mathrm{max}} - f_j^{\mathrm{min}}} \tag{11}$$

and for cost-type criteria:

$$f'_{ij} = \frac{f^{max}j - fij}{f_j^{max} - f_j^{min}} \tag{12}$$

Values are $v_{ij} = w_j, f'_{ij}$, where w_j are objective weights.

To improve robustness, multiple MCDA methods (CODAS, SPOTIS, MABAC, and WASPAS) were combined with different objective weighting schemes (Entropy, Gini, and MEREC), and the final ranking was obtained from their aggregated results.

Objective weighting

Because the final ranking may depend on how much importance is assigned to *Ra* and *MRR*, three objective weighting schemes were considered in this study, namely Entropy, Gini, and MEREC. These methods were used to reduce reliance on a single weighting rule and to examine the stability of the final decision under different weighting perspectives.

For Entropy weighting [5], the normalized contribution of alternative i to criterion j is first defined as $p_{ij} = f'_{ij} / \sum_{i=1}^{n} f'_{ij}$. The entropy value is then calculated using with $k = 1/\ln\, n$ as the normalization coefficient:

$$H_j = -k \sum_{i=1}^{n} p_{ij} \ln p_{ij}\,, \qquad w_j = \frac{1 - H_j}{\sum_{k=1}^{m} (1 - H_k)} \tag{13}$$

For Gini weighting [27], the normalized values are sorted in ascending order, and the degree of dispersion for each criterion is measured by:

$$G_j = 1 - 2 \sum_{i=1}^{n} \frac{i}{n} p_{(i)j}, \qquad w_j = \frac{G_j}{\sum_{k=1}^{m} G_k} \tag{14}$$

For MEREC weighting [12], the average normalized value of criterion j is first written as $\bar{f'}_j = \frac{1}{N} \sum_{i=1}^{n} f'_{ij}$, and the corresponding weight is obtained from the deviation of each alternative from this average:

$$w_j = \frac{\sum_{i=1}^{n} \left| f'_{ij} - \bar{f'}_j \right|}{\sum_{k=1}^{m} \sum_{i=1}^{n} \left| f'_{ik} - \bar{f'}_k \right|} \tag{15}$$

These weighting schemes were applied separately before the MCDA scoring stage, so that the subsequent ranking could be examined under different objective-weighting conditions.

MCDA scoring

After determining the objective weights, each Pareto solution is evaluated using several MCDA methods to obtain comparable scores and rankings. In this study, four methods—CODAS, SPOTIS, MABAC, and WASPAS—are applied under the same normalized decision matrix.

For CODAS [28], the negative-ideal solution $f_j^* = \max_i f'_{ij}$ is used to compute Euclidean and taxicab distances, and the relative assessment score is formed as:

$$S_i = -\sqrt{\sum_{j=1}^{m} w_j \left(f'_{ij} - f_j^*\right)^2} + \tau \sum_{j=1}^{m} \left| f'_{ij} - f_j^* \right| \tag{16}$$

For SPOTIS [29], the distance of each alternative to the ideal point is calculated as:

$$D_i = \sqrt{\sum_{j=1}^{m} w_j \left(f'_{ij} - f_j^*\right)^2}, \qquad S_i = 1 - \frac{D_i - D_{min}}{D_{max} - D_{min}} \tag{17}$$

For MABAC [23], the deviation of each alternative from the border approximation area is evaluated, and the final score is obtained as:

$$S_i = -\sqrt{\sum_{j=1}^{m} w_j \left(f'_{ij} - f_j^*\right)^2} + \tau \sum_{j=1}^{m} \left| f'_{ij} - f_j^* \right| \tag{18}$$

and the final score is

$$S_i = \sum_{j=1}^{m} w_j\,, Q_{ij} \tag{19}$$

For WASPAS [22], the score combines additive and multiplicative aggregation:

$$S_i = \frac{1}{2} \sum_{j=1}^{m} w_j \frac{f'_{ij}}{f_j^*} + \frac{1}{2} \prod_{j=1}^{m} \left(\frac{f'ij}{f_j^*}\right)^{w_j} \tag{20}$$

Each method produces a ranking of the Pareto solutions. These rankings are then used in the subsequent aggregation step to obtain a consensus decision.

Rank aggregation

Since different MCDA methods may produce different rankings, a rank aggregation step is introduced to obtain a more stable and consistent decision. Let $R^{(m)} = [r_{1m}, \dots, r_{nm}]$ denote the ranking obtained from method m, where $m = 1, \dots, M$.

For Borda count [11], each alternative is assigned a score based on its position in each ranking:

$$R_i^{\text{Borda}} = \frac{1}{M}\sum_{m=1}^{M}(n - r_{im}) \tag{21}$$

For Copeland index [30], pairwise comparisons are used. The number of wins and losses for each alternative i are computed as:

$$W_i = \sum_{j\neq i} I\left(r_i > r_j\right), L_i = \sum_{j\neq i} I\left(r_i < r_j\right) \Rightarrow \;\; C_i = W_i - L_i \tag{22}$$

For Kemeny–Young consensus [31], seeks a ranking R^* that maximizes agreement with all individual rankings:

$$R^* = \arg\max_{R} \sum_{m=1}^{M} \tau\left(R, R^{(m)}\right) \tag{23}$$

where τ is Kendall's tau between rankings.

For Robust Rank Aggregation (RRA) [32], each rank is first converted into a normalized value, $p_{im} = r_{im}/n$. The aggregated significance is then estimated by

$$P_i = \min_{k}\left(n\prod_{m=1}^{k} p_{im}\right)^{1/k}, \qquad \text{RRA}_i = -\log 10\,(P_i) \tag{24}$$

Consensus selection

The final consensus score integrates the results of the aggregation methods:

$$\overline{R_i} = \frac{R_i^{\text{Borda}} + C_i + R_i^{\text{Kemeny}} + \text{RRA}_i}{4} \tag{25}$$

The alternative with the highest $\overline{R_i}$ is selected as the recommended machining condition.

Experimental validation

Selected Pareto solutions (x^*) are experimentally verified on the same machine–tool–coolant configuration. The predicted and measured responses are compared using the absolute and relative errors:

$$E_j = \left|y_{j,\exp} - y_{j,\text{pred}}\right|, \qquad RE_j(\%) = \frac{AE_j}{y_{j,\exp}} \times 100 \tag{26}$$

Average relative error within 0-5 % for *Ra* and *MRR* indicates good agreement between predictions and experiment, supporting the reliability of the proposed workflow [24].

4. Results and discussion

4.1 Machine learning model performance

Table 2 reports the predictive accuracy of four surrogate models for *Ra* and *MRR*, using the same train/test split and preprocessing pipeline. Figs. 4 and 5 visualize the agreement between experimental and predicted values on the train and test partitions.

Table 2 Model performance metrics for *Ra* and *MRR*

Model	Surface roughness						Material removal rate					
	Train			Test			Train			Test		
	RMSE	MAE	R^2	RMSE	MAE	R^2	RMSE	MAE	R^2	RMSE	MAE	R^2
KAN	0.0082	0.006	0.999	0.0541	0.042	0.989	0.1343	0.100	0.999	0.5206	0.260	0.996
CAT	0.1012	0.078	0.983	0.0897	0.074	0.968	0.0040	0.003	0.999	2.2987	1.486	0.994
GBR	0.0017	0.001	0.999	0.0767	0.061	0.982	0.1180	0.072	0.999	4.6363	3.543	0.993
LGB	0.1920	0.138	0.941	0.0964	0.074	0.967	1.5290	1.090	0.989	4.7165	3.648	0.952

Surface roughness predictive performance

Across models, *Ra* is predicted with high fidelity, but the generalization gap differs markedly. KAN attains the best test performance (RMSE = 0.0541; MAE = 0.042; R^2 = 0.98), with only a slight drop from its near-perfect training fit (R^2 = 0.999). GBR ranks second on the test set (R^2 = 0.982; RMSE

= 0.0767), followed by CAT (R^2 = 0.968) and LGB (R^2 = 0.967). Notably, LGB shows the clearest sign of underfitting on *Ra* (train R^2 = 0.941; test RMSE = 0.192). Fig. 4 shows KAN lying closest to the 45° line, while tree-boosting models deviate more in the mid-high *Ra* range (1.5-2.5 μm).

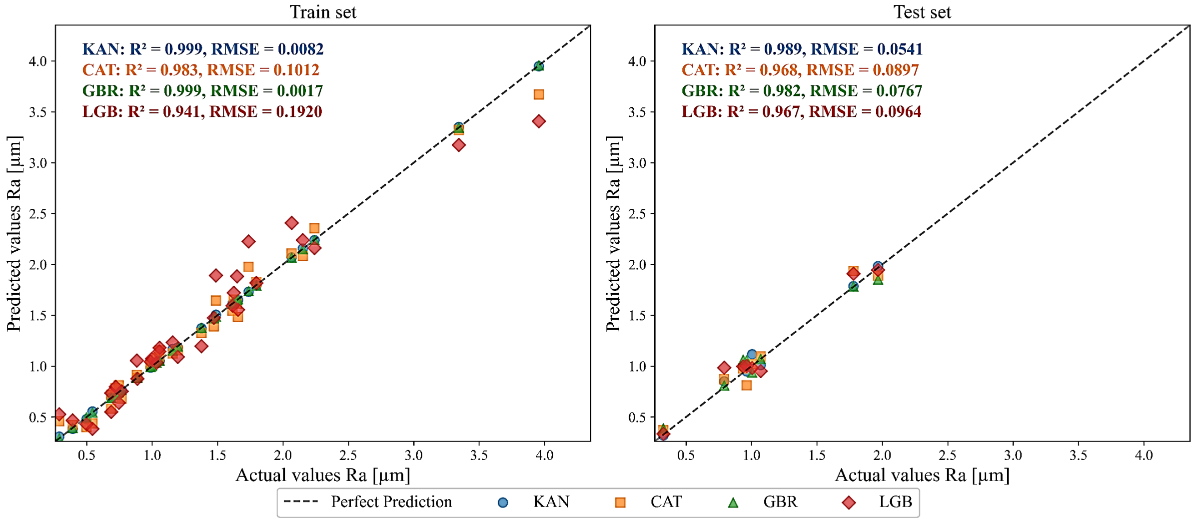

Fig. 4 Experimental vs. predicted values for Ra on train and test sets

Material removal rate predictive performance

Training fits are near-perfect for all, but their out-of-sample behavior diverges. KAN again provides the strongest generalization (test RMSE = 0.5206; R^2 = 0.999), keeping errors at a sub-percent scale relative to the *MRR* range in Fig. 5. In contrast, CAT degrades to RMSE = 2.2987 (R^2 = 0.994); meanwhile, GBR and LGB show larger errors (RMSE = 4.6363 and 4.7165; R^2 = 0.993 and 0.952). Fig. 5 indicates systematic under-prediction at high *MRR* for tree-based models, whereas KAN preserves the trend with minimal bias. Based on the test-set results, KAN showed the strongest generalization for both *Ra* and *MRR* and was therefore retained as the surrogate model for both responses in the subsequent optimization stage.

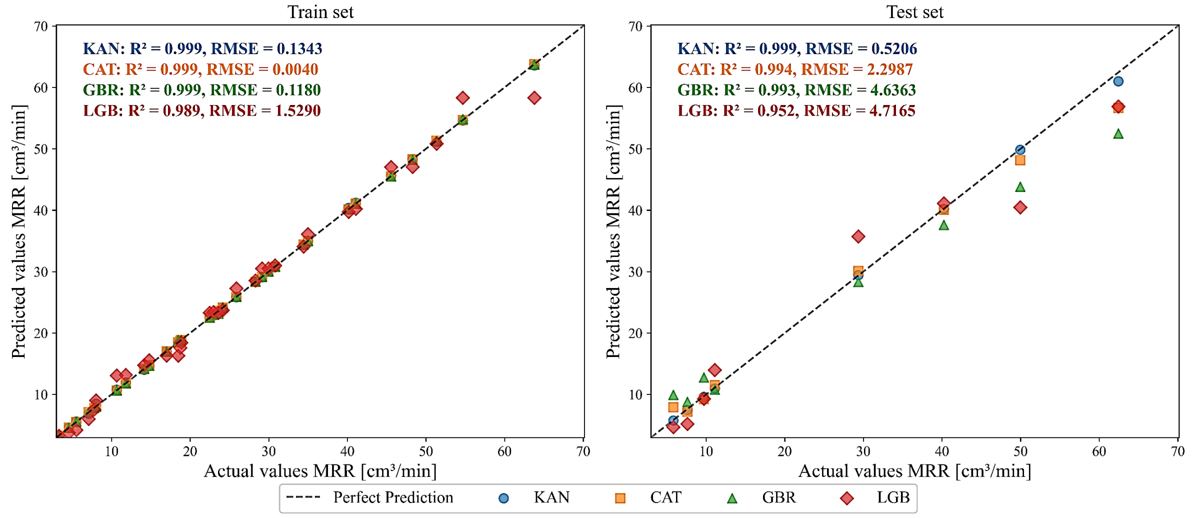

Fig. 5 Experimental vs. predicted values for *MRR* on train and test sets

4.2 Machine learning model explanation

Model explanation for Ra

Fig. 6a highlights the darkest branches from *f* and nose radius R_E, with weaker links from *ap*, *Vc*, and *CL*; this ordering is confirmed by the KAN feature scores in Fig. 6b and the GBR-SHAP violins in Fig. 6c, where high *f* shifts *Ra* upward while large R_E shifts it downward. The dominance of feed on roughness for brass is consistent with recent turning studies on Ms58, CW614N and other copper alloys, which report a substantial, monotonic increase of *Ra* with rising feed due to a thicker undeformed chip and more pronounced feed marks [33]. In parallel, the nose radius acts as a geometric smoother: larger R_E lowers cusp height and improves finish in brass andcopper alloys, a trend echoed by brass-focused machinability reports and broader turning investigations on nose-radius effects [34]. Regarding cutting speed, *Ra* tends to decrease as V_c increases because higher speed suppresses adhesion and built-up edge in lead-free brasses, improving surface topography—again matching the slight negative SHAP trend for V_c [35]. The influence of depth of cut on *Ra* is secondary within our range, mainly through force and vibration pathways; copper-alloy turning with coated tools similarly finds feed most influential and depth-of-cut a weaker contributor to roughness [36]. Finally, coolant shows only a minor direct effect on *Ra* for brass in our DOE, although tailored lubrication or hybrid cryo-MQL can still yield incremental finish improvements—consistent with brass turning tests and recent lead-free brass studies [37].

$$\begin{gathered} Ra = 0.19\,x_1 - 0.06\,x_3 - 0.34\,x_4 + 0.03\,x_5 + 0.02\,e^{0.94\,x_1} \\ +0.16\,e^{1.24\,x_1} - 0.02e^{0.69\,x_2} - 0\cdot 10^{-2}e^{0.72\,x_2} + 0.01\,e^{1.06\,x_3} + 1.8 \\ +0.01\,e^{-0.86\,x_1} - 0.11\,e^{-0.12\,x_1} \end{gathered} \tag{27}$$

With $[x_1, x_2, x_3, x_4, x_5] = [f, V_c, a_p, R_E, CL]$, *Ra* is driven mainly by feed: positive linear and exponential terms in x_1 make *Ra* increase with *f*. Speed enters only via negative exponentials in x_2, so higher V_c lowers *Ra* with a saturating effect. Depth of cut has a weak net influence (small positive exponential offset by a negative linear term). The negative linear term in x_4 shows a larger R_E smooths the surface. The *CL* term is tiny, indicating a negligible direct effect in this DOE.

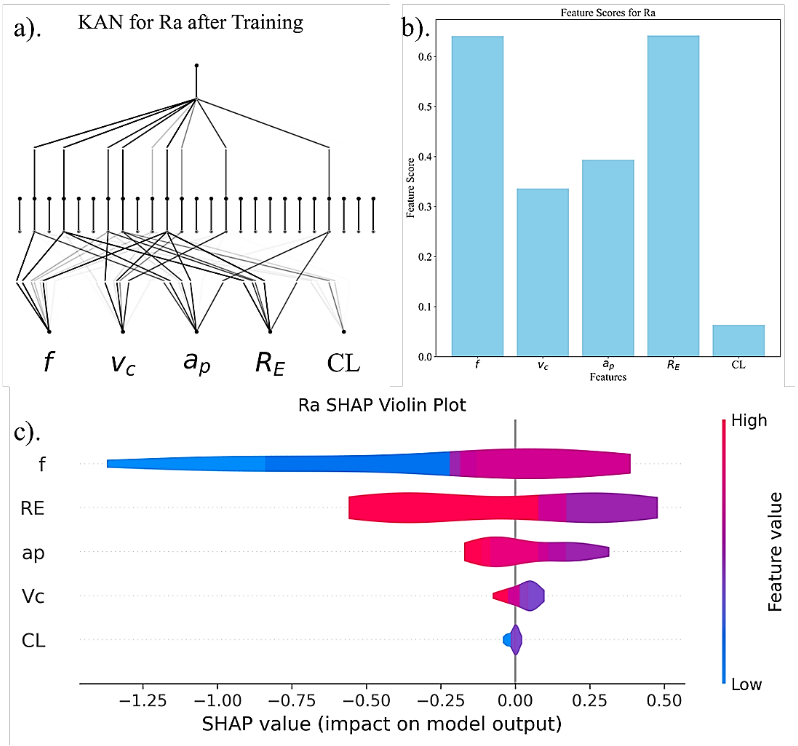

Fig. 6 Explanation for *Ra*: (a) KAN for initialization, (b) KAN feature importance, (c) GBR SHAP violin

Model explanation for MRR

Fig. 7a shows the branches from a_p, V_c, and f to *MRR* with high, medium, and lower intensity, respectively, while the links from R_E and *CL* are very faint—indicating negligible direct influence. This is reinforced in Fig. 7b, the feature-importance plot ranks ap highest, followed by V_c and f, with R_E and *CL* close to zero. Fig. 7c indicates the direction of effects: SHAP distributions for ap and V_c lie mainly on the positive side, and the pink (high-value) portions on the right show that larger a_p or V_c increase *MRR*; the blue segments on the left indicate that smaller values reduce *MRR*. For *f*, the trend is similar but with a smaller magnitude; R_E and *CL* concentrate around zero.

$$MRR = 0.26\,x_3 + 0.28\,e^{0.34\,x_2} + 0.66\,e^{0.48\,x_3+0.91\,e^{0.25\,x_2}-0.37\,e^{-0.55\,x_1}} \\ -1.44 - 0\cdot10^{-2}e^{-0.6\,x_5} - 0.14\,e^{-0.61\,x_1} \tag{28}$$

The positive linear term $0.26x_3$ and the exponential term containing x_3 confirm the dominant role of a_p; positive exponentials in x_2 capture the increase of *MRR* with V_c; the $-0.14\,e^{-0.61\,x_1}$ term explains a amplified contribution from *f* within the tested range; the *CL* coefficient is effectively zero and R_E does not appear—consistent with Fig. 7.

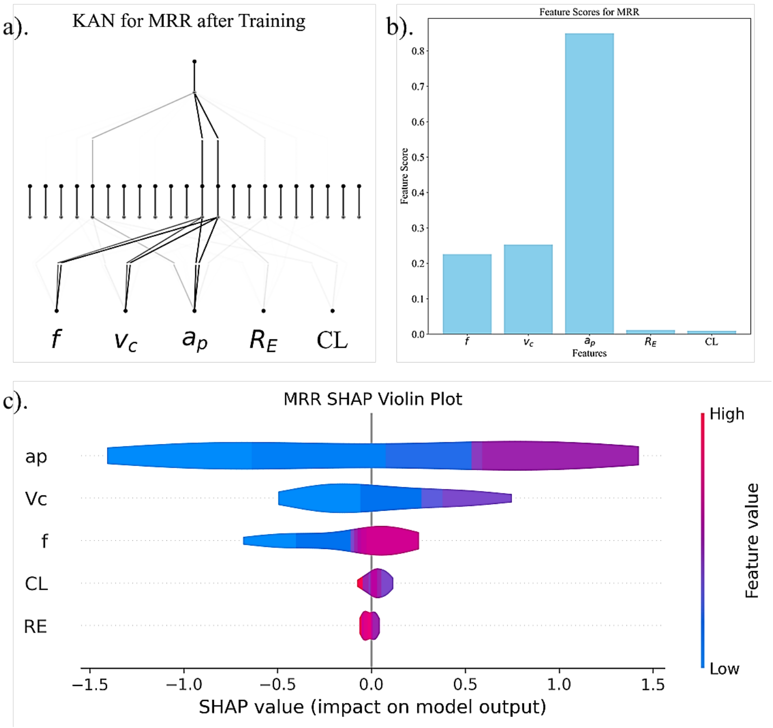

Fig. 7 Explanation for *MRR*: (a) KAN for initialization, (b) KAN feature importance, (c) CAT-SHAP violin

4.3 NSGA-III Multi-Objective optimization

Having established reliable surrogates, we used NSGA-III to identify Pareto-optimal settings that minimize *Ra* and maximize *MRR*. The algorithm ran with a population of 50 for 50 generations, using simulated binary crossover and polynomial mutation to maintain diversity. Similar evolutionary strategies have proved effective for complex manufacturing optimization [10].

Fig. 8a shows the final Pareto front from NSGA-III (*Ra* in range of 0.45-1.644 µm; *MRR* in range of 29.724-80.62 cm^3/min), while Fig. 8b, the hypervolume increases rapidly and then stabilizes, indicating convergence. Fig. 9 overlays the frontier on the DOE trials, confirming the expected trade-off—lower *Ra* comes at the cost of lower *MRR*—and the advantage of model-based search over trial-and-error [38]. In terms of operating windows, our "finish-first" range (*Ra* about 0.45-1.0 µm at low feed and higher speed) agrees with recent brass-turning studies reporting that reducing feed and increasing cutting speed improve surface finish; the "productivity-first" range (*Ra* about 1.3-1.6 µm with *MRR* 70-81 cm^3/min) corresponds to higher feed and depth, consistent with the literature on kinematic drivers of *MRR* [37]. Although a smaller R_E can minimize *Ra* when the feed is kept low (Fig. 6), the multi-objective context favors R_E = 0.8 mm in 8 of the 9 Pareto solutions (Table 3) because a larger nose radius acts as a geometric smoother that permits higher feed at comparable *Ra*, thereby lifting *MRR* without breaching the finish target [33].

Table 3 Optimal solutions generated by NSGA-III

Solution	f (mm/rev)	V_c (m/min)	a_p (mm)	R_E (mm)	CL	Ra (μm)	MRR ($\mathrm{cm^3/min}$)
1	0.114	176.948	1.501	1	0	0.450	29.724
2	0.121	224.867	1.475	1	0	0.585	39.990
3	0.122	221.061	1.842	0	0	0.704	48.373
4	0.133	224.893	1.848	1	0	0.810	55.030
5	0.146	224.893	1.850	1	0	0.945	59.575
6	0.160	224.824	1.849	1	0	1.104	64.060
7	0.185	224.996	1.764	1	0	1.222	69.437
8	0.194	224.970	1.837	1	0	1.322	75.249
9	0.210	224.981	1.850	1	0	1.644	80.620

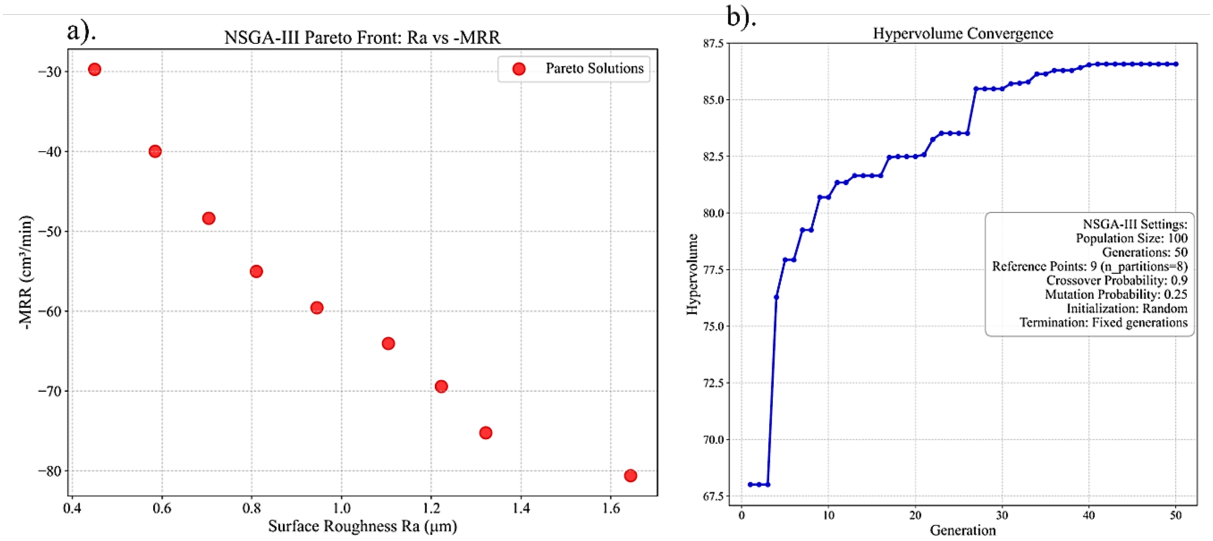

Fig 8 NSGA-III results: (a) Pareto front in the Ra-($-MRR$) space. (b) Hypervolume convergence across generations

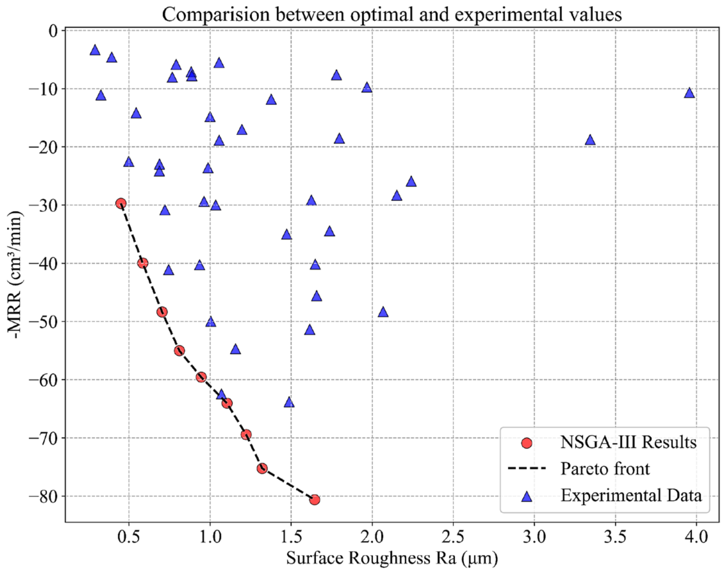

Fig. 9 Comparison of NSGA-III Pareto-optimal solutions with experimental trials in the Ra and ($-MRR$) space

4.4 MCDM-Based selection of the best solution

Although the Pareto front provides multiple feasible choices, industrial decision-makers often need a single recommended solution. This study applied four MCDM methods—CODAS, SPOTIS, MABAC, and WASPAS—to the Pareto-optimal set. The various weighting methods objectively assigned weights to the criteria, eliminating subjective biases.

Table 4 summarizes the Entropy, Gini, and MEREC weights for *Ra* and *MRR*. Table 5 reports, for each weighting scheme, the preference scores and induced ranks across the four MCDA methods; Fig. 10 visualizes the resulting orderings. Under Entropy weighting, all four methods rank Solution 1 first. Under Gini, most methods still favor Solution 1, with MABAC ranking Solution 4 first. Under MEREC, CODAS, SPOTIS, and WASPAS again select Solution 1, whereas MABAC prefers Solution 8. These modest disagreements across methods are typical in MCDA and motivate a principled consensus step.

To reduce weighting method sensitivity, four aggregators—Borda, Copeland, Kemeny–Young, and Robust Rank Aggregation—were applied to the per-method ranks (Table 6; Fig. 11). All four aggregators concur on Solution 1 as the overall best candidate, with Solutions 2-3 following and Solution 9 consistently last. The cross-method agreement indicates that the selected operating point is robust to reasonable changes in weighting and MCDA formulation, in line with recommendations to use consensus procedures when multiple ranking rules are plausible.

Table 4 Calculation weights for various objectives

Objective	MEREC	Entropy	Gini	Type
Ra	0.481	0.642	0.578	cost
MRR	0.519	0.358	0.422	benefit

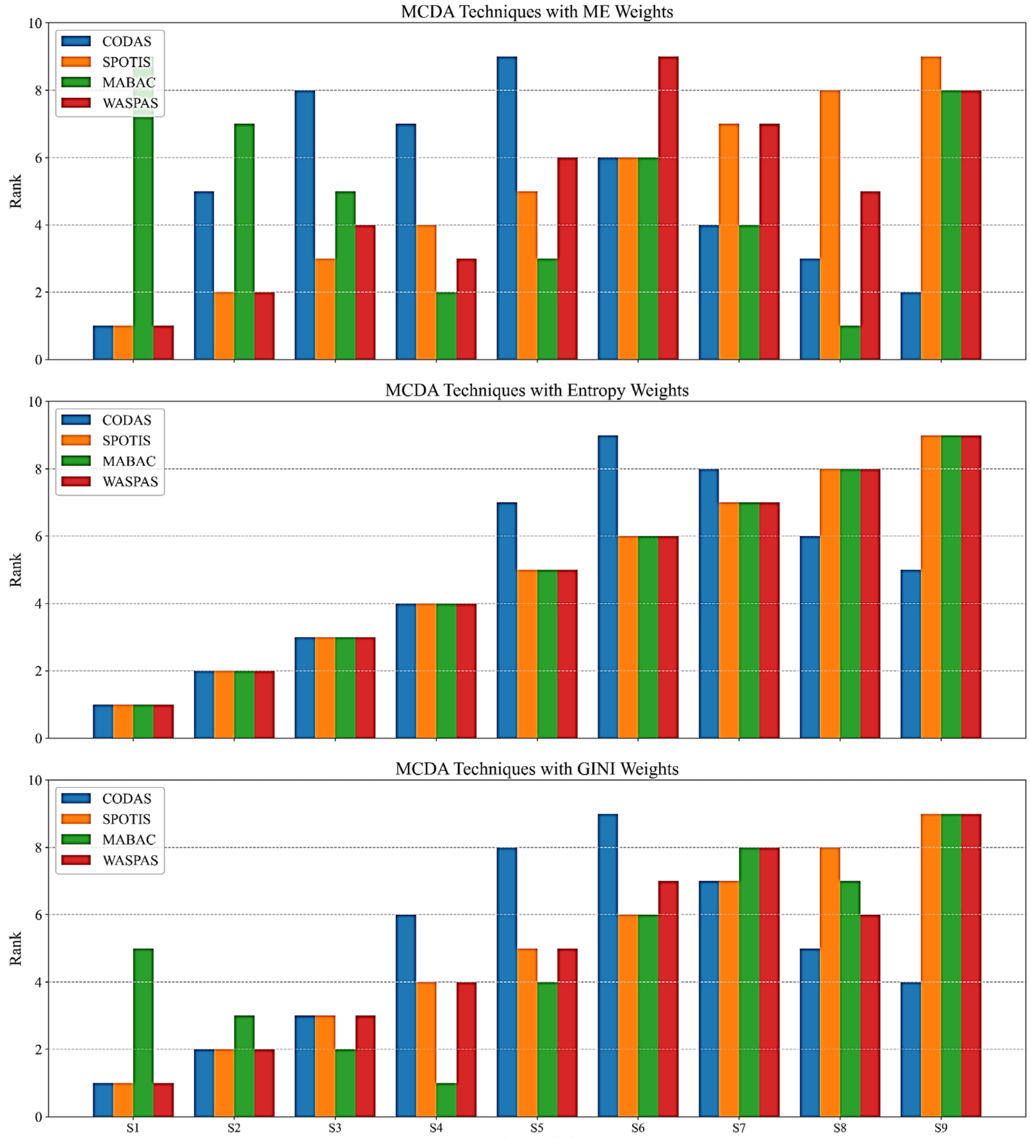

Fig. 10 Ranking of selected solutions by various MCDM methods with various weights

Table 5 MCDM-based ranking of selected Pareto solutions

ENTROPY	CODAS	pref	3.52	1.30	0.22	-0.44	-0.90	-1.14	-1.04	-0.79	-0.73
		rank	1	2	3	4	7	9	8	6	5
	SPOTIS	pref	0.23	0.19	0.15	0.12	0.11	0.09	0.07	0.04	0.03
		rank	1	2	3	4	5	6	7	8	9
	MABAC	pref	0.12	0.12	0.11	0.10	0.06	0.01	-0.02	-0.03	-0.17
		rank	1	2	3	4	5	6	7	8	9
	WASPAS	pref	0.74	0.66	0.62	0.60	0.56	0.53	0.52	0.52	0.48
		rank	1	2	3	4	5	6	7	8	9
GINI	CODAS	pref	2.59	0.72	-0.17	-0.51	-0.76	-0.83	-0.59	-0.27	-0.18
		rank	1	2	3	6	8	9	7	5	4
	SPOTIS	pref	0.27	0.22	0.18	0.14	0.12	0.10	0.07	0.05	0.02
		rank	1	2	3	4	5	6	7	8	9
	MABAC	pref	0.05	0.07	0.08	0.09	0.06	0.02	0.01	0.01	-0.10
		rank	5	3	2	1	4	6	8	7	9
	WASPAS	pref	0.70	0.65	0.62	0.61	0.58	0.56	0.55	0.56	0.53
		rank	1	2	3	4	5	7	8	6	9
MEREC	CODAS	pref	1.17	-0.18	-0.56	-0.56	-0.57	-0.44	-0.08	0.45	0.77
		rank	1	5	8	7	9	6	4	3	2
	SPOTIS	pref	0.33	0.27	0.22	0.17	0.15	0.12	0.09	0.05	0.02
		rank	1	2	3	4	5	6	7	8	9
	MABAC	pref	-0.04	0.01	0.04	0.07	0.06	0.04	0.05	0.07	-0.01
		rank	9	7	5	2	3	6	4	1	8
	WASPAS	pref	0.63	0.62	0.62	0.62	0.61	0.59	0.60	0.61	0.59
		rank	1	2	4	3	6	9	7	5	8

Table 6 Rank aggregation of Pareto solutions: Borda, Copeland, Kemeny–Young, RRA, and final consensus rank

Solution	Borda	Copeland	Kemeny–Young	RRA	Final rank
1	1	1	1	1	1
2	2	2	2	2	2
3	3	3	3	3	3
4	4	4	4	4	4
5	5	5	5	7	5
6	8	6	6	8	8
7	7	8	8	5	7
8	6	7	7	6	6
9	9	9	9	9	9

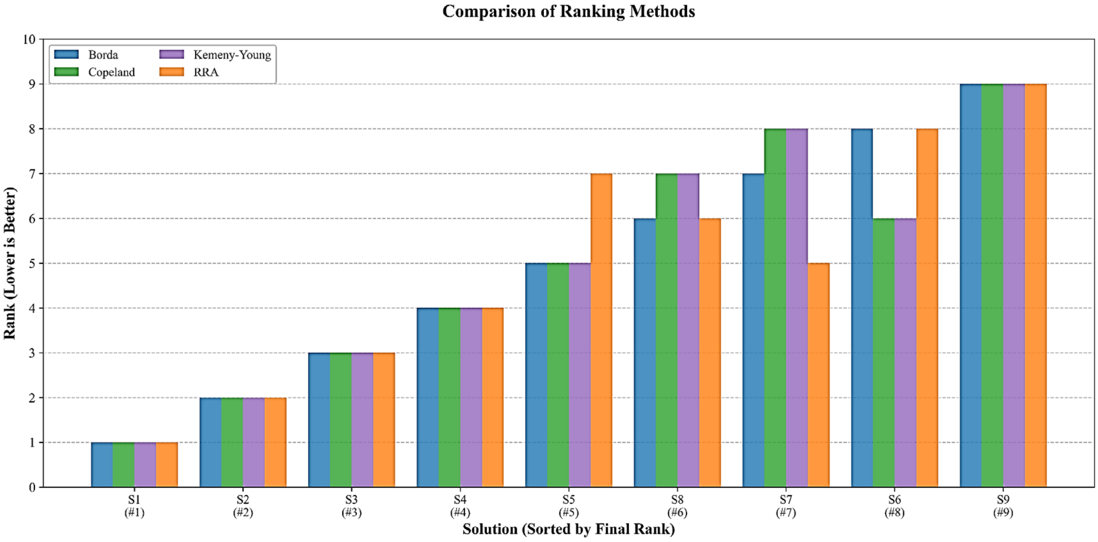

Fig. 11 Comparison of rank-aggregation methods for Pareto candidates—Borda, Copeland, Kemeny–Young, and RRA (solutions ordered by final consensus rank)

Taken together, the evidence from Tables 4-6 and Fig. 10 indicate that Solution 1 is the most suitable choice and is selected for experimental confirmation.

4.5 Experimental confirmation

Validation cuts were conducted at the consensus point S1 and two neighboring points (S2 and S3) using the same machine, fixturing, and coolant condition. Each setting was repeated three times (n = 3) with a fresh cutting edge. Ra and MRR were identified in the Section 3 procedure. Accuracy was assessed using AE_j and $RE_j(\%)$ as defined in Eq. 26. The predefined acceptance criterion was $RE_j(\%) \leq 5$ % for both Ra and MRR. Results in Table 7 indicate close agreement between predictions and measurements; the pattern across S_1–S_3 also confirms the Ra–MRR trade-off observed on the Pareto front. In practice, the confirmation supports R_E = 0.8 mm as the joint optimum: although a smaller R_E can minimize Ra in isolation, the larger radius permits higher f at comparable Ra, thereby increasing MRR without breaching finish targets.

This work presents an integrated data-to-decision workflow for machining optimization, combining surrogate modeling, explainability, multi-objective optimization, and MCDA within a single procedure. Rather than relying on a single model or a fixed decision rule, the approach evaluates the trade-off between surface quality and productivity under multiple weighting and ranking settings, leading to a more consistent basis for selecting the final operating condition.

An important aspect of this study is that the final decision is not tied to a single weighting scheme or ranking method. Instead, several weighting approaches and MCDA methods are considered, and their results are combined through rank aggregation [35]. This reduces the dependence on any individual method and helps obtain a more stable and technically balanced recommendation. The experimental validation further shows that the selected solutions remain close to the predicted values, supporting the practical applicability of the proposed workflow. At the same time, the present validation should be interpreted within the scope of the selected objectives. In this study, Ra and MRR were used as representative quality and productivity responses to demonstrate the workflow in a focused turning case study. In broader industrial applications, however, the final operating condition may also need to account for factors such as tool life, cutting-force stability, machining efficiency, and processing time.

Table 7 Experimental confirmation at Pareto points (mean ± SD over n = 3)

Setting	Cutting conditions	Ra_{pred}	Ra_{exp}	AE (µm)	RE (%)	MRR_{pred}	MRR_{exp}	AE (cm^3/min)	RE (%)
S1	f = 0.114, V_c = 176.948, a_p = 1.50, R_E = 0.8, CL = 0	0.450	0.468 ± 0.012	0.018	3.85	29.724	29.48 ± 0.30	0.244	0.83
S2	f = 0.121, V_c = 224.867, a_p = 1.475, R_E = 0.8, CL = 0	0.585	0.602 ± 0.015	0.017	2.82	39.990	39.35 ± 0.45	0.640	1.63
S3	f = 0.122, V_c = 221.061, a_p = 1.842, R_E = 0.4, CL = 0	0.704	0.741 ± 0.019	0.037	4.99	48.373	47.55 ± 0.55	0.823	1.73

5. Conclusion

This study presents a complete data-to-decision workflow for machining optimization with limited data. The workflow combines surrogate modeling with Bayesian tuning, NSGA-III for generating the Ra–MRR Pareto front, and a decision layer based on MCDA with objective weighting and rank aggregation. For the C3604 brass case, this procedure led to a single final operating condition and was further checked by experiment.

The main findings are as follows:

- The surrogate comparison among KAN, CAT, GBR, and LGB under a unified pipeline showed good generalization on held-out data.
- NSGA-III generated a well-distributed Pareto front, and the hypervolume results indicated stable search behavior.
- The MCDA methods (CODAS, SPOTIS, MABAC, and WASPAS) combined with Entropy, Gini, and MEREC weights produced only minor differences in ranking.
- Rank aggregation using Borda, Copeland, Kemeny–Young, and RRA gave a stable consensus, with Solution 1 ranked first overall.
- Experimental tests at representative Pareto points agreed well with the predictions, with relative errors below 5 % for both Ra and MRR.

This study considered only two responses, *Ra* and *MRR*, and did not include energy, force constraints, or tool wear in the optimization stage. In addition, predictive uncertainty and robust optimization were not treated explicitly. Although the proposed data-to-decision framework is general in structure and can be adapted to other machining systems with different machine configurations, input variables, and output responses, the numerical recommendation obtained in the present C3604 turning case study remains specific to the investigated experimental domain and should not be directly transferred to other machines, tool systems, or coolant settings without re-evaluation.

Future work will extend the framework to include additional objectives such as energy and cost, incorporate wear-related responses, and develop uncertainty-aware decision strategies. A lightweight calibration step across different machines and a real-time GUI for shop-floor use are also planned.

References

[1] Abdelaoui, F.Z.E., Jabri, A., Barkany, A.E. (2023). Optimization techniques for energy efficiency in machining processes-a review, *The International Journal of Advanced Manufacturing Technology*, Vol. 125, No. 7-8, 2967-3001, doi: 10.1007/s00170-023-10927-y.

[2] Tang, K.-E., Lin, G.-Y., Liu, C.-W. (2025). Sustainable orthogonal turn-mill process parameter decision-making based on specific consumption energy model and NSGA-II multi-objective optimization algorithm, *The International Journal of Advanced Manufacturing Technology*, Vol. 137, No. 11-12, 6107-6121, doi: 10.1007/s00170-025-15490-2.

[3] Nguyen, V.-H., Le, T.-T., Le, M.V., Dao Minh, H., Nguyen, A.-T. (2023). Multi-objective optimization based on machine learning and non-dominated sorting genetic algorithm for surface roughness and tool wear in Ti_6Al_4V turning, *Machining Science and Technology*, Vol. 27, No. 4, 380-421, doi: 10.1080/10910344.2023.2235610.

[4] Al-Samarai, R.A., Al-Douri, Y. (2025). *Advanced cutting tool technology and machine processes*, CRC Press, Boca Raton, Florida, USA, doi: 10.1201/9781003604648.

[5] Nguyen, V.-H., Le, T.-T., Nguyen, A.-T., Hoang, X.-T., Nguyen, N.-T., Nguyen, N.-K. (2025). Optimization of milling conditions for AISI 4140 steel using an integrated machine learning-multi objective optimization-multi criteria decision making framework, *Measurement*, Vol. 242, Part A, Article No. 115837, doi: 10.1016/j.measurement.2024.115837.

[6] Zhou, A., Zhang, Q., Zhang, G. (2012). A multiobjective evolutionary algorithm based on decomposition and probability model, In: *Proceedings of 2012 IEEE Congress on Evolutionary Computation (CEC)*, Brisbane, Australia, 1-8, doi: 10.1109/CEC.2012.6252954.

[7] Vu, B.D., Tran, G.N., Dinh, V.T., Bui, H.T., Do, T.T. (2026). Minimizing the cross-sectional area and maximizing efficiency in split-input two-stage gearboxes via NSGA-II with SAW-guided choice, *Engineering, Technology & Applied Science Research*, Vol. 16, No. 1, 31916-31922, doi: 10.48084/etasr.14925.

[8] Nguyen, V.-H., Le, T.-T., Nguyen, A.-T., Hoang, X.-T., Nguyen, N.-T. (2025). Comprehensive machine learning and multi-criteria optimization workflow for trochoidal milling parameter selection in AISI 4140 steel, *The International Journal of Advanced Manufacturing Technology*, Vol. 141, 4071-4094, doi: 10.1007/s00170-025-16916-7.

[9] Sofianidis, G., Rožanec, J.M., Mladenić, D., Kyriazis, D. (2021). A review of explainable artificial intelligence in manufacturing, In: Soldatos, J., Kyriazis, D. (eds.), *Trusted artificial intelligence in manufacturing: A review of the emerging wave of ethical and human centric AI technologies for smart production*, Emerald Publishing Limited, Leeds, United Kingdom, 93-113, doi: 10.1561/9781680838770.ch5.

[10] Deb, K., Pratap, A., Agarwal, S., Meyarivan, T. (2002). A fast and elitist multiobjective genetic algorithm: NSGA-II, *IEEE Transactions on Evolutionary Computation*, Vol. 6, No. 2, 182-197, doi: 10.1109/4235.996017.

[11] Liu, Q., Jing, Y., Yan, Y., Li, Y. (2024). Mean-based Borda count for paradox-free comparisons of optimization algorithms, *Information Sciences*, Vol. 660, Article No. 120120, doi: 10.1016/j.ins.2024.120120.

[12] Keshavarz-Ghorabaee, M., Amiri, M., Zavadskas, E.K., Turskis, Z., Antucheviciene, J. (2021). Determination of objective weights using a new method based on the removal effects of criteria (MEREC), *Symmetry*, Vol. 13, No. 4, Article No. 525, doi: 10.3390/sym13040525.

[13] Vukelic, D., Milosevic, A., Ivanov, V., Kocovic, V., Santosi, Z., Sokac, M., Simunovic, G. (2024). Modelling and optimization of dimensional accuracy and surface roughness in dry turning of Inconel 625 alloy, *Advances in Production Engineering & Management*, Vol. 19, No. 3, 371-385, doi: 10.14743/apem2024.3.513.

[14] Milosevic, A., Simunovic, G., Kanovic, Z., Simunovic, K., Kocovic, V., Vukelic, D. (2025). Modelling and optimization of surface quality and productivity in turning Inconel 825 alloy, *International Journal of Simulation Modelling*, Vol. 24, No. 4, 565-576, doi: 10.2507/IJSIMM24-4-725.

[15] While, L., Hingston, P., Barone, L., Huband, S. (2006). A faster algorithm for calculating hypervolume, *IEEE Transactions on Evolutionary Computation*, Vol. 10, No. 1, 29-38, doi: 10.1109/TEVC.2005.860074.

[16] Ullah, A., Chan, T.-C., Chang, S.-L. (2025). Current trends in vibration control and computational optimization for CNC machine tools: A comprehensive review, *The International Journal of Advanced Manufacturing Technology*, Vol. 139, 5409-5444, doi: 10.1007/s00170-025-16238-8.

[17] Bartels, S., Boomsma, W., González-Duque, M., Hauberg, S., Michael, R., Zainchkovskyy, Y. (2024). A survey and benchmark of high-dimensional Bayesian optimization of discrete sequences, In*: Proceedings of Advances in Neural Information Processing Systems 37,* Vancouver, Canada, 140478-140508, doi: 10.52202/079017-4459.

[18] Wang, H., Bai, Q., Chen, S., Wang, T., Guo, W., Dou, Y. (2025). Neural networks with dual-view fusion feature learning mechanism: A method to improve micro-milling tool wear monitoring performance by enhancing feature generalization capabilities, *Mechanical Systems and Signal Processing*, Vol. 236, Article No. 113038, doi: 10.1016/ j.ymssp.2025.113038.

[19] Lundberg, S.M., Lee, S.-I. (2017). A unified approach to interpreting model predictions, In: *Proceedings of 31st Conference on Neural Information Processing Systems (NIPS 2017),* Long Beach, USA, 4768-4777.

[20] Liu, Z., Wang, Y., Vaidya, S., Ruehle, F., Halverson, J., Soljačić, M., Hou, T.Y., Tegmark, M. (2024). KAN: Kolmogorov-Arnold networks, *arXiv*, doi: 10.48550/arXiv.2404.19756.

[21] Deb, K., Jain, H. (2014). An evolutionary many-objective optimization algorithm using reference-point-based nondominated sorting approach, part I: Solving problems with box constraints, *IEEE Transactions on Evolutionary Computation*, Vol. 18, No. 4, 577-601, doi: 10.1109/TEVC.2013.2281535.

[22] Zavadskas, E.K., Antuchevičienė, J., Šaparauskas, J., Turskis, Z. (2013). MCDM methods WASPAS and MULTIMOORA: Verification of robustness of methods when assessing alternative solutions, *Economic Computation and Economic Cybernetics Studies and Research*, Vol. 47, No. 2, 5-20.

[23] Pamučar, D., Ćirović, G. (2015). The selection of transport and handling resources in logistics centers using Multi-Attributive Border Approximation area Comparison (MABAC), *Expert Systems with Applications*, Vol. 42, No. 6, 3016-3028, doi: 10.1016/j.eswa.2014.11.057.

[24] Montgomery, D.C. (2017). *Design and analysis of experiments*, 9th edition, John Wiley & Sons, Hoboken, New Jersey, USA.

[25] Nguyen, V.-H., Le, T.-T., Truong, H.-S., Le, M.V., Ngo, V.-L., Nguyen, A.T., Nguyen, H.Q. (2021). Applying Bayesian optimization for machine learning models in predicting the surface roughness in single-point diamond turning polycarbonate, *Mathematical Problems in Engineering*, Vol. 2021, No. 1, Article No. 6815802, doi: 10.1155/2021/6815802.

[26] Snoek, J., Larochelle, H., Adams, R.P. (2012). Practical Bayesian optimization of machine learning algorithms, In: *Proceedings of Advances in Neural Information Processing Systems 25 (NIPS 2012),* Lake Tahoe, Nevada, USA, 2951-2959.

[27] Li, G., Chi, G. (2009). A new determining objective weights method-Gini coefficient weight, In: *Proceedings of 2009 First International Conference on Information Science and Engineering*, Nanjing, China, 3726-3729, doi: 10.1109/ICISE.2009.84.

[28] Keshavarz Ghorabaee, M., Zavadskas, E.K., Turskis, Z., Antucheviciene, J. (2016). A new combinative distance-based assessment (CODAS) method for multi-criteria decision-making, *Economic Computation and Economic Cybernetics Studies and Research*, Vol. 50, No. 3, 25-44.

[29] Shekhovtsov, A., Dezert, J., Sałabun, W. (2024). Generalization of stable preference ordering towards ideal solution approach for working with imprecise data, *Operations Research and Decisions*, Vol. 34, No. 3, 243-266, doi: 10.37190/ord2403013.

[30] Özdağoğlu, A., Keleş, M.K., Altınata, A., Ulutaş, A. (2021). Combining different MCDM methods with the Copeland method: An investigation on motorcycle selection, *Journal of Process Management and New Technologies*, Vol. 9, No. 3-4, 13-27, doi: 10.5937/jouproman2103013O.

[31] Phung, X.K., Hamel, S. (2025). Efficient space reduction techniques by optimized majority rules for the Kemeny aggregation problem and beyond, *arXiv*, doi: 10.48550/arXiv.2506.15097.

[32] Võsa, U., Kolde, R., Vilo, J., Metspalu, A., Annilo, T. (2014). Comprehensive meta-analysis of MicroRNA expression using a robust rank aggregation approach, In: Alvarez, M.L., Nourbakhsh, M. (eds.), *RNA Mapping. Methods in Molecular Biology,* Vol. 1182, Humana Press, New York, USA, 361-373, doi: 10.1007/978-1-4939-1062-5_28.

[33] Ateş, E., Serbest, N. (2024). Investigation of effects of feed rate and cutting-edge angle variation on surface roughness in external cylindrical turning process of Ms58 brass material, *Applied Sciences*, Vol. 14, No. 24, Article No. 12039, doi: 10.3390/app142412039.

[34] Atay, G., Zoghipour, N., Kaynak, Y. (2023). Investigation of machining performance of lead-free brass materials forged in different conditions after cooling with liquid nitrogen, In*: Proceedings of The 26th International Esaform Conference on Material Forming, ESAFORM 2023,* Krakow, Poland, Vol. 28, 1357-1366, doi: 10.21741/ 9781644902479-147.

[35] Das, A., Bajpai, V. (2023). Machinability analysis of lead free brass in high speed micro turning using minimum quantity lubrication, *CIRP Journal of Manufacturing Science and Technology*, Vol. 41, 180-195, doi: 10.1016/ j.cirpj.2022.11.023.

[36] Mohanta, D.K., Sahoo, B., Mohanty, A.M. (2024). Experimental analysis for optimization of process parameters in machining using coated tools, *Journal of Engineering and Applied Science*, Vol. 71, Article No. 38, doi: 10.1186/ s44147-024-00370-5.

[37] Hussein, S.G. (2014). An experimental study of the effects of coolant fluid on surface roughness in turning operation for brass alloy, *Journal of Engineering*, Vol. 20, No. 3, 96-104, doi: 10.31026/j.eng.2014.03.09.

[38] Shrivastava, A., Pandey, M. (2024). Integrating and optimizing quality and client satisfaction in resource constrained time-cost trade-off for construction projects with NSGA-III methodology, *Asian Journal of Civil Engineering*, Vol. 25, 5669-5684, doi: 10.1007/s42107-024-01137-2.

APEM journal
Advances in Production Engineering & Management
Volume 21 | Number 1 | March 2026 | pp 75–88
https://doi.org/10.14743/apem2026.1.562
ISSN 1854-6250
Journal home: apem-journal.org
Original scientific paper

A new bilevel model for EV fast charging station location planning with dynamic traffic assignment

Qiu, H.T.[a,*]

[a]School of Management and Engineering, Capital University of Economics and Business, Beijing, P.R. China

ABSTRACT

Intelligent siting of electric vehicle (EV) fast charging stations is of great significance for the development of urban transportation. This study comprehensively considers factors related to the placement of EV fast charging stations, including differences in travel behavior between fuel vehicle travelers and EV travelers, road congestion, vehicle energy consumption, and the geographical location of charging stations. Based on these factors, an advanced bilevel programming model integrating dynamic traffic assignment (DUE) and charging station location selection is developed. Specifically, the upper level uses a genetic algorithm (GA) to solve a system optimization model aimed at minimizing total travel time while accounting for the construction and operation costs of charging stations. Corresponding to the upper-level decisions, the lower level captures the joint selection behaviors of fuel and electric vehicles and is solved by a DUE procedure combined with the method of successive averages (MSA). This lower-level model incorporates travelers' on-route fast-charging behaviors, including departure time choice, charging facility preference, and route selection. The integrated approach provides a sophisticated framework for analyzing and optimizing the interaction between charging station placement, travel time, and associated costs. An iterative dynamic traffic flow algorithm integrating EV charging queue simulation is proposed. Finally, numerical studies conducted on an illustrative network derive optimal location schemes at different EV adoption stages and analyze the complex operational characteristics of the traffic network under the coexistence of EVs and fuel vehicles.

ARTICLE INFO

Keywords:
Electric vehicles;
Fast charging station;
Bilevel programming;
Location planning;
Siting and sizing;
Dynamic user equilibrium;
Traffic assignment;
Charging queueing;
Logit-based traveler choice

**Corresponding author:*
qiuheting@cueb.edu.cn
(Qiu, H.T.)

Article history:
Received 16 June 2025
Revised 11 March 2026
Accepted 17 March 2026

1. Introduction

Reducing carbon emissions is essential for climate governance, and electric vehicles have emerged as a key solution [1]. Driven by national strategies, the industrialization of electric vehicles in China is advancing rapidly. The development of charging facilities is a crucial part of this process, as it directly influences the adoption rate of electric vehicles. As of June 2024, the ownership of new energy vehicles (NEVs) in China has exceeded 20 million units, with the national cumulative charging infrastructure reaching 9.023 million charging points. Despite the steady growth in the number of charging facilities, surveys indicate that many charging piles suffer from low utilization rates. Due to the uneven distribution of resources, some areas face shortages while others experience oversupply. Currently, the establishment of charging stations across various regions in China remains in the fixed-site demonstration construction phase.

The location planning of charging stations and the charging behavior of EV users profoundly impact traffic flow dynamics [2]. A recent study analyzed TealDrive and Weibo user reviews using sentiment analysis and topic modeling, identifying key themes and stressing the value of user feedback for EV charging infrastructure planning [3]. In daily travel, commuters make decisions not only about route selection but also about departure time, yet existing research inadequately addresses the interplay between charging station placement, traffic network efficiency, and user behavior [4, 5].

Research on charging station (CS) location optimization primarily employs two models: point demand and flow demand [6]. Scholars have expanded these frameworks with optimization methods, such as data-driven geographic grid optimization [7], car sharing [8], spatial-statistical coverage models [9], and spatiotemporal taxi charging layouts [10]. A recent work combined the sparrow search algorithm with backpropagation neural networks to build a driving behavior recognition model, enabling accurate evaluation of the impact of driving behaviors on fuel consumption and offering theoretical support for intelligent transportation system design [11]. Certain researchers adopt long short-term memory-gated recurrent units (LSTM-GRU) to forecast electricity usage, thereby easing pressure on the power grid [12]. Others address demand uncertainty, facility reliability, and charging satisfaction [13], yet most neglect the interaction between CS placement and traffic network efficiency, as well as the impacts of traveler behavior.

Route choice is critical in transportation science, where dynamic traffic assignment (DTA) models analyze network equilibrium. Studies explore path transitions [14], travel behavior [15], urban mobility improvement [16] and mode choice via prospect theory [17]. Recent work integrates EVs into traffic flow analysis, such as coordinated traffic-power network planning [18] and time-varying DTA [19]. Xu *et al.* adopted a mileage-based strategy for CS placement to reduce range anxiety [20], while Riemann *et al.* [21] implemented stochastic user equilibrium in their models. Zheng *et al.* constructed a bi-level model for CS location [22], and Zhang *et al.* predicted the spatiotemporal demand of electric vehicles (EVs) [4]. A multi-criteria decision-making method is also proposed to optimize the route [23]. Sun *et al.* put forward a two-layer partition method that divides heterogeneous congestion networks into sub-regions, establishes a multi-region traffic flow balance model, and uses this model to analyze heterogeneous congestion networks [24]. To solve the electric vehicle routing problem with time windows, Wang *et al.* proposed an integer mixed programming model incorporating time and area prices, which enhanced the model's realism [25]. Huang *et al.* developed a joint optimization model for electric vehicle (EV) battery recharging and scheduling under dynamic electricity prices, aiming to determine optimal charging arrangements (recharging time and quantity) and transportation plans (transportation time and quantity) [26]. In the domain of EV charging behavior modeling, simulation-based approaches have gained increasing attention. Tang *et al.* [27] introduced a Q-learning framework for simulating EV charging station recommendations, dynamically adapting to user behaviors to improve recommendation accuracy and station utilization, highlighting the importance of incorporating user preferences into charging infrastructure planning. For charging station location optimization, Can *et al.* [28] developed a novel approach for electric buses, considering the operational constraints of public transit systems, contributing to the growing literature on differentiated charging infrastructure planning. Despite these efforts, queuing delays, the impedance differences between EVs and fuel vehicles, and the influence of departure times remain unaccounted for in these models.

This study develops a bi-level programming model integrating dynamic user equilibrium (DUE) and system optimal (SO) approaches to optimize fast-charging station locations. The model incorporates EV users' charging behavior (arrival, queuing, and charging) and analyzes mixed traffic networks with both EVs and fuel vehicles. Through a micro-level analysis of departure time choices, route selection, and charging patterns, it examines how travel decisions affect station siting. The research elucidates the interactions among travelers, road network conditions, and charging infrastructure to support optimal station placement decisions.

The remainder of this paper is organized as follows. Section 2 presents the problem description and the formulation of the bilevel programming model for EV fast charging station location planning, including its workflow, assumptions, variable definitions, upper/lower model designs and solution algorithms. Section 3 conducts simulation experiments to validate the model and algorithm, presenting location planning results under different EV penetration rates and analyzing traffic flow assignment and departure time distribution. Section 4 discusses model performance by comparing the DUE and SUE models, and analyzes their differences in charging station planning and road network operation efficiency. Finally, Section 5 summarizes the research conclusions, clarifies the study limitations, and proposes future research directions and practical application suggestions for fast charging station location planning.

2. Problem description and model

2.1 Workflow

The methodology for selecting sites for fast charging stations is depicted in Fig. 1. The bi-level location planning model comprises three key components: travelers' behavior, traffic flow assignment, and the determination of optimal charging station locations and capacities. The study focuses on the impact of traffic on the site selection of charging stations, so dynamic charging demands, the road network, and the characteristics of travelers' behavior are mainly considered. By balancing system-level and individual-level optimization, the model identifies a charging station layout that improves overall network efficiency while also enhancing individual travel utility.

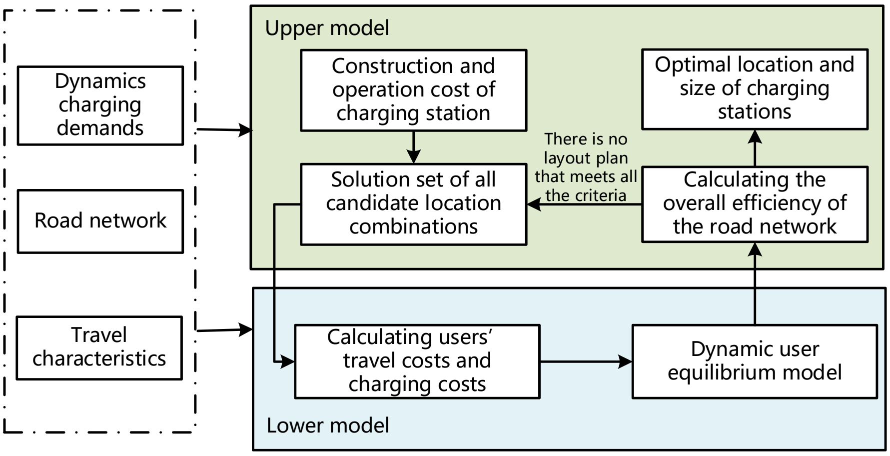

Fig. 1 Process of site selection

2.2 Model assumptions and definitions

This study adopts the following key assumptions: (1) The network includes both EVs and fuel vehicles that select routes based on perceived path resistance. EV drivers optimize charging strategies according to real-time traffic, with energy consumption proportional to the distance traveled. (2) Charging queues form when demand exceeds station capacity. Fast-charging duration follows a normal distribution (this assumption is model-independent). (3) No spatial constraints exist for charger placement, but total construction costs must remain within budget. (4) All network nodes are candidate locations for charging stations. (5) Travelers learn and adapt route choices based on historical travel time data.

To facilitate model development and theoretical validation, this study adopts a deliberate simplification in Assumption (4), treating every network node as a potential charging station site. However, in real-world applications, site feasibility is constrained by multiple factors including land availability and cost, grid connection capacity, zoning regulations, and infrastructure requirements. If only a subset of nodes were feasible, the optimal solution would likely concentrate charging capacity on the remaining feasible nodes, potentially leading to higher congestion at those stations, longer detour distances for EV users, and increased overall network travel time. The model can be extended to incorporate feasibility constraints by adding a binary parameter f_j indicating whether node j is feasible ($f_j = 1$) or not ($f_j = 0$), and modifying the upper-level decision variable such that ω_j can only be 1 if $f_j = 1$. This extension would require additional data collection on node-specific feasibility factors, which we identify as an important direction for future research applying the model to real-world cities.

In this paper, the transportation network is modeled as a graph structure $G = (J, A)$, where J is the set of transportation nodes; A is the set of road segments; a is a road section, $a \in A$; W is the set of origin-destination (OD) pairs in a network, and w is an OD pair in W, $w \in W$; R_w is the set of paths associated with OD pair w, and r denotes one of these paths, $r \in R$. There are two categories of travelers: those who drive electric vehicles, represented by e, and those who drive fuel vehicles, represented by g. The set of vehicle types is denoted as $B = \{b|g, e\}$. The time period $[0, H]$ is discretized to a set of time intervals which contains π time periods, and let ς be the interval length such that $H = \varsigma\pi$. The study period $[0, H]$ is large enough for all peak hour travelers to be able to complete their trips, and the traveler who enters any road section in a certain time period cannot leave the road section in the same time period.

For $\forall t \in [t_1, t_2, \cdots, t_\pi]$, $v_w^{rb}(d,t)$ is the flow of b-type vehicles on the path r at time t of day d v_a^b(d,t) is the flow of b-type vehicles on the link a at time t of day d； $u_a^b(d,t)$ is the inflow of b-type vehicles on the link a at time t of day d; $x_a^b(d,t)$ is the outflow of b-type vehicles on the link a at time t of day d. $T_a(d,t)$ is the travel time of link a at time t on day d, $T_r(d,t)$ is the travel time of route r at time t on day d. $u_{ar}^{wb}(d,t)$, $x_{ar}^{wb}(d,t)$, $v_{ar}^{wb}(d,t)$ are the inflow, outflow and flow of b-type vehicles of link a on route r at time t. In discrete time, the travel time of link a can be expressed as $T_a(\mathrm{d,t}) = [T_a(d,t_1), T_a(d,t_2), \cdots, T_a(d,t_\pi)]$, and the inflow of link a at time $t'(t' \in [t_1, t_1, \cdots, t_\pi])$ can be represented as:

$$u_a(d,t') = \sum_w \sum_r \sum_t \sum_b v_w^{rb}(t) \cdot \varpi_{a,r,t}^{wb}(d,t') \tag{1}$$

The binary variable $\varpi_{a,r,t}^{wb}(d,t')$ denotes the association between link a and route r. Specifically, it takes a value of 1 if travelers departing from the origin at time t can reach link a at time t'; otherwise, $\varpi_{a,r,t}^{wb}(d,t') = 0$.

2.3 Upper model

From the perspectives of charging station construction and traffic management authorities, this section conducts a comprehensive assessment of road network performance, the expenses involved in setting up charging stations, and their impact on existing road conditions. This study establishes a system-optimal objective for the road network and subsequently optimizes the placement and design of charging stations.

Given the notable differences in route choice behaviors between EV and fuel vehicle drivers, the growing adoption of EVs is poised to exert a substantial impact on the operation of the existing traffic network. When the road network is balanced, electric vehicle users will choose the path with the least travel cost. Therefore, decision makers need to consider how to deploy public charging stations to minimize system impedance from a holistic perspective. To balance total travel time minimization with the control of charging station construction and operational costs, the upper-level model employs a dual design combining the objective function and a hard budget constraint: the objective function (Eq. 2) takes the total road network impedance (integrating the travel time of EVs and fuel vehicles) as the core objective to minimize the travel time of the whole network, and the subsequent cost budget constraint (Eq. 3) forms a rigid limit on the total cost, thus realizing a dynamic trade-off between the two optimization objectives. The following model is proposed:

$$min \sum_{r=1}^{R} c_w^r(d,t) = \sum_{r=1}^{R} \left(c_w^{rg}(d,t) + c_w^{re}(d,t) \right) \tag{2}$$

where $c_w^r(d,t)$ denotes the actual path travel impedance for route r between OD pair w on day d at time t, $c_w^{rg}(d,t)$and $c_w^{re}(d,t)$ represent the actual path impedances for fuel vehicles and electric vehicles when they choose path r at time t on day d.

The main constraints include land, construction, and operating costs, as well as the time value of capital. The total annual investment cost is affected by the following factors:

$$\sum_j \omega_j \frac{i(1+i)^Y}{(1+i)^Y - 1} (M_1 + M_2 + M_3) \le M_{max} \tag{3}$$

Let M_1 denote the land price, M_2 the construction cost, and M_3 the operating cost of the charging station at node j. The discount rate i and service life y are also considered. M_{max} refers to the maximum budget allocated by the government for charging station construction. ω_j is a 0-1 variable; specifically, if there is a charging station at node j, ω_j equals 1; otherwise, it equals 0. The total power capacity of the charging station is positively correlated with the number of charging piles s and the rated power of a single pile, and the construction cost M_2 included in the budget constraint (Eq. 3) is associated with the scale of charging piles configuration, which indirectly forms a hard constraint on the total power capacity of the charging station (the total power capacity cannot be infinitely expanded due to the limit of M_{max}).

2.4 Lower model

From the traveler's perspective, the DUE model incorporates multiple attributes influencing path and departure time decisions for both fuel and electric vehicles. It sets optimal individual objectives for travelers and optimizes charging station layouts. Notably, travelers cannot unilaterally boost the network's overall efficiency by changing travel routes or departure times at any moment; this is called equilibrium.

At time t, travelers choose their routes probabilistically. Based on random utility theory, the Logit model is used to describe route-choice behavior. Accordingly, the probability of path selection can be formulated as follows:

$$P_w^r(d,t) = \frac{\exp(-\theta_1 c_w^r(d,t))}{\sum_{r\in R_w} exp(-\theta_1 c_w^r(d,t))}, w \in W, r \in R_w \tag{4}$$

where $P_w^r(d,t)$ denotes the probability that travelers in OD pair w choose path r at time t on day d, $c_w^r(d,t)$ stands for the path impedance when travelers of OD pair w choose path r at time t on day d, θ_1 is a positive parameter. In view of the different path selection features of fuel vehicles and electric vehicles, separate calculations are performed to determine the path impedances for each vehicle type.

We adopt the Bureau of Public Roads (BPR) function as the selected average link travel time function, and also make use of the real-time traffic flow of the link. The travel impedance of vehicles powered by fuel on path r can be expressed as:

$$c_w^{rg}(d,t) = T_w^g(d,t) + F_r^g \tag{5}$$

where $T_r^g(d,t)$ is the travel time of fuel vehicles on path r at time t on day d, $F_r^g(d,t)$ represents the fuel cost, which can be calculated by the length of the link and the fuel cost per unit distance.

EV travel involves three key components: driving time, charging waiting time, and charging duration. An electric vehicle's overall travel duration is largely determined by driving time, in addition to charging waiting time and actual charging duration. The travel cost of using electric vehicles mainly includes recharging cost and electricity consumption, which can be calculated by multiplying route length by the per-kilometer electricity cost.

The travel duration of EVs on a link is determined by the BPR function. The service process at charging stations follows the M/M/S/K queuing model; specifically, the inter-arrival times of customers follow a negative exponential distribution with parameter λ, there are s service stations, each server's service time is independent and follows a negative exponential distribution with parameter μ, and the system capacity is K. Thus, the M/M/S/K queuing model is used to calculate the waiting time at charging station j.

C_{max} is the maximum charge quantity of electric vehicles, and the residual charge quantity is $C_j(d,t)$ when reaching charging station j at time t on day d. User arrival frequency $\lambda_j(d,t)$ is calculated on the basis of the EV inflow u_a^e(d,t) and the residual battery capacity of EVs on the link a at time t:

$$\lambda_j(d,t) = \begin{cases} 0.8 \cdot u_a^e(d,t)\text{ , if } C_j(d,t) \leq C_{max} \cdot 20\ \% \\ 0.6 \cdot u_a^e(d,t)\text{ , if } C_{max} \cdot 20\ \% \leq C_j(d,t) \leq C_{max} \cdot 40\ \% \\ 0.4 \cdot u_a^e(d,t)\text{ , if } C_{max} \cdot 40\ \% \leq C_j(d,t) \leq C_{max} \cdot 60\ \% \\ 0.2 \cdot u_a^e(d,t)\text{ , if } C_{max} \cdot 60\ \% \leq C_j(d,t) \leq C_{max} \cdot 80\ \% \\ 0.1 \cdot u_a^e(d,t)\text{ , if } C_j(d,t) > C_{max} \cdot 80\ \% \end{cases} \tag{6}$$

Let ρ_2 denote the unit charging cost; the total charging fee is $\mathrm{F}_{a1}^e(d,t) = \eta \cdot \rho_2 \cdot T_\Delta(d,t)$, and the electricity consumption cost is $\mathrm{F}_{a2}^e(d,t) = \eta \cdot \rho_2 \cdot s_\mathrm{a}(d,t)$. Of particular relevance is that the arrival rate $\lambda_j(d,t)$ in the queuing model is endogenously determined by the traffic flow from the lower-level DUE model and the residual battery level of EVs, as expressed in Eq. 6. The piecewise coefficients (0.8, 0.6, ⋯) represent a behavioral rule where drivers with lower battery levels are more likely to seek charging, ensuring that queue dynamics are responsive to both traffic conditions and vehicle states.

The service rate μ is derived from the charging time $T_\Delta(d,t)$, which is assumed to vary within a reasonable range [0,10] minutes based on typical fast-charging durations. According to the physical relationship $P = E/T$, the charging time implicitly constrains the charging power limit, where E is the charging energy determined by the battery residual capacity and maximum capacity C_{max}.

The number of chargers s is an upper-level decision variable optimized by the genetic algorithm, with its value limited to [3,10]. It directly determines the maximum concurrent service capacity of the charging station and thus forms a hard constraint on the station throughput. Combined with the endogenously determined arrival rate $\lambda_j(d,t)$, the actual station throughput can further match real-time charging demand. For the system capacity K, we assume it is sufficiently large (effectively infinite) in this strategic planning context, as the focus is on long-term location decisions rather than detailed operational queue management. Therefore, the travel impedance of EVs on link A is:

$$c_w^{ae}(d,t) = T_a(d,t) + T_\Delta(d,t) + W_{q_j}(d,t) + \mathrm{F}_{a1}^{e}(d,t) + \mathrm{F}_{a}^{e}(d,t) \tag{7}$$

where $W_{qj}(d,t)$ denotes the average waiting time of EVs at charging station j, $T_\Delta(\mathrm{d,t})$ is the charging time. The travel impedance of electric vehicles on path r can be formulated as:

$$c_w^{re}(d,t) = \sum_{a\in A}\left(T_a(d,t) + T_\Delta(d,t) + W_{q_j}(d,t) + \mathrm{F}_{a1}^{e}(d,t) + \mathrm{F}_{a}^{e}(d,t)\right) \tag{8}$$

Travelers choose their departure times randomly. Assuming a continuous distribution, the probability of departure time selection is calculated using the Logit model:

$$\tau_w^r(d,t) = \frac{\exp(\theta_2 \varphi_w^r(d,t))}{\sum_{r\in R_w}\exp(\theta_2 \varphi_w^r(d,t))}, w \in W, r \in R_w \tag{9}$$

where $\tau_w^r(d,t)$ and $\varphi_w^r(d,t)$ are the probability and utility associated with departing at time t for travelers in OD pair w on day d, θ_2 is a positive parameter reflecting travelers' sensitivity to different departure time choices. It should be noted that the parameters θ_1 and θ_2 in the Logit models are assumed values that satisfy the theoretical condition $\theta_1 > \theta_2$, which guarantees the existence of a unique solution in the discrete choice framework (see [29] for details). The specific values ($\theta_1 = 1$, $\theta_2 = 0.3$) are chosen for model identifiability and are consistent with common practice in transportation behavior studies. As the primary focus of this paper is to demonstrate the theoretical validity and algorithmic feasibility of the proposed bilevel model, the use of assumed parameters is considered acceptable at this stage. Future work should calibrate these parameters using real-world travel survey data.

Based on the value function in prospect theory, the utility function $\varphi_w^r(d,t)$ is defined as follows.

$$\varphi_w^r(d,t) = \begin{cases} \beta_1(t_e - t_a)^{\alpha_1}, & t_a \le t_e \\ \beta_2(t_a - t_e)^{\alpha_2}, & t_e < t_a \le t^* \\ \beta_3(t_s - t_d)^{\alpha_3}, & t^* < t_a < t_s \\ \beta_4(t_a - t_s)^{\alpha_4}, & t_a > t_s \end{cases} \tag{10}$$

Suppose that t_s is the work start time, t is the traveler's acceptable early arrival time, t^* is the traveler's preferred arrival time, and t_a is the traveler's actual arrival time. To calculate the arrival time of a fuel vehicle, the vehicle's departure time and travel time are added. For an electric vehicle, the arrival time is determined by the sum of the departure time, travel time, charging time, and waiting time for an available charging station.

$\beta_1 \sim \beta_4$, $\alpha_1 \sim \alpha_4$ are parameters. Eq. 10 indicates that if a traveler arrives before t, there is an early arrival penalty; if the traveler arrives after t_s, there is a late arrival penalty. If a traveler arrives within $[t, t_s]$, the traveler gains utility. t^* is the preferred arrival time, at which the traveler obtains the greatest benefit. According to the initial theory of Kahneman and Tversky [30], the parameter values are as follows: $\beta_1 = -1$, $\beta_2 = \beta_3 = 2.25$, $\beta_4 = -1$, $\alpha_1 = \alpha_3 = \alpha_4 = 0.88$, $\alpha_2 = 0.57$. Combined with Eqs. 4 and 9, the joint choice of departure time and travel path can be expressed as:

$$v_w^r(d,t)= D_w \cdot P_w^r(d,t) \cdot \tau_w^r(d,t), w \in W, r \in R_w \tag{11}$$

where $v_w^r(d,t)$ represents the number of vehicles on path r at t time of day d, and D_w is the total demand of the road network. $v_w^r(d) = D_w \cdot P_w^r(d,t)$ represents the total flow of the two types of vehicles on path r for each departure time of the day. $v_w(d,t) = D_w \cdot \tau_w^r(d,t)$ is the total flow of the two vehicle types for each departure time of the day.

Departure time and route selection are sequentially interdependent: the selected departure time affects the dynamic route-choice process, and the resulting route selection in turn affects subsequent departure-time decisions. Travelers need to take the interactive effects of these two factors into account when making optimal travel decisions.

2.5 Solution algorithms

The heuristic algorithm is designed based on the method of successive averages (MSA) and a genetic algorithm. The key to the algorithm is the use of the Logit model to derive the route choice probabilities and departure time selection probabilities of the traveler group, followed by iterations using the MSA algorithm.

Firstly, the initial population (charging station distribution) is formed by selecting the decision variables of the upper-level model based on a genetic algorithm, and the Logit stochastic dynamic user equilibrium (DUE) model of the lower level is solved based on the charging station distribution. For each charging station distribution in the population, the MSA algorithm is used to calculate the traffic flow assignment at different departure times. Once the equilibrium state is achieved, the path flow is updated and fed into the upper-level model, with well-adapted individuals screened out by means of the fitness function. These selected individuals are then imported into the lower-level programming, and the cycle is repeated to seek the global optimal solution. The steps are as follows:

Step1: Initialization. All simple acyclic paths between OD pairs w are considered as the set of valid paths R_w.

Step2: Outer-loop iteration (Genetic Algorithm). The location and capacity of charging stations are digitally coded to form the initial population, where X represents the number of iterations.

Step3: Inner-loop iteration (Path selection and departure time selection). x is the number of iterations.

Step 3.1: Initial path flows for each departure time on the first day are acquired by initializing the path selection probabilities of fuel vehicles and EVs. Path impedances for the two vehicle types are calculated separately for each departure time on the first day.

Step 3.2: Path travel times are computed separately for fuel vehicles and electric vehicles respectively. Subsequently, travelers' utility values for different departure times are calculated according to Eq. 10.

Step 3.3: Path inflow calculations. The path inflow is computed using Eqs. 4 and 9. Subsequently, both the path flow and departure time flow are iteratively updated through the MSA algorithm.

Step 3.4: Convergence check. The iteration terminates when the traffic flow assignment reaches an equilibrium state, satisfying the convergence criteria: $v_w^{r(x)}(d) - v_w^{r(x-1)}(d) \leq \delta$ and $v_w^{r(x)}(d,t) - v_w^{r(x-1)}(d,t) \leq \delta$, where δ represents the predetermined error threshold. If converged, proceed to Step 4; otherwise, return to Step 2 for further iterations.

Step 4: Construct the fitness function and start the genetic algorithm. Digital coding is used to represent the location and capacity of charging stations, with each chromosome corresponding to a specific layout of charging stations. In the crossover and mutation phases, the roulette wheel selection method is applied to pick chromosomes for generating a new population. The set crossover probability is 0.8 and the mutation probability is set at 0.01. For instance, the quantity of charging piles is limited to the range of [3,10].

Step 5: Termination criterion for the genetic algorithm: The iterative optimization process terminates when the condition $\max F^{(X+1)} - \max F^{(X)} < \varepsilon$ is satisfied for generation X, where ε represents the predefined convergence threshold. If not, the algorithm reverts to Step 2 to proceed with the evolutionary iteration process.

3. Simulation experiments and results

3.1 Simulation setup

A test network is adopted in this study to verify the validity of the proposed model and algorithm, whose structure is presented in Fig. 2 and comprises 9 nodes, 12 links and 6 paths. Network nodes are set as optional locations for charging stations, and the number of charging piles configured for each station is in the range of 3 to 10. The initial battery capacity of electric vehicles conforms to a normal distribution of $\mathcal{N}(120,\ 3.6^2)$.

There are six paths in the road network, as shown in Table 1. The initial simulation parameters are presented in Tables 2, 3 and 4.

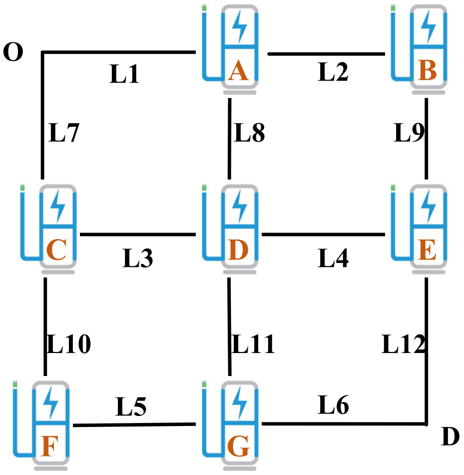

Fig. 2 The example network

Table 1 Paths

Path design	
Path 1: L1 - L2 - L9 - L12	Path 2: L1 - L8 - L4 - L12
Path 3: L1 - L8 - L11 - L6	Path 4: L7 - L3 - L4 - L12
Path 5: L7 - L3 - L11 - L6	Path 6: L7 - L10 - L5 - L6

Table 2 Network parameters

Link	L_a	T_a^0	Link	L_a	T_a^0
1	50	10	7	50	10
2	32	10	8	64	12
3	50	12	9	32	10
4	64	10	10	32	12
5	50	14	11	64	8
6	64	10	12	32	10

Table 3 Model parameters

Parameters	Value	Parameters	Value	Parameters	Value
θ_1	1	θ_2	0.3	ς	10 min
ρ_1	0.6	ρ_2	0.016	D_w	200
C_{max}	200	δ, ε	0.01	i	8 %
$T_\Delta(d,t)$	[0,10]	π	6	η	1.47
t_e	9:00	t^*	9:25	t_s	9:35
Y	20	γ	0.1	M_{max}	20 million

Table 4 Areas of supporting facilities

Functional zone	Area (m^2)	Functional zone	Area (m^2)	Functional zone	Area (m^2)
Transformer room	50	High voltage distribution room	50	Control room	40
Low voltage distribution room	100	Charging set room	60	Service zone	50

3.2 Location planning results

Based on the experimental road network, the optimal scheme for charging station siting and capacity configuration under various electric vehicle penetration rates is derived, as presented in Table 5. The charging station layout aims to maximize the travel utility of users and minimize the overall travel time of the network. The total travel demand of the road network is 200. A–G denotes the charging station index, and the values in the corresponding columns represent the number of charging piles at each station.

According to Table 5, when the EV penetration rate reaches 20 %, the number of charging stations begins to increase to ensure road network efficiency. Yet, with further increases in the number of electric vehicles, efficient charging can be maintained through traffic flow optimization, eliminating the need for additional piles.

Once the local EV penetration rate exceeds 50 %, new charging stations become crucial for network efficiency. The maximum number of charging stations is reached when the electric vehicle density hits 70 %. To optimize charging station placement under rising EV adoption and declining numbers of conventional vehicles, an approach that accounts for departure times and route choices is recommended. This strategy meets charging demands, boosts traffic efficiency, and reduces the number of required stations. Notably, no fixed correlation exists between the number of charging stations and the number of electric vehicles. Optimizing station layout and traffic flow can enhance road network efficiency with fewer stations, rather than simply adding more infrastructure.

Notably, the optimization results of charging station locations in Table 5 also reflect the adaptive adjustment characteristics of the model to the cost-travel time weight: the change of the total number of charging piles with the EV penetration rate is essentially the model's dynamic trade-off between meeting the traffic efficiency demand (reducing travel time) and controlling the construction and operation costs under the fixed budget constraint M_{max}.

Table 5 Location planning results of CS with different penetration rate of EVs

Penetration rate of EVs (%)	A	B	C	D	E	F	G	Total number of charging piles
10	6	5	9	0	5	0	0	25
20	5	5	6	10	8	0	0	34
30	7	5	3	0	10	0	0	25
40	4	3	5	5	7	0	0	24
50	7	7	6	0	5	0	0	25
60	0	8	10	9	5	0	0	32
70	8	9	10	8	6	0	0	41
80	6	9	10	6	4	0	0	35
90	3	0	0	4	0	6	8	21

3.3 Analysis of traffic flow assignment

Tables 6 and 7 illustrate the travel times and selection probabilities of routes for these vehicles at EV proportions of 10 %, 50 %, and 90 %. As shown in Table 6, Paths 1, 3, and 5 have the shortest travel times and the highest route selection probabilities for fuel vehicles. Path 6 has the longest travel time and the lowest selection probability, aligning with the expected utility theory. Notably, at a 50 % EV proportion, Paths 3 and 5 have equal travel times. With 7 charging piles on Path 3 and 6 on Path 5, Path 5 has a higher traffic flow ratio, indicating that fuel vehicles prefer paths with fewer charging piles when travel times are the same.

Table 6 Travel time and path selection of each path for fuel vehicles

Path	Penetration rate of EV								
	10 %			50 %			90 %		
	Travel time	Routing (%)	Number of CPs	Travel time	Routing (%)	Number of CPs	Travel time	Routing (%)	Number of CPs
1	40.6	18.9	16	40.2	19.3	19	40.4	20.4	3
2	42.0	13.9	11	42.2	13.8	12	42.3	14.6	7
3	40.0	21.6	6	40.1	22.1	7	40.3	21.5	15
4	42.0	14.1	14	42.3	14.0	11	42.6	14.4	4
5	40.1	22.1	9	40.1	22.5	6	40.2	21.2	12
6	46.5	9.4	9	46.3	8.3	6	46.6	7.9	14

From Table 7, at a 90 % EV proportion, Path 1 has the shortest travel time, the fewest charging piles, and the lowest traffic flow share. Despite being second in travel time among the six routes, Path 3 has the highest flow distribution ratio due to its largest number of charging piles, suggesting that EV travelers prioritize charging station layout and convenience when choosing routes.

When the EV proportion is 50 %, Path 1 has the highest traffic flow allocation. Its travel time ranks second among the six paths, yet it has the most charging piles. Evidently, at this EV penetration rate, charging stations influence route selection more than travel time.

At a 10 % EV proportion, Path 6 has the longest travel time and the lowest traffic flow share, in line with the expected utility theory. Path 1 has the shortest travel time, but Path 5 has the largest traffic flow allocation proportion, conforming to the principle of random user equilibrium. When Path 1 has far more charging piles than Path 5, the probability of choosing Path 5 is higher, showing that at a 10 % EV proportion, the number of charging piles affects path selection less than travel time.

According to the above results, the location of charging stations has a significant impact on user behavior and the distribution of traffic flow in the road network, which in turn affects the traffic efficiency of the road network.

Table 7 Travel time and path selection of each path for electric vehicles

Path	Penetration rate of EV								
	10 %			50 %			90 %		
	Travel time	Routing (%)	Number of CPs	Travel time	Routing (%)	Number of CPs	Travel time	Routing (%)	Number of CPs
1	59.3	18.6	16	60.1	18.9	19	60.1	7.6	3
2	61.9	18.3	11	62.1	18.3	12	62.0	18.7	7
3	60.0	18.7	6	60.3	18.8	7	60.2	19.2	15
4	62.0	18.2	14	61.8	18.2	11	62.2	17.9	4
5	60.1	18.8	9	60.0	18.7	6	60.4	18.3	12
6	66.6	7.3	9	65.9	7.1	6	66.1	18.2	14

Note: The travel time of an electric vehicle is the sum of the driving time, charging time and charging waiting time of the path

3.4 Analysis of departure time distribution

Table 8 shows the traffic distribution of all travelers at different departure times. Fig. 3 shows the departure time selection results of fuel vehicle travelers and electric-vehicle travelers during the morning rush hour. Obviously, there are significant differences in departure times for different types of vehicle users.

From Fig. 3, it can be observed that fuel vehicles predominantly depart at 8:30 and 8:40, whereas electric vehicles are concentrated at 8:10 and 8:20. This paper assumes that the working time is 9:35 and the optimal arrival time is 9:25. Given that the average travel time of fuel vehicles is 42 minutes and electric vehicles have an average travel time of 62 minutes, the departure time for electric vehicles generally needs to be earlier than that for fuel vehicles to arrive before the start of work. The sensitivity of travelers to departure time proves the validity of the utility function designed in this paper. Combined with the distribution of travelers' departure time selections and the analysis of the utility function of travelers' departure time selection, it can be seen that, in order to make the arrival time close to the optimal arrival time of 9:25, travelers adjust their departure times, which conforms to expected utility theory.

Table 8 Flow distribution at different departure times

Departure time	Penetration rate of EV (%)								
	10	20	30	40	50	60	70	80	90
8:00	1	1	1	1	2	3	4	4	40
8:10	3	4	5	24	10	18	38	40	28
8:20	10	17	24	14	37	35	24	28	19
8:30	24	20	15	11	13	15	12	12	6
8:40	51	50	49	46	34	26	20	13	7
8:50	10	8	6	4	4	4	3	3	1

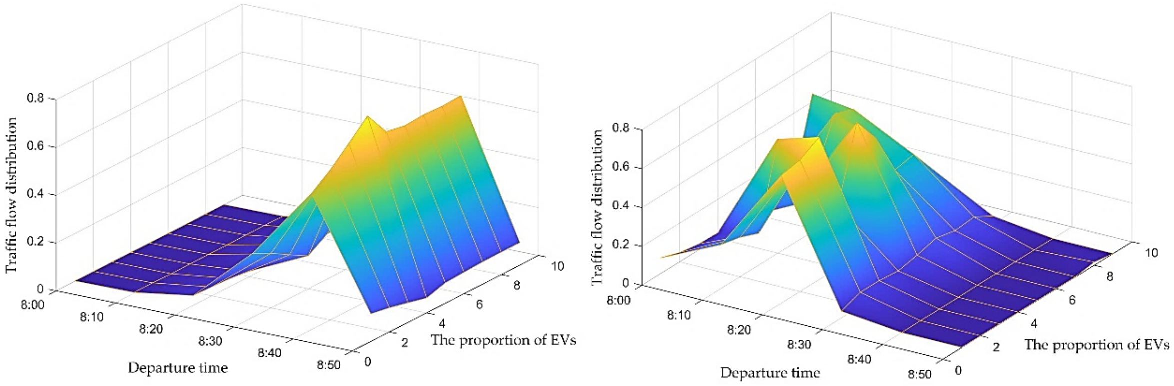

(a) departure time selection of electric vehicles (b) departure time selection of fuel vehicles

Fig. 3 Choice of departure times of fuel vehicles and electric vehicles

4. Discussion

In previous research, the stochastic user equilibrium (SUE) model is used to characterize travelers' path selection behavior without considering the time-varying nature of the dynamic road network or departure time selection. To compare the effects of the SUE and DUE models, a comparative analysis is conducted. By comparing the number of charging piles (Fig. 4), the vacancy rate, and network travel time under the DUE and SUE models, it can be seen that the DUE model describes traveler behavior more realistically and yields a more plausible charging station planning result.

Upon comparing the results of the DUE and SUE models, it was found that there was no significant difference in the total number of charging stations between the two models. However, as the electric vehicle penetration rate increased, the trend in the number of charging stations varied significantly between the two models. While the SUE model showed a decline in the number of charging stations with the rise in the EV penetration rate, the DUE model exhibited a gradual increase until the 60 % threshold, reaching its peak at 70 % adoption before decreasing. The results show that the DUE model, after considering the effects of departure time selection and dynamic traffic flow assignment on route selection and charging station queuing, yields a more practically relevant charging station planning scheme.

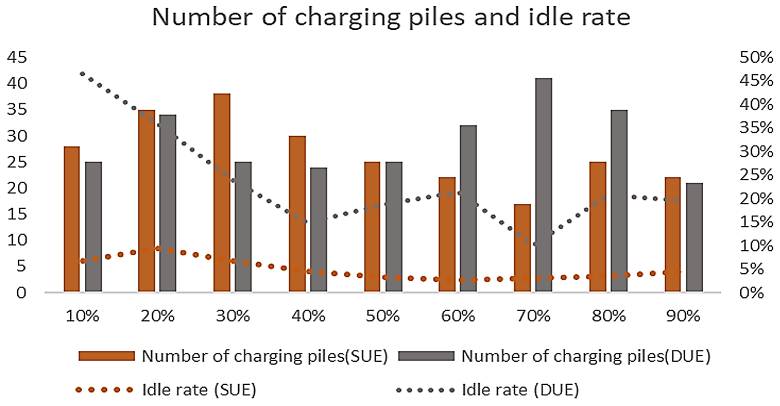

Fig. 4 Optimization results of charging pile number and idle rate

Moreover, a comparison of Fig. 5 shows that the total road network travel time derived from the DUE model is much lower than that derived from the SUE model under any EV penetration rate. However, the vacancy rate of the SUE model is much lower than that of the DUE model. This indicates that in the DUE model, electric vehicle users and fuel vehicle users depart in different time periods because travelers can choose their departure times and different types of travelers have different travel utilities. Under cost constraints, the DUE model significantly reduces the travel time of the road network at the expense of more charging piles and vacancy rates of 10-20 %.

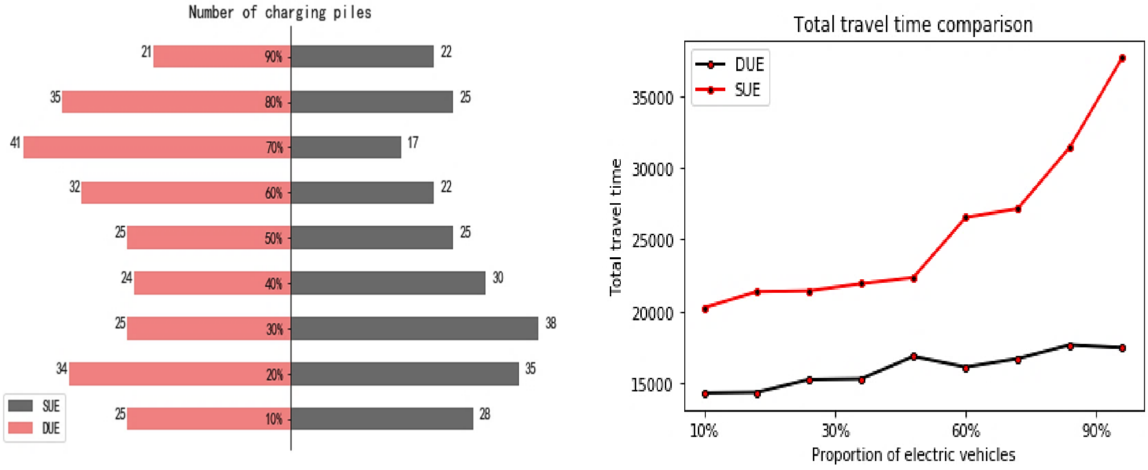

Fig. 5 Comparative analysis of DUE and SUE model results

5. Conclusion

This paper constructs impedance functions for electric and fuel vehicles by considering travel time, energy consumption, charging service, and waiting time. It combines dynamic traffic flow distribution with charging station site selection to create a two-level programming model. By balancing overall and individual optimization, the charging station layout can achieve high traffic efficiency for the overall road network while maximizing individual travel utility. Dynamic user equilibrium theory is used in charging station layout planning to establish a traffic flow allocation model and a solution algorithm for simultaneous departure time and travel path selection, and numerical simulations demonstrate the validity and practicability of the model and algorithm.

The results show the following: (1) High traffic network efficiency does not require adding more charging piles. Optimizing the charging station layout can achieve greater road network efficiency with fewer piles, and the layout significantly impacts road network traffic flow distribution and efficiency. (2) The simulation results are consistent with expected utility theory and stochastic user equilibrium. When the proportion of electric vehicles is low, travel time affects route selection more; when it is high, the number of charging stations matters more. (3) During the morning rush hour, fuel vehicles mainly depart at 8:30-8:40, while electric vehicles do so at 8:10-8:20, validating the effectiveness of the designed departure-time selection utility function.

Constrained by computational complexity and data availability, this study conducts numerical experiments on a 9-node illustrative network to validate the theoretical soundness and algorithmic feasibility of the proposed model. Notably, the scalability of the approach to large-scale networks with hundreds or thousands of nodes requires further investigation. As network size expands, computational complexity increases drastically, primarily stemming from three core factors: the exponential growth of path enumeration, the scaling of the lower-level MSA-based DUE traffic assignment process with the number of nodes, links, and time intervals, and the nested genetic algorithm structure in the upper level—whose time complexity rises significantly with population size and the number of iterations.

Given these challenges, the current implementation is most suitable for strategic planning in medium-sized networks (e.g., up to 50-100 nodes). However, these limitations are not insurmountable. By integrating well-established large-scale optimization techniques—such as path-set reduction methods (e.g., column generation or k-shortest path algorithms), parallel computing, network aggregation strategies, and more efficient metaheuristics (e.g., particle swarm optimization)—the model can be enhanced to maintain acceptable solution quality and computational efficiency when handling large-scale networks. Regarding solution quality, while genetic algorithms are adept at finding near-optimal solutions, global optimality cannot be guaranteed; in large-scale networks, solution quality will be highly dependent on parameter tuning and convergence criteria.

Therefore, future research should test the model on real-world networks (e.g., city-scale networks) using high-performance computing and compare its results with those of other metaheuristics or commercial solvers to systematically evaluate its scalability and solution quality. Such research based on real data will hold significant practical value, with the potential to optimize network traffic efficiency and driving experiences. At the practical application level, administrative authorities can dynamically adjust the service availability and operational strategies of charging stations based on the proportion of electric vehicles on different routes.

Another important consideration for practical application is demand uncertainty. In this study, both the total OD demand D_w and the EV penetration rate are treated as deterministic inputs. However, in reality, these factors may fluctuate from day to day due to various reasons such as special events, weather conditions, or seasonal variations. Under demand uncertainty, the optimal station locations derived from a deterministic model may not perform consistently across all scenarios. High-demand days could lead to severe congestion at certain stations, while low-demand days might result in underutilized infrastructure.

Future research should extend the current framework to account for demand uncertainty. Possible approaches include (1) scenario-based stochastic programming, where multiple demand scenarios are defined with associated probabilities and the objective is to minimize expected total travel time; (2) robust optimization, which seeks locations that perform well under worst-case demand realizations; and (3) sensitivity analysis to evaluate the robustness of deterministic solutions under demand perturbations. Incorporating these methods would enhance the model's applicability to real-world planning, where demand variability is inevitable.

For practical planning of fast charging stations, planners can determine the weight allocation of travel time and construction/operation costs according to the regional traffic development goals and fiscal budget capacity. For traffic-congested urban core areas, the weight of travel time minimization should be appropriately increased (with a moderate relaxation of the cost budget) to deploy charging piles at key traffic nodes and disperse charging demand; for suburban areas or regions with tight fiscal budgets, the weight of cost control should be prioritized to optimize the layout of charging stations at high-demand nodes to achieve cost-effective resource allocation. In specific operation, the weight can be quantified by calibrating the unit travel time delay cost coefficient based on regional traffic survey data and local fiscal expenditure standards for charging infrastructure, to make the weight setting more in line with the actual development needs.

References

[1] Liu, T. (2024). Time-varying influence of policy risk on carbon emissions analysis, *Journal of Service, Innovation and Sustainable Development*, Vol. 5, No. 2, 95-115, doi: 10.33168/SISD.2024.0206.

[2] Türkeş, M., Acatrinei, C. (2024). The effect of drivers and barriers on electric vehicle usage in Romania: Findings from PLS-SEM and MGA, *Economic Computation and Economic Cybernetics Studies and Research*, Vol. 58, No. 4, 195-209, doi: 10.24818/18423264/58.4.24.12.

[3] Yang, X., Xiang, K., Yuan, S., Huang, J. (2024). Vehicle driving behavior recognition and optimization strategies based on cloud computing and SSA-BP algorithm, *Studies in Informatics and Control*, Vol. 33, No. 3, 17-28, doi: 10.24846/v33i3y202402.

[4] Qian, Z., Yi, Z., Zhong, W., Yue, H., Yaojia, S. (2021). Siting and sizing of electric vehicle fast-charging station based on quasi-dynamic traffic flow, *IET Renewable Power Generation*, Vol. 15, No. 18, 4204-4214, doi: 10.1049/iet-rpg.2020.0439.

[5] Vijūnė, J. (2023). Identification of strategic directions for change management in social services sector, *Journal of Service, Innovation and Sustainable Development*, Vol. 4, No. 2, 91-105, doi: 10.33168/SISD.2023.0208.

[6] Li, S., Huang, Y., Mason, S.J. (2016). A multi-period optimization model for the deployment of public electric vehicle charging stations on network, *Transportation Research Part C: Emerging Technologies*, Vol. 65, 128-143, doi: 10.1016/j.trc.2016.01.008.

[7] Vazifeh, M.M., Zhang, H., Santi, P., Ratti, C. (2019). Optimizing the deployment of electric vehicle charging stations using pervasive mobility data, *Transportation Research Part A: Policy and Practice*, Vol. 121, 75-91, doi: 10.1016/j.tra.2019.01.002.

[8] Sarnvanichpitak, T., Mangmeechai, A. (2024). Regional differences in car sharing adoption: Integrating TAM and TPB in Bangkok and Eastern Economic Corridor, Thailand, *Journal of Logistics, Informatics and Service Science*, Vol. 11, No. 12, 71-89, doi: 10.33168/JLISS.2024.1204.

[9] Dong, G., Ma, J., Wei, R., Haycox, J. (2019). Electric vehicle charging point placement optimisation by exploiting spatial statistics and maximal coverage location models, *Transportation Research Part D: Transport and Environment*, Vol. 67, 77-88, doi: 10.1016/j.trd.2018.11.005.

[10] Bhanu, M., Priya, S., Moreira, J.M., Chandra, J. (2023). ST-AGP: Spatio-temporal aggregator predictor model for multi-step taxi-demand prediction in cities, *Applied Intelligence*, Vol. 53, No. 2, 2110-2132, doi: 10.1007/s10489-022-03475-7.

[11] Tang, M., Cao, J., Fan, Z., Gong, D., Xue, G. (2024). Public perceptions of EV charging infrastructure: A combined sentiment analysis and topic modeling approach, *Studies in Informatics and Control*, Vol. 33, No. 2, 59-72, doi: 10.24846/v33i2y202406.

[12] Xia, T., Zhan, S., Xu, J., Ren, X. (2024). An electric vehicle charging control system using LSTM encoding-GRU decoding, *Tehnički Vjesnik – Technical Gazette*, Vol. 31, No. 5, 1530-1535, doi: 10.17559/TV-20230708000789.

[13] Huang, Y., Li, T., Wang, X., Wu, B. (2024). A consumer expectation-based multiple satisfaction model for battery swapping station deployment, *Economic Computation and Economic Cybernetics Studies and Research*, Vol. 58, No. 3, 193-209, doi: 10.24818/18423264/58.3.24.12.

[14] Mounce, R., Carey, M. (2011). Route swapping in dynamic traffic networks, *Transportation Research Part B: Methodological*, Vol. 45, No. 1, 102-111, doi: 10.1016/j.trb.2010.05.005.

[15] Zhu, Z., Zhu, S., Sun, L., Mardan, A. (2024). Modelling changes in travel behaviour mechanisms through a high-order hidden Markov model, *Transportmetrica A: Transport Science*, Vol. 20, No. 1, 1-27, doi: 10.1080/23249935.2022.2130731.

[16] Suryani, E., Hendrawan, R.A., Adipraja, P.F.E., Indraswari, R. (2020). System dynamics simulation model for urban transportation planning: A case study, *International Journal of Simulation Modelling*, Vol. 19, No. 1, 5-16, doi: 10.2507/IJSIMM19-1-493.

[17] Tian, L., Yang, Q., Huang, H., Lü, C. (2016). The cumulative prospect theory-based travel mode choice model and its empirical verification, *Systems Engineering – Theory & Practice*, Vol. 36, No. 7, 1778-1785, doi: 10.12011/1000-6788(2016)07-1778-08.

[18] Wang, X., Shahidehpour, M., Jiang, C., Li, Z. (2019). Coordinated planning strategy for electric vehicle charging stations and coupled traffic-electric networks, *IEEE Transactions on Power Systems*, Vol. 34, No. 1, 268-279, doi: 10.1109/TPWRS.2018.2867176.

[19] Zhou, Z., Zhang, X., Guo, Q., Sun, H. (2021). Analyzing power and dynamic traffic flows in coupled power and transportation networks, *Renewable and Sustainable Energy Reviews*, Vol. 135, Article No. 110083, doi: 10.1016/j.rser.2020.110083.

[20] Xu, M., Yang, H., Wang, S. (2020). Mitigate the range anxiety: Siting battery charging stations for electric vehicle drivers, *Transportation Research Part C: Emerging Technologies*, Vol. 114, 164-188, doi: 10.1016/j.trc.2020.02.001.

[21] Riemann, R., Wang, D.Z.W., Busch, F. (2015). Optimal location of wireless charging facilities for electric vehicles: Flow-capturing location model with stochastic user equilibrium, *Transportation Research Part C: Emerging Technologies*, Vol. 58, Part A, 1-12, doi: 10.1016/j.trc.2015.06.022.

[22] Zheng, H., He, X., Li, Y., Peeta, S. (2017). Traffic equilibrium and charging facility locations for electric vehicles, *Networks and Spatial Economics*, Vol. 17, No. 2, 435-457, doi: 10.1007/s11067-016-9332-z.

[23] Kurnia, A., Oktavia, T. (2024). A multi-criteria decision approach for optimized route planning in retail distribution, *Journal of Logistics, Informatics and Service Science*, Vol. 11, No. 9, 37-53, doi: 10.33168/JLISS.2024.0903.

[24] Sun, H., Zhang, X., Li, D., Tan, J. (2024). Research on intelligent traffic congestion degree collaborative algorithm and path planning based on sensor data, *Tehnički Vjesnik – Technical Gazette*, Vol. 31, No. 4, 1154-1162, doi: 10.17559/TV-20240227001353.

[25] Wang, D.L., Ding, A., Chen, G.L., Zhang, L. (2023). A combined genetic algorithm and A* search algorithm for the electric vehicle routing problem with time windows, *Advances in Production Engineering & Management*, Vol. 18, No. 4, 403-416, doi: 10.14743/apem2023.4.481.

[26] Huang, A.Q., Zhang, Y.Q., He, Z.F., Hua, G.W., Shi, X.L. (2021). Recharging and transportation scheduling for electric vehicle battery under the swapping mode, *Advances in Production Engineering & Management*, Vol. 16, No. 3, 359-371, doi: 10.14743/apem2021.3.406.

[27] Tang, M.C., Cao, J., Gong, D.Q., Xue, G., Khoa, B.T. (2024). Simulation modelling of electric vehicle charging recommendations based on Q-learning, *International Journal of Simulation Modelling*, Vol. 23, No. 3, 495-506, doi: 10.2507/IJSIMM23-3-CO11.

[28] Can, C., Kilic, F., Kaya, Y. (2025). A novel approach for location planning of fast-charging stations for e-buses, *International Journal of Simulation Modelling*, Vol. 24, No. 2, 213-224, doi: 10.2507/IJSIMM24-2-714.

[29] Ben-Akiva, M.E., Lerman, S.R. (1985). *Discrete choice analysis: Theory and application to travel demand*, MIT Press, Cambridge, Massachusetts, USA.

[30] Kahneman, D., Tversky, A. (1979). Prospect theory: An analysis of decision under risk, *Econometrica*, Vol. 47, No. 2, 263-291, doi: 10.2307/1914185.

APEM journal
Advances in Production Engineering & Management
Volume 21 | Number 1 | March 2026 | pp 89–100
https://doi.org/10.14743/apem2026.1.563
ISSN 1854-6250
Journal home: apem-journal.org
Original scientific paper

Condition-based maintenance optimization for multi-component systems in mass production considering customer satisfaction

Zivlak, N.[a], **Dong, M.**[b], **Lalic, B.**[a], **Yun, F.Z.**[c], **Liu, Q.M.**[c,*]

[a]Department of Industrial Engineering and Management, Faculty of Technical Sciences, University of Novi Sad, Serbia
[b]Department of Operations Management, Antai College of Economics and Management, Shanghai Jiao Tong University, P.R. China
[c]Department of Industrial Engineering, Business School, University of Shanghai for Science and Technology, P.R. China

ABSTRACT

When multiple orders with different requirements must be fulfilled under limited capacity, order selection and maintenance planning for multi-component systems become strongly interdependent. To address this problem, this study proposes a condition-based maintenance strategy for multi-component systems and a joint optimization model for multi-order batch production that incorporates customer satisfaction. First, the deterioration trend of each component is described using the proportional hazards model, and the health status of each component is represented by virtual age. Different maintenance modes are then determined according to real-time monitoring results and maintenance thresholds after the completion of each production batch. With profit maximization as the objective, the condition-based maintenance strategy is integrated with a capacitated batch production model and a customer satisfaction model to develop a joint optimization framework for maintenance and multi-order production. Finally, the model is solved using simulated annealing and particle swarm optimization. A case study is used to verify the effectiveness of the proposed approach and to demonstrate its practical relevance, and a sensitivity analysis of the key model parameters is also conducted.

ARTICLE INFO

Keywords:
Condition-based maintenance;
Multi-component systems;
Batch production;
Maintenance optimization;
Proportional hazards model;
Customer satisfaction;
Particle swarm optimization;
Simulated annealing

**Corresponding author:*
lqm0531@163.com
(Liu, Q.M.)

Article history:
Received 19 January 2026
Revised 17 March 2026
Accepted 23 March 2026

1. Introduction

To ensure the economic benefits of an enterprise, it is necessary to consider not only internal operational factors but also external market factors. Therefore, how to incorporate external market factors into basic production and maintenance strategies so that the enterprise can develop more effectively has become an important research focus. Traditional single-component systems have gradually evolved into multi-component systems with complex structures. Therefore, determining an appropriate maintenance method can effectively reduce costs [1]. This paper proposes a condition-based maintenance strategy model for multi-component systems based on customer satisfaction under limited production capacity.

At present, mass production is one of the most important production modes in the manufacturing industry, and there is extensive related research in this area. Huang *et al.* [2] combined the system scheduling problem, considering the completion time of batch production, with the preventive maintenance problem of a system, and built a model with completion time as the objective function. Tambe *et al.* [3] developed inspection, production, and maintenance schedules during mass production to achieve the lowest total cost per unit. Hnaien *et al.* [4] studied the mass production and preventive maintenance scheduling problem for a single machine producing multiple products and proposed a mixed-integer linear programming model with total cost as the objective function. Fitouhi *et al.* [5] combined preventive maintenance with tactical production planning and proposed a model to solve the mass production problem within a finite planning period. Lai *et al.* [6] proposed an optimal decision method for determining production lot size under a defined maintenance policy, considering imperfect manufacturing and emergency maintenance policies. Hadian *et al.* [7] considered mass production systems with stochastic degradation over time and proposed a maintenance strategy based on the predicted failure probability of each machine. Bouabid *et al.* [8] proposed an integrated production planning and preventive maintenance for manufacturing systems prone to quality degradation. Selech *et al.* [9] presented the results of reliability analysis and the corrective maintenance costs of one of the most expensive tram components to repair.

By analysing the failure mechanism and the results of equipment testing, condition-based maintenance (CBM) can avoid functional failures by repairing, adjusting, or replacing equipment when potential failures occur. Equipment can be divided into single-component systems and multi-component systems. Studies related to single-component systems have focused on the influence of external factors on maintenance decisions. Duan *et al.* [10] proposed a situational repair strategy for ship pumps under random repair quality conditions when there was a competing risk. Zhang *et al.* [11] and Zheng *et al.* [12-13] considered the impact of spare parts ordering and spare parts inventory on the development of a condition-based maintenance strategy. Zheng *et al.* [14] considered a condition-based maintenance strategy under a service performance contract. For multi-component systems, Yousefi *et al.* [15] portrayed multiple failure processes experienced by each component due to degradation and shock loading and developed models to determine the state failure thresholds and detection intervals for a multi-component system. Broek *et al.* [16] modelled system planning as a Markov decision process to study the condition-based maintenance strategy for a two-component system with economic dependence under load sharing. Wang *et al.* [17] proposed a condition-based preventive maintenance for systems with identical component equilibria. Xu *et al.* [18] used a non-homogeneous stochastic process model to emphasize the economic dependence between components and stochastic dependencies. Shi *et al.* [19] used a rolling-level method to develop a state-based maintenance decision framework for a multi-component system to meet the reliability requirements of the system.

Most research on maintenance of mass production equipment has focused on traditional corrective or periodic maintenance. As a maintenance strategy proposed in recent years, condition-based maintenance has become a preferred approach in equipment maintenance decision-making with the gradual improvement of sensing and detection technologies. However, because of its relatively short development history, few studies have applied it to mass production equipment.

Customer satisfaction has attracted extensive attention from scholars in recent years. Most of these studies quantified customer satisfaction in a specific aspect in terms of penalty cost. Liu *et al.* [20] proposed the concept of a delivery time window and constructed an early/delay penalty cost affiliation function. Iskandar *et al.* [21] considered the actual losses of port equipment and damaged parts due to maintenance overruns and transformed them into penalty costs. Nezami *et al.* [22] examined the effects of several different maintenance methods on extending equipment life and increasing satisfaction. Ruan *et al.* [23] added customer satisfaction to the total warranty cost and proposed various flexible preventive maintenance strategies.

In this paper, to address the problem of order selection and maintenance decision-making for a multi-component system when multiple orders with different requirements are placed under limited capacity, a joint optimization model of a CBM strategy for a multi-component system based on customer satisfaction and multi-order batch production is proposed. First, the specific deterioration trend of each component is described using the proportional hazards model, and the health status of each component is represented by virtual age. Then, different maintenance methods are determined according to the real-time monitoring results and maintenance thresholds after the end of each production batch. Finally, with profit maximization as the optimization goal, the CBM strategy and the joint optimization model for multi-order batch production are established by combining the limited-capacity batch problem model and the customer satisfaction model.

This study aims to develop a more effective condition-based maintenance optimization model for multi-component systems under mass production conditions. The remainder of this paper is organized as follows. The problem is described in Subsection 2.1, and a new deterioration model is developed in Subsection 2.3. Section 3 proposes a novel condition-based maintenance model for a multi-component system. Moreover, the joint optimization model of the maintenance strategy and multi-order batch production is presented in Section 4. A case study is also analysed and discussed in Section 5, and conclusions are drawn in Section 6.

2. Multi-component system deterioration model

Assume that within a certain period $[0, T_x]$ (Total production time T_x), the enterprise receives s orders with different requirements, and each order completed can obtain corresponding revenue according to the order volume. A large multi-component system in an enterprise can be produced at the rate of p pieces per day. During the production process, the components will gradually deteriorate, and the product quality will also decline. The maintenance actions will restore the status of a system, but it will also generate maintenance costs. If the repair is not timely, it will lead to frequent system failures and an increase in the unqualified rate of products, thus the order cannot be completed as required, resulting in a decrease in customer satisfaction and penalty costs, and the production and storage of products will generate corresponding production costs and inventory costs. Thus, this paper establishes a condition-based maintenance strategy model with the maximum profit of the enterprise as the optimization objective to determine the order selection and ordering, production batch size and maintenance strategy.

Consider a large multi-component production system in which each component is independent, but failure of any one component during operation causes failure of the entire system. In practice, different components fail for different reasons. For example, external parts of a system may corrode because of environmental humidity or temperature changes, whereas internal processing parts may wear because of overload operation or delayed maintenance. Therefore, before condition-based maintenance is carried out, it is necessary to consider both the failure causes and the current deterioration status of each component. Because it is difficult to combine these two aspects to construct an effective quantitative relationship, the proportional hazards model is selected to directly establish the functional relationship between the failure probability of a component and its influencing factors.

The risk function is used to describe the $t + \Delta t, \Delta t \to 0$ probability of t failure of components j at any time without failure. Its function expression is:

$$h_j(t) = \lim_{\Delta t \to 0} P\{N_j(t + \Delta t) - N_j(t)=1\} \tag{1}$$

where, $N_j(t)$ represents the number of failures of component j at time t.

The function expression of the proportional risk model is:

$$h_j(t, X) = h_0(t) \cdot \exp\left(\sum_{i=1}^{n} \alpha_{i,j} X_{i,j}\right) \tag{2}$$

where $X_{i,j}$ represents i-th covariate (influence factor) related to j-th component, $\alpha_{i,j}$ is the regression coefficient corresponding to the i-th covariate, and $h_0(t)$ is the basic risk function.

The Weibull distribution can effectively describe the deterioration law of components. If the basic risk function $h_0(t)$ follows a Weibull distribution, substituting it into Eq. 2 yields the Weibull proportional risk model for component j:

$$h_j(t,X)=\frac{\beta}{\eta}\left(\frac{t}{\eta}\right)^{\beta-1}\exp\left(\sum_{i=1}^{n}\alpha_{i,j}X_{i,j}\right) \tag{3}$$

where, the shape parameters $\beta>1$ and scale parameters $\eta>1$, as well as the covariate coefficients $0<\alpha<1$ can be obtained by constructing the likelihood function, and then using the Newton-Laphson method to estimate the parameters.

3. Condition-based maintenance model for multi-component systems

Condition-based maintenance based on system health status is more economical and effective than single post maintenance and periodic maintenance. When formulating condition-based maintenance strategy, the degree of old and new system components should be considered, which is generally characterized by age [24]. Since the status of each component cannot be obtained in real time during the batch production process, it is necessary to detect after the batch production is completed, and determine the maintenance method in combination with the maintenance threshold. Different maintenance methods will cause the system age to fall back to different degrees, so the virtual age is introduced to more simulate the status change of each component. The current age of component j is $A_j(t)$, and the failure rate of component j is as follows.

$$F\left(A_j(t)\right)=\int_0^{A_j(t)}h_j(t,X)dt=\left(\frac{A_j(t)}{\eta}\right)^{\beta}\exp\left(\sum_{i=1}^{n}\alpha_{i,j}X_{i,j}\right) \tag{4}$$

The CBM strategy in this paper includes preventive maintenance, component replacement, minor maintenance, and opportunistic maintenance. In actual maintenance, preventive maintenance and opportunistic maintenance do not restore a component to an as-new state. The age of component j in the new state is $A_{j,0}=0$, the duration of a single batch production is T, the preventive maintenance threshold is V, and the effectiveness of the n-th repair is denoted by θ. Thus, the virtual age of component j after the end of the n-th batch production can be obtained as follows.

$$A_{j,n}=(1-\theta)A_{j,n-1}+T\exp\left(\sum_{i=1}^{n}\alpha_{i,j}X_{i,j}\right) \tag{5}$$

Preventive maintenance is performed if $A_{j,n}>V$. Solving the above recursive relationship yields the following closed-form expression.

$$\begin{aligned}A_{j,n}&=(1-\theta)^nA_{j,0}+\frac{1-(1-\theta)^n}{\theta}T\exp\left(\sum_{i=1}^{n}\alpha_{i,j}X_{i,j}\right)\\&=\frac{1-(1-\theta)^n}{\theta}T\exp\left(\sum_{i=1}^{n}\alpha_{i,j}X_{i,j}\right)\end{aligned} \tag{6}$$

Because product quality is positively correlated with system deterioration, the number of defective products produced by a system increases as deterioration accelerates due to imperfect maintenance. The functional relationship between the defective rate and virtual age is given as follows:

$$p\big(A_n(t)\big)=p_0+\mu\left(1-\exp\left(-\lambda\left(\frac{\sum_{j=1}^{l}A_{j,n}(t)}{l}\right)^{\gamma}\right)\right) \tag{7}$$

where p_0 is the initial defective rate of a system under the new condition, μ is the boundary value of quality deterioration, λ and γ are given constants. Considering that different orders have different requirements for the defective rate, this paper sets up a quality replacement threshold W to control the product quality. When $p\left(A_{j,n}(t)\right)>W$ after the n-th batch production is completed, the component j will be replaced and restored to a new state.

Opportunistic maintenance refers to the simultaneous repair of two components to improve maintenance economy. At the end of the n-th batch production, suppose that the virtual age of component j is $A_{n,j} \geq V$, while the virtual age of component l is $A_{n,l} < V$ and satisfies $V - A_{n,l} \leq \Delta V$. Here, ΔV denotes the opportunistic maintenance threshold, and the interval $[V - \Delta V, V]$ defines the opportunistic maintenance window. After each batch production, components that have not yet reached the preventive maintenance threshold but whose virtual ages fall within this window are repaired in advance; otherwise, they are not repaired.

During mass production, the system may shut down because of sudden failure. In this case, minor repair is performed without changing the virtual age of each component in the system and without considering maintenance time. The number of sudden failures of component j in the n-th production batch is given as follows.

$$\begin{aligned} \psi_{n,j} &= \int_0^T \frac{1-(1-\theta)^n}{\theta} h_{n,j}(t,X)\ dt = \frac{1-(1-\theta)^n}{\theta} \int_0^T \frac{\beta}{\eta}\left(\frac{t}{\eta}\right)^{\beta-1} \exp\left(\sum_{i=1}^{n} \alpha_{i,j} X_{i,j}\right) dt \\ &= \frac{1-(1-\theta)^n}{\theta} \cdot \exp\left(\sum_{i=1}^{n} \alpha_{i,j} X_{i,j}\right) \cdot \left(\frac{T}{\eta}\right)^{\beta} \end{aligned} \tag{8}$$

4. Joint optimization model of maintenance strategy and multi-order batch production

4.1 Capacitated lot-sizing problem (CLSP) model

The CLSP model is used to solve the problem of batch production decisions under limited capacity and resource conditions. Different mathematical models can be developed based on different influencing factors. In this paper, enterprise costs are divided into maintenance costs, production costs, and inventory costs. Accordingly, the CLSP model is defined as follows.

$$C_{CLSP} = \sum_{n=1}^{N} \sum_{j=1}^{m} MC_{n,j} + \sum_{n=1}^{N} (PC_n + IC_n) \tag{9}$$

$$T = T_1 = T_2 = \ldots = T_n \tag{10}$$

$$\sum_{n=1}^{N} t_{M,n} + t_{P,n} \leq t_{total} \tag{11}$$

$$\sum_{r=1}^{S} O_r \leq \sum_{n=1}^{N} pT_n \tag{12}$$

In Eq. 9, $1 \leq N < T_x/Q$ is the total number of production cycles, and $m \geq 3$ denotes the number of components. Eq. 10 represents the characteristic of equal batch production time length, and T is the single batch production time length. Eq. 11 is the constraint of the total production duration under limited capacity, $t_{M,n}$ and $t_{P,n}$ is the maintenance duration and production duration of the n-th production cycle, respectively. Eq. 12 is the balance constraint between the total order quantity and the total capacity, and Q_r is the order quantity of r-th order.

System maintenance cost $MC_{n,j}$

According to the maintenance strategy in Section 2, all components of a system are tested after the end of n-th batch production to calculate the corresponding virtual age, and compared with the preventive maintenance threshold V, component replacement threshold W and opportunity maintenance threshold ΔV to determine the maintenance actions. The maintenance effect of opportunity maintenance is the same as that of preventive maintenance, but in a complex large system, downtime maintenance includes inspection, disassembly, and system shutdown and restart. Thus, in this paper, opportunity maintenance is defined as more economical preventive maintenance. Record the maintenance cost per unit day of preventive maintenance, component replacement and opportunity maintenance as mc_1, mc_2, mc_3 and the maintenance time as t_{mc_1}, t_{mc_2}, t_{mc_3} ($mc_3 < mc_1 < mc_2$, $t_{mc_1} = t_{mc_3} < t_{mc_2}$), respectively. The minor repair cost is mc_4, and the n-th maintenance cost for a system can be obtained.

$$MC_{n,j} = \psi_{n,j} \cdot mc_4 + \sum_{k=1}^{3} mc_k \cdot t_{mc_k} \cdot \chi(A_k) \tag{13}$$

The three maintenance actions are mutually exclusive. Therefore, an indicator function $\chi(A_k)$ is introduced in Eq. 13.

$$\chi(A_i) = \begin{cases} 1\,, A_i \text{ occur} \\ 0\,, A_i \text{ does not occur} \end{cases} \tag{14}$$

Production costs PC_n

The production speed of a system is P per day, and the duration of a single batch production is T days. The production cost of a single product is denoted by *pc*, and the production cost of the n-th batch production is as follows.

$$PC_n = PTpc \tag{15}$$

Inventory cost IC_n

Based on the assumptions of this paper, products currently in batch production are not included in inventory. Therefore, the inventory cost generated in the n-th batch depends on the total number of products I_{n-1} produced in the previous production cycle $n-1$. The inventory cost generated during the n-th maintenance activity is related to the total number of products $I_n = I_{n-1} + PT$ produced in *n* previous production. Let the inventory cost of a single product be denoted by ic. The inventory cost in the n-th production cycle is then given as follows.

$$IC_n = ic\left(I_{n-1}T + I_n t_{mc_k}\right) \tag{16}$$

If the order delivery $(0 < t < T)$ occurs during batch production and the order quantity is Q_r, then

$$IC_n = ic\left(I_{n-1}t + (I_{n-1} - O_r)(T - t) + t_{mc_k}(I_n - O_r)\right) \tag{17}$$

If the order delivery $(T < t < T + t_{mc_k})$ occurs during the repair process, then

$$IC_n = ic\left(I_{n-1}T + I_n(t - T) + (I_n - O_r)\left(T + t_{mc_k} - t\right)\right) \tag{18}$$

4.2 Customer satisfaction model

In this paper, customer satisfaction is related to order delivery time and product quality. The requirement of r-th order is $Q_r(q_r, t_r)$, where Q_r is the order demand, and q_r and t_r are the quality and delivery time requirements, respectively. For $t = t_r$, if the system is in the n-th batch production stage or in the n-th maintenance stage, the product inventory I_n, the number of defective products DI_n, and the defective rate p before delivery are given as follows, respectively.

$$\begin{cases} \begin{cases} I_n(t_r)^- = I_{n-1} + pT \\ DI_n(t_r)^- = DI_{n-1} + p\left(A_{j,n}(T)\right)PT \quad n - \text{th batch production} \\ p_{t_r}{}^- = DI_n(t_r)^-/I_n(t_r)^- \end{cases} \\ \begin{cases} I_n(t_r)^- = I_{n-1} \\ DI_n(t_r)^- = DI_{n-1} + p\left(A_{j,n}(t_r)\right)Pt_r \quad n - \text{th maintenance} \\ p_{t_r}{}^- = DI_n(t_r)^-/I_n(t_r)^- \end{cases} \end{cases} \tag{19}$$

The remaining inventory, defective products, and defective rate after delivery can be divided into two cases: the inventory satisfies the order demand, and the inventory is insufficient.

$$\begin{cases} \left.\begin{cases} I_n(t_r)^+ = I_n(t_r)^- - O_r \\ \begin{cases} DI_n(t_r)^+ = DI_n(t_r)^- - O_r q_r \\ p_{t_r}{}^+ = DI_n(t_r)^+/I_n(t_r)^+ \end{cases} \text{ if } DI_n(t_r)^- > O_r q_r \\ \begin{cases} DI_n(t_r)^+ = 0 \\ p_{t_r}{}^+ = 0 \end{cases} \text{ if } DI_n(t_r)^- < O_r q_r \end{cases}\right\} \text{ if } I_n(t_r)^- > O_r \\ \left.\begin{cases} I_n(t_r)^+ = 0 \\ DI_n(t_r)^+ = 0 \\ p_{t_r}{}^+ = 0 \end{cases}\right\} \text{ if } I_n(t_r)^- < O_r \end{cases} \tag{20}$$

If the quantity of products in the inventory does not meet the order demand or the defective rate is greater than the quality requirement when the delivery time arrives, the time penalty cost TPC_r and quality penalty cost QPC_r will be obtained.

$$\begin{cases} \begin{cases} TPC_r = tpc\left(\dfrac{O_r - I_n(t_r)}{O_r}\right) & \text{if } I_n(t_r) < O_r \\ TPC_r = 0 & \text{if } I_n(t_r) \geq O_r \end{cases} \\ \begin{cases} QPC_r = qpc\left(\dfrac{p_{t_r} - q_r}{q_r}\right) & \text{if } p_{t_r} > q_r \\ QPC_r = 0 & \text{if } p_{t_r} \leq q_r \end{cases} \end{cases} \tag{21}$$

Here, TPC and QPC are the time and quality penalty coefficients, respectively. Thus, the customer satisfaction model is as follows.

$$C_{sat} = \sum_{r=1}^{s} TPC_r + QPC_r \tag{22}$$

The total cost model: $\max D = C_{CLSP} + C_{sat}$. The revenue of an enterprise during a given period depends on the number of completed orders. Insufficient order acceptance results in idle system capacity and wasted productivity. However, accepting too many orders not only leads to high maintenance costs caused by excessive system use and deterioration, but may also prevent the enterprise from completing orders with the required quality and quantity, leading to lower customer satisfaction and even compensation. Therefore, this paper constructs a total profit model in which the batch production size Q, the preventive maintenance threshold V, the component replacement threshold W, and the opportunity maintenance threshold ΔV are taken as decision variables. The maximum enterprise profit under different orders within the planning time period $[0, T_x]$ is used as the overall optimization objective to determine the optimal order selection, production sequence, and corresponding decision-variable values. The income from the production of a single product is x, and the joint model is as follows.

$$\begin{aligned} \max C &= \max\left(x\sum_{r=1}^{s} O_r - C_{CLSP} - C_{sat}\right) \\ &= \max\left(x\sum_{r=1}^{s} O_r - \left(\sum_{n=1}^{N}\sum_{j=1}^{m} MC_{n,j} + \sum_{n=1}^{N}(PC_n + IC_n)\right) - \left(\sum_{r=1}^{s} TPC_r + QPC_r\right)\right) \end{aligned} \tag{23}$$

$$T = T_1 = T_2 = \ldots = T_n \tag{24}$$

$$\sum_{n=1}^{N} t_{M,n} + t_{P,n} \leq t_{total} \tag{25}$$

$$\sum_{r=1}^{s} O_r \leq \sum_{n=1}^{N} pT_n \tag{26}$$

4.3 Model solving

To solve the model, it is necessary to select and sequence a given number of orders with different requirements. Therefore, the model can be regarded as a combinatorial optimization problem combining the knapsack problem and the traveling salesman problem. Considering that order selection needs to satisfy the constraints of Eq. 26, and for computational convenience and efficiency, this paper uses an enumeration method for order selection and a simulated annealing algorithm (SA) for sequencing. After the number and order of the selected orders are determined, the particle swarm optimization algorithm (PSO) is used to obtain the maximum value of the model under the given conditions. To ensure search efficiency and model convergence, the domain of the decision variables is first determined based on experience and a small number of Monte Carlo simulation results, and then a sufficient number of iterations is set to ensure that the global optimum of the model can be found. The specific algorithm steps are as follows.

Step 1. Initialize the SA parameters and PSO parameters: initial temperature T, maximum number of external iterations n_1, number of iterations at the same temperature n_2, and temperature drop rate δ, weight coefficient w, two acceleration factors c_1 and c_2, iteration times n_3, and population size z.

Step 2. Randomly select orders $s[s_1, s_2, \dots, s_k]$ from all orders that satisfy the target function definition domain.

Step 3. Randomly generate the completion order $(s_1 \to s_2 \to \cdots \to s_k)$.

Step 4. Randomly generate the particle population. Each particle contains four parameters: the preventive maintenance threshold V, the quality replacement threshold W, the opportunity maintenance threshold ΔV, and the production batch size Q.

Step 5. Calculate the fitness of each particle according to the fitness function.

Step 6. Obtain the best individual fitness $pbest$ and the best global fitness $gbest$.

Step 7. Update the position and velocity of each particle.

Step 8. Check whether the PSO termination conditions are satisfied. If not, return to Step 5. Otherwise, record the current global best value.

Step 9. Use the two-transformation method to change the completion order of two orders, and repeat Steps 4-7 to generate a new solution $gbest_{new}$.

Step 10. Calculate the increment $\Delta = gbest_{new} - gbest$. If $\Delta > 0$, $gbest_{new}$ is accepted as the new optimal solution; otherwise, it is accepted as the new optimal solution with probability p.

Step 11. Check whether the SA termination conditions are satisfied. If not, return to Step 9. Otherwise, record the current solution $gbest$.

Step 12. Reduce the temperature and repeat Steps 9-11 until the minimum temperature is reached or no new solution is generated for several consecutive iterations. Then compare all recorded solutions $gbest$ in Step 11 and retain the maximum value.

Step 13. Return to Step 2, randomly select all possible orders again, compare all recorded values $gbest$ from Step 12, and output the final maximum value $gbest_{max}$.

5. Case study

5.1 Data preparation

One enterprise receives 15 orders with different requirements within a certain period, and the estimated production time is $T_x = 1000$ days. Through reference and analysis of the historical data of the three-component production system in a factory, the shape parameters and scale parameters are approximately $\beta = 3.5201$, $\eta = 523.254$. The system can produce at a rate of 50 pieces/day; the unit production cost is 5 RMB/piece, and the selling price is 10 RMB/piece. The specific requirements of the order are shown in Table 1, and the cost unit price and maintenance days are shown in Table 2. Other parameters are $\alpha_{1,1} = 0.1$, $\alpha_{1,3} = 0.12$, $\alpha_{1,2} = 0.11$, $\theta = 0.8$, $\mu = 1$, $\lambda = 0.3$, $\gamma = 0.5$, $tpc = qpc = 10000$, and $ic = 0.005$.

Table 1 Order requirements

Order No	Order quantity (Piece)	Quality requirements (Defective rate)	Time requirement (Days)
1	8000	0.03	250
2	7500	0.04	230
3	5200	0.03	150
4	10000	0.04	280
5	9100	0.06	240
6	6800	0.04	220
7	8000	0.05	200
8	7700	0.03	240
9	9800	0.05	290
10	6600	0.03	230
11	9000	0.05	250
12	5900	0.06	180
13	10600	0.05	270
14	5500	0.04	100
15	11000	0.06	250

Table 2 Maintenance costs and maintenance durations for different maintenance methods

Maintenance action	Maintenance cost	Maintenance days
Preventive maintenance	1000	3
Component replacement	3000	5
Opportunity maintenance	1000	3
Minor repair	100	0

5.2 Result analysis

The above parameters are substituted into the joint optimization model, which is solved using Python 3.7. The initial temperature was $T = 100$, the temperature drop rate was $\delta = 0.95$, the maximum number of external iterations was $n_1 = 100$, and the number of iterations at each temperature $n_2 = 100$ in the SA process. In the PSO process, the population size was $k = 50$, the number of iterations was $n_2 = 300$, two acceleration factors were $c_1 = c_2 =2$, and the inertia weight was $w(k) = w_{start} - (w_{start} - w_{end})(T_{max} - k)/T_{max}$. The optimal solution of the model was to produce orders in the sequence 7 → 13 → 5 → 15 → 14 with $Q = 5300$, $V = 112$, $W = 138$, and $\Delta V = 8$, which maximizes the profit of the enterprise to $C_{max} = 170363$. The convergence curve of the fitness function of PSO algorithm under the optimal solution is shown in Fig. 1.

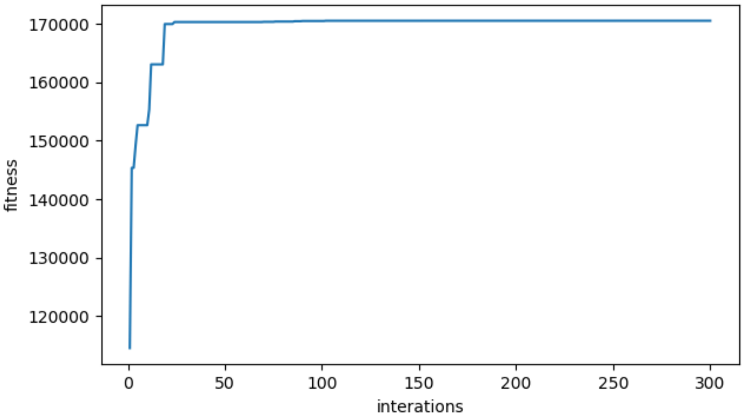

Fig. 1 Fitness function of the PSO algorithm under the optimal solution

Most optimization studies reported in the literature have used cost as the objective function. Using the same parameters, this paper also solves the optimization model with cost minimization as the objective. The optimal solution is to produce the orders in the sequence 7 → 4 → 5 → 12 → 6, with $Q = 4200$, $V = 108$, $W = 132$, and $\Delta V = 10$, which minimizes the total cost of the enterprise to $D_{min} = 68592$. The optimal solutions of the two models are shown in Tables 3 and 4.

By calculation, the total cost of the enterprise under the optimal solution of the profit function is $D_{min} = 79637$. The total profit of the enterprise under the optimal solution of the cost function is $C_{max} = 130408$. These results show that using profit as the objective function increases the production batch size and maintenance threshold, thereby reducing the number of repairs within a limited time. However, this may prevent the enterprise from completing all orders as required and may therefore generate penalty costs. As a result, the cost increases by 13.8 %, but the overall enterprise income increases by 23.45 %.

Table 3 Maintenance status under the optimal solution when profit is the objective function

Component	mc_1	mc_2	mc_3	mc_4	TPC	QPC
1	6	1	2	18	1	1
2	5	2	2	19		
3	3	3	3	21		

Table 4 Maintenance status under the optimal solution when cost is the objective function

Component	mc_1	mc_2	mc_3	mc_4	TPC	QPC
1	7	1	3	12	0	0
2	6	1	4	12		
3	5	2	4	14		

5.3 Sensitivity analysis

To examine the relationship between the optimal decision variables and total enterprise profit, it is necessary to analyze the sensitivity of the optimal maintenance strategy to the maintenance cost parameters. This paper analyzes the impact of different parameter values on the optimal decision-making strategy by changing one parameter while keeping the others unchanged. Opportunity maintenance can be regarded as a special case of preventive maintenance, so no additional analysis is carried out for it. This paper considers the impact of preventive maintenance cost mc_1, component replacement cost mc_2, and minor repair costs on the optimal strategy. In general, the maintenance costs satisfy $mc_2 > mc_1 > mc_4$, and the parameter variation range is specified accordingly. The specific change results are shown in Table 5.

The size of batch production Q is sensitive to replacement cost mc_2 and minor repair cost mc_4. When mc_2 increases, Q will decrease rapidly to shorten the time of system production, reduce the number of times from system deterioration to component replacement, and reduce the maintenance cost. When mc_4 increases, Q decreases in order to reduce the number of unexpected system failures and, consequently, the number of minor repairs.

Preventive maintenance threshold V and opportunistic maintenance threshold ΔV are only slightly sensitive to preventive maintenance cost mc_1. Although mc_1 varies over the same range, the actual values of V and ΔV change only slightly. As mc_1 increases, both V and ΔV gradually increase, thereby reducing the number of preventive maintenance actions.

The component replacement threshold W is most sensitive to the component replacement cost mc_2 and is also sensitive to mc_1 and the minor repair cost mc_4. When mc_1 or mc_4 increases, the value of W decreases, accelerating component replacement and reducing the number of preventive maintenance actions and minor repairs. When mc_2 increases, the value of W increases significantly, making the components more inclined toward the more economical preventive maintenance strategy.

Total profit C is the most sensitive to the replacement cost mc_2, followed by preventive maintenance cost mc_1, and the least sensitive is minor repair cost mc_4. Due to $mc_2 > mc_1 > mc_4$, the effect of component replacement is better than preventive maintenance. If the two values are similar, the maintenance strategy becomes more inclined toward increasing the number of component replacements; conversely, more preventive maintenance will be adopted.

Table 5 Results of the sensitivity analysis

Parameter	Range of variation (%)	Q	V	W	ΔV	C
\	\	5300	112	138	8	170363
mc_1	-50	5100	110	141	9	181251
	-25	5300	111	140	8	176489
	+25	5400	112	137	7	165334
	+50	5400	114	136	7	159641
mc_2	-50	5800	111	131	8	188343
	-25	5600	112	134	8	181376
	+25	5000	112	142	7	162373
	+50	4800	113	147	8	151335
mc_4	-50	5600	113	140	8	178131
	-25	5400	113	139	7	173164
	+25	5100	112	138	7	168779
	+50	5000	111	136	7	163498

6. Conclusion

This paper proposes a condition-based maintenance strategy model based on customer satisfaction. In the modeling process, the limited production time is divided into multiple production cycles of equal length, and the maintenance action after each cycle is determined based on the deterioration of each component in the system and the maintenance thresholds. The limited-capacity batch problem model is formed by combining the maintenance, inventory, and production costs generated during enterprise operation with the production constraints, after which the order requirements are compared with the actual delivery performance. If the order requirements are not met, corresponding penalty costs are incurred, thereby forming the customer satisfaction model. This paper integrates the batch production problem under limited capacity, the customer satisfaction problem in order delivery, and the condition-based maintenance strategy, and takes the maximization of enterprise profit as the optimization objective. An optimal condition-based maintenance strategy model is established, and its effectiveness is verified through a case study.

Acknowledgement

The work presented in this paper was supported by the National Natural Science Foundation of China (No. 72271161).

References

[1] Rajković, T., Makajić-Nikolić, D., Lečić-Cvetković, D., Aničić, N. (2025). The most commonly used Industry 4.0 technologies in manufacturing: A systematic literature review, *Advances in Production Engineering & Management*, Vol. 20, No. 4, 507-528, doi: 10.14743/apem2025.4.555.

[2] Huang, J., Wang, L., Jiang, Z. (2019). A method combining rules with genetic algorithm for minimizing makespan on a batch processing machine with preventive maintenance, *International Journal of Production Research,* Vol. 58, No. 13, 4086-4102, doi: 10.1080/00207543.2019.1641643.

[3] Tambe, P.P., Kulkarni, M.S. (2022). A reliability based integrated model of maintenance planning with quality control and production decision for improving operational performance, *Reliability Engineering & System Safety,* Vol. 226, Article No. 108681, doi: 10.1016/j.ress.2022.108681.

[4] Hnaien, F., Yalaoui, F., Mhadhbi, A., Nourelfath, M. (2016). A mixed-integer programming model for integrated production and maintenance, *IFAC-PapersOnLine,* Vol. 49, No. 12, 556-561, doi: 10.1016/j.ifacol.2016.07.694.

[5] Fitouhi, M.-C., Nourelfath, M. (2012). Integrating noncyclical preventive maintenance scheduling and production planning for a single machine, *International Journal of Production Economics,* Vol. 136, No. 2, 344-351, doi: 10.1016/j.ijpe.2011.12.021.

[6] Lai, X., Chen, Z., Sarker, B.R. (2020). Optimal production lot sizing for an imperfect manufacturing system with machine breakdown and emergency maintenance policy, *Kybernetes,* Vol. 49, No. 5, 1533-1560, doi: 10.1108/K-12-2018-0687.

[7] Hadian, S.M., Farughi, H., Rasay, H. (2023). Development of a simulation-based optimization approach to integrate the decisions of maintenance planning and safety stock determination in deteriorating manufacturing systems, *Computers & Industrial Engineering,* Vol. 178, Article No. 109132, doi: 10.1016/j.cie.2023.109132.

[8] BouAbid, H., Dhouib, K., Gharbi, A. (2024). Integrated production and maintenance policy for manufacturing systems prone to products' quality degradation, *Advances in Production Engineering & Management*, Vol. 19, No. 4, 512-526, doi: 10.14743/apem2024.4.521.

[9] Selech, J., Matijosius, J., Kilikevicius, A., Marinkovic, D. (2025). Reliability analysis and the costs of corrective maintenance for a component of a fleet of trams, *Tehnički Vjesnik – Technical Gazette*, Vol. 32, No. 1, 205-216, doi: 10.17559/TV-20241121002144.

[10] Duan, C., Li, Z., Liu, F. (2020). Condition-based maintenance for ship pumps subject to competing risks under stochastic maintenance quality, *Ocean Engineering,* Vol. 218, Article No. 108180, doi: 10.1016/j.oceaneng.2020.108180.

[11] Zhang, X., Liao, H., Zeng, J., Shi, G., Zhao, B. (2021). Optimal condition-based opportunistic maintenance and spare parts provisioning for a two-unit system using a state space partitioning approach, *Reliability Engineering & System Safety,* Vol. 209, Article No. 107451, doi: 10.1016/j.ress.2021.107451.

[12] Zheng, R., Zhou, Y., Gu, L., Zhang, Z. (2021). Joint optimization of lot sizing and condition-based maintenance for a production system using the proportional hazards model, *Computers & Industrial Engineering,* Vol. 154, Article No. 107157, doi: 10.1016/j.cie.2021.107157.

[13] Zheng, R., Chen, B., Gu, L. (2020). Condition-based maintenance with dynamic thresholds for a system using the proportional hazards model, *Reliability Engineering & System Safety,* Vol. 204, Article No. 107123, doi: 10.1016/j.ress.2020.107123.

[14] Zheng, M., Ye, H., Wang, D., Pan, E. (2021). Joint optimization of condition-based maintenance and spare parts orders for multi-unit systems with dual sourcing, *Reliability Engineering & System Safety,* Vol. 210, Article No. 107512, doi: 10.1016/j.ress.2021.107512.

[15] Yousefi, N., Coit, D.W., Song, S., Feng, Q. (2019). Optimization of on-condition thresholds for a system of degrading components with competing dependent failure processes, *Reliability Engineering & System Safety,* Vol. 192, Article No. 106547, doi: 10.1016/j.ress.2019.106547.

[16] Uit Het Broek, M.A.J., Teunter, R.H., de Jonge, B., Veldman, J. (2021). Joint condition-based maintenance and load-sharing optimization for two-unit systems with economic dependency, *European Journal of Operational Research,* Vol. 295, No. 3, 1119-1131, doi: 10.1016/j.ejor.2021.03.044.

[17] Wang, J., Qiu, Q., Wang, H., Lin, C. (2021). Optimal condition-based preventive maintenance policy for balanced systems, *Reliability Engineering & System Safety,* Vol. 211, Article No. 107606, doi: 10.1016/j.ress.2021.107606.

[18] Xu, J., Liang, Z., Li, Y.-F., Wang, K. (2021). Generalized condition-based maintenance optimization for multi-

component systems considering stochastic dependency and imperfect maintenance, *Reliability Engineering & System Safety,* Vol. 211, Article No. 107592, doi: 10.1016/j.ress.2021.107592.

[19] Shi, Y., Zhu, W., Xiang, Y., Feng, Q. (2020). Condition-based maintenance optimization for multi-component systems subject to a system reliability requirement, *Reliability Engineering & System Safety,* Vol. 202, Article No. 107042, doi: 10.1016/j.ress.2020.107042.

[20] Liu, B., Wang, Y., Yang, H., Segerstedt, A., Zhang, L. (2021). Maintenance service strategy for leased equipment: Integrating lessor-preventive maintenance and lessee-careful protection efforts, *Computers & Industrial Engineering,* Vol. 156, Article No. 107257, doi: 10.1016/j.cie.2021.107257.

[21] Iskandar, B.P., Husniah, H. (2017). Optimal preventive maintenance for a two dimensional lease contract, *Computers & Industrial Engineering,* Vol. 113, 693-703, doi: 10.1016/j.cie.2017.09.028.

[22] Nezami, F.G., Yildirim, M.B. (2013). A sustainability approach for selecting maintenance strategy, *International Journal of Sustainable Engineering,* Vol. 6, No. 4, 332-343, doi: 10.1080/19397038.2013.765928.

[23] Ruan, Y., Wu, G., Luo, X. (2022). Optimal joint design of two-dimensional warranty and preventive maintenance policies for new products considering learning effects, *Computers & Industrial Engineering,* Vol. 166, Article No. 107958, doi: 10.1016/j.cie.2022.107958.

[24] Brenière, L., Doyen, L., Bérenguer, C. (2020). Virtual age models with time-dependent covariates: A framework for simulation, parametric inference and quality of estimation, *Reliability Engineering & System Safety,* Vol. 203, Article No. 107054, doi: 10.1016/j.ress.2020.107054.

APEM journal
Advances in Production Engineering & Management
Volume 21 | Number 1 | March 2026 | pp 101–116
https://doi.org/10.14743/apem2026.1.564
ISSN 1854-6250
Journal home: apem-journal.org
Original scientific paper

Attention-guided unsupervised representation network for anomaly detection in electronic component manufacturing images

Liu, B.[a,*], **Li, C.S.**[b]

[a]Chengdu Aeronautic Polytechnic University, Chengdu, P.R. China
[b]Geely University of China, Chengdu, P.R. China

ABSTRACT

In modern industrial production, electronic component manufacturing imposes increasingly stringent requirements on quality inspection. To address the susceptibility of traditional detection methods to noise interference, the difficulty of localizing abnormal regions in images, and insufficient feature extraction capability, an improved industrial image anomaly detection method based on the original AGUR-Net (Attention-Guided Unsupervised Representation Network) model is proposed. This method enhances the recognition of abnormal regions by introducing attention gate modules and preactivated fusion residual blocks, while simultaneously combining stacked sparse denoising autoenco-ders to enhance the model's robustness to noise and suppress redundant information. The experimental results show that the proposed method achieves an accuracy of 84.26 % in locating abnormal regions on the MVTecAD dataset after 185 iterations, which is higher than the dual attention generative adversarial network (79.21 %), long short-term memory non-destructive testing network (79.31 %), and bidirectional long short-term memory network (81.63 %). At 400 iterations, the average loss value of this method for detecting abnormal images of industrial products is 0.016. In addition, the processing time for single images of Class A, B, and C defects in the actual factory environment is 372 ms, 329 ms, and 378 ms, respectively, demonstrating high detection efficiency. Overall, this method can accurately identify and locate abnormal images in the surface treatment and quality inspection stages of electronic component production, which helps to improve the quality control level in the manufacturing process and provides effective technical support for intelligent industrial production.

ARTICLE INFO

Keywords:
Electronic component manufacturing;
Industrial anomaly detection;
Unsupervised anomaly detection;
Anomaly localization;
Attention gate;
Stacked sparse denoising autoencoder;
Multimodal generative adversarial network (MGAN)

*Corresponding author:
liubing@cap.edu.cn
(Liu, B.)

Article history:
Received 21 July 2025
Revised 25 April 2026
Accepted 26 April 2026

1. Introduction

Image anomaly detection is a computer vision technology that meets practical application needs in industrial quality control, medical diagnosis support, and remote sensing with geographic information systems [1]. In industrial production, it helps detect appearance defects on products, such as tiny scratches on semiconductor chips, bubbles in glassware, and dents on screws [2, 3]. By using image anomaly detection for real-time quality monitoring, production efficiency can be improved. Traditional image detection methods for industrial products include threshold-based and edge-based techniques [4]. These methods can quickly detect shape changes and cracks in images. However, they are sensitive to noise and often miss surface defects on products with rich textures [5]. To address the difficulty of accurate defect identification, Ullah *et al.*

proposed an intelligent defect chip detection framework and introduced an inverse feature matching mechanism to improve the interpretability of abnormal region localization. Their experiments showed that the method effectively distinguished fine-grained defect details in chips [6]. To solve the time consumption problem in bearing defect detection, Liu *et al*. proposed an integrated unsupervised learning method based on autoencoder and generative adversarial networks. The results showed high detection efficiency, making the method suitable for real-time applications [7]. Image anomaly detection also plays an important role in part segmentation during industrial production. Threshold segmentation divides image pixels into categories and separates the target from the background to locate abnormal regions effectively [8]. To address challenges in detecting complex anomalies, Bergmann *et al*. proposed a logic-constrained method for unsupervised anomaly detection and localization. Experimental results confirmed that the method reduced ambiguity in locating logical anomalies [9]. However, many of these detection techniques are still highly affected by noise and environmental interference, making the detection results unstable. A new method is needed to improve feature recognition in industrial product images.

As the scale of industrial production continues to grow, image anomaly detection is expected to offer higher detection accuracy and more precise localization [10]. In response, researchers have explored various algorithms. Zhang *et al*. proposed a deep unsupervised learning method based on an improved adversarial autoencoder to solve the problem of data imbalance in anomaly detection. Their experiments showed that the method detects diseased samples by identifying significant deviations from the normal distribution under unsupervised conditions [11]. Sun *et al*. introduced a stochastic anomaly multi-scale feature focusing autoencoder network to reduce the missed detection of abnormal samples. The method successfully solved the problem of blurry image reconstruction [12]. Although these image anomaly detection algorithms can effectively extract abnormal features, they require long inference times and substantial computing resources, and thus cannot be readily applied to the detection of subtle abnormal areas in industrial commodities from raw material preparation to packaging and transportation [13]. Therefore, in view of the difficulty in detecting local abnormal image areas at each stage of electronic component production management, this study proposes an abnormal image detection method for electronic component production based on the Attention-Guided Unsupervised Representation Network (AGUR-Net). This method improves the feature extraction ability for abnormal areas in industrial commodity images. This method can precisely locate abnormal local areas such as short circuits and open circuits on the circuit board, ensuring that the raw materials put into production are qualified in the quality inspection of raw materials for electronic component production. Not only that, using the AGUR-Net industrial image anomaly detection algorithm to collect images of randomly selected electronic components on the production line and analyze the internal structure can further ensure that the product quality meets the standards. The concept of "unsupervised" needs to be clearly defined: this method only uses normal sample images during the training phase and does not rely on any position or category labeling of abnormal samples, thus belonging to unsupervised learning in terms of method properties. However, in the performance evaluation stage of the model, in order to quantitatively measure the accuracy of anomaly localization and classification, the experiment used a standard dataset with category labels and category-based evaluation indicators. This "unsupervised training, supervised evaluation" model is quite common in the field of industrial anomaly detection and does not change the unsupervised nature of the model training process. It is expected that this method can reduce the occurrence of false inspections in industrial quality inspection and provide a more comprehensive and intelligent solution for industrial production. Unlike the original AGUR-Net model, the main contribution of this paper lies in two aspects: first, an improved attention gate module and a pre-activated fusion residual block are introduced in the U-shaped decoding path, replacing the traditional skip connection method and allowing the network to dynamically focus on potential abnormal areas rather than uniformly processing all spatial positions [14]. Second, the stacked sparse denoising autoencoder and multimodal generative adversarial learning module are embedded into the front-end feature processing flow of AGUR-Net to suppress noise interference during image acquisition and enhance multimodal feature expression. The above components are all designed for abnormal detection scenarios in electronic component production in this study, rather than being directly transferred from existing literature. In contrast, the hollow space pyramid pooling module and efficient channel attention module used in the model are based on existing research, and their main function is to provide multi-scale contextual information and channel weight calibration for the network. By combining the new and old components mentioned above, the proposed method can improve the localization accuracy and detection robustness of abnormal areas while maintaining computational efficiency.

2. Methods and materials

2.1 Design of the anomaly image detection algorithm based on AGUR-Net

With continued technological progress, image anomaly detection is being applied increasingly widely in industry, security, and healthcare [15, 16]. This technology can effectively detect product defects such as scratches and cracks, and also identify abnormal behaviors and suspicious objects. Although traditional detection methods can detect abnormalities, they are easily affected by noise and local changes, and their performance is unsatisfactory [17, 18]. To address the difficulties of anomaly localization and insufficient feature extraction, an AGUR-Net-based anomaly image detection algorithm is proposed to improve detection efficiency. The overall framework of the algorithm is shown in Fig. 1.

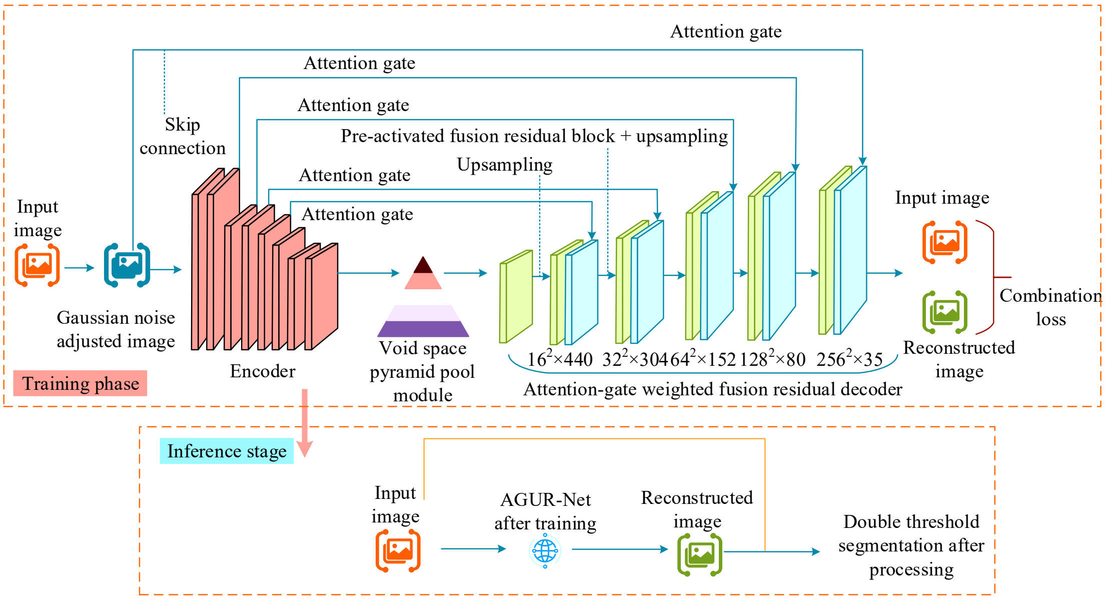

Fig. 1 Image anomaly detection algorithm framework based on AGUR-Net

As shown in Fig. 1, the framework of the AGUR-Net-based anomaly detection algorithm includes a training phase and an inference phase. In the training phase, the input image is first sent into the network and adjusted by introducing Gaussian noise. Then, the adjusted image passes through the encoder to extract features while gradually reducing the size of the feature maps. Next, the Atrous Spatial Pyramid Pooling (ASPP) module processes the encoded features to obtain multi-scale context information. During this process, attention gates in the residual decoder are used to enhance key features through weighted fusion. The encoder and attention gates reconstruct the structure and details of the image to optimize training. In the inference phase, the test image is input into the trained AGUR-Net. A double-threshold segmentation post-processing method is applied to the reconstruction result to locate and identify anomaly regions. The calculation of the atrous convolution in the improved ASPP module is shown in Eq. 1.

$$f'[i] = \sum_{k} f\,[i + r \cdot k]W[k] \tag{1}$$

In Eq. 1, i and f represent the position and input feature, $f'[i]$ and $W[k]$ represent the output feature map and kernel convolution, and r denotes the sampling stride of the atrous convolution. The attention gate coefficient is calculated as shown in Eq. 2 [19].

$$\alpha_i^l = \sigma_2\left(q_{att}^l\left(x_i^l, g_i; \Theta_{att}\right)\right) \tag{2}$$

In Eq. 2, q_{att}^l is the intermediate variable in the attention module, g_i is the gating signal, x_i^l is the input feature vector of layer l, σ_2 is the Sigmoid activation function, and Θ_{att} is the set of all learnable parameters in the attention module. The improved attention gate module and pre-activation residual block are shown in Fig. 2.

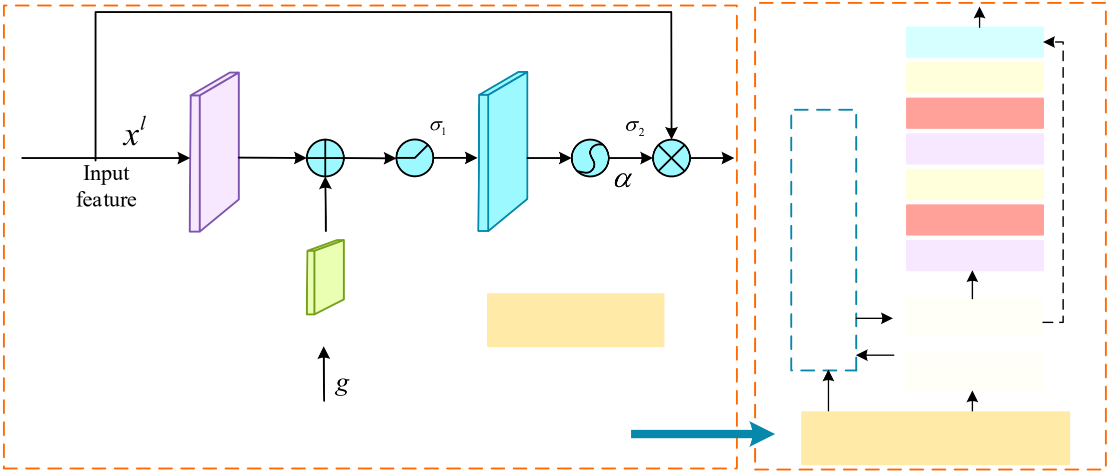

Fig. 2 Improved attention gate module and pre-activation fusion residual block

As shown in Fig. 2, the attention gate module receives input feature x^l and gate feature g. These features are separately processed through 1×1 convolution layers to adjust dimensions and are then fused. The fused feature passes through a ReLU activation function to enhance feature representation. Finally, the Sigmoid function generates the attention coefficient, which is multiplied with x^l to highlight important features. In the pre-activation residual block, channel-wise concatenation is done through upsampling. Then, the attention gate mechanism adaptively adjusts feature weights. After that, the convolution output is normalized and passed through the ReLU function to introduce non-linearity and complete the residual connection. To perform deeper anomaly detection, the algorithm introduces a deep anomaly scoring network based on AGUR-Net to further distinguish abnormal image data. This network learns complex features automatically and adapts well to high-dimensional data [20, 21]. The anomaly score is calculated as shown in Eq. 3.

$$\xi\left(f_{ij}, \theta_s\right) = \sum_{n=1}^{L} w_n^o f_{ijk} + w_{L+1}^o \tag{3}$$

In Eq. 3, f_{ij} and θ_s are the feature vector and weight, w_{L+1}^o is the anomaly score bias term, and k is the number of terms. The anomaly score mapping is calculated as shown in Equation (4).

$$\psi\left(x_{ij}, \theta\right) = \xi\left(\varphi\left(x_{ij}; \theta_f\right); \theta_s\right) \tag{4}$$

In Eq. 4, ψ and θ_f represent the anomaly score mapping and weight matrix. The global compression feature in the improved Efficient Channel Attention (ECA) module is calculated as shown in Eq. 5.

$$y = \frac{1}{W \times H} \sum_{v=1}^{W} \sum_{b=1}^{H} x_{(e,r)} \tag{5}$$

In Eq. 5, H is the height, W is the width of the feature map, $x_{(v,\mathrm{b})}$ is the feature value, and y is the global compression feature. The improved ECA module first inputs a feature map with height

H, width W, and channel number C. Then global pooling is applied to compress the spatial dimensions, producing an output of size $1 \times 1 \times C$. The globally pooled channel information is mapped to capture dependencies between channels. The result is passed through the Sigmoid function σ to obtain attention weights with output dimension $1 \times 1 \times C$. These weights are multiplied with the corresponding channels of the original feature map for channel-wise weighting. The final output is calculated as shown in Eq. 6.

$$\hat{x} = W_z \cdot x \tag{6}$$

In Eq. 6, W_z is the important channel weight. W_z is calculated as shown in Eq. 7 [22].

$$W_z = \sigma\big(D_r(y)\big) \tag{7}$$

In Eq. 7, r is the kernel size for one-dimensional convolution, and D_r is the one-dimensional convolution result. By calculating the importance of each channel, the overall detection efficiency improves while ensuring parameter sharing. Channel information is calculated as shown in Eq. 8.

$$z_c^1 = F_{GAP}(F_c) = \frac{1}{H \times W} \sum_{v=1}^{H} \sum_{b=1} F_c\,(v, b) \tag{8}$$

In Eq. 8, z_c^1 is the channel information, and F_c represents the feature map after channel fusion of c. In conclusion, the deep anomaly scoring network and AGUR-Net can accurately capture anomaly data and detect industrial product defects. The improved AGUR-Net structure is shown in Fig. 3.

It can be seen from Fig. 3 that the improved AGUR-Net anomaly image detection algorithm consists of three modules: front-end feature extraction and processing, deep anomaly scoring network, and back-end reconstruction and post-processing. The front-end module encodes using a U-shaped network, receives input features through the attention gate module, combines 1×1 convolution and feature fusion to enhance the feature learning ability, and refines the processing through multi-scale feature fusion. The deep anomaly scoring network maps the processed features to the anomaly scoring space and calibrates the anomaly scores to determine the location and degree of anomalies. Finally, the back-end module restores the image features through the decoder and locates and segments the abnormal areas by using operations such as double-threshold segmentation. This algorithm can detect abnormalities in real time during processes such as the assembly and soldering of electronic components, and promptly issue alerts to feed back to the production line control system.

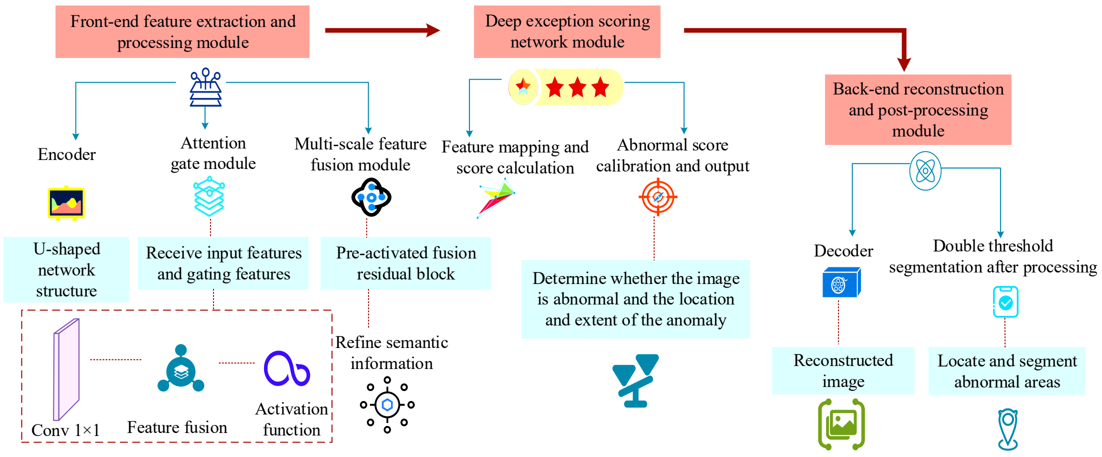

Fig. 3 The improved AGUR-Net abnormal image detection algorithm structure

2.2 Optimization of the detection method based on AGUR-Net and SSDAE

To address the limitations of the AGUR-Net algorithm in detecting minor defects in electronic components, as well as the vulnerability of traditional methods to noise interference, this study proposes an improved method integrating SSDAE. By enhancing the anti-noise ability and extracting key features, the detection accuracy of micro-defects in industrial scenarios is improved. SSDAE suppresses redundant information and reduces noise during image collection [23]. The improved SSDAE network structure is shown in Fig. 4.

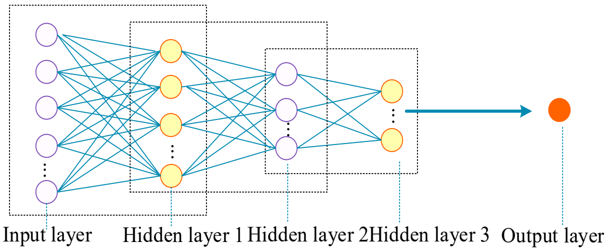

Fig. 4 Improved SSDAE network structure

As shown in Fig. 4, the SSDAE structure consists of input, hidden, and output layers. The input layer includes multiple purple circles, each representing an input neuron. It receives raw data and sends it to Hidden Layer 1. Hidden Layer 1 neurons are trained with the input neurons to learn patterns and features. Then, the output of Hidden Layer 1 is used as the input of Hidden Layer 2 for further processing. Hidden Layer 3 performs deeper extraction on the features from Hidden Layer 2 to enhance the feature representation for industrial anomaly detection. The final output layer returns denoised images after training. The compression process is shown in Eq. 9.

$$K_q^l = f_{sigmoid}\left(z_q^l\right) = f\left(\sum_{a=1}^{n} W_{ql}^{l-1} \cdot x_a^{l-1} + b_q^{l-1}\right) \tag{9}$$

In Eq. 9, l and q are the current hidden layer index and number of neurons, a is the number of neurons in the previous layer, and W is the feature weight coefficient. The sparse autoencoder loss function is calculated as shown in Eq. 10.

$$K_L\left(\rho \| \hat{\rho}_q \|\right) = p\log\frac{\rho}{\hat{\rho}_q} + (1-\rho)\log\frac{1-\rho}{1-\hat{\rho}_q} \tag{10}$$

In Eq. 10, $\hat{\rho}_q$ is the average sparse activation value, $K_L\left(\rho \| \hat{\rho}_q \|\right)$ is the relative entropy distance, and ρ is the sparsity parameter. $\hat{\rho}_q$ is calculated as shown in Eq. 11.

$$\hat{\rho}_q = \frac{1}{m}\sum_{a}^{m}\left[n_q(x_a)\right] \tag{11}$$

In Eq. 11, n_q is the activation state of the hidden neurons, and x_a is the unlabeled actual anomaly data. In addition, this study applies the Multimodal Generative Adversarial Learning Algorithm (MGAN) to improve multimodal training effects such as color and texture. MGAN enhances feature expression and reduces missed and false detections [24]. The MGAN structure is shown in Fig. 5.

As shown in Fig. 5, MGAN takes spatial-domain and frequency-domain samples as input. The spatial-domain sample is raw data, and the frequency-domain sample is processed through Fourier transform. These samples are sent to corresponding generators for encoding and feature extraction. Then, the decoders generate images similar to the original spatial and frequency distributions. The discriminator judges whether the input is an anomaly or a near-normal sample generated by the generator. The reconstruction error of the spatial branch is calculated as shown in Eq. 12.

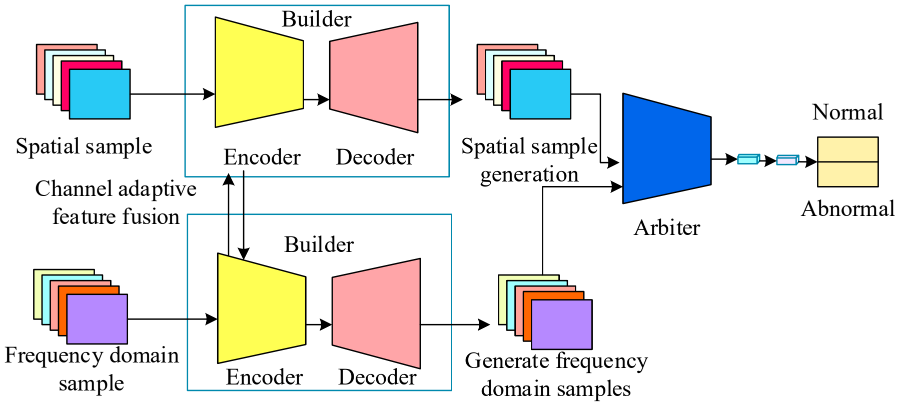

Fig. 5 Schematic diagram of MGAN structure

$$L_{consS} = E_{I\sim p_n}\left[I - \hat{I}_S\right]_1 \tag{12}$$

In Eq. 12, S is the spatial-domain sample and I is the spatial image. The reconstruction error of the frequency branch is calculated as shown in Eq. 13 [25].

$$L_{conF} = E_{I\sim p_n}\left[I - \hat{I}_F\right]_1 \tag{13}$$

In Eq. 13, F is the frequency-domain sample. The adversarial loss is calculated as shown in Eq. 14.

$$L_{adv} = \mathbb{E}_{\hat{I}_{12}\sim p_r}\left[D\left(\hat{I}_{12}\right)\right] - \mathbb{E}_{\hat{I}_3\sim p_r}\left[D\left(\hat{I}_{13}\right)\right] \tag{14}$$

In Eq. 14, $\hat{I}_{12}$ and $\hat{I}_{13}$ are the pixel values of the frequency and spatial branches, and p_r and $D(\cdot)$ are the probability distribution and discriminator function. The improved Fourier transform is calculated as shown in Eq. 15.

$$U(u,v) = \sum_{x=0}^{M-1}\sum_{y=0}^{N-1} f\,(x,y)\cdot e^{-j2\pi\left(\frac{ux}{M}+\frac{vy}{N}\right)} \tag{15}$$

In Eq. 15, $U(u,v)$ is the pixel value in the frequency domain, and u and v are the frequency coordinates. In conclusion, MGAN and SSDAE detect fine features such as texture. The framework based on AGUR-Net for industrial anomaly detection is shown in Fig. 6.

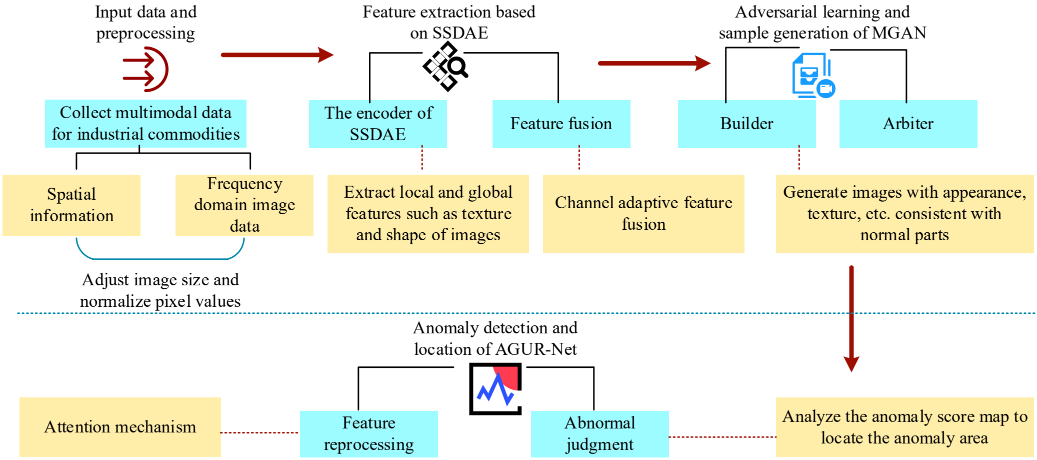

Fig. 6 Workflow of AGUR-Net industrial commodity abnormal image detection method

As can be seen from Fig. 6, the abnormal image detection method for electronic component production based on AGUR-Net first collects and standardizes multimodal data, such as spatial domain and frequency domain image data. Then, the local and global features of the image are extracted using the SSDAE feature extraction module, and adaptive feature fusion is carried out. Then, images similar to normal parts are generated through MGAN adversarial learning to determine the authenticity of the images. Finally, AGUR-Net is used to further detect and locate the abnormal features and output the abnormal score image. This method can regularly inspect the components in the warehouse management of electronic parts and promptly detect surface abnormalities such as discoloration and spots.

3. Results

3.1 Validation of the effectiveness of the AGUR-Net anomaly image detection algorithm

To verify the performance advantages of the AGUR-Net anomaly image detection algorithm, it was compared with three detection algorithms: Dual-Attention Generative Adversarial Network (DAGAN), Long Short-Term Memory-Non-destructive Testing (LSTM-NDT), and Bi-directional Long Short-Term Memory (BiLSTM). Among them, LSTM-NDT and BiLSTM have been widely applied in industrial image anomaly detection tasks in recent years. The core idea is to use image pixel sequences or feature map sequences as temporal inputs, and utilize the memory ability of recurrent neural networks to capture long-range dependencies and anomaly patterns in images. Therefore, these two methods can serve as reasonable comparison baselines for image-based anomaly detection tasks. DAGAN is an image anomaly detection method based on generative adversarial architecture, which is closer to the task setting of our research method. By comparing multiple methods simultaneously, the performance of AGUR-Net in industrial image anomaly detection can be more comprehensively evaluated. The experiments were conducted on Ubuntu 20.04 with an NVIDIA Tesla V100 GPU (16 GB memory), and all code was implemented using the PyTorch framework. The experiments used the MVTecAD and KSDD2 datasets for training and testing. The MVTecAD dataset contained 5,354 high-resolution color images that covered various industrial anomalies such as scratches and dents. The KSDD2 dataset included 3,336 high-resolution images with 356 labeled defect images. The morphology and texture of abnormal samples in the MVTecAD dataset are highly similar to typical defects on the surface of electronic components, and are therefore used to evaluate the model's ability to locate and detect anomalies related to electronic manufacturing. The data in the KSDD2 dataset is directly related to the surface defect detection tasks of metal and plastic components in electronic component production, and is therefore used to validate the performance of the model on actual electronic manufacturing parts. All test images were resized to 256×256, and the batch size was set to 16. Four anomaly detection algorithms were tested for anomaly region localization, and the results are shown in Fig. 7.

As shown in Fig. 7(a), on the MVTecAD dataset, AGUR-Net achieved an anomaly region localization accuracy of 84.26 % after 185 iterations. At the same iteration count, DAGAN reached 78.63 %. According to Fig. 7(b), on the KSDD2 dataset, AGUR-Net reached a stable accuracy range of 82 % to 96 % after 150 iterations. At 150 iterations, LSTM-NDT and BiLSTM achieved localization accuracies of 77.26 % and 81.96 %, respectively. These results indicated that AGUR-Net effectively located defect regions in industrial quality inspection tasks and demonstrated good applicability. To further verify the accuracy of AGUR-Net in anomaly image detection, it was compared with DAGAN, LSTM-NDT, and BiLSTM on industrial anomaly detection accuracy. The results are shown in Fig. 8.

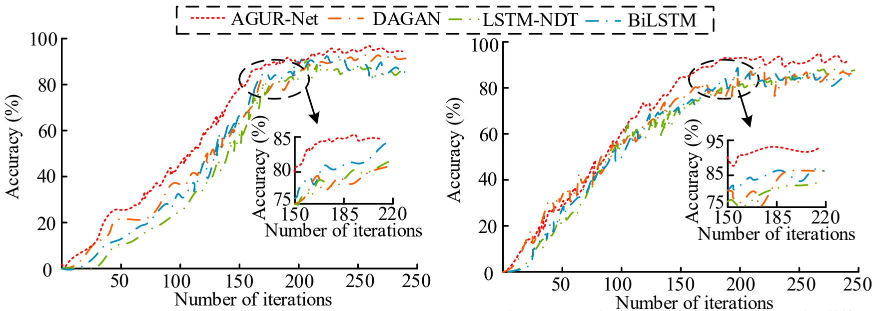

(a) Test results of positioning accuracy in different algorithm anomaly regions in MVTecAD dataset

(b) Test results of positioning accuracy in different algorithm anomaly regions in KSDD2 dataset

Fig. 7 Anomaly region localization accuracy test results

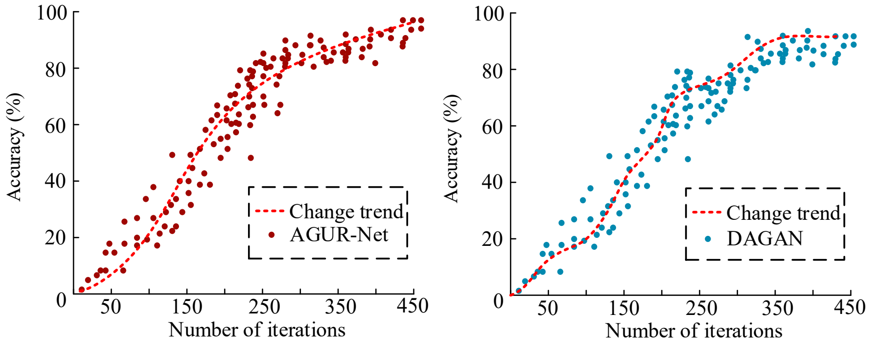

(a) Test results of anomaly detection accuracy of AGUR-Net algorithm (b) Test results of anomaly detection accuracy of DAGAN algorithm

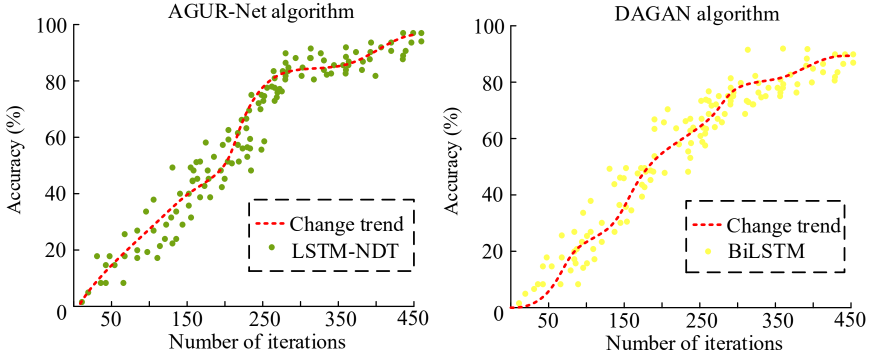

(c) Test results of anomaly detection accuracy of LSTM-NDT algorithm (d) Test results of anomaly detection accuracy of BiLSTM algorithm

Fig. 8 Anomaly detection accuracy test results

Fig. 8(a) shows that AGUR-Net achieved an industrial anomaly detection accuracy of 43.69 % at 150 iterations. After 250 iterations, the accuracy exceeded 75 %, peaking at 97.26 %. Fig. 8(b) shows that the accuracy of DAGAN fluctuated significantly between 100 and 250 iterations, reaching 73.12 % at 300 iterations. Fig. 8(c) shows that LSTM-NDT maintained an accuracy range of 75 % to 82 % between 250 and 350 iterations. Fig. 8(d) shows that BiLSTM achieved a maximum accuracy of 76.31 % at 275 iterations. Overall, AGUR-Net demonstrated higher detection accuracy and ensured safety in the manufacturing of critical components such as those in aerospace. To further evaluate the classification performance, the algorithm was tested alongside DAGAN, LSTM-NDT, and BiLSTM for anomaly classification, as shown in Fig. 9.

Fig. 9(a) shows that without classification, capsule, screw, leather, and canvas anomaly images were scattered. Fig. 9(b) shows that after classification by AGUR-Net, canvas anomaly images clustered around the coordinate (-3, 3). However, a few canvas images were mistakenly classified into the capsule region. Fig. 9(c) shows that DAGAN struggled with capsule classification, with some being misclassified as leather. Fig. 9(d) shows that LSTM-NDT achieved good classification results for screw and leather anomalies, clustering around (2, -2) and (4, 2), respectively. Fig. 9(e) shows that BiLSTM performed well in classifying leather anomalies, with most clustering around (2, 3). These results indicated that AGUR-Net effectively classified different types of anomalies, helping users quickly identify defect types. Furthermore, AGUR-Net, DAGAN, LSTM-NDT, and BiLSTM were evaluated using the Area Under the Curve (AUC) metric. The anomaly rate in the datasets was set to 10 % to ensure sufficient anomaly samples. To enhance result diversity, the Fashion-MNIST dataset was added. It contained images from 10 categories of fashion items such as coats and shirts with diverse textures and shapes, making it suitable for classification tasks. The Fashion-MNIST dataset, although not directly derived from industrial electronic component production scenarios, has diverse texture, shape, and edge features. The purpose of introducing this dataset is not to simulate the actual detection task of electronic components, but to evaluate the generalization ability and feature discrimination ability of various algorithms on a wider range of image distributions. The results are shown in Table 1.

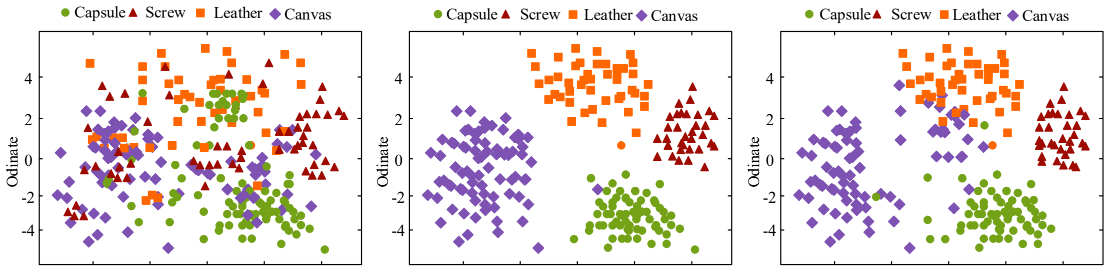

(a) Effect when abnormal image classification is not performed

(b) The effect of AGUR-Net algorithm on abnormal image classification

(c) The effect of DAGAN algorithm on abnormal image classification

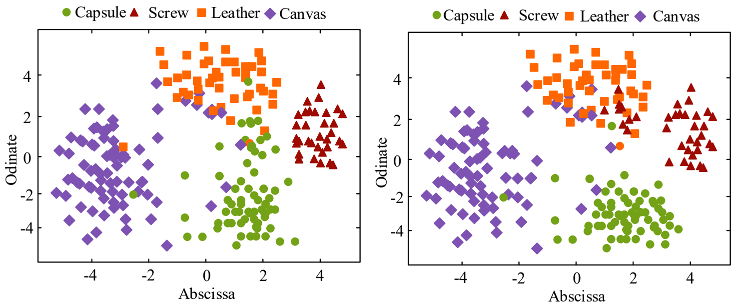

(d) The effect of LSTM-NDT algorithm on abnormal image classification

(e) The effect of BiLSTM algorithm on abnormal image classification

Fig. 9 Anomaly classification results of different detection algorithms

Table 1 Anomaly detection AUC test results of different data sets

Dataset	Correct class	AGUR-Net	DAGAN	LSTM-NDT	BiLSTM
MVTecAD	Bottle	0.836	0.812	0.769	0.746
	Cable	0.923	0.894	0.816	0.836
	Hazelnut	0.946	0.832	0.874	0.816
	Transistor	0.874	0.798	0.816	0.803
KSDD2	Gear wheel	0.913	0.826	0.813	0.781
	lock	0.936	0.864	0.885	0.752
	Plastic case	0.904	0.829	0.836	0.811
	Chip	0.876	0.864	0.814	0.809
Fashion-MNIST	Bag	0.896	0.821	0.838	0.823
	Sandal	0.937	0.903	0.726	0.874
	Pullover	0.948	0.897	0.798	0.893
	Coat	0.968	0.814	0.823	0.846

As shown in Table 1, all four algorithms achieved AUC values above 0.750 on the MVTecAD dataset. For cable samples, AGUR-Net achieved an AUC of 0.923, which was 0.029 higher than DAGAN's 0.894. On the KSDD2 dataset, AGUR-Net achieved an AUC of 0.936 for lock samples, outperforming DAGAN (0.864), LSTM-NDT (0.885), and BiLSTM (0.752). On the Fashion-MNIST dataset, AGUR-Net, DAGAN, LSTM-NDT, and BiLSTM achieved AUC values of 0.937, 0.903, 0.726, and 0.874, respectively, for sandal samples. These results demonstrated that AGUR-Net had a strong ability to distinguish anomalies and maintained high generalization.

3.2 Validation of the AGUR-Net industrial product anomaly image detection method

After verifying the performance of the AGUR-Net anomaly image detection algorithm, the proposed method was further compared with three anomaly image detection methods for electronic component production, namely DAGAN, LSTM-NDT, and BiLSTM. The experiments were conducted on PyTorch 1.8.1, with an initial learning rate of 0.4, and the network was optimized using the Adam optimizer. To ensure the authenticity and reliability of the experiments, the YDFID-1 and ECD datasets were used. The YDFID-1 dataset contained industrial product data such as metal sheets and plastic parts, with 15,000 labeled defects and 3,500 training samples. The data source of the YDFID-1 dataset is relatively close to the raw material and intermediate product detection stages in electronic component production, and is used to test the generalization performance of the model on different industrial materials and defect types. The ECD dataset is specifically designed for common electronic components, including high-definition images, and is suitable for object detection, classification, and defect recognition tasks. It is the most suitable test set for practical application scenarios. The visualization results of anomaly location for four abnormal image detection methods of electronic component production are shown in Fig. 10.

Fig. 10(a) shows five abnormal images corresponding to stage 1 (raw material preparation), stage 2 (processing and manufacturing), stage 3 (surface treatment), stage 4 (quality inspection), and stage 5 (packaging and transportation). Fig. 10(b) indicates that the actual abnormal defect is located in the central area of the image in the surface treatment stage. Fig. 10(c) shows that the AGUR-Net-based anomaly image detection method for electronic component production performs better in localizing anomalies in images from the surface treatment stage, and the heat-map distribution is relatively concentrated. Fig. 10(e) shows that the LSTM-NDT abnormal image detection method for electronic component production is not very accurate in the abnormal location of images in the quality inspection stage, and the defect area below the image is not detected. Fig. 10(f) shows that the BiLSTM electronic component production anomaly image detection method has a less effective anomaly location detection effect on images in the processing and manufacturing stage, quality inspection stage, and packaging and transportation stage than the method proposed in the study. Some undamaged areas are detected as abnormal areas. In addition, the study also conducted tests on the average loss values of abnormal electronic component production image detection using four abnormal image detection methods for electronic component production, namely AGUR-Net, DAGAN, LSTM-NDT, and BiLSTM. The test results are shown in Fig. 11.

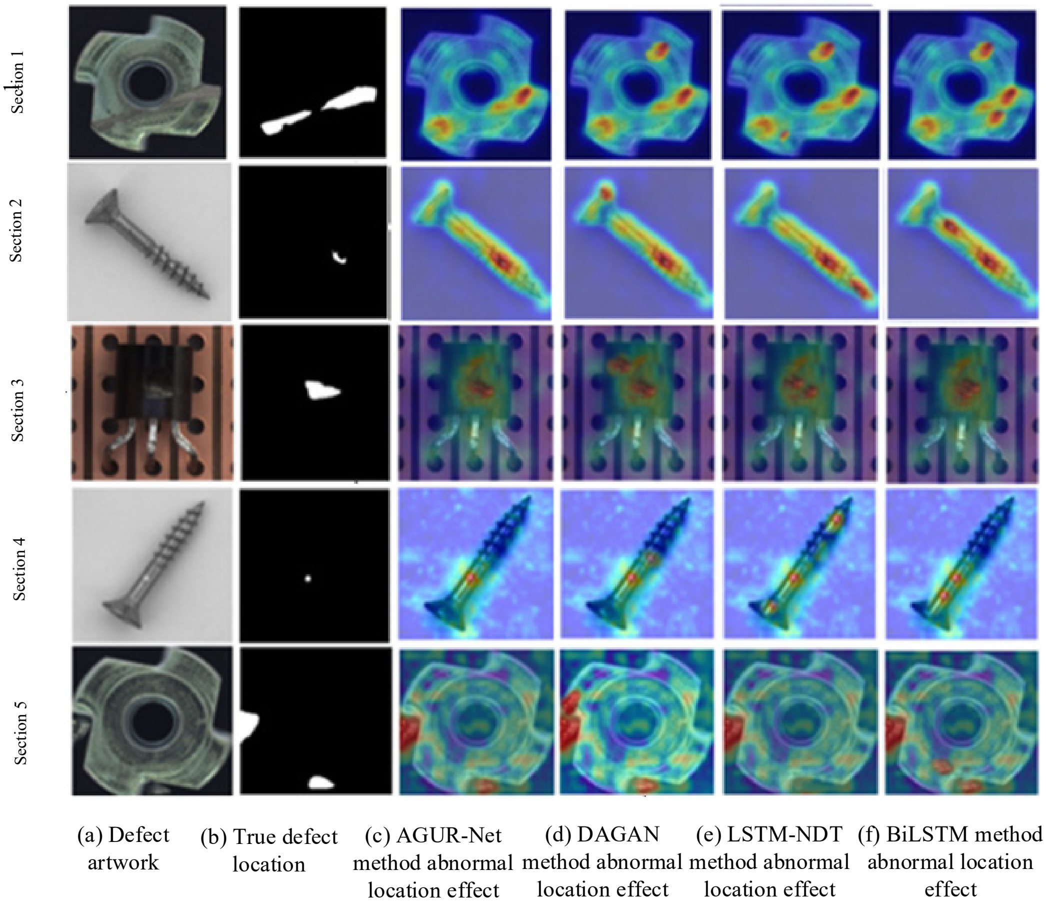

(a) Defect artwork (b) True defect location (c) AGUR-Net method abnormal location effect (d) DAGAN method abnormal location effect (e) LSTM-NDT method abnormal location effect (f) BiLSTM method abnormal location effect

Fig. 10 Comparison of visualization effects of anomaly localization

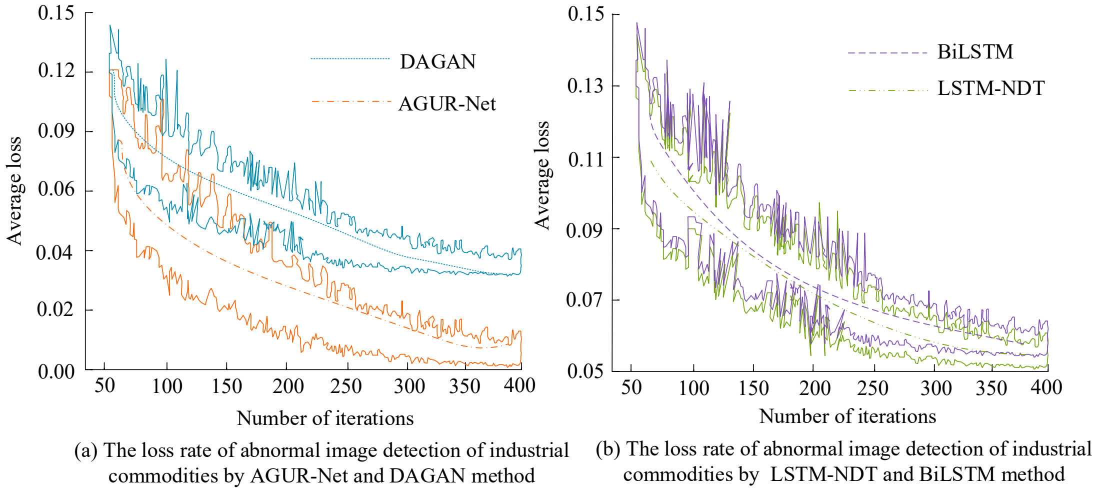

(a) The loss rate of abnormal image detection of industrial commodities by AGUR-Net and DAGAN method

(b) The loss rate of abnormal image detection of industrial commodities by LSTM-NDT and BiLSTM method

Fig. 11 Average loss value test results

Fig. 11(a) shows that AGUR-Net achieved an average loss of 0.016 at 400 iterations. DAGAN had an average loss ranging from 0.05 to 0.07 between 350 and 400 iterations. Fig. 11(b) shows that LSTM-NDT's average loss ranged from 0.053 to 0.082 between 200 and 250 iterations. BiLSTM's loss stabilized after 250 iterations, with a minimum of 0.053. To sum up, the AGUR-Net abnormal image detection method for electronic component production has good training convergence performance and can better capture abnormal features. To further validate its performance, AGUR-Net, DAGAN, LSTM-NDT, and BiLSTM were tested in real-time at Factory X1 and Factory X2. Two additional methods, Multi-Scale Convolutional Denoising Autoencoder (MSCDAE) and Conditional Normalizing Flow (CFlow), were included to increase diversity. These two methods were suitable for tiny defect detection and high-precision anomaly detection. Results are shown in Fig. 12.

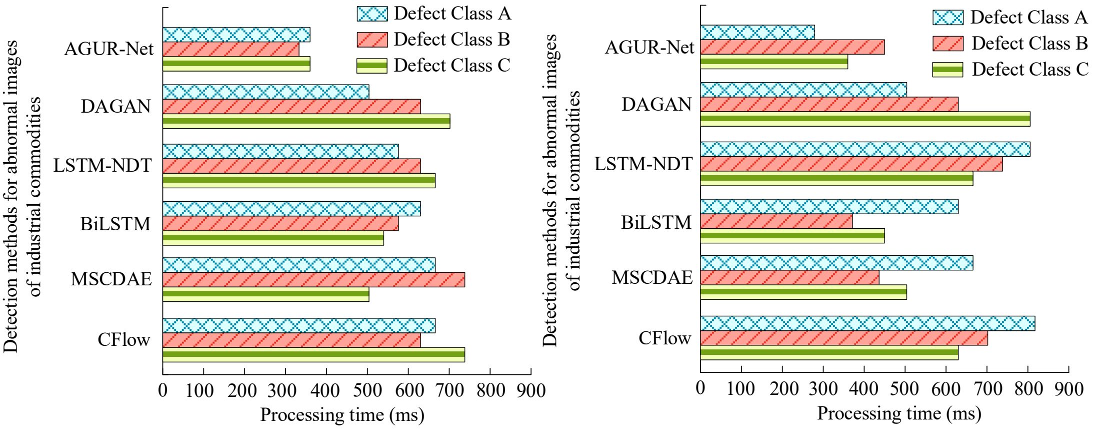

(a) Processing time results of single anomaly images with different detection methods in X1 factory

(b) Processing time results of single anomaly images with different detection methods in X2 factory

Fig. 12 Time results of processing a single abnormal image in different data sets

Fig. 12(a) shows that at Factory X1, AGUR-Net processed a single image with type-A, type-B, and type-C defects in 372 ms, 329 ms, and 378 ms, respectively. Fig. 12(b) shows that at Factory X2, the processing times for a single type-A defect image using AGUR-Net, DAGAN, LSTM-NDT, BiLSTM, MSCDAE, and CFlow were 289 ms, 507 ms, 806 ms, 623 ms, 672 ms, and 812 ms, respectively. AGUR-Net achieved faster processing due to its improved attention gate module, which precisely focused on target regions. Overall, AGUR-Net demonstrated high efficiency in real applications. In addition, six methods for detecting abnormal images of electronic component production, namely AGUR-Net, DAGAN, LSTM-NDT, BiLSTM, MSCDAE and CFlow, were also used in the study to test the F1 Score (F1) of abnormal images of industrial electronic component production. The test results are shown in Table 2.

Table 2 F1-score test results in different datasets

Dataset	Method	The number of abnormal samples				
		50	100	150	200	250
YDFID-1	AGUR-Net	0.971	0.939	0.947	0.927	0.935
	DAGAN	0.903	0.893	0.841	0.867	0.836
	LSTM-NDT	0.872	0.810	0.726	0.734	0.712
	BiLSTM	0.813	0.798	0.836	0.874	0.788
	MSCDAE	0.857	0.772	0.802	0.817	0.836
	CFlow	0.826	0.813	0.831	0.846	0.814
ECD	AGUR-Net	0.974	0.963	0.947	0.922	0.917
	DAGAN	0.923	0.903	0.896	0.882	0.873
	LSTM-NDT	0.902	0.895	0.883	0.862	0.814
	BiLSTM	0.877	0.871	0.863	0.763	0.741
	MSCDAE	0.891	0.826	0.831	0.846	0.819
	CFlow	0.863	0.825	0.817	0.798	0.774

According to Table 2, on the YDFID-1 dataset, AGUR-Net achieved an F1-score of 0.971 when detecting 50 anomalies, and 0.935 for 250 anomalies. On the ECD dataset, AGUR-Net achieved F1-scores of 0.974, 0.963, and 0.947 for 50, 100, and 150 anomalies, respectively. When detecting 200 anomalies, the F1-scores of LSTM-NDT, BiLSTM, MSCDAE, and CFlow were 0.862, 0.763, 0.846, and 0.798, all lower than AGUR-Net's 0.922. In summary, the AGUR-Net image detection method for anomaly detection in electronic component production can reduce the occurrence of false detections and missed detections and shows good overall performance in inspecting defects in industrial products. To quantify the contribution of each module to the final performance, ablation experiments were designed on the ECD dataset. Using the base U-Net, with all improved modules removed, as the baseline model, SSDAE, MGAN, the improved ECA module, attention gates, and pre-activated residual blocks were gradually added to test anomaly detection performance under each configuration. All experiments were repeated 5 times in the same environment, with different random seeds used to initialize network parameters, and the mean and standard deviation of each indicator were calculated to reflect the stability of the results. The evaluation indicators include AUC, F1 score, Precision, Recall, and single image processing time. The results of the ablation experiment are shown in Table 3.

According to Table 3, after adding SSDAE alone, AUC increased from 0.812 to 0.851, F1 score increased from 0.834 to 0.869, accuracy and recall increased to 0.874 and 0.864, respectively, indicating that denoising processing plays an important role in industrial image anomaly detection. After further adding MGAN, the AUC increased to 0.878, F1 score reached 0.893, accuracy and recall reached 0.896 and 0.890, respectively, verifying the effectiveness of multimodal feature expression for texture-related anomaly detection. Improving the ECA module resulted in a 0.013 increase in AUC and a 0.011 increase in F1 score, as well as a 0.011 and 0.011 increase in accuracy and recall, respectively. At the same time, there was a relatively small increase in parameter count. After adding attention gates and pre-activated residual blocks, the complete method achieved an AUC of 0.922, F1 score of 0.931, accuracy of 0.933, and recall of 0.929, which were improved by 0.110, 0.097, 0.092, and 0.102 respectively compared to the basic U-Net. In terms of the balance between accuracy and recall, the difference between the two indicators of the complete method is only 0.004, indicating that the model has achieved a good balance between reducing false positives and reducing missed detections. In terms of processing time, the complete method takes 378 ms for a single image, which is higher than the 246 ms of the basic U-Net, but still meets real-time requirements in practical industrial detection. The gradual increase of each module did not lead to a significant deterioration in processing time. In addition, the standard deviation of the 5 repeated experiments ranged from 0.005 to 0.012, indicating that the experimental results under all configurations had good stability, and the impact of random initialization on the final performance was relatively small. The above results demonstrate the effectiveness of each proposed module and also indicate that the source of performance improvement in the complete method is the collaborative effect of multiple modules rather than the contribution of a single component.

Table 3 Results of ablation experiment

Model configuration	AUC	F1-score	Precision	Recall	Processing time (ms)
Basic U-Net	0.812 ±0.011	0.834 ± 0.010	0.841± 0.012	0.827 ± 0.009	246
+ SSDAE	0.851± 0.009	0.869 ± 0.008	0.874 ± 0.010	0.864 ± 0.007	283
+ SSDAE + MGAN	0.878 ± 0.008	0.893 ± 0.007	0.896 ± 0.009	0.890 ± 0.008	319
+ SSDAE + MGAN + improved ECA	0.891 ± 0.007	0.904 ± 0.006	0.907 ± 0.008	0.901 ± 0.007	337
Complete method	0.922 ± 0.006	0.931 ± 0.005	0.933 ± 0.007	0.929 ± 0.006	378

4. Discussion

The proposed AGUR-Net anomaly image detection algorithm showed excellent performance in comparison experiments. In terms of anomaly region localization and anomaly image detection accuracy, AGUR-Net outperformed the LSTM-NDT, BiLSTM, and MSCDAE algorithms. In particular, on the MVTecAD and KSDD2 datasets, AGUR-Net maintained high localization accuracy and stability. This performance mainly resulted from its optimized design and strong image feature extraction ability. These results were consistent with the findings of Yan *et al*. and Song *et al*. in 2023 [26, 27]. AGUR-Net also achieved high anomaly image detection accuracy. After 250 iterations, the accuracy of industrial anomaly image detection remained above 75 %, reaching a maximum of 97.26 %, further confirming the algorithm's effectiveness. In the AUC test with a 10 % anomaly rate, AGUR-Net also performed well. Compared with LSTM-NDT, BiLSTM, and MSCDAE, the proposed algorithm consistently achieved an AUC above 0.850, proving its ability to classify industrial products accurately. On the MVTecAD dataset, AGUR-Net reached the highest AUC of 0.946 for the hazelnut samples, while the AUC values of DAGAN, LSTM-NDT, and BiLSTM were 0.832, 0.874, and 0.816 respectively. This advantage was mainly attributed to the improved attention gate module and pre-activation fusion residual block in AGUR-Net, which enhanced its responsiveness to defect regions and its robustness to interference. The results were in agreement with those obtained by Duan *et al*. in their evaluation of anomaly detection algorithms [28].

When the recognition performance for different industrial anomaly images was analyzed, AGUR-Net also demonstrated clear advantages. In the average-loss test for abnormal images from the processing and manufacturing stage of industrial products, the AGUR-Net-based anomaly image detection method for electronic component production achieved an average loss value of 0.016 after 400 iterations. When the number of iterations was between 100 and 200 times, the overall detection average loss value decreased rapidly. In contrast, after 400 iterations, the average loss of LSTM-NDT, BiLSTM, and MSCDAE reached 0.058, 0.061, and 0.067 respectively, all higher than that of the proposed method. This is mainly attributed to the MGAN module in the AGUR-Net-based anomaly image detection method for electronic component production, which improves feature representation and enhances anomaly discrimination in images from the processing and manufacturing stages. Compared with related studies, the anomaly image detection method for electronic component production proposed in this study showed greatly improved performance. In real-time single-image detection speed tests at Factory X2, AGUR-Net also outperformed other methods. It required only 289 ms to process a single image with a type-A defect, while DAGAN, LSTM-NDT, BiLSTM, MSCDAE, and CFlow took 507 ms, 806 ms, 623 ms, 672 ms, and 812 ms respectively. These results proved the superior detection efficiency of AGUR-Net.

The main contributions of this research are twofold: first, a new AGUR-Net anomaly image detection algorithm was designed; second, an image detection method for anomaly detection in electronic component production based on this algorithm was proposed. During the design process, the combination of MGAN and SSDAE networks for image location and classification has improved the accuracy of abnormal target recognition. These contributions have provided new ideas and effective solutions for complex image defect recognition in the fields of intelligent manufacturing and electronic component manufacturing.

5. Conclusion

To address difficulties in identifying defect images and localizing anomalies in the production process of electronic components such as resistors and capacitors, this study proposes an anomaly image detection method for electronic component production based on the AGUR-Net algorithm to improve anomaly detection accuracy in industrial products. The experimental results show that the AGUR-Net abnormal image detection algorithm has high abnormal location accuracy. Furthermore, the empirical results for the proposed anomaly image detection method for electronic component production show that, in single-image processing tests on industrial products, the method requires less time and achieves higher overall detection efficiency. Moreover, anomaly localization is carried out on images from the stages of raw material preparation, processing and manufacturing, surface treatment, quality inspection, and packaging and transportation of parts. The AGUR-Net anomaly image detection method for electronic component production has a better anomaly localization effect on images in the surface treatment stage, and the heat-map distribution area is relatively concentrated. Overall, the AGUR-Net-based anomaly image detection method for electronic component production can not only accurately classify industrial targets, but also precisely localize anomalies in the production processes of different industrial products. However, there are still limitations to the research, and its generalization ability in factory production lines or other industrial scenarios still needs further testing. There may be significant differences between different factories in terms of image acquisition equipment, lighting conditions, product materials and textures, defect type distribution, etc., all of which may lead to a decrease in model performance. Therefore, future work can proceed in the following directions: first, conducting cross-factory transfer learning experiments to verify the degree of performance degradation when the model is directly applied to a target-domain factory after training in the source domain. Second, exploring few-sample or unsupervised domain adaptation methods to enable the model to adapt quickly using only a small number of unlabeled images from the target factory. Finally, the prototype system should be deployed in the actual production line and a long-term online evaluation should be conducted, collecting real testing data from different batches, different lighting conditions, and different product specifications to comprehensively measure the robustness and deployability of the method.

Acknowledgement

This work was supported by the Natural Science Foundation of Chengdu Aeronautic Polytechnic University (Grant No. ZZX0623061) and the Indoor Space Layout Optimization and Safety Assurance Laboratory of Chengdu Normal University (Project No. SNKJ202513).

References

[1] Leung, J.-H., Tsao, Y.-M., Karmakar, R., Mukundan, A., Lu, S.-C., Huang, S.-Y., Saenprasarn, P., Lo, C.-H., Wang, H.-C. (2024). Water pollution classification and detection by hyperspectral imaging, *Optics Express*, Vol. 32, No. 14, 23956-23965, doi: 10.1364/OE.522932.

[2] Zhao, T., Gu, Y., Yang, J., Usuyama, N., Lee, H.H., Kiblawi, S., Naumann, T., Gao, J., Crabtree, A., Abel, J., Moung-Wen, C., Piening, B., Bifulco, C., Wei, M., Poon, H., Wang, S. (2025). A foundation model for joint segmentation, detection and recognition of biomedical objects across nine modalities, *Nature Methods*, Vol. 22, No. 1, 166-176, doi: 10.1038/s41592-024-02499-w.

[3] Abid, A., Jemili, F., Korbaa, O. (2024). Real-time data fusion for intrusion detection in industrial control systems based on cloud computing and big data techniques, *Cluster Computing*, Vol. 27, No. 2, 2217-2238, doi: 10.1007/s10586-023-04087-7.

[4] Yang, Z., Zhang, M., Chen, Y., Hu, N., Gao, L., Liu, L., Song, J.I. (2024). Surface defect detection method for air rudder based on positive samples, *Journal of Intelligent Manufacturing*, Vol. 35, No. 1, 95-113, doi: 10.1007/s10845-022-02034-8.

[5] Ma, Y., Yin, J., Huang, F., Li, Q. (2024). Surface defect inspection of industrial products with object detection deep networks: A systematic review, *Artificial Intelligence Review*, Vol. 57, Article No. 333, doi: 10.1007/s10462-024-10956-3.

[6] Ullah, W., Khan, S.U., Kim, M.J., Hussain, A., Munsif, M., Lee, M.Y., Baik, S.W. (2024). Industrial defective chips detection using deep convolutional neural network with inverse feature matching mechanism, *Journal of Computational Design and Engineering*, Vol. 11, No. 3, 326-336, doi: 10.1093/jcde/qwae019.

[7] Liu, R., Xiao, D., Lin, D., Zhang, W. (2024). Intelligent bearing anomaly detection for industrial Internet of Things based on auto-encoder Wasserstein generative adversarial network, *IEEE Internet of Things Journal*, Vol. 11, No. 13, 22869-22879, doi: 10.1109/JIOT.2024.3358871.

[8] Gong, Y., Wang, X., Zhou, C., Ge, M., Liu, C., Zhang, X. (2025). Human-machine knowledge hybrid augmentation method for surface defect detection based few-data learning, *Journal of Intelligent Manufacturing*, Vol. 36, No. 3, 1723-1742, doi: 10.1007/s10845-023-02270-6.

[9] Bergmann, P., Batzner, K., Fauser, M., Sattlegger, D., Steger, C. (2022). Beyond dents and scratches: Logical constraints in unsupervised anomaly detection and localization, *International Journal of Computer Vision*, Vol. 130, 947-969, doi: 10.1007/s11263-022-01578-9.

[10] Liu, Y., Zhang, Y., Jiang, Y., Liu, W., Yang, F. (2023). UWB-INS fusion positioning based on a two-stage optimization algorithm, *Tehnički Vjesnik – Technical Gazette*, Vol. 30, No. 1, 185-190, doi: 10.17559/TV-20221019035741.

[11] Zhang, H., Guo, W., Zhang, S., Lu, H., Zhao, X. (2022). Unsupervised deep anomaly detection for medical images using an improved adversarial autoencoder, *Journal of Digital Imaging*, Vol. 35, No. 2, 153-161, doi: 10.1007/s10278-021-00558-8.

[12] Sun, Z., Wang, J., Li, Y. (2024). RAMFAE: A novel unsupervised visual anomaly detection method based on autoencoder, *International Journal of Machine Learning and Cybernetics*, Vol. 15, 355-369, doi: 10.1007/s13042-023-01913-7.

[13] Wei, Z.H., Yan, L., Yan, X. (2024). Optimizing production with deep reinforcement learning, *International Journal of Simulation Modelling*, Vol. 23, No. 4, 692-703, doi: 10.2507/IJSIMM23-4-CO17.

[14] Zhang, H., Wang, S., Lu, S., Yao, L., Hu, Y. (2023). Attention-Gate-based U-shaped Reconstruction Network (AGUR-Net) for color-patterned fabric defect detection, *Textile Research Journal*, Vol. 93, No. 15-16, 3459-3477, doi: 10.1177/00405175221149450.

[15] Li, C., Qi, L., Geng, X. (2025). A SAM-guided two-stream lightweight model for anomaly detection, *ACM Transactions on Multimedia Computing, Communications and Applications*, Vol. 21, No. 2, 1-23, doi: 10.1145/3706574.

[16] Korovin, A., Vasilev, A., Egorov, F., Saykin, D., Terukov, E., Shakhray, I., Zhukov, L. Budennyy, S. (2023). Anomaly detection in electroluminescence images of heterojunction solar cells, *Solar Energy*, Vol. 259, 130-136, doi: 10.1016/j.solener.2023.04.059.

[17] Yin, S., Li, H., Laghari, A.A., Gadekallu, T.R., Sampedro, G.A., Almadhor, A. (2024). An anomaly detection model based on deep auto-encoder and capsule graph convolution via Sparrow Search Algorithm in 6G Internet of Everything, *IEEE Internet of Things Journal*, Vol. 11, No. 18, 29402-29411, doi: 10.1109/JIOT.2024.3353337.

[18] Abdelmawla, A., Ma, S., Yang, J.J., Kim, S.S. (2023). Subsurface anomaly detection utilizing synthetic GPR images and deep learning model, *Geomechanics and Engineering*, Vol. 33, No. 2, 203-209, doi: 10.12989/gae.2023.33.2.203.

[19] Liu, H., Li, L. (2023). Anomaly detection of high-frequency sensing data in transportation infrastructure monitoring system based on fine-tuned model, *IEEE Sensors Journal*, Vol. 23, No. 8, 8630-8638, doi: 10.1109/JSEN.2023.3254506.

[20] Faber, K., Corizzo, R., Sniezynski, B., Japkowicz, N. (2023). VLAD: Task-agnostic VAE-based lifelong anomaly detection, *Neural Networks*, Vol. 165, 248-273, doi: 10.1016/j.neunet.2023.05.032.

[21] Yun, H., Kim, H., Jeong, Y.H., Jun, M.B.G.(2023). Autoencoder-based anomaly detection of industrial robot arm using stethoscope based internal sound sensor, *Journal of Intelligent Manufacturing*, Vol. 34, 1427-1444, doi: 10.1007/s10845-021-01862-4.

[22] Wang, Y., Fang, R. (2023). An approach for fast fault detection in virtual network, *Tehnički Vjesnik – Technical Gazette*, Vol. 30, No. 4, 1146-1151, doi: 10.17559/TV-20230207000330.

[23] Wang, X., Liu, C., Hou, J., Zhou, L. (2024). Advancing crack segmentation detection: Introducing AAMC-Net algorithm for image crack analysis, *Computer Science and Information Systems*, Vol. 21, No. 4, 1435-1455, doi: 10.2298/CSIS230725042W.

[24] Liu, J., Zhou, G. (2024). Learning discriminative representations through an attention mechanism for image-based person re-identification, *Computer Science and Information Systems*, Vol. 21, No. 4, 1483-1498, doi: 10.2298/CSIS230829044L.

[25] Aka, A.C., Atta, A.F., Keupondjo, S.G.A., Oumtanaga, S. (2023). An efficient anchor-free localization algorithm for all cluster topologies in a wireless sensor network, *International Journal of Computers Communications & Control*, Vol. 18, No. 3, Article No. 4961, doi: 10.15837/ijccc.2023.3.4961.

[26] Yan, S., Chen, P., Chen, H., Mao, H., Chen, F., Lin, Z. (2024). Multiresolution feature guidance based transformer for anomaly detection, *Applied Intelligence*, Vol. 54, No. 2, 1831-1846, doi: 10.1007/s10489-024-05283-7.

[27] Song, J., Lee, Y.C., Lee, J. (2023). Deep generative model with time series-image encoding for manufacturing fault detection in die casting process, *Journal of Intelligent Manufacturing*, Vol. 34, No. 7, 3001-3014, doi: 10.1007/s10845-022-01981-6.

[28] Duan, M., Mao, L., Liu, R., Liu, W., Liu, Z. (2024). Unified model based on reinforced feature reconstruction for metro track anomaly detection, *IEEE Sensors Journal*, Vol. 24, No. 4, 5025-5038, doi: 10.1109/JSEN.2023.3348118.

APEM journal
Advances in Production Engineering & Management
Volume 21 | Number 1 | March 2026 | pp 117–138
https://doi.org/10.14743/apem2026.1.565

ISSN 1854-6250
Journal home: apem-journal.org
Original scientific paper

Numerical modeling and experimental validation of an adaptive pneumatic gripper for collaborative robotic palletizing

Karabegović, I.[a,*], Isić, S.[b], Vojić, S.[c], Husak, E.[c], Banjanović-Mehmedović, L.[d], Mahmić, M.[c], Bičo Ćar, M.[e], Radončić, A.[f]

[a]Academy of Sciences and Arts of Bosnia and Herzegovina, Sarajevo, Bosnia and Herzegovina
[b]University "Džemal Bijedić" of Mostar, Mechanical Faculty, Mostar, Bosnia and Herzegovina
[c]University of Bihać, Technical Faculty Bihać, Bihać, Bosnia and Herzegovina
[d]University of Tuzla, Faculty of Electrical Engineering, Tuzla, Bosnia and Herzegovina
[e]University of Sarajevo, School of Economic and Business, Sarajevo, Bosnia and Herzegovina
[f]International BURCH University of Sarajevo, Sarajevo, Bosnia and Herzegovina

ABSTRACT

This paper presents the development and experimental validation of an adaptive pneumatic gripper for collaborative robotic palletizing of packages with varying mass and surface characteristics. The main objective is to determine the optimal gripping-force and minimum operating pressure required to ensure stable and safe handling without slippage. A dynamic mathematical model was developed, incorporating the effects of package mass, friction coefficient, contact surface area, and inertial forces during manipulation. Numerical analysis was performed for different friction conditions (μ = 0.30-0.90) and contact configurations, enabling the determination of the minimum required gripping-forces and corresponding operating pressures. Experimental validation was conducted on a real industrial system with a collaborative robot. The results show a linear relationship between pressure and gripping-force, described by $F = 22.152\,p - 17.535$, with a high correlation coefficient ($R^2 \approx 0.998$). The maximum experimentally obtained gripping-force was approximately 70-75 N at a pressure of around 4 bar. Quantitative deviations between numerical and experimental results (65-75 %) were observed and corrected by introducing a calibration factor ($k_{corr} \approx$ 0.30). The proposed model and experimental system enable reliable optimization of gripping-force and improve manipulation stability under real industrial conditions. The main contribution of this study lies in the integration of analytical modelling, numerical optimization, and industrial experimental validation for collaborative robotic palletizing systems

ARTICLE INFO

Keywords:
Adaptive pneumatic gripper;
Collaborative robotic palletizing;
Gripping-force optimization;
Friction-based gripping;
Pneumatic actuation;
Numerical modelling;
Experimental validation;
Industrial robotics

**Corresponding author:*
isak1910@hotmail.com
(Karabegović, I.)

Article history:
Received 3 March 2026
Revised 4 April 2026
Accepted 9 April 2026

1. Introduction

In recent years, the implementation of Industry 4.0 technologies has significantly transformed manufacturing systems, enabling higher efficiency, flexibility, and reliability of production processes. Material handling operations, including picking, sorting, and palletizing, have become key components of automation in modern production and logistics systems [1]. Alongside conventional industrial robots, the growing implementation of collaborative robots (cobots) has enabled safer human–robot interaction and more flexible integration into modern manufacturing environments. This technological advancement has accelerated the development of adaptive and soft robotic grippers capable of manipulating objects with diverse dimensions, masses, and surface properties [2-4]. Despite recent advances, reliable manipulation and palletizing of heterogeneous packages remain a major challenge. Conventional grippers are typically designed for uniform objects, which limits their applicability in dynamic production environments and may lead to unstable gripping, product deformation, and reduced operational efficiency. The need for adaptive and flexible gripping solutions has been confirmed in studies addressing multi-object grasping and modular or detachable gripper concepts [5, 6]. Motivated by these challenges, this paper focuses on the development and optimization of an adaptive pneumatic gripper for collaborative robotic palletizing of packages with masses up to 10 kg. A dynamic mathematical model of gripping-force is developed, considering the effects of friction, contact surface, and inertial forces during manipulation. In contrast to previous studies that are primarily based on simulations or laboratory experiments, the proposed model is experimentally validated under real industrial conditions [7-9]. The main contribution of this research lies in the integration of analytical modelling, numerical optimization, and experimental validation, providing a reliable framework for the design and application of adaptive grippers in collaborative robotic systems.

2. Critical review of contemporary research on adaptive robotic grippers

2.1 Adaptive grippers in collaborative robotics

During the handling and manipulation of materials, semi-finished products, and finished products of different dimensions and shapes in manufacturing processes, flexible and adaptive grippers represent one of the fundamental components in the automation of production systems. In recent years, research and development of soft adaptive grippers have intensified through the implementation of advanced elastic materials, combined actuation mechanisms, and contact control systems between the gripper fingers and manipulated objects, as widely reported in studies on soft robotic grippers and granular jamming-based gripping systems [10, 11].

Of particular importance is the concept of variable stiffness, which enables an increase in gripping-force while maintaining adaptation to the shape of the object. Systems such as the Variable Stiffness Particle Phalange demonstrate an efficient transition between flexible and rigid manipulation modes [12, 13]. Hybrid systems that combine flexible and rigid elements expand the functional range of manipulation, simultaneously enabling stable gripping and high adaptability to the object. With the implementation of collaborative robots in manufacturing automation, technical requirements are increasingly shaped by safety standards and the need for safe human–robot interaction. Iqbal *et al.* [6] in their research propose the concept of detachable grippers that increase system flexibility and operational safety. The implementation of reconfigurable finger joints and optimized cobot operating parameters enables controlled stiffness variation during real-time operation, thereby ensuring safe and efficient adaptation of the manipulation process in collaborative industrial environments [14, 15].

2.2 Contemporary grasping techniques and product manipulation in intelligent manufacturing processes

Grippers used in traditional and collaborative industrial robots employ mechanical, pneumatic, and hybrid approaches, while recent development trends are directed toward adaptive systems based on sensory feedback. Recent approaches also include the application of reinforcement learning methods for adaptive robotic manipulation in human–robot collaboration environments, enabling improved grasping performance under uncertain and dynamic conditions [16]. Recent developments also include adaptive force control strategies for soft robotic gripping systems [17]. Soft pneumatic grippers are constructed on the principle of interconnected pressurized chambers, structures based on the jamming effect, and combined actuators that enable high contact adaptability. Grippers with variable stiffness mechanisms, capable of transitioning from a soft, flexible state to a rigid state through the application of external pressure or vacuum, are particularly effective in manipulating sensitive or deformable objects without causing damage [18-20]. Biomechanically inspired designs with multiple curvatures and variable stiffness optimize contact pressure distribution and enhance gripping stability. Palletizing system configurations within Industry 4.0 manufacturing environments are evolving toward modular and intelligent architectures that integrate adaptive grippers and sensory feedback, thereby improving flexibility, reliability, and cycle efficiency in dynamic production cells [21, 22].

2.3 Limitations of existing solutions and development perspectives

Despite significant technological progress achieved in recent years, existing gripper solutions remain limited in terms of load capacity, long-term reliability, and performance validation in real, continuous industrial operations. Many grippers are optimized for specific tasks or uniform objects, whereas highly adaptable configurations remain insufficiently investigated under industrial operating conditions. From the perspective of operational safety, Patalas-Maliszewska [23] emphasizes that the requirements of ISO/TS 15066 are often not systematically integrated during the early design stages of gripper design, particularly in soft and hybrid systems. Although variable stiffness represents a promising concept, its real-time control in dynamic industrial cells remains a technical challenge [24]. These shortcomings indicate the need to develop adaptive grippers that are energy-efficient, safety-compliant, sensor-equipped, and capable of stable and reliable gripping-force control. The proposed methodology integrates an analytical model, numerical optimization, and industrial experimental validation in order to improve existing solutions.

3. Research methodology

The research focuses on the development of an adaptive gripper for automated manipulation and palletizing of products with different masses and dimensions. The proposed methodology combines engineering calculations, numerical modeling, simulation analysis, and experimental verification within a collaborative robotic system. The applied methodological framework enables the development of an adaptive gripper capable of reliably handling packages weighing up to 10 kg, with a focus on stable gripping, operational safety, and optimal distribution of contact forces. The research methodology is divided into two parts:

- development and investigation of the numerical model of gripping-force, and
- design and implementation of experimental research for the purpose of verifying the obtained results.

3.1 Development of the numerical model of gripping-force

The development of the gripping-force model for the adaptive gripper begins with defining the characteristics of the products handled and palletized by the system. The analysis included product geometry, mass, surface stiffness, as well as the coefficient of friction occurring between the gripper fingers and the product during gripping. The adaptive gripper is designed to handle products weighing up to 10 kg while ensuring reliable handling, uniform distribution of contact forces, and prevention of slipping during lifting and transportation. During lifting and transfer of the product, the interaction between contact forces, gripping stability, and variable stiffness characteristics must be carefully considered. These factors are essential for minimizing deformation and ensuring reliable force distribution during the manipulation of objects with different geometric and mechanical properties, as emphasized in [25]. The listed parameters directly influence the selection of the gripping mechanism and the required gripping-force, particularly for products of different masses and variable shapes.

Based on the functional requirements, the technical characteristics of the adaptive gripper were defined as follows:

- maximum allowable load up to 10 kg,
- minimum gripping depth for objects with irregular geometric shapes,
- optimal cycle time in a real industrial environment,
- structural limitations caused by stiffness and deformation in the contact zone,
- compliance with the safety requirements defined by ISO/TS 15066 for collaborative robots.

Based on recommendations from the literature, the gripper design included an assessment of safety risks under conditions of close human–collaborative robot interaction, defining safety force limits as well as control mechanisms to prevent overload during object gripping. After defining the requirements, the optimal gripping principle using the gripper was selected. The package-handling system employs an adaptive gripper with two rigid fingers, where gripping stability results from mechanical strength and proper dimensioning of the contact surfaces. In accordance with previous research, systems based on rigid mechanical construction provide high stability and reliability of manipulation. Adjustment of the gripping-force is achieved through the control system, enabling precise real-time control of the gripping-force, which is particularly important when handling different loads in palletizing processes.

Within the numerical analysis, the following steps were carried out:

- 3D modeling of the gripper,
- force analysis using the finite element method (FEA),
- optimization of contact geometry,
- simulation of lifting packages weighing up to 10 kg.

The simulations analyzed deformations, stress distribution, and the response of flexible elements under load. Dynamic simulations were also conducted to assess gripping stability during robot acceleration in palletizing cycles. This approach enabled design optimization prior to manufacturing the physical prototype.

3.2 Definition of experimental configuration parameters

The integration of the adaptive gripper with the collaborative robot was realized using a standard flange connection, in accordance with ISO 9409-1. The mechatronic gripper–collaborative robot system was equipped with sensors for measuring pressure, force, and displacement, enabling real-time data acquisition and verification of numerical values of the gripping-force.

The experiment defined the following parameters:

- verification of safety limits of the gripping-force,
- positioning accuracy during palletizing,
- repeatability of gripping and releasing cycles,
- manipulation stability under vertical and horizontal accelerations.

During experimental investigations, the listed system parameters were tested under real industrial conditions, with different product masses and varying contact conditions, including different coefficients of friction and contact surfaces between the adaptive gripper fingers and the product. Effective force control ensured stable manipulation of different loads, confirming the industrial applicability of the system. Final system verification was conducted through testing of the palletizing cycle with two different product masses. The obtained results confirmed the reliability, stability, and operational efficiency of the gripper under industrial operating conditions.

3.3 Research hypothesis

The integration of an analytical gripping-force model based on stability conditions, combined with numerical optimization of contact parameters and experimental validation, enables accurate prediction of the required gripping-force and ensures stable and safe handling of packages with variable mass (up to 10 kg) in collaborative robotic systems under real industrial conditions.

The key analytical relations used in the gripping-force model are given below. For clarity and consistency, the following notation is adopted throughout the analytical and numerical analysis:

- external load acting on the package,
- gravitational force acting on the package,
- inertial force generated during robot motion,
- friction force at the finger–package interface,
- minimum required normal gripping-force,
- operational gripping-force generated by the pneumatic actuator,
- contact area between the gripper fingers and the package,
- effective pneumatic-cylinder piston area.

The minimum required normal gripping-force is determined from the friction stability condition:

$$F_{N,min} = \frac{m \cdot g}{\mu} \tag{1}$$

where m is the package mass, g is the gravitational acceleration, and μ is the friction coefficient between the gripper fingers and the package surface.

The operational gripping-force generated by the pneumatic actuator is determined as:

$$F_{op} = p \cdot A_p \tag{2}$$

where p denotes the pneumatic operating pressure and A_p represents the effective pneumatic-cylinder piston area.

4. Development of an adaptive gripper

4.1 Conceptual analysis and design of the adaptive gripper

Conceptual approach and definition of geometry

In the design development process of an adaptive gripper, it is necessary to begin with its geometric solution, which should enable universal application in the manipulation of products (in this case boxes) of different dimensions and shapes. The structure of the adaptive gripper itself is based on a combination of elastic and rigid elements in order to achieve the capability of adapting to the contact surface of the product being manipulated. The application of variable stiffness in the gripper enables the adaptation of the structure to operational requirements, thereby increasing the stability and safety of manipulation. Such an approach in the development of the adaptive gripper design contributes to increased reliability when handling heavier loads, as confirmed in relevant research.

Structural elements and material selection

The selection of appropriate materials for the construction of the adaptive gripper plays a key role in achieving the durability of the gripper itself and in attaining functional adaptability. For the adaptive gripper we used an aluminum structure with two fingers, and in the aluminum two-finger gripper the change of stiffness is not achieved through elastic chambers or jamming mechanisms, but stability and gripping-force are regulated by pneumatic drive and the mechanical structure of the lever system. Such a gripper structure ensures high mechanical resistance and minimal deformations under load, while adaptation to different packages is achieved by adjusting the operating pressure in the cylinder. In this way, control and regulation of the gripping-force is enabled depending on the mass and dimensions of the product. The fingers that provide the contact surfaces are coated with industrial rubber with a high coefficient of friction, thereby compensating for the lack of elastic adaptive elements and ensuring stable contact without slipping. The aluminum frame structure of the adaptive gripper is modular, allowing easy replacement of fingers or pads, as well as adjustment of the gripping width without complex structural interventions. Consequently, a reliable and technically simple configuration suitable for industrial and logistics applications is achieved.

Adaptation to packages of different dimensions

With the adaptive aluminum two-finger gripper, adaptation to different package dimensions for lifting is achieved by mechanical adjustment of the finger stroke range and force regulation through the pneumatic system. Controlled opening and closing of the gripper is achieved by a double-acting cylinder, while the adjustable gripping width enables manipulation of packages with different dimensions without requiring complex adaptive mechanisms. Optimal contact with the object surface is achieved by parallel movement of the fingers and uniform distribution of force through rubber contact pads. Regulation of the working air pressure enables precise adjustment of the gripping-force in accordance with the mass and characteristics of the package, thereby preventing slipping or deformation of the packaging. The simple mechanical structure of the adaptive gripper achieved by a lever system ensures stability and synchronized finger movement without increasing control complexity. Consequently, reliable and efficient adaptation to standard logistics packages of different dimensions is achieved, while maintaining the robustness and industrial applicability of the system.

Integrated sensor system

The adaptive gripper is equipped with force and pressure sensors, as well as contact-detection modules. These components continuously monitor deformations and stresses within the structure. Positioning sensors additionally enable precise determination of the relative position of the fingers in relation to the object. In the adaptive aluminum two-finger gripper, the structure is optimized to achieve both low mass and sufficient mechanical strength. During the product-gripping phase, the system adapts to the contact surface through the geometric configuration of the fingers and controlled clamping pressure. During load transport, the structure ensures stable force transmission with minimal deformation due to the appropriate dimensioning of profiles and joints. The CAD model of the gripper was developed in a 3D environment, where all key elements were modeled: aluminum supports, finger actuation mechanism, contact surfaces, and mounting interface to the robotic arm. It must be emphasized that special attention was devoted to optimization of mass and stiffness of the structure through material selection (aluminum alloy) and appropriate cross-sections. The functionality and mechanical reliability of the structure were verified by numerical simulations, including FEA analyses of deformations, stress distribution, and safety factor under different loads. After the analytical-numerical analysis of the structure, experimental testing of the gripper was performed on objects of different masses and dimensions, thereby confirming gripping stability, uniform force distribution, and reliable operation under real industrial operating conditions.

4.2 A new concept of an adaptive gripper for manipulation of packages of different dimensions

For the development of the design of an adaptive gripper for manipulation of packages of different dimensions, we had four concepts with structures of three and two fingers, as shown in Fig. 1. During the realization of the structure, we decided on the design of the adaptive gripper shown in Fig. 1d. The gripper shown in Fig. 1d was designed as a compact, lightweight, and modular unit intended to be integrated with a collaborative robot for operation in an industrial environment. The structure of the presented adaptive gripper is optimized for the manipulation of packages of different masses and dimensions, while ensuring stability, safety, and high repeatability of grasping operations during palletizing of finished products in an industrial environment. Modern approaches to the development of adaptive grippers integrated with collaborative robots emphasize the need to balance mechanical strength and adaptability, particularly in applications where direct human–robot interaction is present [23]. The load-bearing structure of the adaptive gripper consists of an aluminum profile frame (as shown in Fig. 1d), which enables a favorable ratio between mass and mechanical resistance. The use of aluminum contributes to the reduction of system inertia, which is crucial for operation with collaborative robots where safety standards require limited kinetic energy. The modular concept allows easy integration of additional sensing and control components. According to contemporary research in the field of flexible grippers, modularity and reconfigurability represent key factors in adaptive manipulation systems [26]. In the gripper, the central working mechanism is a double-acting pneumatic cylinder located in the upper part of the structure. Motion transmission is realized through a lever system that synchronously actuates two symmetrical fingers. Pneumatic drive enables fast and repeatable working cycles, which is of particular importance in logistics applications with high package throughput. By regulating the input pressure of compressed air, precise control of the gripping-force is achieved, ensuring stable manipulation without damaging the packaging.

Research in the field of variable stiffness and adaptive grippers confirms that controlled force regulation directly influences contact stability and significantly reduces the risk of slipping during manipulation [27]. The gripper fingers are made of aluminum alloy with protruding triangular elements for mass reduction (as shown in Fig. 1d), while their contact surfaces are coated with industrial rubber with a high coefficient of friction (EPDM or NBR). Consequently, a solution is obtained that increases grasping stability and reduces the required normal contact force. The coefficient of friction represents one of the key parameters in calculating the minimum gripping-force, as emphasized in research on adaptive and soft-grip systems [28]. The implemented structure of the adaptive gripper is suitable for manipulation of cardboard boxes, plastic containers, and other objects with flat contact surfaces typical for e-commerce and logistics systems. The developed adaptive gripper structure demonstrates high efficiency in production processes involving products of different masses and dimensions. However, certain limitations occur when handling packages heavier than 10 kg, deformable products, or irregularly shaped items. When manipulation of such products is required, it is necessary to use more advanced solutions such as vacuum or soft robotic grippers. Despite the mentioned limitations, the simplicity of the structure, operational reliability, and optimized mass make this adaptive gripper a practical solution for collaborative robotic applications in modern industrial environments.

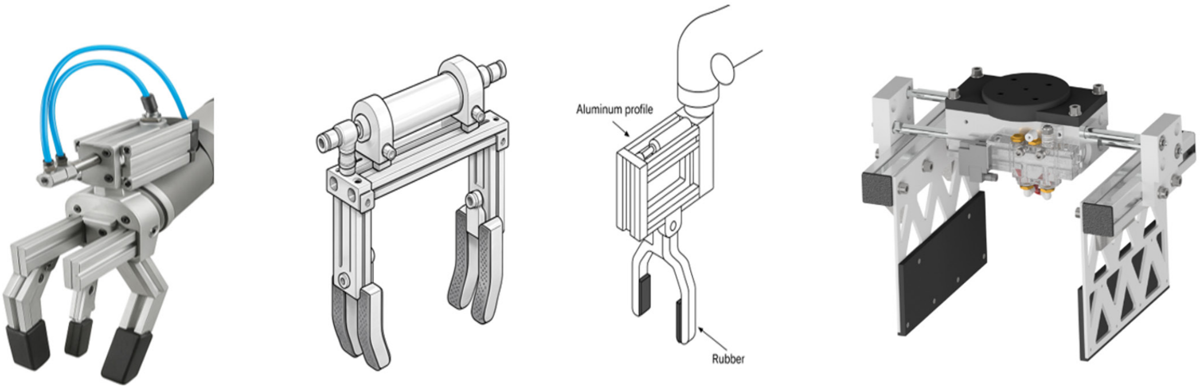

a) b) c) d)

Fig. 1 Different design solutions of the adaptive gripper for package grasping

Technical characteristics and performance analysis of the adaptive gripper

The adaptive aluminum two-finger gripper is designed for production processes in which finished products are transferred from a conveyor belt onto a Euro pallet. In addition to this application, the gripper is intended for use in warehouses, e-commerce distribution systems, logistics centers, and assembly lines, where it can be integrated with collaborative robots from various manufacturers, including KUKA iiwa, FANUC CRX, UR, Hanwha, Doosan, and JAKA.

Structure and materials

- The load-bearing frame is made of aluminum profiles with dimensions 30×30 mm,
- The fingers are designed and manufactured from aluminum alloy sheet metal with a thickness of 5 mm (where certain areas are removed in triangular shapes to reduce weight) with joint mechanisms,
- Contact coating: industrial rubber (EPDM, NBR),
- Drive element: double-acting pneumatic cylinder,
- Transmission mechanism: system of levers and sliding joints.

Pneumatic performance

- Operating pressure: 4-7 bar,
- Cycle time: approximately 0.1-0.3 s,
- Gripping-force regulation is ensured by adjusting the input pressure.

Mass and payload

- Gripper mass: 0.5-1.2 kg (depending on configuration),
- Payload capacity: 2-10 kg, depending on finger width and coefficient of friction.

Integration

- Standardized flange according to ISO 9409-1,
- Possibility of integrating additional sensor and soft-grip modules.

The adaptive pneumatic aluminum gripper offers several advantages, including modularity, low mass, adjustable gripping-force, and simple integration into existing industrial processes. However, limitations occur when handling non-standard or sensitive packages. At the same time, the identified disadvantages and limitations indicate areas that require further technological improvement, particularly when handling non-standard or sensitive packages. These technical characteristics provide a reliable basis for further numerical and experimental evaluation of the gripper's performance under real industrial conditions. A quantitative analysis of key technical parameters was performed with the aim of objectively assessing the functional and operational properties of the adaptive pneumatic aluminum gripper. Relevant indicators of cycle efficiency, safety factor, coefficient of friction, maximum gripping-force, and deformation behavior of the system under load were analyzed and evaluated. Objective quantitative verification of robotic end-effectors and safe physical human–robot interaction represents a dominant research approach in collaborative robotic systems operating alongside humans [29, 30]. Certain parameters, such as minimum gripping-force, safety coefficient, contact stability, and adaptive force regulation, are directly related to manipulation reliability and prevention of object slipping during handling operations. In the analysis of the adaptive pneumatic gripper, analytical and performance-evaluation approaches based on the relationship between load mass, gravitational acceleration, coefficient of friction, and adaptive force regulation are increasingly used to optimize gripping-force without unnecessarily increasing contact pressure. Similar optimization principles have also been discussed in studies on bio-inspired soft robotic concepts [31, 32]. The obtained results provide a reliable basis for validation of the structural solution and further optimization of operational performance.

The analysis of the data presented in Table 1 confirms that the adaptive pneumatic gripper achieves high operational reliability and stability when manipulating standard logistics packages. A safety factor greater than 1.5 ensures stable handling even under variations in mass, while the coefficient of friction has a decisive influence on the optimization of gripping-force and the prevention of slipping. Such an approach to quantitative evaluation is aligned with contemporary methodologies for the validation of industrial robotic systems, particularly in the case of collaborative robots.

Table 1 Quantitative performance analysis of the adaptive pneumatic gripper

Evaluation parameter	Description of functional aspect	Typical values (Experimental range)	Engineering interpretation
Cycle efficiency (%)	Ratio of successful grasps to total number of operations	96-99 %	High repeatability and manipulation reliability
Cycle time (s)	Time required for opening and closing of the fingers	0.10-0.30 s	Suitable for high-frequency logistics processes
Safety factor (k_s)	Ratio of maximum load capacity to nominal load	1.5-2.2	Ensures stability under variations in package mass
Coefficient of friction (μ)	Rubber–cardboard / rubber–plastic contact	0.60-0.85	Directly influences the required gripping-force
Maximum gripping-force (N)	Generated force at an operating pressure of 6 bar	120-250 N	Adjustable by regulating input pressure
Maximum elastic deformation (mm)	Finger deformation under full load	0.5-1.8 mm	Within allowable elastic limits
Energy consumption per cycle (J)	Compressed air consumption per operation	8-18 J	Depends on cylinder volume and operating pressure
Maximum payload (kg)	Maximum allowable package mass	2-10 kg	Depending on finger width and friction

5. Numerical analysis of gripping-force

The numerical analysis of the gripping-force of the object (package) was carried out by performing an analysis of the optimal gripping-force. The optimal gripping-force is determined based on the mass of the product, the coefficient of friction of the finger material, and the geometry of the contact surface. Excessive force may cause deformation of the package, while insufficient force increases the risk of slipping. The numerical analysis of the gripping-forces was modeled by applying a sliding friction model and contact pressure occurring on the fingers of the analyzed gripper. The optimal gripping-force for object manipulation (packages) is defined by relating it to the weight of the package lifted by the gripper and the coefficient of friction:

$$
\begin{gathered}
F_\mu = \mu \cdot F_N \\
F_\mu \geq m \cdot g \\
F_N \geq \frac{m \cdot g}{\mu}
\end{gathered}
\tag{3}
$$

Here, F_N denotes the total normal gripping-force applied by the gripper fingers, while F_μ represents the friction force generated at the contact interface.

The optimization model for determining the gripping-force is based on the package mass and the contact area between the gripper fingers and the package. After determining the minimum required normal gripping-force, the force distribution over the contact surface is analyzed in order to avoid local damage and deformation of the package during manipulation. The contact pressure between the gripper fingers and the package is defined by Eq. 4 and is determined based on the operational gripping-force and the total contact area.

The contact pressure between the gripper fingers and the package is defined as:

$$
p_k = \frac{F_{op}}{A_k}
\tag{4}
$$

where p_k denotes the contact pressure between the gripper fingers and the package, is the operational gripping-force generated by the pneumatic actuator, and A_k represents the total contact area between the gripper fingers and the package.

The pneumatic actuators integrated into the gripper structure enable precise regulation of the gripping-force through adjustment of the input pressure, thereby facilitating reliable manipulation of packages with different masses and geometric characteristics. Their fast response and simple mechanical configuration make them well suited for industrial robotic grippers, where stable and adaptive force control is required. By integrating force sensors, adaptive control algorithms, and advanced robotic end-effector frameworks into the gripper system, higher operational accuracy and continuous monitoring of the contact force at the object interface are achieved, enabling improved force regulation, adaptive gripping performance, and manipulation stability under real operating conditions [33, 34]. Based on this feedback, the system can adaptively adjust the gripping-force in real time, reducing the risk of deformation of sensitive products or dropping of the object (load slipping). Consequently, a more stable and safer manipulation process is achieved, especially in applications where objects differ in mass, material, or friction characteristics. Adaptive adjustment of the gripping-force requires the integration of a sensor-feedback-based control system, as illustrated in Fig. 2. Autonomous control enables feedback based on measured values, rather than predefined pressure settings. The control algorithm of the pneumatic (or vacuum) robotic gripper used for object handling is shown in the block diagram in Fig. 2, where the signal flow from the sensor, through the controller, to the actuator is clearly illustrated.

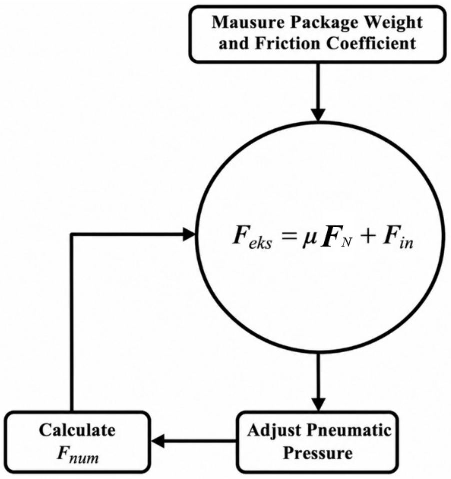

Fig. 2 Optimization control diagram of the adaptive pneumatic gripper

The control scheme of the pneumatic gripper begins with the determination of the package mass and the coefficient of friction between the gripper fingers and the object surface, as grasp stability, adaptive force regulation, and contact interaction are critical factors in the robotic manipulation of objects with varying stiffness and surface characteristics [35]. The pressure regulator controls the pneumatic actuator in order to achieve the desired gripping-force, while feedback obtained from the integrated force sensors enables adaptive real-time adjustment and prevents the application of excessive contact force. Consequently, the implemented control structure improves manipulation stability and enables wider grasping capability through adaptive stiffness regulation of the gripper fingers under varying operating conditions [36].

5.1 Numerical estimation of the gripping-force as a function of the variable coefficient of friction and effective contact area in the palletizing production process

This section presents a numerical example of calculating the optimal gripping-force for lifting a package based on real input parameters. The numerical analysis was performed on a finished product in the production process, a package with dimensions 280 × 190 × 100 mm and a mass of 6 kg, shown in Fig. 3. The package consists of six jars of jam wrapped in smooth plastic film. The packages arrive at the production line, where they are picked up by a collaborative robot equipped with a gripper and placed onto a pallet. The numerical analysis included different coefficients of friction ($\mu = 0.30\text{-}0.90$), corresponding to typical contact conditions between the gripper fingers and the package surface. In this part of the analysis, the safety factor k_s, applied by some authors, was not included. The safety factor will be considered at a later stage of the analysis. The intention was to perform a numerical evaluation that reflects real industrial operating conditions.

Fig. 3 Product for palletizing – package of jam jars with a mass of m = 6 kg

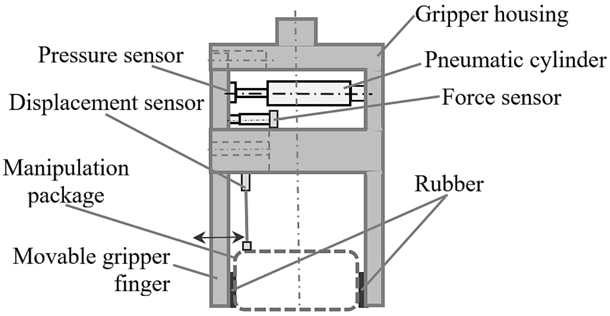

Fig. 4 Schematic representation of the adaptive gripper for package palletizing

The design of the adaptive gripper, shown in Fig. 4, consists of two fingers — one fixed and the other movable — which are actuated by a pneumatic cylinder connected to an industrial compressed air supply.

The presented gripper is used for palletizing packages with the dimensions and mass shown in Fig. 3. The input data for the numerical analysis are as follows [35]: package mass m = 6.00 kg, gravitational acceleration g = 9.81 m/s^2, and coefficient of friction μ = 0.40. The minimum required normal gripping-force was determined for a two-finger adaptive gripper. The required normal gripping-force calculated from the friction condition amounts to 147.15 N and represents the minimum normal gripping-force required to prevent package slipping during manipulation. This value is important for proper gripper dimensioning, pneumatic-cylinder selection, and determination of the required operating pressure. Two contact configurations were considered:

- Variant I: each finger has three contact points, resulting in a total of six contact points and a contact area of A_k = 24 cm^2.
- Variant II: each finger has one contact point, resulting in a total of two contact points and a contact area of A_k = 40 cm^2.

To ensure reliable lifting of the package without slipping, the friction force generated at the contact surfaces between the gripper fingers and the package must be greater than the total external load acting on the package. In addition to the gravitational force, inertial forces generated during lifting and transfer must also be taken into account. The corresponding analytical relations are given in Eq. 5.

$$\begin{gathered} F_\mu = \mu \cdot F_{N,min} \ \geq \ F_{req} \\ G = m \cdot g \\ F_{inv} = m \cdot a_v; \ \ F_{inh} = m \cdot a_h \\ F_{req} = G + F_{in} \\ F_{N,min} = \frac{F_{req}}{\mu} \end{gathered} \tag{5}$$

where F_μ denotes the friction force at the contact interface, is the minimum required normal gripping-force, G represents the gravitational force acting on the package, while F_{inv} and F_{inh} represent the vertical and horizontal components of the inertial force generated during lifting and transfer of the package.

Inertial forces generated during gripping and lifting must be considered in the gripping-force analysis. In order to ensure stable palletizing operation without accumulation of packages on the conveyor belt, the following operating accelerations of the gripper were assumed: vertical acceleration 0.5 m/s^2, and horizontal acceleration 0.5 m/s^2.

The F_{inh} vertical inertial-force component and the F_{inh} horizontal inertial-force component were determined according to Eq. 5. The total inertial force generated during gripper operation amounts to F_{in} = 4.242 N, while the total external load acting on the package equals F_{req} = 63.10 N.

In Variant I, each finger has three contact surfaces of 4 cm^2, resulting in a total contact area of 24 cm^2. In Variant II, each finger has one contact surface of 20 cm^2, resulting in a total contact area of 40 cm^2.

Table 2 summarizes the calculated operational gripping-force values for the two contact configurations under the considered friction and pneumatic-pressure conditions. The values presented in Table 2 represent operational gripping-force values generated under predefined pneumatic-pressure conditions and are therefore not directly equivalent to the theoretical minimum normal gripping-force defined by Eq. 5.

The values presented in Table 2 represent operational gripping-force values generated under predefined pneumatic-pressure conditions and are therefore distinct from the theoretical minimum normal gripping-force obtained from the friction stability condition.

At first glance, the results presented in Table 2 may appear to contradict the classical friction-based relation, according to which the required minimum gripping-force decreases with an increase in the coefficient of friction. However, it is important to emphasize that the values presented in Table 2 are not derived solely from the analytical minimum normal gripping-force relation $F_{N,min} = \frac{mg}{\mu}$, but from an extended model that includes the influence of pneumatic pressure, contact configuration, contact area, and inertial forces during manipulation. In the presented numerical analysis, the operational gripping-force is calculated based on the pressure–force relationship $F_{op} = p \cdot A_p$ where the pneumatic operating pressure is treated as a controlled variable. For each friction coefficient, the operating pressure is adjusted to ensure stable and reliable manipulation under dynamic operating conditions, including vertical and horizontal accelerations during palletizing.

Table 2 Calculated operational gripping force values for different contact configurations and pneumatic-pressure conditions during manipulation of a 6 kg package

Friction Coefficient μ	Pneumatic pressure p (bar)	Variant I. contact area A_k (cm^2)	Variant II. contact area A_k (cm^2)	Variant I. operational gripping-force F_{op} (N)	Variant I. gripping-force including inertial effects $F_{op} + F_{in}$ (N)	Variant II. operational gripping-force F_{op} (N)	Variant II. gripping-force including inertial effects $F_{op} + F_{in}$ (N)
0.30	0.30	24	40	21.60	25.84	36.00	40.24
0.35	0.35	24	40	29.40	33.64	49.00	53.24
0.40	0.40	24	40	38.40	42.64	64.00	68.24
0.45	0.45	24	40	48.60	52.84	81.00	85.24
0.50	0.50	24	40	60.00	64.24	100.00	104.24
0.55	0.55	24	40	72.60	76.84	121.00	125.24
0.60	0.60	24	40	86.40	90.64	144.00	148.24
0.65	0.65	24	40	101.40	105.64	169.00	173.24
0.70	0.70	24	40	117.60	121.84	196.00	200.24
0.75	0.75	24	40	126.00	130.24	225.00	229.24
0.80	0.80	24	40	153.69	157.93	256.00	260.24
0.85	0.85	24	40	173.40	177.64	289.00	294.24
0.90	0.90	24	40	194.40	198.64	324.00	328.24

As a result, an increase in the friction coefficient is accompanied by an increase in the applied pressure, which leads to a corresponding increase in the calculated gripping-force. Therefore, the observed trend does not represent the theoretical minimum gripping-force, but rather the required operational gripping-force under predefined operating conditions. This approach reflects real industrial practice, where the gripping-force is often intentionally increased to ensure stability, compensate for dynamic effects, and maintain safety margins. Such numerical analysis enables the assessment of the minimum forces and pneumatic requirements necessary for reliable manipulation of a package with a mass of 6 kg. The diagram shown in Fig. 5 presents the results of the numerical analysis from Table 2, carried out for the verification of the calculated gripping-forces and the behavior of the pneumatic gripper under real operating conditions. The diagram illustrates the relationship between the operating pressure and the achieved gripping-force for Variant I and Variant II contact configurations between both gripper fingers and the package during palletizing, thereby enabling the determination of the minimum pressure required for safe lifting of the package. The diagram shows that the gripping-force F_v increases linearly with the increase of the operating pressure in the pneumatic actuator, for both Variant I and Variant II. Higher pressure proportionally increases the normal force exerted by the gripper fingers on the package.

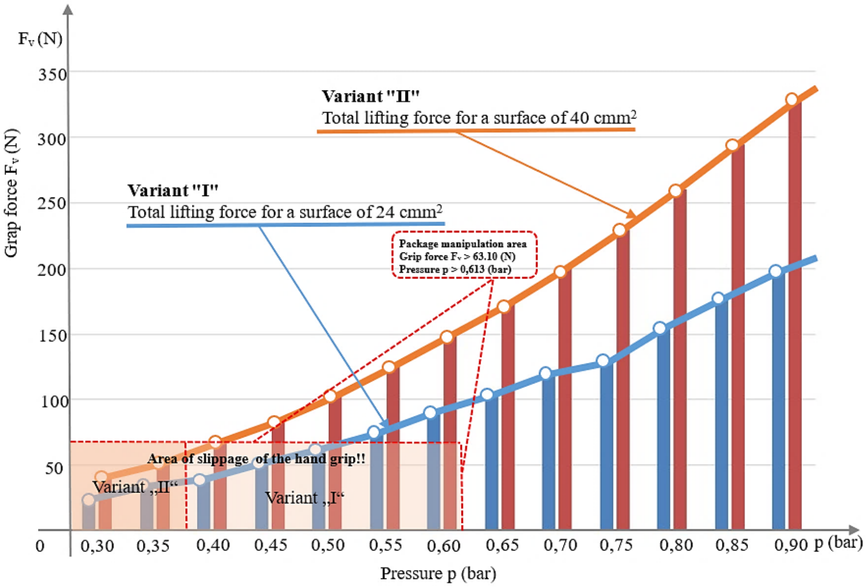

Fig. 5 Numerical values of the operational gripping-force F_{num} as a function of the operating pressure p

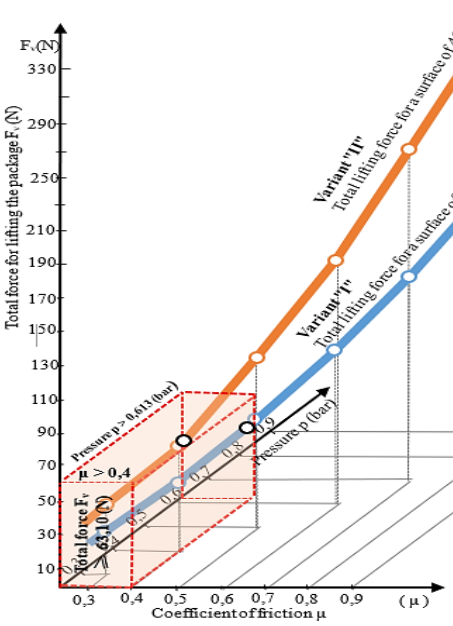

Fig. 6 Numerical values of the operational gripping-force F_{num} as a function of the coefficient of friction μ and the operating pressure p

The curve enables determination of the optimal pressure required to ensure reliable gripping without slipping or excessive loading of the package. Fig. 6 illustrates the variation in the operational gripping-force of the adaptive gripper in Variants I and II as a function of the coefficient of friction and the operating pressure. It also shows the dependence of the total lifting force required to prevent slipping on the coefficient of friction μ and the operating pressure required for normal palletizing of the package. The variation of the force required for proper gripper operation during palletizing confirms the influence of different contact materials on the gripper performance. Furthermore, the lifting force is also a function of the operating pressure and the contact area between the gripper fingers and the package. These diagrams are useful for the engineering design of pneumatic grippers and for determining the safety margins required for their normal operation.

6. Conducting the experiment and analysis of the obtained results

6.1 Experimental setup

The experiment for testing the adaptive pneumatic gripper was conducted in a work cell designed as an integrated system for automated package picking and placement onto a Euro pallet (automated palletizing) in a real industrial environment. The work cell consists of a belt conveyor on which jam packages arriving from production, each containing six jars, are transported; a collaborative robot equipped with an adaptive pneumatic gripper of proprietary design; a Euro pallet on which the packages are stacked; and an accompanying sensor and control system.

In the production process, the belt conveyor is used for the continuous delivery of packages to the location where automated palletizing onto a Euro pallet is performed. The packages arriving from the production process consist of six glass jars of jam, grouped in a cardboard holder and additionally wrapped in plastic (stretch) film for stability during handling, as shown in Fig. 3. The dimensions and mass of the package (given in Section 5.1) correspond to typical food products intended for retail, which enables a realistic simulation of the industrial process. The collaborative robot is positioned beside the belt conveyor so that its workspace covers both the package pick-up zone on the conveyor and the Euro pallet onto which the packages are stacked. An adaptive pneumatic gripper is mounted on the end-effector of the collaborative robot. The gripper, which integrates all sensors required for gripping-force optimization, is designed for the safe handling of packages of different dimensions and masses on the belt conveyor and for their palletizing onto a Euro pallet through adjustment of the contact surface, operating pressure, and clamping force.

Package placement on the conveyor

Packages with six jars of jam arrive from the packaging cell, grouped in a cardboard holder and additionally wrapped in plastic (stretch) film, and are transported on the belt conveyor. They are placed with a correct orientation, with the longer side parallel to the direction of conveyor movement. The conveyor belt speed is constant (but can be adjusted) and enables the delivery of packages with jars to a predefined pick position where the packages are taken by the adaptive pneumatic gripper, as shown in Fig. 7. In the package pickup zone, a reference point (pick point) is defined using a presence sensor (as shown in Fig. 7). In this way, precise positioning of the package relative to the robot coordinate system is ensured. This approach minimizes the need for additional trajectory corrections and increases the repeatability of package picking and placement onto the Euro pallet.

Fig. 7 Work cell for package palletizing

Integration with the Euro pallet

The jam packages are picked up by the adaptive pneumatic gripper integrated on the collaborative robot, and the robot transfers and stacks them onto a Euro pallet of standard dimensions (1200 × 800 mm), which is placed within the robot workspace with a clearly defined base coordinate in the control system. The palletizing system is implemented using a layer-by-layer programming pattern, where the arrangement between rows and layers is predefined in order to achieve a stable load structure on the pallet for further transport. After picking the package from the conveyor, the robot generates an optimal trajectory to the target position on the pallet, with controlled lowering and gradual unloading of the gripper. After releasing the package, the robot returns to the initial position and the cycle repeats. Particular attention was paid to aligning the stacking height with the maximum allowable pallet load height, as well as maintaining the stability of packages wrapped in stretch film.

Sensor system

The package-palletizing work cell was equipped with a sensor system for monitoring and analyzing key process parameters during the experiments, including operating pressure in the pneumatic cylinder, gripping-force, package displacement, and package arrival at the conveyor pick-up zone, as shown in Fig. 7 [26, 29]. The sensor system in the work cell includes the following sensors:

- Package presence sensor on the conveyor belt (detection of arrival in the pick zone),
- Pressure sensor in the pneumatic system (measurement of operating pressure in the gripper cylinder),
- Force sensor on the gripper contact surface (measurement of package clamping force),
- Displacement/slip sensor (detection of possible relative package movement during lifting),
- Internal feedback of the collaborative robot (position, speed, and joint torques).

Table 3 Overview of sensors integrated into the experimental robotic palletizing cell

No.	Sensor type	Sensor model	Measuring range / Technical characteristics	Output signal type	Sensor accuracy	Position in robotic cell	Function in the system
1	Non-contact displacement sensor	BALLUFF BAW M12 (alternative: HC-SR04 Ultrasonic Arduino sensor)	Detection range up to 2 mm (alternative: 3-400 cm); sampling rate: 50-100 Hz	Analog (0-10 V) (alternative: digital)	± 0.3 % FS (alternative: ± 10 cm)	Above the conveyor belt in the pick zone	Detection of package arrival and activation of the robot pick-and-place sequence; input signal for cycle synchronization
2	Strain-gauge pressure sensor	P8AP	Measuring range: 0 kPa to 2 MPa; calibrated according to manufacturer specifications	Analog (0-2 mV/V)	± 0.3 % FS	Pneumatic line of the gripper	Monitoring of operating pressure and stability of the pneumatic gripper system; validation of pressure–force relationship
3	Force sensor (Load cell)	U2B	Single-axis force measurement; nominal capacity adapted to gripping range; sampling rate: 100 Hz	Analog (0-2 mV/V)	± 0.3 % FS	Integrated between the side plates of the gripper	Measurement of package clamping force and optimization of gripping-force; experimental validation of analytical model
4	Acceleration sensor	ASC 5631	Measurement of acceleration in three orthogonal directions; frequency range up to 1 kHz	Analog (0.5-4.5 V)	± 1 % FS	Integrated on the gripper	Measurement of dynamic load during robot motion; detection of transient disturbances affecting gripping stability
5	Linear displacement sensor (LVDT)	WA20	Precise linear displacement measurement up to 20 mm; high repeatability (< 0.1 % FS)	Analog (0-10 V)	± 0.3 % FS	On the gripper mechanism	Detection of possible slipping or displacement of the package during manipulation; validation of gripping stability condition

The specified sensor models, along with their technical characteristics and functions in the palletizing work cell, are presented in Table 3. The sensor-system enables comprehensive monitoring of both static and dynamic parameters of the gripping and package-manipulation process under real industrial conditions. The integration of force, pressure, and displacement sensors provides direct experimental validation of the analytical gripping-force model, while the accelerometer provides insight into dynamic disturbances that may affect manipulation stability. In particular, measurements of gripping-force and pressure in the pneumatic system were used to verify the force–pressure relationship, while displacement data and possible package slippage were used to confirm the stability condition defined in the research hypothesis. Such an approach ensures high reliability of the results, reproducibility of the experiment, and direct applicability of the developed model in industrial applications of collaborative robotics. All sensors were calibrated prior to the experiment to ensure measurement accuracy and repeatability of the obtained results.

6.2 Measurement of the minimum gripping-force

The measurement of the minimum gripping-force was conducted with the aim of experimentally determining the lowest force required for stable and safe manipulation of packages without slipping during lifting and transportation in the palletizing process. The obtained experimental results were compared with the numerical values defined in Chapter 5, where the minimum gripping-force was determined as a function of package mass, friction coefficient, and contact conditions between the gripper fingers and the package. During the experimental investigation, the minimum gripping-force was determined by gradually increasing the operating pressure in the pneumatic actuator until stable gripping without slipping was achieved. The values of gripping-force and pressure were continuously monitored using the integrated sensor system described in Chapter 6.1, which enabled precise determination of the boundary conditions for stable manipulation under real industrial operating conditions. For the experiment, the minimum and maximum coefficients of friction at the contact interface between the gripper and the package, both covered with protective film, were determined, and the results are shown in Fig. 8.

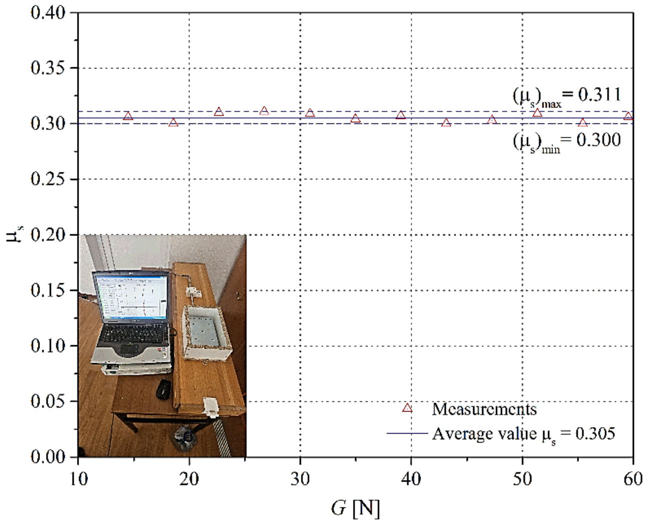

Fig. 8 Experimental results of determining the coefficient of friction at the contact point between the gripper and the package

Experimental determination of the coefficient of friction was carried out at the contact point between the gripper and the package, where both contact surfaces were covered with protective film. During testing, the minimum and maximum values of the coefficient of friction were determined, amounting to $\mu_{s,min} = 0.300$ and $\mu_{s,max} = 0.311$, while the mean value is $\mu_{s,avg} = 0.305$. The obtained results show low dispersion of values, which indicates high repeatability of measurements and stable contact conditions between the gripper and the package. The low variability of the coefficient of friction confirms the reliability of the experimental method and enables its use as a relevant input parameter in the numerical model. The experimental results are shown in Fig. 9, where the experimental determination of compressor pressure and pressure in the pneumatic cylinder was performed with the aim of analyzing their relationship with the achieved gripping-force required for lifting the package. During testing, the operating pressure of the compressor and the force exerted by the gripper on the package were continuously measured under real operating conditions. Based on the obtained data, it was possible to estimate the minimum pressure required for stable gripping without slipping. The experimental results are presented in the diagram. From the diagram, it can be observed that the compressor pressure (blue line) increases almost linearly over time up to approximately 4.1 bar, after which system stabilization occurs. At the same time, the gripping-force (red line) increases progressively and reaches a value of approximately 72-74 N, which represents the maximum achieved force in the experiment. In the initial phase of operation (up to ~ 20 s), the force is very low due to insufficient pressure to achieve effective contact between the gripper and the package. After that, a rapid increase in force occurs, indicating a direct dependence of force on the pressure in the cylinder.

In the final stage of the experiment, force saturation is observed, although the pressure slightly increases, which indicates the presence of losses in the system and limitations of the mechanical structure. Such behavior confirms real operating conditions of the pneumatic system, where an increase in pressure does not always lead to a proportional increase in force due to the influence of friction, deformations, and internal losses. The relationship between compressor pressure and gripping-force was experimentally determined in order to define the actual relationship between the input pneumatic pressure and the force achieved by the gripper. During testing, the compressed air pressure and the corresponding force exerted by the gripper on the package were continuously measured. The experimentally obtained relationship between pneumatic pressure and the gripping-force exerted by the gripper on the package is presented in Fig. 10.

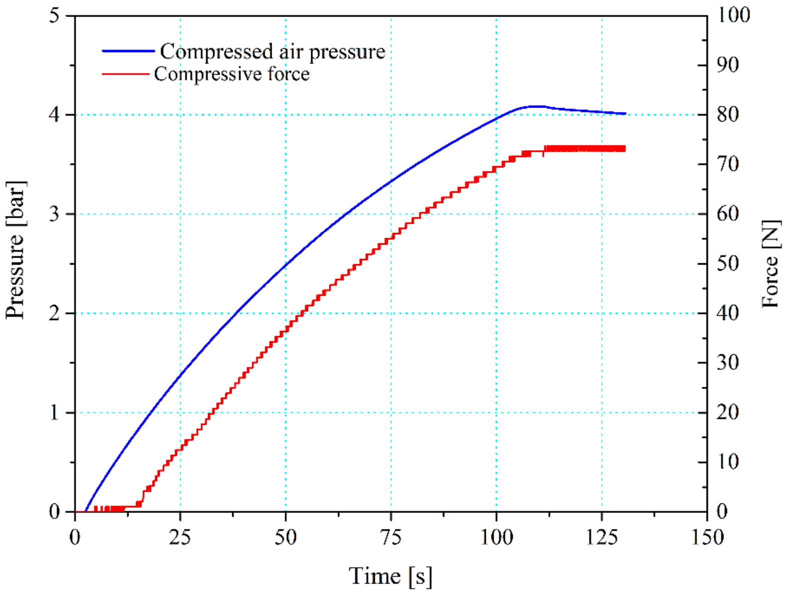

Fig. 9 Experimental variation of compressor pressure and gripping-force during package lifting

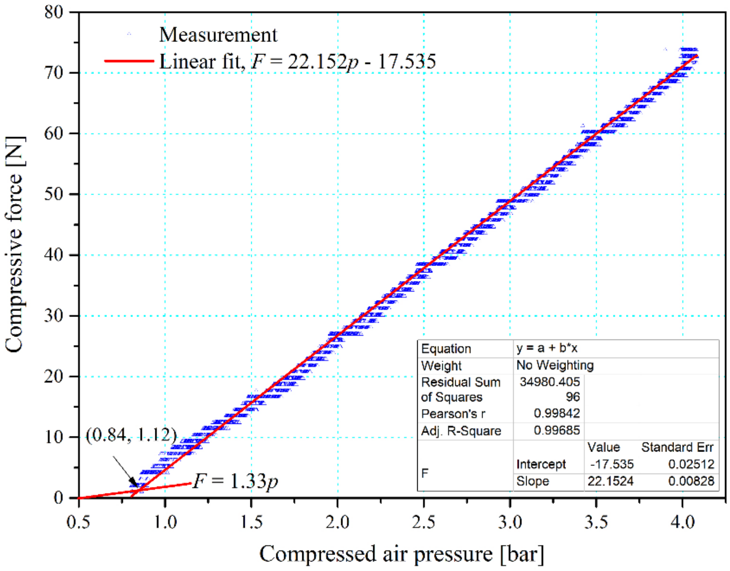

Fig. 10 Gripping-force as a function of pneumatic-cylinder pressure

During testing, the compressed air pressure and the corresponding force exerted by the gripper on the package were continuously measured. Based on the experimental data, it was possible to determine the functional dependence of force on pressure, as well as to evaluate the efficiency of the pneumatic system. The obtained results are presented in the diagram. From the diagram, a nearly linear relationship between compressed air pressure and gripping-force can be clearly observed, which is confirmed by the linear regression defined by the expression $F = 22.152\,p - 17.535$. The experimental points show high agreement with the regression line, which confirms a high correlation coefficient ($R^2 \approx 0.998$), indicating high measurement accuracy. In the initial region (below approximately 1 bar), the force is very small or negligible, indicating the existence of a system activation threshold due to mechanical and pneumatic losses. After this threshold, a stable and linear increase in force occurs with increasing pressure, where the force reaches values of approximately 70-75 N at a pressure of around 4 bar. Minor deviations of the experimental points from the regression line are caused by real effects such as friction in the cylinder, elastic deformations, and non-ideal contact conditions. Overall, the diagram confirms a reliable and predictable characteristic of the pneumatic system, which is crucial for precise control of gripping-force in industrial conditions.

Each experimental condition (defined by a specific pressure level and contact configuration) was repeated a minimum of five times in order to ensure the reliability and repeatability of the obtained results. The reported gripping-force values represent the averages of the repeated measurements, while the variation between trials remained within ± 3-5 %, indicating a high level of measurement consistency.

The relatively low dispersion of the results confirms the stability of the experimental setup, as well as the reliability of the sensor system used for force and pressure measurements. This ensures that the obtained results are statistically representative and suitable for comparison with the numerical model. This level of repeatability is consistent with standard industrial measurement practices.

7. Discussion of numerical and experimental results

The comparison between numerical and experimental results shows a high level of agreement in terms of the functional dependence between gripping-force and pneumatic pressure. Both approaches confirm a linear relationship, which validates the analytical model for engineering applications. The experimental results exhibit a high correlation coefficient ($R^2 \approx 0.998$), confirming the reliability and repeatability of the measurements. However, quantitative differences between the numerical and experimental results were observed, with the numerical model predicting higher force values. A systematic deviation of approximately 65-75 % was observed between the numerical and experimental models, depending on the operating pressure. For example, at a pressure of $p \approx 4$ bar, the experimental force reaches approximately 70-75 N, while the numerical model predicts significantly higher values. These deviations are primarily caused by real system effects such as internal friction in the pneumatic actuator, mechanical losses in the transmission system, elastic deformations, and non-ideal contact conditions. The experimental results confirm that the actual gripping-force is lower than the theoretical value, which highlights the importance of model calibration for industrial applications. The introduction of a correction factor ($k_{corr} \approx 0.30$) improves the agreement between the numerical and experimental models. Despite these differences, the consistency of trends confirms the reliability and applicability of the developed model for engineering design and optimization of gripping systems.

7.1 Model calibration and correction factor for industrial application

In order to improve the agreement between the numerical model and experimental results, a calibration procedure was performed based on the experimentally obtained relationship between gripping-force and pneumatic pressure.

The experimental results show that the actual gripping-force can be described by a linear relationship:

$$F_{exp} = 22.152\,p - 17.535 \tag{6}$$

while the numerical model predicts a proportional relationship of the form:

$$F_{num} = k \cdot p \tag{7}$$

Here, k is the theoretical proportionality coefficient derived from the analytical gripping model. A comparison of the slopes of these functions reveals a significant discrepancy between the numerical and experimental results. This discrepancy is primarily caused by real system effects, including:

- internal friction in the pneumatic cylinder,
- mechanical losses in the lever transmission mechanism,
- elastic deformation of the gripper structure,
- non-ideal contact conditions between the gripper and the package.

To account for these effects, a correction (calibration) factor is introduced:

$$k_{corr} = \frac{F_{exp}}{F_{num}} \tag{8}$$

Based on the experimental data, the average value of the correction factor is:

$$k_{corr} \approx 0.30 \tag{9}$$

The introduction of this correction factor enables more accurate prediction of gripping-force under real industrial operating conditions and significantly improves the applicability of the developed model in engineering design and optimization of pneumatic gripping systems.

7.2 Analysis of the deviation between numerical and experimental results

To quantitatively evaluate the deviation between numerical and experimental results, a relative error analysis was performed. The relative error is defined as:

$$\varepsilon = \frac{\mid F_{num} - F_{exp} \mid}{F_{num}} \cdot 100\ \% \tag{10}$$

Based on the experimental data, the average deviation between the numerical and experimental results ranges between 65 % and 75 %, depending on the operating pressure. The error decreases slightly at higher pressures due to improved mechanical stability and reduced relative influence of friction losses. The main sources of error include:

- nonlinear friction effects in the pneumatic actuator,
- mechanical inefficiencies in the transmission system,
- structural compliance of the gripper,
- simplified assumptions in the analytical model.

Despite these deviations, the consistent linear trend observed in both numerical and experimental results confirms the validity of the model for engineering applications. From an engineering perspective, the results indicate that direct use of the analytical model without calibration may lead to overestimation of the required gripping-force. The introduction of a correction factor enables more realistic system design, reduces energy consumption, and minimizes the risk of product damage. This is particularly important in collaborative robotic applications, where excessive force may compromise safety and efficiency.

Furthermore, by introducing the correction factor defined in Subsection 7.1, the numerical model can be reformulated in a calibrated form:

$$F_{cal} = k_{corr} \cdot F_{num} \tag{11}$$

where $k_{corr} \approx 0.30$ represents the experimentally determined correction coefficient.

The application of the calibrated model significantly reduces the deviation between the numerical and experimental results, bringing the relative error to a level acceptable for engineering applications. This confirms that the initially high deviation (65-75 %) is not a consequence of model inadequacy, but rather of simplified assumptions and unmodeled real system losses. Therefore, the calibrated model provides a reliable basis for the design and optimization of pneumatic gripping systems in real industrial environments. To further generalize the applicability of the proposed system, the following considerations can be made:

- Although the experimental validation was conducted on a specific type of packaged product, the proposed adaptive pneumatic gripper is designed to handle a wider range of package geometries, materials, and surface conditions. The gripper utilizes a mechanical two-finger configuration with adjustable stroke and pressure-controlled gripping-force, enabling adaptation to packages of different dimensions and masses.
- The use of high-friction rubber contact surfaces (EPDM/NBR) allows stable gripping of various materials such as cardboard, plastic, and composite packaging commonly found in industrial and logistics environments. Variations in surface conditions, including smooth, coated, or slightly irregular surfaces, are compensated through adjustment of the pneumatic pressure, which directly controls the applied gripping-force.
- For regular-shaped packages (e.g., boxes and containers), the gripper ensures uniform force distribution and stable contact. However, for highly irregular, deformable, or very low-friction objects, the gripping performance may be limited, and alternative solutions such as vacuum or soft robotic grippers may be more suitable.

- These considerations indicate that the proposed system is applicable to a broad range of industrial packaging types while also clarifying its operational limitations, which will be further investigated in future research.

8. Conclusion

This paper presents the development, numerical modeling, and experimental validation of an adaptive pneumatic gripper for collaborative robotic palletizing applications. The proposed analytical model enables the determination of the optimal gripping-force as a function of package mass, friction coefficient, and contact conditions. Experimental results confirm a strong linear relationship between pneumatic pressure and gripping-force, described by the relation $F = 22.152\,p - 17.535$, with a high correlation coefficient ($R^2 \approx 0.998$), indicating excellent measurement accuracy and system repeatability. The maximum experimentally obtained gripping-force was approximately 70-75 N at an operating pressure of approximately 4 bar. Although quantitative deviations between numerical and experimental results were observed (approximately 65-75 %), these differences are attributed to real system effects, including pneumatic losses, mechanical friction, structural compliance, and non-ideal contact conditions. The introduction of a correction factor ($k_{corr} \approx\ 0.30$) significantly improves the agreement between the model and experimental data, enabling more accurate prediction of gripping-force under real industrial conditions. The developed system demonstrates reliable and stable performance in handling packages up to 10 kg, with optimized force control and reduced risk of slippage or product damage. The proposed methodology integrates analytical modelling, numerical optimization, and experimental validation. This approach provides a robust framework for the design and implementation of adaptive grippers in collaborative robotic systems. Future research will focus on the integration of real-time adaptive control strategies, sensor-based force regulation, and extension of the model to variable surface conditions and heterogeneous objects in dynamic industrial environments.

The proposed approach provides a practical framework for the design and optimization of adaptive pneumatic grippers in real industrial environments and helps bridge the gap between theoretical modelling and industrial implementation.

Although the experimental validation presented in this study focuses on short-term operation under controlled industrial conditions, the proposed adaptive pneumatic gripper is designed in accordance with standard industrial requirements for durability, repeatability, and continuous operation. The mechanical structure of the gripper, based on an aluminum frame and a pneumatic actuation system, ensures high robustness and low susceptibility to wear under cyclic loading conditions.

The use of industrial-grade components, including pneumatic cylinders and rubber contact surfaces, enables reliable operation in repetitive palletizing tasks typical for industrial environments. Furthermore, the observed high repeatability of experimental results and stable force–pressure characteristics indicate that the system is capable of maintaining consistent performance over extended operational cycles.

However, long-term performance aspects such as component wear, fatigue, and maintenance requirements were not the primary focus of this study and will be addressed in future research through extended lifecycle testing under continuous industrial operation.

These findings indicate that real-system effects, including pneumatic losses, mechanical friction, and structural compliance, significantly contribute to the deviation between numerical and experimental results, leading to an overestimation of the gripping-force in the analytical model. Therefore, for practical industrial application, the use of the calibrated model with the correction factor ($k\_corr \approx 0.30$) is essential to ensure accurate force prediction, avoid excessive gripping-force, and enhance system efficiency and operational safety.

Acknowledgement

This paper was supported by the Federal Ministry of Education and Science of Bosnia and Herzegovina under the project *Development of an Adaptive End-Effector for Collaborative Robots for Palletizing Heterogeneous Products (RAPK)*, 2025.

References

[1] Karabegović, I., Kovačević, A., Banjanović-Mehmedović, L., Dašić, P. (2020). *Handbook of research on integrating Industry 4.0 in business and manufacturing,* IGI Global Scientific Publishing, Hershey, USA, doi: 10.4018/978-1-7998-2725-2.

[2] Turek, J., Miškařík, L., Vojtěšek, J., Kopeček, L., Svacinová, L., Mizera, A. (2025). Soft robotics in industrial automation: Adaptive industrial gripper design and evaluation, *EAI Endorsed Transactions on Digital Transformation of Industrial Processes,* Vol. 1, No. 1, 1-9, doi: 10.4108/dtip.8719.

[3] Karabegović, I., Karabegović, E., Mahmić, M., Husak, E. (2020). The implementation of Industry 4.0 by using industrial and service robots in the production processes, In*:* Karabegović, I., Kovačević, A., Banjanović-Mehmedović, L., Dašić, P. (eds.), *Handbook of Research on Integrating Industry 4.0 in Business and Manufacturing,* IGI Global Scientific Publishing, Hershey, USA, 1-30, doi: 10.4018/978-1-7998-2725-2.ch001.

[4] Polygerinos, P., Wang, Z., Galloway, K.C., Wood, R.J., Walsh, C.J. (2015). Soft robotic glove for combined assistance and at-home rehabilitation, *Robotics and Autonomous Systems*, Vol. 73, 135-143, doi: 10.1016/j.robot.2014.08.014.

[5] Friedl, W. (2024). Evaluation of different robotic grippers for simultaneous multi-object grasping, *Frontiers in Robotics and AI*, Vol. 11, Article No. 1351932, doi: 10.3389/frobt.2024.1351932.

[6] Iqbal, Z., Pozzi, M., Prattichizzo, D., Salvietti, G. (2021). Detachable robotic grippers for human-robot collaboration, *Frontiers in Robotics and AI*, Vol. 8, Article No. 644532, doi: 10.3389/frobt.2021.644532.

[7] Liu, C., Cheng, J., Li, Z., Cheng, C., Zhang, C., Zhang, Y., Zhong, R.Y. (2020). Design of a self-adaptive gripper with rigid fingers for Industrial Internet, *Robotics and Computer-Integrated Manufacturing*, Vol. 65, Article No. 101976, doi: 10.1016/j.rcim.2020.101976.

[8] Wang, Y., Guo, S., Zhang, J., Ding, H., Zhang, B., Cao, A., Sun, X., Zhang, G., Tian, S., Chen, Y., Ma, J., Chen, G. (2025). Optimized design and deep vision-based operation control of a multi-functional robotic gripper for an automatic loading system, *Actuators*, Vol. 14, No. 6, Article No. 259, doi: 10.3390/act14060259.

[9] Hao, L., Wang, Z., Chen, Y., Li, X. (2022). Design and analysis of an adaptive robotic gripper for grasping objects with variable stiffness and shape, *The International Journal of Advanced Manufacturing Technology*, Vol. 120, 4567-4580, doi: 10.1007/s00170-022-09015-5.

[10] Shintake, J., Cacucciolo, V., Floreano, D., Shea, H. (2018). Soft robotic grippers, *Advanced Materials*, Vol. 30, No. 29, Article No. 1707035, doi: 10.1002/adma.201707035.

[11] Amend, J.R., Brown, E., Rodenberg, N., Jaeger, H.M., Lipson, H. (2012). A positive pressure universal gripper based on the jamming of granular material, *IEEE Transactions on Robotics*, Vol. 28, No. 2, 341-350, doi: 10.1109/TRO.2011.2171093.

[12] Zhou, J., Chen, Y., Hu, Y., Wang, Z., Li, Y., Gu, G., Liu, Y. (2020). Adaptive variable stiffness particle phalange for robust and durable robotic grasping, *Soft Robotics*, Vol. 7, No. 6, 743-757, doi: 10.1089/soro.2019.0089.

[13] Zhu, J., Chen, H., Chai, Z., Ding, H., Wu, Z. (2024). A dual-modal hybrid gripper with wide tunable contact stiffness range and high compliance for adaptive and wide-range grasping objects with diverse fragilities, *Soft Robotics*, Vol.11, No. 3, 371-381, doi: 10.1089/soro.2023.0022.

[14] Javernik, A., Buchmeister, B., Ojsteršek, R. (2022). Impact of cobot parameters on the worker productivity: Optimization challenge, *Advances in Production Engineering & Management*, Vol. 17, No. 4, 494-504, doi: 10.14743/apem2022.4.451.

[15] Coulson, R., Stabile, C.J., Turner, K.T., Majidi, C. (2022). Versatile adhesion based gripping via an unstructured variable stiffness membrane, *Soft Robotics*, Vol. 9, No. 2, 189-200, doi: 10.1089/soro.2020.0088.

[16] Husaković, A., Banjanović-Mehmedović, L., Gurdić-Ribić, A., Prljača, N., Karabegović, I. (2025). Reinforcement learning for robot manipulation tasks in human-robot collaboration using the CQL/SAC algorithms, *Advances in Production Engineering & Management*, Vol. 20, No. 1, 5-15, doi: 10.14743/apem2025.1.523.

[17] MacDonald, I., Dubay, R. (2024). Development of an adaptive force control strategy for soft robotic gripping, *Applied Sciences*, Vol. 14, No. 16, Article No. 7354, doi: 10.3390/app14167354.

[18] Kim, Y., Cha, Y. (2020). Soft pneumatic gripper with a tendon driven soft origami pump, *Frontiers in Bioengineering and Biotechnology*, Vol. 8, Article No. 461, doi: 10.3389/fbioe.2020.00461.

[19] Li, L., Xie, F., Wang, T., Wang, G., Tian, Y., Jin, T., Zhang, Q. (2022). Stiffness tunable soft gripper with soft rigid hybrid actuation for versatile manipulations, *Soft Robotics*, Vol. 9, No. 6, 1108-1119, doi: 10.1089/soro.2021.0025.

[20] Song, E.J., Lee, J.S., Moon, H., Choi, H.R., Koo, J.C. (2021). A multi-curvature, variable stiffness soft gripper for enhanced grasping operations, *Actuators*, Vol. 10, No. 12, Article No. 316, doi: 10.3390/act10120316.

[21] Li, J., Liu, L., Liu, Y., Leng, J. (2019). Dielectric elastomer spring roll bending actuators: Applications in soft robotics and design, *Soft Robotics*, Vol. 6, No. 1, 1-12, doi: 10.1089/soro.2018.0037.

[22] Shan, X., Xu, L., Li, X. (2024). A variable stiffness design method for soft robotic fingers based on grasping force compensation and linearization, *Robotica*, Vol. 42, No. 6, 2061-2083, doi: 10.1017/S026357472400081X.

[23] Patalas-Maliszewska, J., Łosyk, H., Dudek, A. (2025). Improving safety in human–robot collaboration towards sustainable production in Industry 5.0, *Journal of Intelligent Manufacturing*, Vol. 36, doi: 10.1007/s10845-025-02676-4.

[24] Zhang, Y., Man, J., Liu, X., Li, S., Cao, B., Yu, L., Tan, X. (2025). Soft robotic grippers: A review, *Frontiers in Materials*, Vol. 12, Article No. 1692206, doi: 10.3389/fmats.2025.1692206.

[25] Cardin-Catalan, D., Ceppetelli, S., del Pobil, A.P., Morales, A. (2022). Design and analysis of a variable-stiffness robotic gripper, *Alexandria Engineering Journal*, Vol. 61, No. 2, 1235-1248, doi: 10.1016/j.aej.2021.06.045.

[26] Villani, V., Pini, F., Leali, F., Secchi, C. (2018). Survey on human-robot collaboration in industrial settings: Safety, intuitive interfaces and applications, *Mechatronics*, Vol. 55, 248-266, doi: 10.1016/j.mechatronics.2018.02.009.

[27] Karabegović, I. (2022). Sensory technology is one of the basic technologies of Industry 4.0 and the fourth industrial revolution, *ACTA Technica Corviniensis – Bulletin of Engineering*, Vol. 15, No. 4, 33-39.

[28] Rus, D., Tolley, M.T. (2015). Design, fabrication and control of soft robots, *Nature*, Vol. 521, 467-475, doi: 10.1038/nature14543.

[29] Bauer, A., Wollherr, D., Buss, M. (2008). Human-robot collaboration: A survey, *International Journal of Humanoid Robotics*, Vol. 5, No. 1, 47-66, doi: 10.1142/S0219843608001303.

[30] Haddadin, S., Croft, E. (2016). Physical human-robot interaction, In: Siciliano, B., Khatib, O. (eds.), *Springer handbook of robotics*, 2nd ed., Springer, Cham, 1835-1874, doi: 10.1007/978-3-319-32552-1_69.

[31] Trivedi, D., Rahn, C.D., Kier, W.M., Walker, I.D. (2008). Soft robotics: Biological inspiration, state of the art, and future research, Applied Bionics and Biomechanics, Vol. 5, No. 3, 99-117, doi: 10.1080/11762320802557865.

[32] Kim, S., Laschi, C., Trimmer, B. (2013). Soft robotics: A bioinspired evolution in robotics, *Trends in Biotechnology*, Vol. 31, No. 5, 287-294, doi: 10.1016/j.tibtech.2013.03.002.

[33] Torielli, D., Bertoni, L., Fusaro, F., Tsagarakis, N., Muratore, L. (2023). ROS end-effector: A hardware-agnostic software and control framework for robotic end-effectors, *Journal of Intelligent & Robotic Systems*, Vol. 108, No. 4, Article No. 70, doi: 10.1007/s10846-023-01911-5.

[34] Galloway, K.C., Becker, K.P., Phillips, B., Kirby, J., Licht, S., Tchernov, D., Wood, R.J., Gruber, D.F. (2016). Soft robotic grippers for biological sampling on deep reefs, *Soft Robotics*, Vol. 3, No. 1, 23-33, doi: 10.1089/soro.2015.0019.

[35] Cheewaratchanon, S., Auysakul, J., Neranon, P., Romyen, A. (2026). Self-adaptive control of a two-point contact gripper for the precise handling of compliant objects in industrial robotics, *Cognitive Robotics*, Vol. 6, 1-19, doi: 10.1016/j.cogr.2025.11.001.

[36] El-Sayed, A.M. (2025). A novel approach to enhancing smart stiffness of soft robotic gripper fingers for wider grasping capability, *International Journal of Intelligent Robotics and Applications*, Vol. 9, No. 2, 553-573, doi: 10.1007/s41315-024-00398-z.

APEM journal
Advances in Production Engineering & Management
Volume 21 | Number 1 | March 2026 | pp 139–155
https://doi.org/10.14743/apem2026.1.566
ISSN 1854-6250
Journal home: apem-journal.org
Original scientific paper

A human-robot collaborative delivery model for instant orders in metropolitan areas

Xie, X.L.[a,*], **Chen, X.**[a], **Wu, J.Y.**[a], **Zhang, X.F.**[a], **Kong, L.K.**[a], **Xiao, Y.**[b]

[a]Logistics School, Beijing Wuzi University, Beijing, P.R. China
[b]School of Economics and Management, Suqian University, Suqian Jiangsu, P.R. China

ABSTRACT

In metropolitan instant delivery systems, rising operational costs and poor delivery timeliness pose significant challenges. This study addresses these issues by investigating optimal order allocation and route optimization in a hybrid delivery system that integrates autonomous delivery vehicles (ADVs) with human riders. Analysis of historical order data indicates that inefficient order assignment between ADVs and riders is a major operational bottleneck. To address this problem, a collaborative human-ADV delivery model is formulated with the objective of minimizing total logistics costs under constraints related to delivery time windows, vehicle capacity, and routing requirements. The proposed model is applied to a real-world case involving QX Fresh Supermarket, comprising 80 orders and 16 community transfer points. An improved genetic algorithm is developed to solve the optimization problem efficiently. Empirical results for off-peak, normal, and peak periods show that the collaborative delivery approach significantly improves ADV utilization and reduces total delivery costs by more than 30 % without compromising timeliness. These findings provide both a sound theoretical basis and practical guidance for the advancement of human-machine collaborative logistics.

ARTICLE INFO

Keywords:
Instant delivery;
Unmanned delivery vehicle;
Human-robot collaboration;
Order allocation;
Route optimization;
Genetic algorithm;
Last-mile logistics

**Corresponding author:*
xiexiaoling@bwu.edu.cn
(Xie, X.L.)

Article history:
Received 1 December 2025
Revised 7 April 2026
Accepted 10 April 2026

1. Introduction

The global retail sector is undergoing a profound transformation toward the "New Retail" model, integrating online and offline channels to prioritize experiential consumption. The fresh grocery segment leads this trend, having demonstrated remarkable resilience in the post-pandemic period. In 2024, the global fresh food retail market reached approximately USD 1.35 trillion, with projected annual growth of around 6 %. This surge is evident worldwide: in North America, platforms such as Instacart and Amazon Fresh are reshaping consumption; in Europe, Ocado’s automated warehouses set new efficiency standards; and in Asia, Hema Fresh pioneers data-driven logistics. China, with a fresh grocery online penetration rate of 14.6 % in 2022, exemplifies this shift yet still faces the universal "last-mile" bottleneck: fragmented, high-frequency orders with tight delivery windows make traditional centralized distribution inefficient.

Consequently, the logistics industry is transitioning toward Autonomous Delivery Vehicles (ADVs). In China, enterprises like Meituan and JD.com have achieved rapid growth in delivery volumes, supported by policies promoting "vehicle-road-cloud integration." However, full commercialization faces a severe "cost trap." While ADVs offer superior payload capacity and operational continuity compared to riders, the marginal cost of resolving the final 1 % of complex driving scenarios (the "long-tail problem") remains prohibitive. Furthermore, the industry currently struggles with "diseconomies of scale," where current fleet sizes cannot yet offset high R&D and hardware costs. Fully autonomous systems still falter in complex urban environments, while traditional human delivery is constrained by rising labor costs and limited scalability.

Therefore, a collaborative delivery model that integrates the flexibility of human riders with the cost-efficiency of ADVs presents a critical strategic direction. This study investigates order allocation and route optimization in a hybrid human-ADV delivery system in Chinese metropolitan areas. By constructing a multi-constraint optimization model and solving it using an improved genetic algorithm, this study addresses the gap in operationalizing human-machine collaboration. It provides a theoretical framework for hybrid fleet management and offers actionable strategies to enhance efficiency and reduce operational costs by over 30 %, contributing to the sustainable development of urban logistics systems globally.

2. Literature review

This section systematically reviews and synthesizes the literature concerning three core research issues: human-machine collaboration, order allocation, and delivery route optimization, with the objective of identifying current research progress, limitations, and future directions. First, the human-machine collaboration perspective examines effective coordination mechanisms between human operators and intelligent systems. Second, order allocation strategies are analyzed with respect to their impacts on delivery efficiency. Finally, delivery route optimization approaches are evaluated, with particular emphasis on algorithmic applications for enhancing distribution performance. Through this comprehensive literature review, the current study establishes a theoretical foundation for subsequent model development and methodological improvements.

2.1 Human-machine collaboration (HRC)

HRC, which focuses on synergistic task execution between humans and robotic systems, is foundational to modern logistics. Early research laid the theoretical groundwork, and recent advances have been driven by developments in artificial intelligence and sensor technologies.

A critical challenge in HRC is dynamic task allocation. Traditional models often rely on predefined rules, but recent studies emphasize adaptability. For instance, Alirezazadeh and Alexandre [1] developed a dynamic task scheduling framework that allows for real-time task reallocation in response to environmental changes. Furthermore, Wu *et al.* [2] presented a trust-based task allocation method for human-robot collaboration, optimizing the assignment process by establishing a trust model between humans and robots. Ranz *et al.* [3] proposed a capability-based task allocation approach that dynamically assigns tasks according to human and robot capabilities, thereby improving collaboration efficiency.

Decision-making methodologies in HRC have evolved to support complex joint actions. Cai *et al.* [4] investigated collaborative decision-making for resource-constrained field inspection tasks, optimizing task execution under limitations.

Ensuring safety and adaptability remains paramount. Studies have moved beyond physical safeguards to cognitive models. Yao *et al.* [5] developed a task reallocation algorithm incorporating dynamic fatigue assessment, enhancing operator safety by adjusting workloads based on real-time states. Faccio *et al.* [6] further contributed by modeling variable robot speeds within task allocation, enabling finer control over collaborative efficiency. Zhao *et al.* [7] further emphasized the importance of safety in HRC and proposed an integrated task allocation framework balancing both safety and efficiency. Bruno and Antonelli [8] developed a dynamic task classification and allocation method that adapts task assignments based on task requirements and team capabilities to enhance collaborative performance.

The application of HRC in industrial logistics is well-documented. Vahedi-Nouri *et al.* [9] extended this to reconfigurable manufacturing systems, presenting an optimized scheduling method for dynamic production needs.

While HRC has advanced significantly, it still faces limitations, including oversimplified human factor models, a lack of studies in multi-robot environments, and underexplored cross-domain applications. Xu *et al*. [10] investigated fairness concerns in symmetric manufacturing enterprises and found that such concerns exhibit heterogeneity, directionality, and reinforcement, which significantly affect the stability of resource-sharing strategies. This provides a useful reference for understanding human-machine collaboration in manufacturing contexts. To overcome these limitations, future research should focus on deeply integrating human cognition with machine intelligence, thereby facilitating broader adoption across diverse and complex scenarios.

2.2 Order allocation

Order allocation, as a specific instantiation of task allocation in logistics, is critical for operational efficiency. Research has evolved from static models toward dynamic, multi-objective optimization frameworks.

Multi-objective optimization is central to modern approaches, balancing conflicting goals such as cost, time, and service level. Sodenkamp *et al*. [11] incorporated collaborative effects into a multi-criteria decision model for supplier selection and order allocation. Xiang *et al*. [12] developed a multi-objective optimization model for order allocation within clustered multi-supply-and-demand networks, optimizing for cross-network resource utilization.

The application of intelligent algorithms has revolutionized this field. Zhang *et al*. [13] proposed an improved adaptive variable neighborhood search algorithm to solve stochastic order allocation problems, enhancing robustness and solution efficiency.

Dynamic and real-time allocation is essential for contemporary on-demand logistics. Huq *et al*. [14] utilized Long Short-Term Memory (LSTM) models to predict cross-regional food delivery demand, informing real-time order allocation decisions to optimize service quality. In crowdsourced delivery, which is a highly flexible model, studies mainly focus on real-time matching. As emphasized by Silva *et al*. [15], optimizing last-mile operational models is key to reversing the trend of rising fuel costs and emissions caused by high delivery volumes.

Seghezzi and Mangiaracina [16], and Seghezzi *et al*. [17] conducted in-depth economic analyses comparing crowdsourced logistics against traditional delivery models for B2C e-commerce. Their studies, utilizing cost models applied to Milan, demonstrated that crowdsourcing significantly reduces per-delivery costs for both express and multi-parcel services. Specifically, they identified cost savings of approximately 11 % compared to traditional vans, attributing this advantage to the operational flexibility and higher delivery success rates inherent in the crowdsourcing model.

This study builds upon these foundations by formulating the order allocation problem between riders and ADVs as a dynamic, multi-objective optimization solved with a metaheuristic algorithm.

2.3 Delivery route optimization

The Vehicle Routing Problem (VRP) is the cornerstone of delivery optimization. This research focuses specifically on VRP with Time Windows (VRPTW), which is paramount for time-sensitive fresh grocery delivery.

Research on VRP with Time Windows has diversified to model various real-world constraints. A key distinction is made between hard (infeasible to violate) and soft (violatable with penalty) time windows. Errico *et al*. [18] addressed a VRPTW with stochastic service times using a two-stage stochastic programming model solved by a branch-cut-and-price algorithm, providing exact solutions for medium-scale problems. Ghannadpour *et al*. [19] tackled uncertainty by introducing fuzzy time windows in a multi-objective dynamic VRP solved with a genetic algorithm.

The rise of collaborative and multi-modal delivery has introduced new VRP variants. Wang *et al*. [20] studied a two-stage location-routing problem with hard time windows, solved with an improved NSGA-II algorithm.

In the context of two-echelon distribution network optimization, Jiao *et al*. [21] investigated the low-carbon multimodal vehicle logistics route optimization problem with timetable limits using Particle Swarm Optimization, demonstrating the synergistic effects of multimodal transportation in reducing both carbon emissions and costs. Furthermore, Xiao and Lan [22] proposed a two-echelon drone-truck collaborative TSP-based routing model for humanitarian logistics with time windows and stochastic demand, providing important methodological references for the two-echelon human-robot relay delivery network in this study.

Solving algorithms for these complex NP-hard problems are predominantly metaheuristic or hybrid in nature. Mohammed *et al*. [23] applied an improved genetic algorithm for campus bus routing. Huang *et al*. [24] used a genetic algorithm hybridized with local search (IGALS) for a VRPTW with simultaneous pickup and delivery. Hybrid approaches are particularly effective. Zhang *et al*. [25] combined an artificial bee colony algorithm with tabu search for cold chain logistics VRP. Zhang *et al*. [26] established a single-objective model to minimize the maximum delivery time for emergency rescue, demonstrating that reducing waiting and transport times is essential for system effectiveness. Similarly, our study prioritizes strict delivery time windows to ensure the freshness and punctuality of instant orders.

Li *et al*. [27] developed a cost model for drone-rider collaborative food delivery. By optimizing transfer station locations using genetic algorithms and conducting comprehensive cost analysis, they identified specific service radii where the total cost of collaboration undercuts the rider-only mode, providing crucial quantitative support for human-robot collaboration strategies. In metropolitan environments, static path planning often fails to meet the strict timeliness requirements of instant delivery due to fluctuating traffic conditions. Li *et al*. [28] demonstrated the effectiveness of integrating real-time traffic flow prediction into path planning algorithms. Similarly, our collaborative model accounts for dynamic travel times to optimize the interaction between riders and ADVs. To effectively manage the complexity of large-scale logistics networks (e.g., 120 nodes), decomposing the problem is often necessary. Zhang *et al*. [29] proposed a two-stage algorithm design that utilizes K-means clustering to group demand points before applying a genetic algorithm for routing.

Recently, Zhao *et al*. [30] published a study on synchronized deliveries with a bike and a self-driving robot (TSPBR), a problem setting highly similar to the human-ADV collaborative model in this paper. Beyond this comparison, the novelty of our work lies in two aspects. First, operationally, we address the practical limitations of current ADVs (short range, high empty-load rate, chaotic routes) by integrating them with riders into a unified delivery system that leverages complementary strengths. Second, algorithmically, we improve the genetic algorithm by redesigning the chromosome encoding scheme: unlike traditional encoding that includes only one rider type and uses the store as the separator, our scheme sequentially incorporates full-route riders, relay riders, and ADVs within one chromosome, with relay rider sub-paths separated by transfer points instead of the store. These distinctive features constitute the main novelty of this paper compared to existing two-echelon, relay, and collaborative routing studies.

Recent studies have also explored customer-centric last-mile delivery optimization. Wang and Huang [31] investigated urban end-delivery paths considering consumers' delivery time preferences using an ALNS algorithm, showing that personalized delivery time services increase delivery costs by approximately 20 % while generating additional revenue. Zhao *et al*. [32] further studied the vehicle routing problem considering customers' multiple preferences (delivery time, location, and mode) and demonstrated that preference constraints significantly affect total delivery costs when the average preference probability exceeds 0.5. These studies highlight the importance of incorporating customer preferences into last-mile delivery optimization, which aligns with the time window constraints considered in our human-robot collaborative model.

In summary, while extensive literature exists on HRC, order allocation, and VRP individually, their intersection in the context of a human-ADV hybrid delivery system for fresh supermarkets remains underexplored. This research synthesizes concepts from these three streams to develop an integrated model and solution methodology for this emerging logistics paradigm.

2.4 Unmanned delivery policies and development trends

The global regulatory framework for unmanned delivery is rapidly evolving as nations seek to balance innovation with public safety concerns. The United States has adopted a decentralized approach in which the National Highway Traffic Safety Administration provides federal guidance while states like California and Texas have developed their own specific regulations governing autonomous delivery vehicle testing and deployment. The European Union has implemented a comprehensive Strategy on Automated Mobility that emphasizes standardization and cross-border testing compatibility, though its strict privacy regulations under the GDPR create additional compliance requirements for drone operations. Japan stands out for its proactive legislative approach, having formally revised its Road Traffic Act to explicitly accommodate unmanned delivery vehicles in public spaces. Singapore has emerged as a particularly progressive testing ground through initiatives like the TRUST trial framework and National Drone Initiative that actively encourage real-world commercialization and even cross-border drone logistics experiments. These international policy developments demonstrate a spectrum of regulatory philosophies, ranging from cautious permission to active promotion, while addressing core concerns about safety, privacy, and integration with existing transportation systems. Some other countries have adopted a relatively loose regulatory approach, leaving the development of driverless and unmanned delivery to autonomous exploration by enterprises or local organizations, with the relevant policies, as shown in Fig. 1.

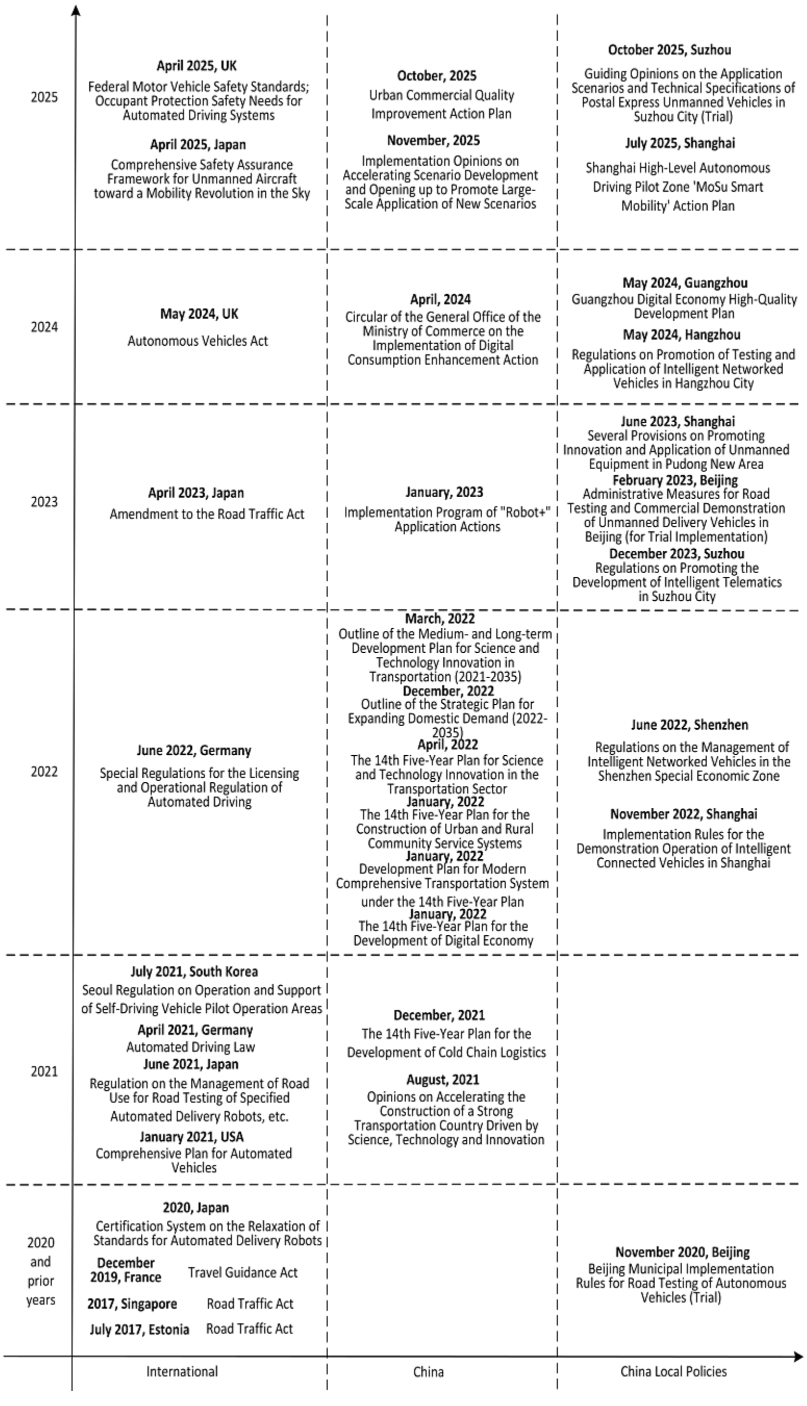

2025	**April 2025, UK** Federal Motor Vehicle Safety Standards; Occupant Protection Safety Needs for Automated Driving Systems **April 2025, Japan** Comprehensive Safety Assurance Framework for Unmanned Aircraft toward a Mobility Revolution in the Sky	**October, 2025** Urban Commercial Quality Improvement Action Plan **November, 2025** Implementation Opinions on Accelerating Scenario Development and Opening up to Promote Large-Scale Application of New Scenarios	**October 2025, Suzhou** Guiding Opinions on the Application Scenarios and Technical Specifications of Postal Express Unmanned Vehicles in Suzhou City (Trial) **July 2025, Shanghai** Shanghai High-Level Autonomous Driving Pilot Zone 'MoSu Smart Mobility' Action Plan
2024	**May 2024, UK** Autonomous Vehicles Act	**April, 2024** Circular of the General Office of the Ministry of Commerce on the Implementation of Digital Consumption Enhancement Action	**May 2024, Guangzhou** Guangzhou Digital Economy High-Quality Development Plan **May 2024, Hangzhou** Regulations on Promotion of Testing and Application of Intelligent Networked Vehicles in Hangzhou City
2023	**April 2023, Japan** Amendment to the Road Traffic Act	**January, 2023** Implementation Program of "Robot+" Application Actions	**June 2023, Shanghai** Several Provisions on Promoting Innovation and Application of Unmanned Equipment in Pudong New Area **February 2023, Beijing** Administrative Measures for Road Testing and Commercial Demonstration of Unmanned Delivery Vehicles in Beijing (for Trial Implementation) **December 2023, Suzhou** Regulations on Promoting the Development of Intelligent Telematics in Suzhou City
2022	**June 2022, Germany** Special Regulations for the Licensing and Operational Regulation of Automated Driving	**March, 2022** Outline of the Medium- and Long-term Development Plan for Science and Technology Innovation in Transportation (2021-2035) **December, 2022** Outline of the Strategic Plan for Expanding Domestic Demand (2022-2035) **April, 2022** The 14th Five-Year Plan for Science and Technology Innovation in the Transportation Sector **January, 2022** The 14th Five-Year Plan for the Construction of Urban and Rural Community Service Systems **January, 2022** Development Plan for Modern Comprehensive Transportation System under the 14th Five-Year Plan **January, 2022** The 14th Five-Year Plan for the Development of Digital Economy	**June 2022, Shenzhen** Regulations on the Management of Intelligent Networked Vehicles in the Shenzhen Special Economic Zone **November 2022, Shanghai** Implementation Rules for the Demonstration Operation of Intelligent Connected Vehicles in Shanghai
2021	**July 2021, South Korea** Seoul Regulation on Operation and Support of Self-Driving Vehicle Pilot Operation Areas **April 2021, Germany** Automated Driving Law **June 2021, Japan** Regulation on the Management of Road Use for Road Testing of Specified Automated Delivery Robots, etc. **January 2021, USA** Comprehensive Plan for Automated Vehicles	**December, 2021** The 14th Five-Year Plan for the Development of Cold Chain Logistics **August, 2021** Opinions on Accelerating the Construction of a Strong Transportation Country Driven by Science, Technology and Innovation	
2020 and prior years	**2020, Japan** Certification System on the Relaxation of Standards for Automated Delivery Robots **December 2019, France** Travel Guidance Act **2017, Singapore** Road Traffic Act **July 2017, Estonia** Road Traffic Act		**November 2020, Beijing** Beijing Municipal Implementation Rules for Road Testing of Autonomous Vehicles (Trial)
	International	China	China Local Policies

Fig. 1 Domestic and foreign policies related to unmanned delivery industry

China has demonstrated a strong national commitment to developing its unmanned delivery sector through coordinated policy support and local implementation. The central government has established a clear strategic direction through a series of top-level policies that provide both guidance and standards for industry development. Ji *et al*. [33] developed an evolutionary game model between government and automobile enterprises, demonstrating that reward and punishment policies significantly influence firms' transition to new energy production and that erroneous policy implementation can alter equilibrium outcomes. This finding highlights the importance of policy design in guiding industrial transformation. This national framework has been effectively operationalized at the local level, with key cities including Beijing, Shanghai, and Shenzhen creating detailed implementation rules and designated zones for testing and demonstration operations. This multi-level governance approach has created a structured yet adaptable environment that supports technological advancement while maintaining oversight, reflecting China's methodical strategy for nurturing emerging technologies through policy-enabled ecosystems.

Driven by falling costs and tech upgrades like V2X, the unmanned delivery market is surging, particularly in China. Application scenarios are expanding from food delivery to medical and campus logistics. Meanwhile, policymakers worldwide are refining regulations to support safe, large-scale deployment.

3. Mathematical model

3.1 Problem statement and assumptions

The optimization of last-mile delivery in China's major cities, characterized by high order density and complex logistics networks, presents significant challenges for contemporary retail models. To investigate these challenges in a concrete operational context within the Chinese market, this study selects QX Fresh Supermarket as a representative case for empirical analysis. This research addresses the last-mile delivery optimization problem for QX Fresh Supermarket within the new retail context. The supermarket operates on an “online order, offline delivery” model, featuring a hierarchical distribution network with a “single distribution center – multiple transfer points – multiple customers” structure, as shown in Fig. 2. Customers place orders via an online platform, specifying their expected delivery time windows, which are then fulfilled by the nearest store.

Fig. 2 Schematic diagram of the distribution network structure

Currently, QX Fresh Supermarket employs two delivery modes:

1. Direct Rider Delivery: Riders collect orders from the store and deliver them directly to all customers before returning to the store.
2. Human-Robot Relay Delivery: Unmanned delivery vehicles transport batches of orders to designated transfer points, where relay riders subsequently complete the delivery from the transfer point to the final customers.

However, significant issues exist in the current operation: order allocation between riders and unmanned vehicles relies heavily on experience, lacking systematic optimization. This results in low loading rates for unmanned vehicles, resource idling, and a failure to fully leverage their inherent cost advantages. Consequently, the core research problem is to scientifically allocate orders to riders or unmanned vehicles while simultaneously optimizing their respective delivery routes, aiming to minimize the total distribution cost, all under the constraints of customer time windows and vehicle capacity.

3.2 Parameters and decision variables

The following fundamental assumptions are made to formulate the mathematical model:

1. The travel speeds of unmanned vehicles and riders are constant and unaffected by traffic congestion.
2. The demand, delivery location, and time window for all customer orders are known.
3. A single order cannot be split and must be completed by the same delivery unit.
4. Relay riders are immediately available for handover when unmanned vehicles arrive at transfer points, resulting in zero waiting time.
5. The service time at customer points and transfer points is a fixed constant.

Table 1 Parameters and decision variables

Type	Symbol	Definition
Model parameters	M	Set of customer points to be served, $g, h \in M$
	N	Set of transfer points, ($i, j = 0$ denotes the store) $i, j \in N$
	K	Set of autonomous delivery vehicles, $k \in K$
	P	Set of full-route riders, $p \in P$
	U	Set of relay riders, $u \in U$
	Q_1	Maximum order capacity per autonomous vehicle
	Q_2	Maximum order capacity per rider
	q_j	The quantity of delivery orders reaching the transfer point j
	v_k	Average delivery speed of autonomous vehicles
	v_p	Average delivery speed of riders
	e_1	Per-kilometer delivery cost for autonomous vehicles
	e_2	Per-order delivery cost for full-route riders
	e_3	Per-order delivery cost for relay riders
	e_4	Loading cost per order for autonomous vehicles
	D_{ij}	the distance of the unmanned delivery vehicle from transfer point i to transfer point j
	d_{gh}	the distance from customer point g to customer point h for the rider
	ET_g	Earliest delivery time at customer
	LT_g	Latest delivery time at customer
Auxiliary variables	t_{ij}	The time it takes for the unmanned delivery vehicle to travel from transfer point i to transfer point j,t_{0i}represents the time it takes to travel from the store to transfer point i
	t_{gh}	The time it takes for the rider to travel from customer point g to customer point h,t_{og} indicates the time it takes to travel from the store to customer point g
	t_λ	Service time required by the rider at a single customer point
	t_μ	Service time required by the unmanned delivery vehicle at a single transfer point
Decision variables	X_{ij}^k	Binary variable: $X_{ij}^k = 1$ if unmanned delivery vehicle k travels from transfer point i to transfer point j; $X_{ij}^k = 0$otherwise
	Y_{gh}^p	Binary variable:$Y_{gh}^p = 1$ if full-route rider p travels from customer point g to customer point h; $Y_{gh}^p = 0$ otherwise
	Z_{gh}^u	Binary variable: $Z_{gh}^u = 1$ if shuttle rider u travels from customer point g to customer point h; $Z_{gh}^u = 0$otherwise
	W_{ig}	Binary variable: W_{ig}if customer point g is served by transfer point i; W_{ig} otherwise
	V_{ug}	Binary variable: $V_{ug} = 1$ if shuttle rider u serves customer point g; $V_{ug} = 0$ otherwise
	R_i^k	Binary variable: $R_i^k = 1$ if unmanned delivery vehicle k serves transfer point i; $R_i^k = 0$ otherwise

It should be noted that Assumption 4 (zero waiting time at transfer points) is an idealized simplification of reality. In practice, the temporal uncertainty of human behavior can significantly affect collaboration efficiency. A potential approach to address this issue is to adopt a two-layer optimization framework combining offline pre-optimization with online reactive adjustment. In future research, such a framework can be explored to incorporate stochastic waiting times at transfer point handovers into our model, enhancing its applicability in real dynamic environments.

The model parameters, auxiliary variables, and decision variables are listed in Table 1.

3.3 Model formulation

The objective of this study is to minimize the total distribution cost, which primarily consists of three components:

1. Unmanned vehicle transportation cost C_1: Proportional to the total travel distance.

$$C_1 = \sum_{k=1}^{K}\sum_{i=0}^{N}\sum_{j=0}^{N} e_1 D_{ij} X_{ij}^{k} \tag{1}$$

2. Unmanned vehicle loading cost C_2: Proportional to the total number of orders delivered by unmanned vehicles.

$$C_2 = \sum_{i=1}^{N}\sum_{g=1}^{M}\sum_{k=1}^{K} e_4 W_{ig}\, R_i^{k} \tag{2}$$

3. Rider delivery cost C_3: Includes the costs of both direct riders and relay riders.

$$C_3 = \sum_{p=1}^{P}\sum_{g=0}^{M}\sum_{h=0}^{M} e_2 Y_{gh}^{p} + \sum_{u=1}^{U}\sum_{g=0}^{M}\sum_{h=0}^{M} e_3 Z_{gh}^{u} \tag{3}$$

Thus, the total objective function is:

$$C = C_1 + C_2 + C_3 = \sum_{k=1}^{K}\sum_{i=0}^{N}\sum_{j=0}^{N} e_1 D_{ij} X_{ij}^{k} + \sum_{i=1}^{N}\sum_{g=1}^{M}\sum_{k=1}^{K} e_4 W_{ig}\, R_i^{k} + \sum_{p=1}^{P}\sum_{g=0}^{M}\sum_{h=0}^{M} e_2 Y_{gh}^{p} + \sum_{u=1}^{U}\sum_{g=0}^{M}\sum_{h=0}^{M} e_3 Z_{gh}^{u} \tag{4}$$

Eqs. 5-7 enforce flow conservation for unmanned delivery vehicles, ensuring they originate from and return to the distribution center while maintaining flow balance at transfer points. Similarly, routing logic and path continuity for full-route and relay riders are defined by Eqs. 8-13. Service completeness is guaranteed by Eqs. 14-15, which mandate that each customer order is fulfilled exactly once by a single rider. Capacity constraints for ADVs, full-route riders, and relay riders are formulated in Eqs. 16-18, respectively. Eqs. 19-22 govern the temporal aspects, ensuring arrival times fall within customer time windows and calculating travel duration between nodes. Finally, the logical dependencies between order assignment and routing variables are established in Eqs. 23-24.

$$\sum_{i=1}^{N} X_{i0}^{k} = 1, k \in K \tag{5}$$

$$\sum_{j=1}^{N} X_{0j}^{k} = 1, k \in K \tag{6}$$

$$\sum_{i=1}^{N} X_{ij}^{k} = \sum_{i=1}^{N} X_{ji}^{k}, j \in N, k \in K \tag{7}$$

$$\sum_{g=1}^{M} Y_{g0}^{p} = 1, p \in P \tag{8}$$

$$\sum_{h=1}^{M} Y_{0h}^{p} = 1, p \in P \tag{9}$$

$$\sum_{g=1}^{M} Y_{gh}^{p} = \sum_{g=1}^{M} Y_{hg}^{p}, h \in M, p \in P \tag{10}$$

$$\sum_{g=1}^{M} Y_{gh}^{p} = \sum_{g=1}^{M} Y_{hg}^{p}, h \in M, p \in P \tag{11}$$

$$\sum_{h=1}^{M} Z_{0h}^{u} = 1, u \in U \tag{12}$$

$$\sum_{g=1}^{M} Z_{gh}^{u} = \sum_{g=1}^{M} Z_{hg}^{u}, h \in M, u \in U \tag{13}$$

$$\sum_{i=1}^{N} W_{ig} + \sum_{p=1}^{P} \sum_{h=1}^{M} Y_{hg}^{p} = 1, g \in M \tag{14}$$

$$\sum_{g=0}^{M} \sum_{p=1}^{P} Y_{gh}^{p} + \sum_{g=0}^{M} \sum_{u=1}^{U} Z_{gh}^{u} = 1, h \in M \tag{15}$$

$$\sum_{i=0}^{N} \sum_{j=0}^{N} q_j X_{ij}^{k} \leq Q_1, k \in K \tag{16}$$

$$\sum_{g=0}^{M} \sum_{h=0}^{M} Y_{gh}^{p} \leq Q_2, p \in P \tag{17}$$

$$\sum_{g=1}^{M} \sum_{h=0}^{M} Z_{gh}^{u} \leq Q_2, u \in U \tag{18}$$

$$ET_g \leq t_{0g} \leq LT_g, g \in M \tag{19}$$

$$t_{0j} = \left(t_{0i} + t_{\mu} + t_{ij}\right) X_{ij}^{k}, i, j \in N, k \in K \tag{20}$$

$$t_{0h} = \left(t_{0g} + t_{\lambda} + t_{gh}\right) Y_{gh}^{p}, g, h \in M, p \in P \tag{21}$$

$$t_{0h} = \left(t_{0g} + t_{\lambda} + t_{gh}\right) Z_{gh}^{u}, g, h \in M, u \in U \tag{22}$$

$$\sum_{g=1}^{M} \sum_{h=1}^{M} \sum_{p=1}^{P} Y_{gh}^{p} + \sum_{g=1}^{M} \sum_{h=1}^{M} \sum_{u=1}^{U} Z_{gh}^{u} = M \tag{23}$$

$$\sum_{g=1}^{M} \sum_{k=1}^{K} X_{ji}^{k} \cdot W_{ig} = \sum_{g=1}^{M} \sum_{u=1}^{U} V_{ug} \cdot W_{ig}, i \in N \tag{24}$$

This formulation constitutes a complex Mixed-Integer Linear Programming (MILP) model, which is computationally intractable for large-scale instances when using exact methods. Therefore, Section 4 presents an efficient metaheuristic algorithm to obtain high-quality solutions.

4. Solution algorithm

In terms of algorithm design, Ostermeier and Huf [34] studied the multi-vehicle truck-and-robot routing problem and proposed a specialized heuristic based on a novel neighborhood search. Their algorithmic framework provides a useful reference for the design of our Improved Genetic Algorithm (IGA).

To build a suitable solution methodology, this section conducts an adaptability analysis of various intelligent optimization algorithms for the complex human-robot collaborative delivery problem. Han and Song [35] applied hybrid metaheuristic algorithms to robot path planning problems in shop-floor environments. Given the multiple nonlinear constraints in this problem, the genetic algorithm demonstrates greater applicability to the route optimization problem in this study than other intelligent algorithms, such as particle swarm optimization and simulated annealing, owing to its population-based search mechanism and strong global optimization capability.

Accordingly, the main procedure of the Improved Genetic Algorithm is illustrated in Fig. 3. It iteratively evolves a population of solutions by simulating the processes of natural selection and genetics, ultimately converging towards an optimal or near-optimal solution.

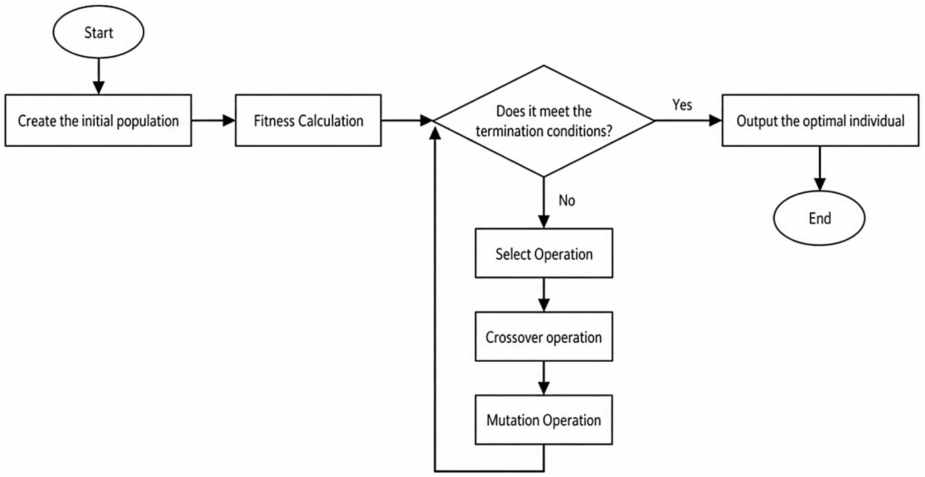

Fig. 3 Flowchart of the Improved Genetic Algorithm

Step 1: Encoding and decoding

Natural number encoding is adopted to represent the solution. The chromosome structure is defined as a sequence, where [symbol] represents the distribution center, [symbol] denotes customer nodes, and [symbol] denotes transfer points. During decoding, the algorithm sequentially reads the gene sequence and assigns tasks to full-route riders, ADVs, or relay riders by strictly verifying capacity and time window constraints.

Step 2: Population initialization

To ensure both population diversity and solution quality, a hybrid initialization strategy is implemented comprising four sub-strategies:

- Spatiotemporal clustering: Grouping orders with close geographical locations and overlapping time windows.
- Loading rate optimization: Prioritizing sequences that maximize vehicle capacity utilization.
- Transfer point constraints: Ensuring relay orders are mapped to their feasible transfer service scopes.
- Random permutation: Introducing randomness to prevent the algorithm from getting trapped in local optima early.

Step 3: Fitness function

Since the objective is to minimize the total delivery cost, the fitness function is defined as the reciprocal of the objective function value to convert the minimization problem into a maximization one.

Step 4: Genetic operators

Selection: A hybrid mechanism combining tournament selection and roulette wheel selection is employed. This approach maintains sufficient selection pressure to preserve elite individuals while ensuring population diversity.

Crossover: The Order Crossover (OX) operator is utilized to generate offspring. By preserving the relative order of genes from parent chromosomes, OX helps maintain valid permutations in permutation-based encoding, although additional decoding and feasibility checks are still required to satisfy problem-specific constraints. The crossover probability is set to 0.8.

Mutation: An adaptive Inversion Mutation operator is applied. Two gene loci are randomly selected, and the sequence between them is reversed. This operation enhances the algorithm's local search ability. The mutation probability is initially set to 0.2 and adjusts adaptively based on population diversity. Păun *et al*. [36] successfully applied an improved multi-objective genetic algorithm to optimize power consumption in flexible manufacturing systems.

Although Zhang and Zhou [37] focused on factory AGV systems rather than urban instant delivery, their AIGC-enhanced MPC framework for dynamic congestion management still provides a useful methodological reference for extending our static IGA model toward dynamic, real-time scheduling.

5. Numerical experiments

5.1 Case setup

To validate the effectiveness of the proposed model and algorithm, this study employs real operational data from an offline store of QX Fresh Supermarket in Beijing. The store's delivery service covers an area within a 3-kilometer radius. Experimental data consists of 80 orders placed within a 15-minute time window (10:00 – 10:15 AM) on a specific Saturday. This period ensures sufficient order volume and wide geographical distribution, effectively covering the entire delivery area. For computational convenience, all time data were converted into timestamp format using Eq. 25.

$$T_n = [T_0] + \frac{(T_0 - [T_0]) \times 100}{60} \tag{25}$$

The store's delivery network includes 16 pre-set transfer points. Travel distances and times between any two points were obtained using the Amap API to reflect real road conditions, rather than approximating them with Euclidean or Manhattan distances. The spatial distribution of the store, transfer points, and the 80 customer points is visualized in Fig. 4, where the red square represents the store, blue triangles represent transfer points, and green circles represent customer points.

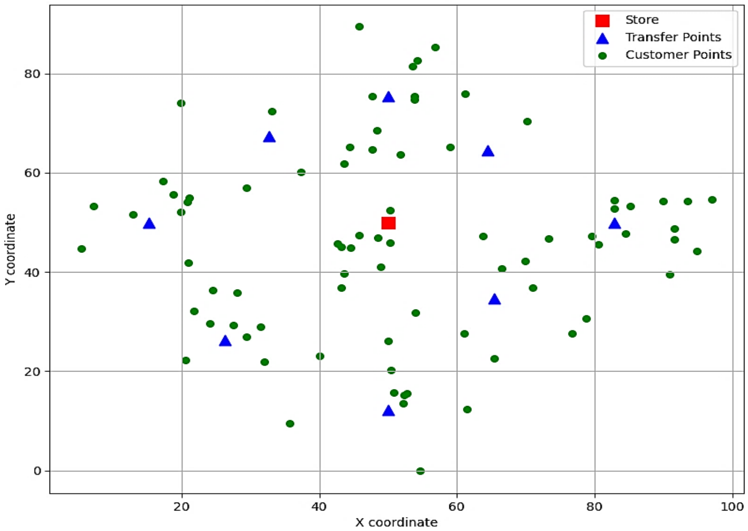

Fig. 4 Customer point distribution diagram

5.2 Parameter setting

Experimental parameters were set based on field research and are categorized into model parameters and algorithm parameters, as detailed in Table 2.

Table 2 Model and algorithm parameters

Parameter type	Parameter name	Parameter value
Model parameters	Unmanned vehicle speed	11 km/h
	Full-route rider speed	25 km/h
	Shuttle rider speed	25 km/h
	Unmanned vehicle capacity	16 orders
	Rider electric vehicle capacity	6 orders
	Unmanned vehicle loading cost	¥0.5/order
	Unmanned vehicle travel cost	¥0.2/km
	Full-route rider delivery fee	¥6/order
	Shuttle rider delivery fee	¥3/order
Algorithm parameters	Population size	80
	Crossover probability	0.8
	Mutation probability	0.2
	Iteration count	200

5.3 Solution process and results

The model was implemented in Python 3.11 and executed on a PC with a 13th Gen Intel i5 processor and 16 GB of RAM. The convergence process of the Improved Genetic Algorithm is shown in Fig. 5. The algorithm converged after approximately 20 generations, with the objective function value (total delivery cost) stabilizing at 341.9 CNY, demonstrating satisfactory convergence performance.

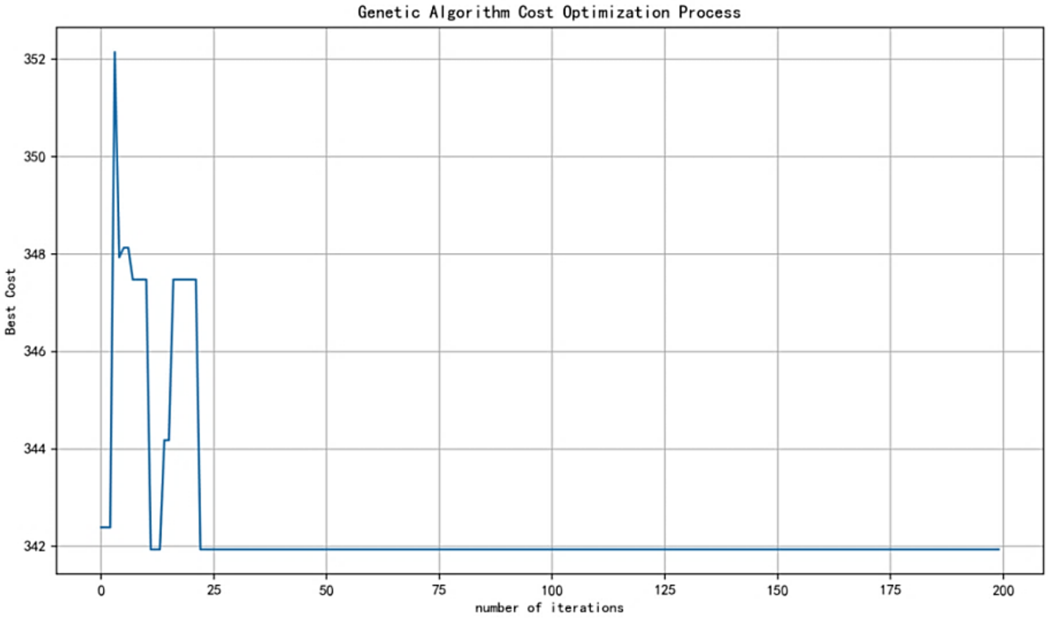

Fig. 5 Cost iteration graph

The optimized delivery plan for the 80 orders is as follows: the task is completed collaboratively by 7 full-route riders, 19 transfer riders, and 6 unmanned delivery vehicles. Among these, 20 orders are delivered directly by full-route riders, while the remaining 60 orders are delivered via the human-robot relay mode. Fig. 6 illustrates the final delivery routes, where cool-colored dashed lines represent full-route rider paths and warm-colored dotted lines represent transfer rider paths.

The specific routes for the unmanned delivery vehicles are listed in Table 3. The results indicate a relatively balanced order allocation across transfer points. The proposed scheme satisfies all customer time window constraints while achieving optimized delivery costs.

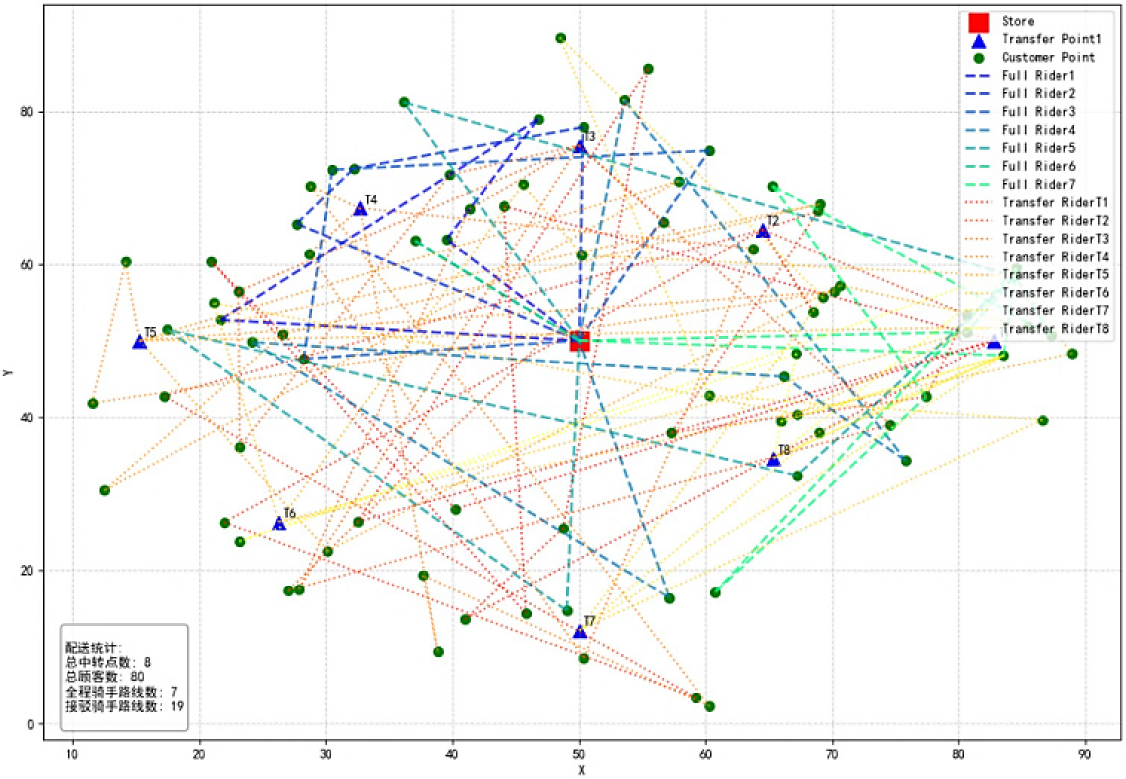

Fig. 6 Order delivery routes

Table 3 Delivery routes of unmanned delivery vehicles

Vehicle ID	Delivery Route
1	0-1-8-0
2	0-2-3-0
3	0-4-5-0
4	0-6-7-0

5.4 Sensitivity analysis

To comprehensively evaluate the model's performance, additional scenarios with low (30 orders), regular (60 orders), and peak (120 orders) order volumes were tested. The human-robot collaborative delivery mode was compared with the traditional full-route rider delivery mode. The results are summarized in Table 4.

Key findings include:

- The human-robot collaboration mode effectively reduces delivery costs by 30-34 % across all order volume scenarios.
- As the order volume increases, the average loading rate of unmanned vehicles significantly improves from 36 % during the low period to 70 % during the peak period, highlighting the economies of scale.
- During the peak period, the average delivery load per transfer rider reaches 4 orders, indicating optimized resource utilization.

Table 4 Statistics on delivery conditions for different order volumes

Order volume	Original delivery cost (¥)	Human-robot collaborative cost (¥)	Cost reduction (%)	Full-route rider orders	Shuttle rider orders	Unmanned vehicles deployed	Vehicle utilization rate
30 orders	180	117.2	34	7	23	4	0.36
60 orders	360	244.8	32	15	45	6	0.47
120 orders	720	504.5	30	30	90	8	0.7

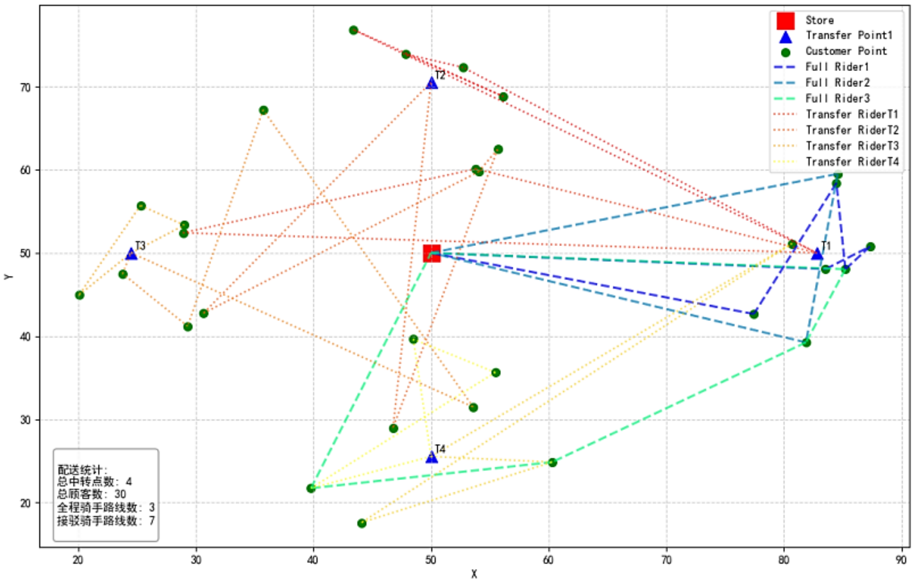

Fig. 7 Delivery routes for low volume (30 orders)

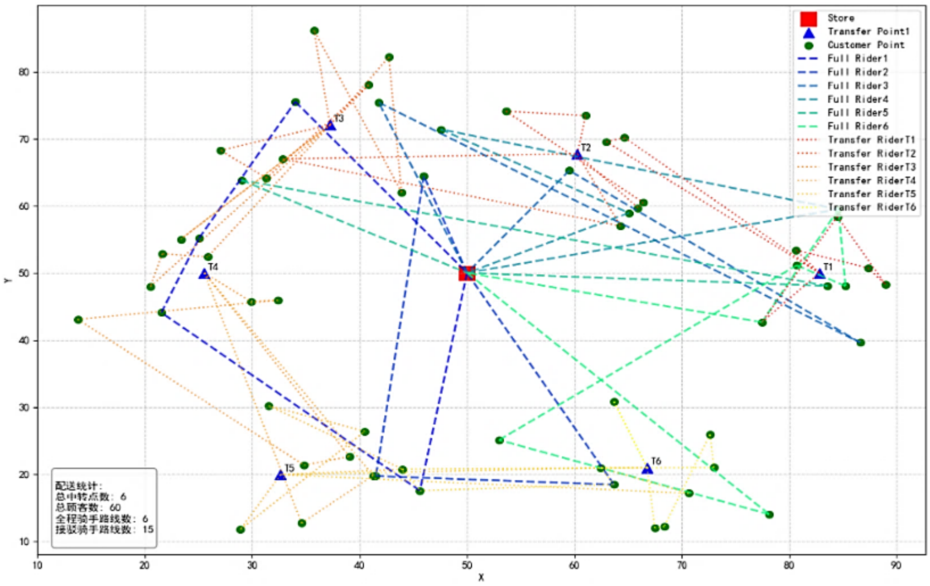

Fig. 8 Delivery route map for regular volume (60 orders)

The visualized delivery routes for the three scenarios are shown in Fig. 7 (Low), Fig. 8 (Regular), and Fig. 9 (Peak), respectively.

This section investigates the impact of key resource configurations (number of transfer points, number of unmanned vehicles) on the total cost. Sensitivity analyses were conducted by varying these two parameters under different order volumes.

Low Order Volume (30 orders): As shown in Table 5, the lowest total cost (117.2 CNY) is achieved with 4 transfer points and 4 unmanned vehicles. Considering resource conservation, using 4 transfer points and 2 vehicles slightly increases cost but significantly improves the vehicle loading rate.

Regular Order Volume (60 orders): Table 6 shows that configuring 6 transfer points with 6 vehicles, or 8 transfer points with 8 vehicles, are both cost-effective options. The key is to ensure that the number of vehicles is not less than the number of transfer points, while avoiding a significant surplus of vehicles.

Peak Order Volume (120 orders): According to Table 7, configuring 8 transfer points and 8 unmanned vehicles achieves the optimal cost (504.5 CNY) and the highest vehicle loading rate.

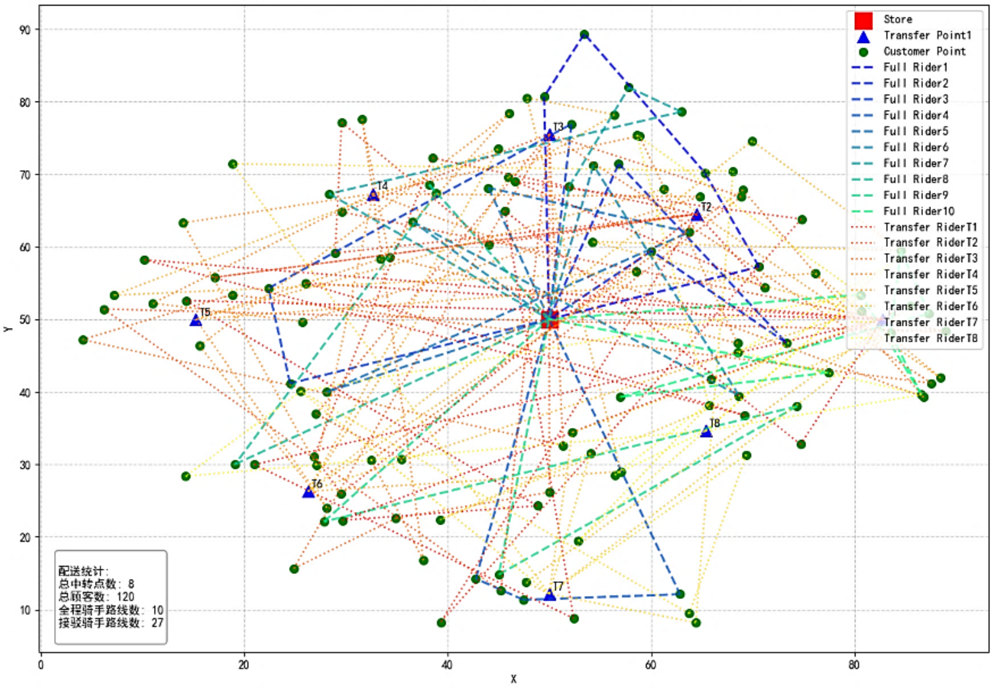

Fig. 9 Delivery route map for peak volume (120 orders)

Table 5 Delivery cost for low order volume

Cost of delivery for 30 orders	Unmanned vehicles deployed		
Number of transfer points	2	3	4
2	121.4	121.4	121.4
4	119.7	119.3	117.2
6	-	120.1	118.4

Table 6 Delivery cost for regular order volume

Cost of delivery for 60 orders	Unmanned vehicles deployed		
Number of transfer points	4	6	8
4	264	260.6	260.1
6	251.5	244.8	246.4
8	254	246.8	243.4

Table 7 Delivery cost for peak order volume

Cost of delivery for 120 orders	Unmanned vehicles deployed		
Number of transfer points	6	8	10
6	523.4	521.6	517.2
8	518.3	504.5	506.2
10	515.6	517.3	512.3

6. Conclusion

This study establishes the core mechanism of human-robot collaborative delivery under static conditions, thereby providing a theoretical foundation for more complex dynamic extensions. Specifically, we address the last-mile delivery optimization problem for the fresh food retail sector by constructing a human-robot collaborative delivery model. Taking QX Fresh Supermarket as a case study, we formulate a multi-constraint optimization model that incorporates customer time windows, vehicle capacity constraints, and hybrid order allocation. To solve this NP-hard problem, we design an Improved Genetic Algorithm (IGA) that employs a natural number encoding scheme and adaptive genetic operators.

Empirical experiments demonstrate that the proposed collaborative mode significantly outperforms traditional rider-only models. Specifically, the hybrid approach achieves a total cost reduction of over 30 % across low, regular, and peak order volume scenarios. Sensitivity analysis further reveals that the optimal configuration of unmanned vehicles and transfer points varies with demand density, highlighting the necessity of dynamic resource scheduling.

The findings provide actionable strategies for urban logistics management. First, the adoption of Autonomous Delivery Vehicles (ADVs) effectively mitigates the "diseconomies of scale" associated with high labor costs in pure manual delivery, particularly for medium-distance, batch transport. Second, managers should move beyond static fleet sizing; dynamic deployment based on historical order density is crucial to balancing cost and efficiency. Finally, investing in intelligent decision support systems is essential to replace experience-based scheduling, ensuring precise coordination between riders and ADVs.

While this study validates the efficacy of human-robot collaboration, several avenues warrant further investigation. First, the current model focuses on one-way delivery; future research should integrate reverse logistics (e.g., returns) to better reflect complex operational realities. Second, although the IGA proved effective, this study does not include a systematic comparison with other metaheuristics. Comparative studies involving other metaheuristics (e.g., Ant Colony Optimization and Large Neighborhood Search) could further validate the robustness of the algorithm. Lastly, extending the model from static, single-period optimization to dynamic, real-time scheduling under stochastic demand remains a critical direction for future work.

Acknowledgment

The authors acknowledge the financial support from the Jingdong Modern Industry Institute Open Fund of Suqian University.

References

[1] Alirezazadeh, S., Alexandre, L.A. (2022). Dynamic task scheduling for human-robot collaboration, *IEEE Robotics and Automation Letters*, Vol. 7, No. 4, 8699-8704, doi: 10.1109/LRA.2022.3188906.

[2] Wu, B., Hu, B., Lin, H. (2017). Toward efficient manufacturing systems: A trust based human robot collaboration, In: *Proceedings of 2017 American Control Conference (ACC)*, Seattle, USA, 1536-1541, doi: 10.23919/ACC.2017.7963171.

[3] Ranz, F., Hummel, V., Sihn, W. (2017). Capability-based task allocation in human-robot collaboration, *Procedia Manufacturing*, Vol. 9, 182-189, doi: 10.1016/j.promfg.2017.04.011.

[4] Cai, H., Mostofi, Y. (2019). Human-robot collaborative site inspection under resource constraints, *IEEE Transactions on Robotics*, Vol. 35, No. 1, 200-215, doi: 10.1109/TRO.2018.2875389.

[5] Yao, B., Li, X., Ji, Z., Xiao, K., Xu, W. (2024). Task reallocation of human-robot collaborative production workshop based on a dynamic human fatigue model, *Computers & Industrial Engineering*, Vol. 189, Article No. 109855, doi: 10.1016/j.cie.2023.109855.

[6] Faccio, M., Granata, I., Minto, R. (2024). Task allocation model for human-robot collaboration with variable cobot speed, *Journal of Intelligent Manufacturing*, Vol. 35, No. 2, 793-806, doi: 10.1007/s10845-023-02073-9.

[7] Zhao, R.H., Tao, S.C., Li, P.Z. (2025). Safety-efficiency integrated assembly: The next-stage adaptive task allocation and planning framework for human-robot collaboration, *Robotics and Computer-Integrated Manufacturing*, Vol. 94, Article No. 102942, doi: 10.1016/j.rcim.2024.102942.

[8] Bruno, G., Antonelli, D. (2018). Dynamic task classification and assignment for the management of human-robot collaborative teams in workcells, *The International Journal of Advanced Manufacturing Technology*, Vol. 98, No. 9, 2415-2427, doi: 10.1007/s00170-018-2400-4.

[9] Vahedi-Nouri, B., Tavakkoli-Moghaddam, R., Hanzálek, Z., Dolgui, A. (2024). Production scheduling in a reconfigurable manufacturing system benefiting from human-robot collaboration, *International Journal of Production Research*, Vol. 62, No. 3, 767-783, doi: 10.1080/00207543.2023.2173503.

[10] Xu, W., Xu, S., Liu, D.Y., Awaga, A.L., Rabia, A.C., Zhang, Y.Y. (2024). Impact of fairness concerns on resource-sharing decisions: A comparative analysis using evolutionary game models in manufacturing enterprises, *Advances in Production Engineering & Management*, Vol. 19, No. 2, 223-238, doi: 10.14743/apem2024.2.503.

[11] Sodenkamp, M.A., Tavana, M., Di Caprio, D. (2016). Modeling synergies in multi-criteria supplier selection and order allocation: An application to commodity trading, *European Journal of Operational Research*, Vol. 254, No. 3, 859-874, doi: 10.1016/j.ejor.2016.04.015.

[12] Xiang, W., Song, F.S., Ye, F.F. (2014). Order allocation for multiple supply-demand networks within a cluster, *Journal of Intelligent Manufacturing*, Vol. 25, No. 6, 1367-1376, doi: 10.1007/s10845-013-0735-0.

[13] Zhang, Z.Z., Zhang, L., Li, W.C. (2025). An improved adaptive variable neighborhood search algorithm for stochastic order allocation problem, *Scientific Reports*, Vol. 15, Article No. 481, doi: 10.1038/s41598-024-84663-y.

[14] Huq, F., Sultana, N., Roy, P., Razzaque, M.A., Huda, S., Hassan, M.M. (2025). Cross regional online food delivery: Service quality optimization and real-time order assignment, *Computers & Operations Research*, Vol. 173, Article No. 106877, doi: 10.1016/j.cor.2024.106877.

[15] Silva, K.O.A.N., Lima, R.S., Alves, R. (2024). The impacts of the pandemic on urban freight deliveries: A case study in a Brazilian carrier, *International Journal of Simulation Modelling*, Vol. 23, No. 1, 65-76, doi: 10.2507/IJSIMM23-1-672.

[16] Seghezzi, A., Mangiaracina, R. (2021). Investigating multi-parcel crowdsourcing logistics for B2C e-commerce last-mile deliveries, *International Journal of Logistics Research and Applications*, Vol. 25, No. 3, 260-277, doi: 10.1080/13675567.2021.1882411.

[17] Seghezzi, A., Mangiaracina, R., Tumino, A., Perego, A. (2021). 'Pony express' crowdsourcing logistics for last-mile delivery in B2C e-commerce: An economic analysis, *International Journal of Logistics Research and Applications*, Vol. 24, No. 5, 456-472, doi: 10.1080/13675567.2020.1766428.

[18] Errico, F., Desaulniers, G., Gendreau, M., Rei, W., Rousseau, L.M. (2016). A priori optimization with recourse for the vehicle routing problem with hard time windows and stochastic service times, *European Journal of Operational Research*, Vol. 249, No. 1, 55-66, doi: 10.1016/j.ejor.2015.07.027.

[19] Ghannadpour, S.F., Noori, S., Tavakkoli-Moghaddam, R., Ghoseiri, K. (2014). A multi-objective dynamic vehicle routing problem with fuzzy time windows: Model, solution and application, *Applied Soft Computing*, Vol. 14, 504-527, doi: 10.1016/j.asoc.2013.08.015.

[20] Wang, Y., Assogba, K., Liu, Y., Ma, X.L., Xu, M.Z., Wang, Y.H. (2018). Two-echelon location-routing optimization with time windows based on customer clustering, *Expert Systems with Applications*, Vol. 104, 244-260, doi: 10.1016/j.eswa.2018.03.018.

[21] Jiao, Z.H., Duan, H.W., Zhou, Y.J., Xiang, X. (2025). Low-carbon multimodal vehicle logistics route optimization with timetable limit using Particle Swarm Optimization, *Advances in Production Engineering & Management*, Vol. 20, No. 2, 173-190, doi: 10.14743/apem2025.2.534.

[22] Xiao, N., Lan, H. (2025). Two-echelon drone–truck collaborative TSP-based routing for humanitarian logistics with time windows and stochastic demand, *Advances in Production Engineering & Management*, Vol. 20, No. 3, 351-368, doi: 10.14743/apem2025.3.545.

[23] Mohammed, M.A., Abd Ghani, M.K., Hamed, R.I., Mostafa, S.A., Ahmad, M.S., Ibrahim, D.A. (2017). Solving vehicle routing problem by using improved genetic algorithm for optimal solution, *Journal of Computational Science*, Vol. 21, 255-262, doi: 10.1016/j.jocs.2017.04.003.

[24] Huang, W., Zhang, T. (2016). An improved genetic algorithm for vehicle routing problem with simultaneous pickups and deliveries and time windows, In: *Proceedings of 2016 35th Chinese Control Conference (CCC)*, Chengdu, China, 9639-9643, doi: 10.1109/ChiCC.2016.7554885.

[25] Zhang, D.F., Cai, S.F., Ye, F.R., Si, Y.-W., Nguyen, T.T. (2017). A hybrid algorithm for a vehicle routing problem with realistic constraints, *Information Sciences*, Vol. 394-395, 167-182, doi: 10.1016/j.ins.2017.02.028.

[26] Zhang, H.K., Zheng, Q.M., Yang, S., Ojsteršek, R. (2025). Bare-bones particle swarm optimization for emergency scheduling in public events, *International Journal of Simulation Modelling*, Vol. 24, No. 2, 273-284, doi: 10.2507/IJSIMM24-2-726.

[27] Li, Y., Liu, M., Hu, H., Jiang, X. (2025). A cost analysis of the collaborative delivery mode of drones and riders in food delivery scenarios, *International Journal of Logistics Research and Applications*, 1-30, doi: 10.1080/13675567.2025.2480636.

[28] Li, J., Li, J., Fang, H., Jiang, J. (2024). Dynamic energy-efficient path planning for electric vehicles using an enhanced Ant Colony Algorithm, *Tehnički Vjesnik – Technical Gazette*, Vol. 31, No. 2, 434-441, doi: 10.17559/TV-20230510000618.

[29] Zhang, Y., Chen, Y., Yu, P., Li, X., Wang, Y., Zhang, J., Pang, J. (2024). Optimization of multi-temperature joint distribution paths for convenience store chains, *Tehnički Vjesnik – Technical Gazette*, Vol. 31, No. 5, 1734-1746, doi: 10.17559/TV-20230812000875.

[30] Zhao, Y., Cattaruzza, D., Kang, N., Roberti, R. (2024). Synchronized deliveries with a bike and a self-driving robot, *Transportation Science*, Vol. 58, No. 1, 219-239, doi: 10.1287/trsc.2023.0169.

[31] Wang, W., Huang, Q. (2023). Research on urban end-delivery paths considering the consumer's delivery time demand, *Tehnički Vjesnik – Technical Gazette*, Vol. 30, No. 4, 1209-1216, doi: 10.17559/TV-20221212144331.

[32] Zhao, S., Li, P., Li, Q. (2024). The vehicle routing problem considering customers' multiple preferences in last-mile delivery, *Tehnički Vjesnik – Technical Gazette*, Vol. 31, No. 3, 734-743, doi: 10.17559/TV-20230717000807.

[33] Ji, X., Xu, W., Aslam, R., Yin , Y. (2024). The influence of government on automobile enterprise's production methods: An evolutionary game based study, *Economic Computation and Economic Cybernetics Studies and Research*, Vol. 58, No. 4, 223-240, doi: 10.24818/18423264/58.4.24.14.

[34] Ostermeier, M., Huf, T. (2026). The truck-and-robot routing problem with pickups and deliveries, *European Journal of Operational Research*, Vol 333, No. 1, 174-191, doi: 10.1016/j.ejor.2025.11.034.

[35] Han, Y., Song, T. (2024). Path planning for shop-floor material transfer robots incorporating particle swarm and ant colony algorithms, *Studies in Informatics and Control*, Vol. 33, No. 3, 49-59, doi: 10.24846/v33i3y202405.

[36] Păun, M.-A., Coandă, H.-G., Mincă, E., Iliescu, S.S., Duca, O.G., Stamatescu, G. (2024). Improved multi-objective genetic algorithm used to optimizing power consumption of an integrated system for flexible manufacturing, *Studies in Informatics and Control*, Vol. 33, No. 1, 27-36, doi: 10.24846/v33i1y202403.

[37] Zhang, X.R., Zhou, J.N. (2025). Simulation of AIGC-enhanced congestion management in factory autonomous driving, *International Journal of Simulation Modelling*, Vol. 24, No. 4, 718-729, doi: 10.2507/IJSIMM24-4-CO19.

Calendar of events

- 59th CIRP International Conference on Manufacturing Systems, 19–21 May 2026, Austin, Texas, USA.
- 54th North American Manufacturing Research Conference (NAMRC 54), 14–18 June 2026, State College, Pennsylvania, USA.
- 20th CIRP Conference on Intelligent Computation in Manufacturing Engineering (CIRP ICME 2026), 8–10 July 2026, Napoli, Italy.
- 2026 IEEE 22nd International Conference on Automation Science and Engineering, 17–21 August 2026, Shenyang, China.
- 75th CIRP General Assembly (CIRP GA 2026), 23–29 August 2026, Torino, Italy.
- 31st IEEE International Conference on Emerging Technologies and Factory Automation, 8–11 September 2026, Västerås, Sweden.
- ICAM 2026 – ASTM International Conference on Advanced Manufacturing, 28 September–2 October 2026, Orlando, FL, USA.
- 2026 8th International Conference on Industry of the Future and Smart Manufacturing (ISM 2026), 10–14 November 2026, Padua & Venice, Italy.
- 2026 MRS Fall Meeting & Exhibit, 29 November–4 December 2026, Boston, MA, USA.

Notes for contributors

General

Articles submitted to the *APEM journal* should be original and unpublished contributions and should not be under consideration for any other publication at the same time. Manuscript should be written in English. Responsibility for the contents of the paper rests upon the authors and not upon the editors or the publisher. The content from published paper in the *APEM journal* may be used under the terms of the Creative Commons Attribution 4.0 International Licence (CC BY 4.0). For most up-to-date information please see the APEM journal homepage *apem-journal.org*.

Submission of papers

A submission must include the corresponding author's complete name, affiliation, address, phone and fax numbers, and e-mail address. All papers for consideration by *Advances in Production Engineering & Management* should be submitted by e-mail to the journal Editor-in-Chief:

Miran Brezocnik, Editor-in-Chief
UNIVERSITY OF MARIBOR
Faculty of Mechanical Engineering
Chair of Production Engineering
Smetanova ulica 17, SI – 2000 Maribor
Slovenia, European Union
E-mail: apem@apem-journal.org

Manuscript preparation

Manuscript should be prepared in *Microsoft Word 2010* (or higher version) word processor. *Word .docx* format is required. Papers on A4 format, single-spaced, typed in one column, using body text font size of 11 pt, should not exceed 12 pages, including abstract, keywords, body text, figures, tables, acknowledgements (if any), references, and appendices (if any). The title of the paper, authors' names, affiliations and headings of the body text should be in *Calibri* font. Body text, figures and tables captions have to be written in *Cambria* font. Mathematical equations and expressions must be set in *Microsoft Word Equation Editor* and written in *Cambria Math* font. For detail instructions on manuscript preparation please see instruction for authors in the *APEM journal* homepage *apem-journal.org*.

The review process

Every manuscript submitted for possible publication in the *APEM journal* is first briefly reviewed by the editor for general suitability for the journal. Notification of successful submission is sent. After initial screening, and checking by a special plagiarism detection tool, the manuscript is passed on to at least two referees. A double-blind peer review process ensures the content's validity and relevance. Optionally, authors are invited to suggest up to three well-respected experts in the field discussed in the article who might act as reviewers. The review process can take up to eight weeks on average. Based on the comments of the referees, the editor will take a decision about the paper. The following decisions can be made: accepting the paper, reconsidering the paper after changes, or rejecting the paper. Accepted papers may not be offered elsewhere for publication. The editor may, in some circumstances, vary this process at his discretion.

Proofs

Proofs will be sent to the corresponding author and should be returned within 3 days of receipt. Corrections should be restricted to typesetting errors and minor changes.

Offprints

An e-offprint, i.e., a PDF version of the published article, will be sent by e-mail to the corresponding author. Additionally, one complete copy of the journal will be sent free of charge to the corresponding author of the published article.

APEM
journal

Advances in Production Engineering & Management

Chair of Production Engineering (CPE)
University of Maribor
APEM homepage: apem-journal.org

Volume 21 | Number 1 | March 2026 | pp 1-158

Contents

Published by CPE, University of Maribor

ISSN 1854-6250
9 771854 625008

apem-journal.org